THE ELECTRIFICATION OF STRATIFORM ANVILS

by

Dennis J. Boccippio

B.S.E., Princeton University (1990)

Submitted to the Department of Earth, Atmospheric and Planetary Science
in partial fulfillment of the requirements for the degree of

Doctor of Philosophy

at the

MASSACHUSETTS INSTITUTE OF TECHNOLOGY

December 1996
[February 1997]

Author ....
Department of Earth, Atmospheric and Planetary Science
September 26, 1996

Certified by ....
Kerry Emanuel
Thesis Co-Supervisor

Certified by ....
Earle R. Williams
Thesis Co-Supervisor

Accepted by ....
Thomas Jordan
Chairman, Departmental Committee on Graduate Students

The electrification of stratiform anvils

by

Dennis J. Boccippio

Submitted to the Department of Earth, Atmospheric and Planetary Science
on September 26, 1996, in partial fulfillment of the
requirements for the degree of
Doctor of Philosophy

Abstract

Stratiform precipitation regions accompany convective activity on many spatial scales. The electrification of these regions is anomalous in a number of ways. Surface and above-cloud fields are often "inverted" from normal thunderstorm conditions. Unusually large, bright, horizontal "spider" lightning and high current and charge transfer positive cloud-to-ground (CG) lightning dominates in these regions. Mesospheric "red sprite" emissions have to date been observed exclusively over stratiform cloud shields.

We postulate that a dominant "inverted dipole" charge structure may account for this anomalous electrification. This is based upon laboratory observations of charge separation which show that in low liquid water content (LWC) environments, or dry but ice-supersaturated environments, precipitation ice tends to charge positively (instead of negatively) upon collision with smaller crystals. Under typical stratiform cloud conditions, liquid water should be depleted and this charging regime favored. An inverted dipole would be the natural consequence of large-scale charge separation (net flux divergence of charged ice), given typical hydrometeor profiles.

The inverted dipole hypothesis is tested using radar and electrical observations of four weakly organized, late-stage systems in Orlando, Albuquerque and the Western Pacific. Time-evolving, area-average vertical velocity profiles are inferred from single Doppler radar data. These profiles provide the forcing for a 1-D steady state microphysical retrieval, which yields vertical hydrometeor profiles and ice/water saturation conditions. The retrieved microphysical parameters are then combined with laboratory charge transfer measurements to infer the instantaneous charging behavior of the systems.

Despite limitations in the analysis technique, the retrievals yield useful results. Total charge transfer drops only modestly as the storm enters the late (stratiform) stage, suggesting a continued active generator is plausible. Generator currents show an enhanced lowermost inverted dipole charging structure, which we may infer will result in a comparable inverted dipole charge structure, consistent with surface, in-situ and remote observations. Fine-scale vertical variations in ice and liquid water content may yield multipolar generator current profiles, despite unipolar charge transfer regimes. This suggests that multipoles observed in balloon soundings may not necessarily conflict with the simple ice-ice collisional charge separation mechanism. Overall, the results are consistent with, but not proof of, the inverted dipole model.

Thesis Supervisor: Kerry Emanuel
Title: Director, Center for Meteorology and Physical Oceanography, MIT

Thesis Supervisor: Earle R. Williams
Title: MIT Parsons Laboratory

Acknowledgments

I deeply thank Earle Williams for what has unquestionably been a wonderful and rewarding apprenticeship in my years at MIT. You have provided unique support, insight, encouragement and opportunities, and have always been open to new possibilities and healthy debate. If anyone's ever had my best interests in mind, it's been you. Thanks for a fantastic six years.

The work in this thesis wouldn't have been possible without the generous contributions of many colleagues. Mark Weber and Steve Rutledge deserve particular thanks for supporting my "extracurricular" use of the MIT C-band radar facilities. Vlad Mazur, Paul Krehbiel, Ken Cummins, Walt Lyons and Pierre LaRoche generously provided important lightning observations, often prior to their own publication of these data. Josh Wurman, Stan Heckman, Bob Boldi, Kevin Driscoll, Rob Cifelli and Walt Petersen deserve thanks for many hours of valuable discussion, encouragement and insight. Finally, I deeply thank Steve Goodman and Hugh Christian for a unique and rewarding co-op experience at NASA/MSFC.

My time at MIT would have been a sorry stay without the comaraderie of my colleagues. To my friends Chris Forest, Michael Morgan, James Risbey, Lars Schade, Danny Kirk-Davidoff and Gerard Roe; I'll always have the fondest memories of our many diversions from the travails of grad school. Election years will never be the same again!

I offer special thanks to Phildon and Stephen for your immeasurable patience, support and love. You both will always be a central part of these years.

As for patience, who has had more than my family, who never thought they'd see the end? Mom, Dad, Dan, and all my grandparents ... Thank You.

Finally, I must thank the crews at Mildred's and Five Points Espresso for endless hours of conversation, java and free electricity. Hardly a page contained herein wasn't written or revised at these two coffee shops. Thanks, guys! *DJB, September 1996*

When I heard then learn'd astronomer,
When the proofs, the figures, were ranged in columns before me,
When I was shown the charts and diagrams, to add, divide, and measure them,
When I sitting heard the astronomer where he lectured with much applause
in the lecture-room,
How soon unaccountable I became tired and sick,
Till rising and gliding out I wander'd off by myself,
In the mystical moist night-air, and from time to time,
Look'd up in perfect silence at the stars.

- Walt Whitman, 1865

Table of Contents

List of Figures

List of Tables

Chapter 1

Introduction

1.1 Characteristics of stratiform "anvil" systems

Mature precipitation systems of various scales typically share a common characteristic: stratiform precipitation. Weakly organized cloud clusters, squall lines, tropical and midlatitude Mesoscale Convective Systems (MCSs) and Mesoscale Convective Complexes (MCCs) all develop areally extensive cloud shields, initially consisting of condensate detrained from active convection. Depending on the extent of convective organization, these precipitation regions may be temporally and spatially coincident with, or separate from, the parent storms.

These stratiform precipitation regions are comparatively uniform in lateral structure. Microphysically, they are frequently characterized by weak surface rainfall (radar echoes 15-35 dBZ or 0.5-4.0 mm/hr), low ice water content (IWC) aloft, low (if any) liquid water content (LWC) aloft, and a coherent radar bright band *(Houze, 1977, Leary and Houze, 1979, Stewart et al., 1984, Houze, 1989, Zrnic et al., 1993)* (Fig. 1.1). The weak but extensive surface precipitation often comprises a significant fraction (15-40%) of total precipitation from the convective system *(Houze, 1977, Cifelli and Rutledge, 1994)*. Throughout this work, such regions exhibiting surface precipitation and radar bright band will be termed "stratiform anvil systems", as distinct from nonprecipitating, upper level cirrus anvils detrained from isolated storms and supercell systems.

The thermodynamic characteristics of these systems are well-established. Within the anvil cloud, ice saturation or supersaturation dominates, typically down to the melting level. A weak isothermal layer is occasionally found at and below the melting level, and can reach up to 1 km depth. A superadiabatic base is sometimes found below this layer *(Stewart et al., 1984, Willis and Heymsfield, 1989)*. Below this base, lapse rates are nearly dry adiabatic and the air is significantly subsaturated. Near the surface, relative humidity is higher and a stable layer is often found. Taken as a whole, thermodynamic profiles typically resemble the "onion soundings" described by *Zipser (1977)*.

Kinematically, stratiform systems exhibit relatively weak vertical motions (±1 m/s or less), consisting generally of updrafts aloft and downdrafts in the lower troposphere *(Houze, 1989, Cifelli and Rutledge, 1994, Boccippio, 1995)*.[1] Horizontal divergence profiles are usually consistent with this structure: divergence is found aloft and near the surface, with convergence at midlevels *(Cifelli et al., 1996)*. Relative to the parent convection, front-to-rear (FTR) horizontal flow is typical aloft, with rear-to-front (RTF) horizontal flow at mid and low levels. This RTF flow typically peaks in a midlevel "rear inflow jet" near cloud base *(Smull and Houze, 1987, Zhang and*

---

[1] In Chapter 4 it will be demonstrated that this vertical motion structure exhibits a systematic evolution with time which appears to be coupled to the electrification of the system.

Gao, 1989, Klimowski, 1993). In some systems, a third layer of FTR flow is found in a shallow layer near the surface, consisting of convective downdraft outflow (Fig. 1.2).

The microphysical, thermodynamic and kinematic charactersitics of stratiform anvils have been at least qualitatively understood since the mid-1970's. More recently, attention has been given to the unique electrical characteristics of stratiform regions. Surface and above-cloud electric field measurements often reverse polarity in the late stages of both isolated and organized storms *(Moore and Vonnegut, 1977, Livingston and Krider, 1978, Chauzy et al., 1985, Krehbiel, 1986, Engholm et al., 1990, Marshall et al., 1996).* In some systems, concentrated positive charge is found near the melting level *(Stolzenburg et al., 1994, Shepherd et al., 1996).* Positive cloud-to-ground (CG) lightning flashes, which comprise only 5-15% of all ground flashes, are preferentially found in stratiform regions *(Orville et al., 1988, Rutledge et al., 1990).* These flashes statistically exhibit higher peak currents, total charge transfer, areal extent, luminosity and duration than negative ground flashes *(Brook et al., 1983, Rust, 1986, Orville et al., 1987, Mach and Rust, 1993, Boccippio et al., 1996).* They occur at a comparatively low flash rate, and have an atypical horizontal (rather than vertical) component, sometimes developing horizontally extensive dendrite networks within the cloud ("spider lightning") which may finger for up to a hundred kilometers along cloud base *(Teer and Few, 1974, Fuquay, 1982, Williams et al., 1985, Mazur et al., 1994).* Upper mesospheric electrical activity (e.g. the optical "red sprite" emission) has to date been observed exclusively above stratiform regions, and is associated with positive CG lightning *(Boccippio et al., 1995, Lyons, 1996).*

These electrical characteristics are both anomalous and important. High energy, infrequent positive flashes in the late stages of storms are believed to be a significant trigger of forest fires, and pose risks to aviation safety and airport refueling operations. Areally extensive above-cloud fields may be a relevant contribution to the DC global electrical circuit *(Marshall et al., 1996)*, and the large charge transfers associated with positive CGs appear to couple disproportionately into the AC global electrical circuit (the Schumann Resonances) *(Sentman, 1987, Burke and Jones, 1996, Boccippio et al., 1996)*. Repeated electrical upper mesospheric activity above stratiform regions may locally perturb the lower D-region of the ionosphere, and concurrent red sprites may impact the upper atmospheric NO_x budget *(Armstrong et al., 1996)*. Clearly, the anomalous electrification of stratiform precipitation regions is a significant feature which warrants characterization and explanation.

1.2 Theories for stratiform anvil electrification

1.2.1 Necessary components

The microphysical, kinematic and electrical characteristics of stratiform anvil systems described above have rarely been observed concurrently within the same system, often due to limitations in individual field observation programs or the rapid translation of large scale systems. In this work, a theory of anvil electrification is sought which is general enough to extend to both weakly and strongly organized systems. Greatest attention is paid to relatively stationary, weakly organized cloud clusters, primarily because of the ease of observation and the hope of screening out secondary effects which may complicate interpretation. The hope here is that primary mechanisms of electrification may be found in the simpler systems, which will also provide the "lowest order" signal in the larger systems.

In the context of an appropriate theory, the disparate and sometimes confusing observations of stratiform anvil electrification in various systems may be easier to interpret. If the theory is sufficiently extensible and self-consistent, the various observations taken as a whole can then be used both quantitatively and heuristically in support of the theory. (Similarly, the observations may be used to test, and potentially reject, the theory.) Under this approach, it will be useful to first identify the electrical characteristics of simple, weakly organized systems that an adequate theory must, at minimum, explain. The theory may then, with somewhat lesser justification, be mapped onto more strongly organized systems.

Some of the earliest measurements of storm electrification were obtained from single-station observations of the near-surface vertical electric field, E_{z_0}. Such measurements are a poor way to characterize the electrical characteristics of a thunderstorm, since the time-varying E_{z_0} is a "lumped" measurement, incorporating the integrated effects of a storm's (likely complicated) internal charge structure and current generator. Interpretation of E_{z_0} measurements typically requires an *a priori* model of the actual charge structure. Fortunately, the observed time evolution of E_{z_0} and the transient effects upon it by lightning discharges is common enough that relatively simple models of storm electrification have sufficed to describe the general characteristics of isolated thunderstorms.

The conventional model presents the electrical structure as a simple dipole, in which positive charge overlies negative *(Wilson, 1920, Krehbiel, 1986)*. In this model, positive fields (negative charge dominant or closest overhead)[2] are found at the surface, with individual lightning strokes depleting the negative charge center, lowering this charge to ground and making the field more negative (segment "A" of Fig. 1.3 is characteristic). The field reversal observed in segment "B" of Fig. 1.3 is also a common occurrence, and was orginally noted by *Moore et al. (1958).* Early interpretations of this reversal (the electrical "End Of Storm Oscillation", or EOSO) were based upon a purely geometric effect: as the storm dipole moved away from the surface field mill sensor, field lines from the assumed upper positive charge center would be exposed and terminate on the mill. More recent concurrent measurements of E_{z_0} and storm radar reflectivity suggest that this interpretation is at times inadequate: an EOSO may occur while the precipitating storm core is still located above the sensor. In these situations, a reconfiguration of the storm's internal charge structure seems a more likely explanation for the observed surface fields. Specifically, the observed "negative" fields suggest that a positive charge region is electrically "closest" to the surface sensor, and when charge regions are integrated, dominates the surface field.

The dramatic decrease in transient activity (lightning flash rate) during the EOSO perhaps suggests a weakening of the storm's current generator (widely accepted to be the separation of charge by differential air and particle fall speed motions *(Williams et al., 1985, Williams, 1989)*). Consistent with this interpretation, the EOSO is typically found in the late stages of storms, when storm updrafts lessen. However, in the case presented in Fig. 1.3, flash activity does not cease entirely: opposite polarity discharges persist, at a lower flash rate, through the EOSO. These

---

[2] The convention used in this work is to denote field polarity by the direction of motion of a positive test charge. Thus, "foul" weather fields associated with negative charge overhead are "positive" fields. "Fair" weather (negative) fields are associated with positive charge overhead.

discharges tend to make the integrated field more positive, suggesting a removal of positive charge from overhead. These discharges must either be simply depleting extant charge regions, or be sustained by ongoing charge advection or a continuing *local* generator mechanism.

A last figure of note in Fig. 1.3 is the brief reversal of E_{z_0} to positive polarity (segment "C"), prior to a return to undisturbed (negative) field values. In more organized systems, several such reversals may be observed *(Chauzy et al., 1985).*

Fig. 1.3 is only one example of E_{z_0} evolution in the late stages of storms. In the moist, low-shear central Florida environment in which it was taken, this evolution is quite common. In stronger shear environments and more highly organized systems, surface field evolution is more complicated. However, temporary excursions to fair weather polarity are not atypical, and a dominance of positive cloud-to-ground (CG) flashes in the late stages of storms or the oldest regions of some systems is certainly commonplace. Fig 1.4 presents EOSO traces from a line-oriented system near Albuquerque and a cloud cluster in the Western Pacific. Surface field values of E_z soundings in North American and West African Mesoscale Convective System (MCS) stratiform regions reveal at least local areas of negative electric field *(Chauzy et al., 1985, Stolzenburg et al., 1994).* In addition, recent soundings *above* MCS stratiform regions reveal fields and discharge signals of reversed polarity, also suggestive of an anomalous coarse charge structure *(Marshall et al., 1996).*

To summarize, we seek to explain several common electrical characteristics of mature or late-stage storm systems:

1. building negative E-field strength, followed by sustained negative surface (and, in some cases, above-cloud) fields
2. the prevalence of anomalous polarity lightning (+CG flashes and intracloud flashes which make surface fields more positive)
3. the continuing charge supply (i.e., current generator, or charge separation mechanism) for these flashes, inferrable from (1)

If the anomalous electrification of late-stage systems is indeed linked to an anomalous internal charge structure, then (2) and (3) will likely be the more universal observables, as lightning discharges originate within the charged storm regions. However, as noted above, E_{z0} and $E_{z_{top}}$ are integrated quantities, and may be complicated by secondary effects irrelevant to in-cloud electrical processes (cloud-edge screening layers, charged rainfall particles, charged particles in the boundary layer, etc). Hence, (1) may be observable only when such incidental charge regions are weak or absent. We hypothesize here that a common (dominant) internal electrification mechanism may be found in, e.g., Florida cloud clusters and Great Plains or tropical MCSs.

1.2.2 Discounted theories

Several early explanations for the EOSO and related discharge anomalies deserve brief discussion. The original "geometric effect" (a normal dipole, upright storm advected away from the surface sensor revealing upper positive charge; pg. 22) may have some value for isolated storms. However, examination of concurrent radar data (as will be presented in Chapter 4) quickly reveals that EOSO features may be observed while storm centers are still located above surface field sensors. Furthermore, it is difficult to account for surface fields of reversed polarity *and* comparable magnitude with the translating dipole model.

Another early explanation for the EOSO was based upon an extension of the "convective hypothesis" for storm charging: *Moore et al. (1958)* suggested that that downdrafts occurring during storm dissipation expose the upper positive charge in the "normal dipole" and transport it to lower levels. While such an explanation may be partially consistent with the area-average evolution of vertical motion fields in weakly organized storms *(Boccippio, 1995)*, it fails to address a crucial aspect of late-stage electrification: the apparent continued existence of a storm generator current that feeds the horizontally extensive intracloud and positive cloud-to-ground lightning discharges often observed during the EOSO and in trailing or detached stratiform regions. As the "convective hypothesis" is also currently disfavored (although not disproven) as a storm electrification mechanism, this explanation is discounted in the current work.

1.2.3 Tilted dipole hypothesis

Most studies of stratiform region electrification have been conducted in environments of moderate to high vertical wind shear. Such shear has been well established as a key factor in storm system organization into squall lines, MCS and MCC systems (see *Cotton and Anthes (1989)* for a review of the interaction of storm system evolution with environmental shear). In such sheared environments, the normal "upright" vertical dipole structure of thunderstorms will eventually develop a distinct horizontal component; e.g. in squall line or MCS systems, the upper positive charge can be expected to be carried rearward (in a storm-relative sense) in the divergent, upper level, FTR flow.[3] Such organization led several investigators to suggest a "tilted dipole" hypothesis for the prevalence of positive discharges in the trailing stratiform regions of shear-organized systems *(Brook et al., 1982, Hill, 1988, Orville et al., 1988, Rutledge and MacGorman, 1988, Engholm et al., 1990).* Under this hypothesis, the rearward-advected positive charge is electrically "closest" to the ground and results in positive CG strokes to ground. Such an explanation was also motivated by observations of CG strikes through clear air from the underside of detrained, nonprecipitating anvils from simpler convective systems. This explanation was also not inconsistent with contemporary knowledge of the internal charge structure of such anvils *(Byrne et al., 1989, Marshall et al., 1989)*, which appeared to consist primarily of a positive charge core surrounded by weak negative screening layers near anvil boundaries.

A parallel body of observations has also evolved focusing on Japanese and Atlantic winter storms. Such storms are the second major class of systems which exhibit predominantly positive lightning. The tilted dipole hypothesis was initially suggested by *Brook et al. (1982)* to account for these observations.[4] Commonality between winter storm electrification in the GALE experiment and squall line electrification in the COHMEX experiment was demonstrated by *Engholm et al. (1990)*, who focused largely on the environmental and system shear and again invoked the tilted dipole hypothesis.

Lateral advection and displacement of the upper positive charge center in or-

---

[3] Actually, most storm updrafts are "tilted", even in low-shear environments. However, from an electrical standpoint, significant lateral charge advection is also required for the upper positive charge to be "visible" to surface sensors.

[4] Brook notes that D. Raymond was actually the first to suggest the idea of a tilted dipole.

ganized systems undoubtedly occurs, particularly upon detrainment of upper level anvils. In organized systems, such charge advection may even be large enough to account for observed positive discharge rates: assuming 1 km thick charge layers of O(1nC/m^3) *(Stolzenburg et al., 1994)* and FTR flow of O(10 m/s) across a 100 km wide region, charge advection rates of O(1 C/s) are conceivable. Because positive CGs are believed to transfer tens to hundreds of Coulombs of charge per flash *(Brook et al., 1983, Goto and Narita, 1995, Boccippio et al., 1996)*, positive CG flash rates of 1 per minute in squall line or MCS systems may possibly be fed by lateral charge advection alone. Such discharges, however, will not necessarily exhibit the pronounced horizontal character often reported in the literature, as advected charge will be situated closest to the active storm generator (leading edge of the system).

The tilted dipole hypothesis cannot be ruled out as an electrification mechanism in some highly organized systems. However, the relative importance of this hypothesis may be resolved in the near future with the aid of several instrumental platforms:

1. Cloud-top lightning channel morphology can be obtained from the spaceborne Optical Transient Detector (OTD) and Lightning Imaging Sensor (LIS) instruments. This optical data can be used to characterize the horizontal extent of flashes in squall line or MCS systems, and more importantly, their connectivity (if any) with the parent storm cells in the system's leading edge. Under a pure tilted-dipole hypothesis, repeated discharge events occurring in the stratiform region alone would quickly deplete the supply of advected charge. The observation of such events would almost require that an active *local* generator be present in the stratiform region.

2. Direct estimates of the total dipole moment changes of positive CG flashes (and

hence, inferences of total charge transfer) are obtainable from single-station Schumann resonance data being collected in West Greenwich, Rhode Island *(Williams, 1992, Wong, 1996, Boccippio et al., 1996).* Rough estimates may be made of the total charge depletion of an MCS system by positive CG flashes over its evolution. Such estimates may help to determine if advected charge alone can indeed support observed positive CG flash rates in MCS stratiform anvils.

3. Concurrent electric field measurements both above and below stratiform regions during spider or +CG occurrence would help infer the actual charge structure (*Marshall et al. (1996)* documents such measurements from cloud-top only). The NASA ER-2 would be an ideal platform for such measurements, as the AMPR microwave sensor could be fielded in tandem and provide further microphysical characterization of these systems. The Kennedy Space Center area would be an optimal location, as use could be made both of the surface field mill network and the LDAR time-of-arrival lightning mapping system.

A more important limitation of the tilted dipole hypothesis is that it cannot be invoked to explain *all* instances of anomalous stratiform anvil electrification, as described below.

1.2.4 Inverted dipole hypothesis

The tilted dipole hypothesis becomes increasingly questionable as a "universal" mechanism for stratiform anvil electrification when recent observations from central Florida (the core data for this thesis) are considered. The summertime Florida environment is characterized by high CAPE (Convective Available Potential Energy) but almost negligible vertical shear and very weak mean winds. In such an environment, cloud clusters often form, organize, mature, detrain and progress to precipitating stratiform anvils more or less “in place”. Most importantly, many of the relevant and anomalous electrical features of stratiform anvil electrification (surface EOSO, positive CGs) may be observed in these systems, *after* the active storm cores (i.e., the conventional current generators) have weakened or even disappeared. These systems must thus either be running down an existing charge supply, or undergoing continuing charge reconfiguration and separation adequate to drive the system. Recalling that a common feature of central Florida EOSOs is a *sustained* surface negative field, which recovers to DC negative values after positive discharges, we may infer that a generator mechanism of some sort is indeed still active, and that the system is not simply depleting old charge reservoirs.

The common alternative to a tilted dipole hypothesis is a purely local charge reconfiguration. This is typically assumed to be an “inverted dipole” in which the principal structure is of negative charge overlying positive.[5] The inverted dipole hypothesis was posed as an alternative explanation by *Markson and Anderson (1988), Rutledge and MacGorman (1988), Engholm et al. (1990)*, and subsequently considered in further detail by *Rutledge et al. (1990), Williams et al. (1994), Rutledge et al. (1995)*. These studies have provided support for an inverted dipole explanation, but as yet a compelling argument for the presence of a completely local generator mechanism resulting in an inverted dipole charge structure has not been offered. Part of the difficulty is the dominance of organized systems in observational studies; in these,

---

[5] This hypothesis does not rule out smaller, incidental charge regions, such as cloud-edge screening layers or even detrained upper positive charge. It simply stipulates that the dominant charge centers; i.e., those directly being separated by processes unique to the anvil environment, are vertically reversed from a “normal dipole”.

both charge advection and local charge separation may be occurring simultaneously. Recent direct soundings of vertical charge structure in MCS stratiform anvils *(Stolzenburg et al., 1994, Shepherd et al., 1996)* do appear to reveal horizontally extensive layers in which the conventional charge structure is reversed, with dominant layers of positive charge, of $O(1 - 2nC/m^3)$ near the melting level and negative charge 1-2 km above. Unfortunately, these soundings also reveal a variety of other charge layers both above and below this embedded inverted dipole, whose origins are obscure and may either be dissipative (i.e., screening layers) or historical (old advected charge). As such, the central Florida observations become even more valuable: if there is a fundamental, microphysically or kinematically based charging process unique to the stratiform anvil environment, it should be much easier to detect in the Florida storms, where the obfuscating effects of continued, adjacent charge separation and advection are absent.

Two possible means of achieving an inverted dipole structure have been offered in the literature. The first, charging by melting, shall be discussed for completeness; however, little data is available at present to confirm or refute this hypothesis, and it necessarily must be left for future study. The second, reversed non-inductive charging in a high temperature, low liquid water content environment, is a direct extension of a widely accepted theory of "normal" storm electrification, and will form the working hypothesis for this thesis.

Charging by melting

As noted above, a frequent characteristic of stratiform anvils in organized MCS systems is a horizontally extensive layer of positive charge near the melting level *(Stolzenburg et al., 1994)*. This layer may be up to 500 m deep and exhibits net positive charge densities of $1 - 4\,\mathrm{nC/m^3}$. It typically begins at slightly subzero temperatures (-0.5 to -1.0 C) (and is sometimes entirely confined to these temperatures) and rarely extends below the quasi-isothermal layer at 0-1 deg C *(Shepherd et al., 1996)*. The prevalence of this feature in organized stratiform anvil systems, and the close coincidence of surface field reversal with appearance of a radar bright band in the less organized central Florida cases (to be presented in Chapter 4) is perhaps indicative of a charge separation mechanism related to the melting of detrained and settling anvil ice.

Early laboratory studies *(Dinger and Gunn, 1946)* suggested that melting ice acquires positive charge, while negative space charge is found in the melting environment. Subsequent laboratory experiments and field measurements imposing rapid melting of artificial and naturally falling snow crystals in the 30-400 μm diameter range confirmed that, at least in a statistical sense, initially non- and negatively-charged ice becomes positively charged upon melting *(Magono and Kikuchi, 1963, MacReady and Proudfit, 1965a)*. A followup study extended this result to initially positively charged ice, and also suggested some relation of the charging intensity to the complexity of crystal habit and the ejection of trapped bubbles from bound meltwater *(Magono and Kikuchi, 1965)*. The transfer of negative charge away from melting specimens on ejected bubbles was then confirmed, again statistically, by *Kikuchi (1965a,b)*. A later, more detailed laboratory study *(Drake, 1968)* found almost exclusive positive charging of melting ice, and related the total charging to the vigor of convection currents within the meltwater (carrying bubbles from the ice surface to the meltwater surface, from which they were ejected). This study also found increasing charging with increasing environmental temperature, wind speed and, most importantly, mean heat transfer away from the melting specimen.

The forced-melting experiments, both in the laboratory and outdoors, offer tantalizing evidence that significant positive charging can occur during ice melting. However, their relevance to actual charging within stratiform anvil environments is questionable. The results contrast with one in-situ aircraft measurement of precipitation charge through the melting layer, which found positively charged ice changing to negatively charged rain upon melting *(MacReady and Proudfit, 1965b)*. Second, the forced-heating experiments of Magono and Kikuchi on small ice crystals may not accurately reflect actual heat transfer rates of melting ice. Specifically, small ice crystals (<1 mm diameter) "will melt entirely in falling 0.5 km from the 0 deg C level through normal lapse rates, and ... under these conditions the heat transfer is insufficient to develop strong convection in the melt water" *(Drake and Mason, 1966, Drake, 1968)*. Such meltwater convection will be even less vigorous on descent through well-formed isothermal layers. The forced melting experiments on 30-400 μm crystals may thus be irrelevant to actual anvil melting conditions (although Drake's results for larger crystals may still hold).[6]

The greatest difficulty with a charging mechanism in which falling condensate of

---

[6] Alternatively, these same findings can be used to support a melting hypothesis: Drake notes that melting ice <1 mm in diameter fails to develop adequate internal convection currents, while ice >5 mm diameter sheds meltwater too rapidly to charge efficiently. Interestingly, the remaining sizes (1-5 mm) of falling ice are precisely that portion of the condensate spectrum which increases most dramatically due to aggregation in actual anvil melting layers *(Willis and Heymsfield, 1989)*.

either initial sign charges positively upon melting is that it contradicts actual measurements of net charge density in MCS anvil electric field soundings *(Stolzenburg et al., 1994, Shepherd et al., 1996)* (and yet has been offered by these authors as a possible, although disfavored, explanation for the observations). Specifically, if the meltwater charges positively and ejects negative space charge, we would expect to find a net *negative* charge layer near the melting level, as negative charge bound on tiny ejected droplets is left behind when the positively charged meltwater increases its terminal velocity, resulting in a net positive charge flux divergence out of the layer. The net positive charge would instead be expected in a vertically extensive layer well *below* the melting layer, diminishing as the falling precipitation interacted with subcloud negative space charge. Furthermore, the mechanism cannot explain observations of net positive charge beginning above the melting layer, or indeed anywhere colder than 0 deg C. It is possible that sporadic convective adjustment of the observed superadiabatic base of the isothermal layer *(Findeisen, 1940)* periodically transports space charge aloft, but again, the sign of the space charge is incorrect, and any uplifted melted condensate large enough to charge positively *(Drake, 1968)* would rapidly settle to lower altitudes.

In summary, while laboratory studies certainly suggest that natural and laboratory ice tends to charge positively under vigorous melting conditions, there is insufficient support from in-situ observations to conclude that this mechanism can account for lower positive charge at or above the melting level in many actual stratiform clouds. A single exception can be found in the literature: the "DNC-2" sounding presented as Fig. 11d in *(Stolzenburg et al., 1994)* and Fig. 15 in *Shepherd et al. (1996)*. This profile reveals a thin $-3\,\mathrm{nC/m^3}$ negative charge layer at 6 km altitude (not atypical among these soundings) and a vertically extensive (and diminishing) $+0.2\,\mathrm{nC/m^3}$ positive charge layer from the melting level nearly down to the surface. This latter feature *is* anomalous, as are the ambient microphysical conditions. This sounding was taken through the heart of an MCS secondary precipitation band, in which 54 dBZ (extremely high) reflectivity was observed in the bright band and 42 dBZ rainfall observed at the surface. It is possible that under these ambient conditions, the laboratory-observed melting charging process may be enabled.

Charge reversal microphysics

An alternative hypothesis for the creation of an inverted dipole charge structure in stratiform anvil systems, and the one to be tested in this thesis, invokes the "mixed phase microphysics" mechanism of thunderstorm charging. The laboratory results of *Takahashi (1978)* form the basis for this theory; under different ambient temperature and liquid water content conditions, a riming ice target was found to charge either positively or negatively. These various ambient conditions were shown to correspond with different microphysical growth regimes of the ice target *(Williams et al., 1991)*; riming targets in low liquid water content (LWC) environments are in a depositional growth state; targets in cold and wet enough conditions are heated enough by riming to undergo sublimation, while targets in warm and very high LWC environments are promoted to a "wet growth" state (as in hail formation) and undergo evaporation. Respectively, these conditions appear to correspond to positive, negative and positive charging of the rimed target (see Fig. 3.2 on pg. 120). A storm charging theory which couples these laboratory results with separation of precipitation and cloud particles under varying updraft and particle fall speed conditions appears to account well for actual storm electrical development *(Williams et al., 1991, Saunders et al., 1991, Williams et al., 1994, Randell et al., 1994, Williams, 1995)*. Specifically, under "normal" thunderstorm conditions, the dominant temperature and LWC environment in the mixed-phase region favors negative charging of precipitation-sized rimed ice (graupel), with positive charge left on smaller cloud particles. Positively charged ice is carried aloft in storm updrafts, while negatively charged graupel falls to lower levels, thus creating the "normal" storm dipole.

Takahashi's laboratory results indicate that for low liquid water contents ($< 0.5\ \mathrm{g/m^3}$) (i.e., the depositional growth regime) precipitation sized particles will charge exclusively positively. This result is somewhat in contradiction with laboratory studies by the Manchester group *(Jayaratne et al., 1983, Keith and Saunders, 1990, Saunders et al., 1991)*, reviewed by *Saunders (1994)*, which appear to yield positive charging at temperatures higher than -11 deg C only if the effective water content (EWC) is greater than $0.2\ \mathrm{g/m^3}$ (the actual LWC is slightly higher than the EWC used in Saunders' work).[7] Either set of experiments suggests that if the lower mixed phase regions of storms become significantly depleted of liquid water (e.g., as updrafts weaken during the dissipating stages of active storm cells and the subsequent evolution to stratiform anvil clouds), precipitation-sized ice in a mixed phase environment will charge positively. For the temperature range in which the negative charge center is typically found located in "normal" storm dipoles (-10 to -15 deg C), the threshold LWC for reversed charging appears to be about $0.2 - 0.5\ \mathrm{g/m^3}$, with this threshold

---

[7] Saunders *10th ICAE (1996)* has recenetly stressed the results of *Baker (1987)* that the charging polarity is actually dependent upon which of the two ice specimens (precipitation and crystal) is growing *faster* in the mixed-phase environment. Under many environmental conditions, this interpretation may not be inconsistent with the separation of charging polarity based upon target growth regime *(Williams et al., 1991)*.

lessening (or disappearing) with increasing temperature. This microphysical environment may be representative of stratiform anvil clouds, and such "charge reversal microphysics" has been offered as an explanation for the (postulated) inverted dipole structure of such clouds *(Williams et al., 1994)*.

Even in the absence of supercooled liquid water, laboratory studies have found that precipitation ice growing by vapor deposition will charge positively *(Baker et al., 1987, Williams et al., 1991, Caranti et al., 1991)*, although less effectively than under three-phase conditions. Vapor deposition will dominate in a two-phase system so long as supersaturation with respect to ice is maintained. Furthermore, the thermal inertia of graupel or snow falling from colder cloud levels will support deposition at even slightly sub-ice-saturated conditions *(Williams et al., 1994)*.

Hence, four possible scenarios arise in which ambient temperature and saturation conditions may influence (laboratory-inferred) charging in stratiform anvil clouds:

1. Water saturation is maintained in the 0 to -15 deg C temperature range, and LWC is in the range $0.2 - 0.5\,\mathrm{g/m^3}$. Such a condition might be expected if updrafts extend through this region and are sufficient to maintain the LWC supply. This condition is the most favorable for charge-reversal microphysics, under both Takahashi's and the Manchester group's laboratory experiments.

2. Water saturation is maintained in the 0 to -15 deg C temperature range, with LWC in the range $0.0 - 0.2\,\mathrm{g/m^3}$. This condition is more likely to obtain under actual updraft magnitudes typical of stratiform clouds. A charge-reversal microphysics hypothesis would agree with Takahashi's results in this condition, but conflict with the Manchester results.

3. Water saturation is not maintained in the 0 to -15 deg C region, but ice supersaturation (or near saturation) persists. Such a condition would obtain if updrafts are too weak to resupply liquid water under prevalent Bergeron-type growth to small ice particles, or if downdrafts persist but small ice crystal concentrations are large enough to resupply the ambient vapor by sublimation. Under this regime, precipitation ice will still be undergoing (two-phase) depositional growth, and charging positively (albeit weakly). Using the results of *Caranti et al. (1991)*, an inverted dipole could still be explained.

4. Significant subsaturation with respect to ice exists in the 0 to -15 deg C range. This condition might obtain under deep downdraft conditions in this region. In this regime, laboratory-based microphysical charging mechanisms could not explain the (inferred) inverted dipole structure.[8]

This thesis shall focus on the inverted dipole hypothesis based upon charge reversal microphysics to explain observed anomalous stratiform anvil electrification. This theory is attractive for several reasons: first, it is a direct extension (into new parameter regimes) of a strong theory for "normal" storm electrification. Second, as noted above, it agrees well with recent studies of large scale storm electrification. Finally, it is easily testable by direct in-situ measurements, or by indirect retrieval, of the (T,LWC) regime characteristic of stratiform anvils. As tailored in-situ microphysical measurements of stratiform anvils are few and far between, the focus here shall be on retrieval of these fields.

---

[8] While precipitation ice warmed to the point of sublimation in 3-phase (riming) environments appears to charge negatively, it is unclear that sublimating ice in 2-phase environments will charge negatively as well.

1.3 Methodology

To summarize the charge reversal microphysics argument, we postulate a simple heuristic causal chain: an anvil cloud's ambient environment (CAPE, total water content, shear) sets the storm morphology, including the total amount of ice detrained. This detrained ice sets the anvil's initial microphysical conditions. Subsequent evolution of the anvil (as in the parent storm) are primarily governed by this initial condensate population, and by the time-evolving vertical velocity structure. The vertical velocity structure will determine the microphysical growth regime of anvil condensate. This growth regime in turn sets the polarity of charging of precipitation and cloud ice (as inferred from laboratory studies).

The methodology to be employed here is fairly direct. Guided by the observed horizontal uniformity of many isolated stratiform anvil systems, a local 1-D assumption is employed, at least on scales (60-80 km diameter) comparable to individual radar volume scans, which supply the primary data here. Time-evolving vertical velocity profiles are first deduced from radar data with high temporal (5 minute update) and spatial (250 m deep vertical layer) resolution. A description of the detailed calculation of these fields, including refinements and improvements to conventional velocity retrieval methods, is presented in Chapter 2. Actual retrievals are presented and discussed in Chapter 4, in the larger context of storm electrification and radar reflectivity measurements.

The vertical velocity fields are then used as the primary input to a 1-D, steady-state bulk microphysical retrieval from which cloud LWC, cloud ice, precipitation ice, rain and saturation condition can be diagnosed. The retrieval is an outgrowth of a generation of earlier bulk microphysical models; its real and parameterized physics (and improvements to the latter) are described in Chapter 3. Actual retrieval results are discussed in Chapter 4, and the adequacy of the charge-reversal microphysics hypothesis is tested. Finally, in Chapter 5, the results of this work are combined with new, recent measurements of anvil electrification and positive lightning to strengthen the heuristic argument for a common "inverted dipole" structure in anvil systems of varying degrees of organization. These new measurements support the idea that a charge reversal microphysics mechanism is the dominant cause.

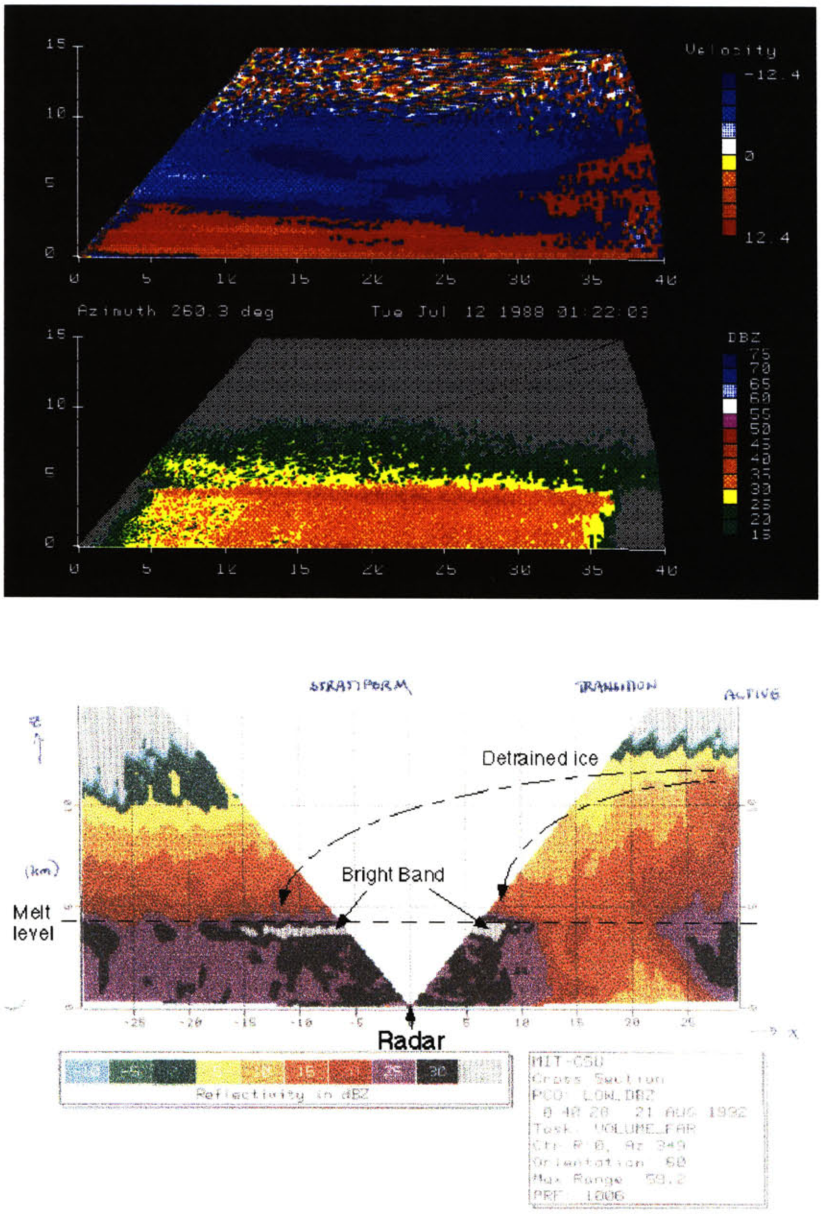

Figure 1.1: Radar cross sections of various stratiform regions. The first panel depicts a small, detached stratiform region with low cloud tops observed in Huntsville, AL in 1987. The second panel shows a reconstructed cross-section (from radar PPI scans) through a squall-line system in Orlando, FL in 1992. Common features include radar bright band, horizontal uniformity aloft and weak surface rainfall.

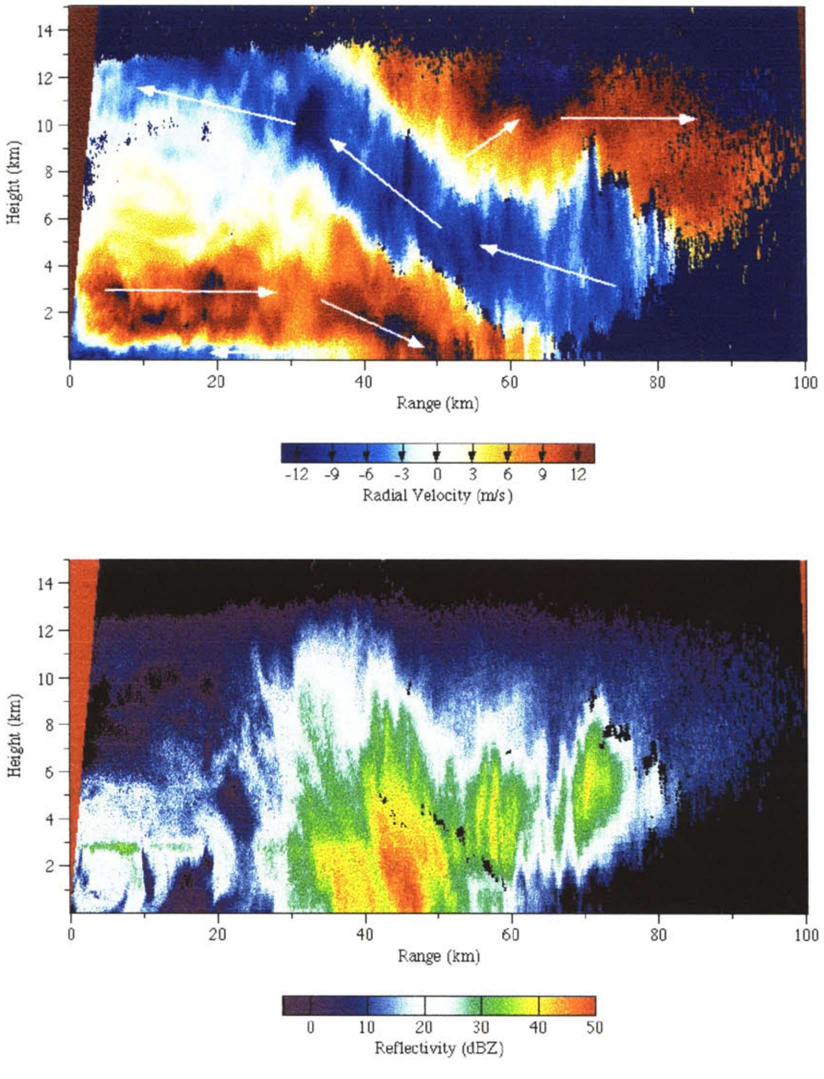

Figure 1.2: Sample RTF (rear-to-front) and FTR (front-to-rear) flow and reflectivity structure of the leading edge of a New Mexico squall line. Flow structures continue rearward into the stratiform component of this system (not shown).

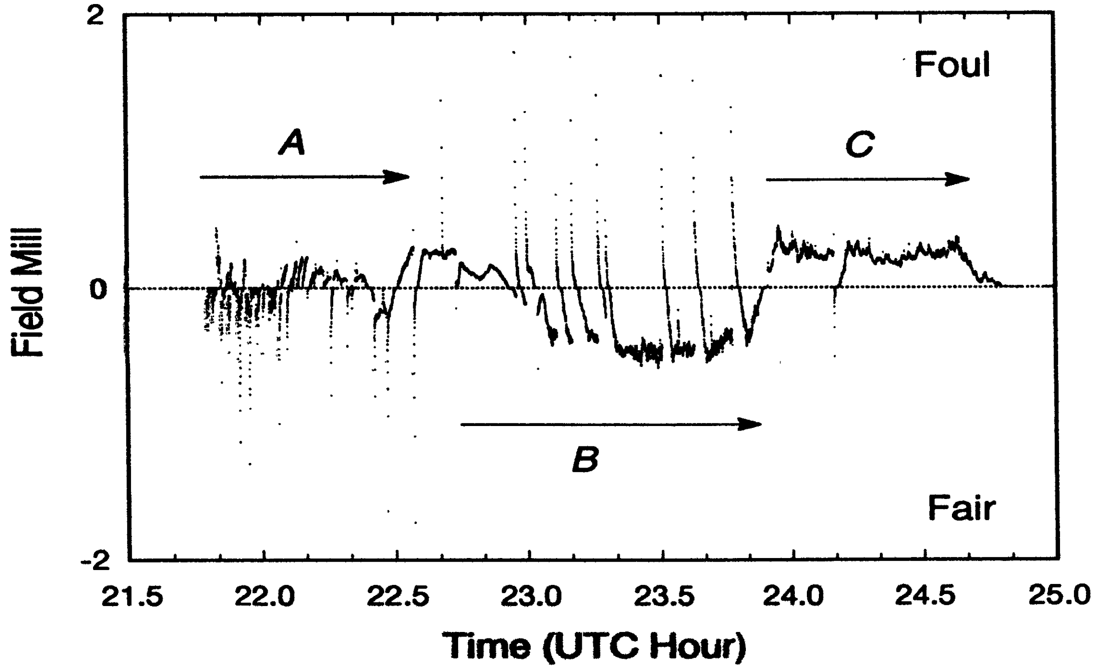

Figure 1.3 Sample End-of-Storm-Oscillation (EOSO) trace from a cloud cluster in Orlando, FL on 6 August 1992. The data is taken from surface corona current measurements and roughly approximates the surface electric field E_{z_0}. Sign convention is such that positive fields (foul weather) indicate negative charge overhead, and negative fields (fair weather) indicate positive charge overhead.

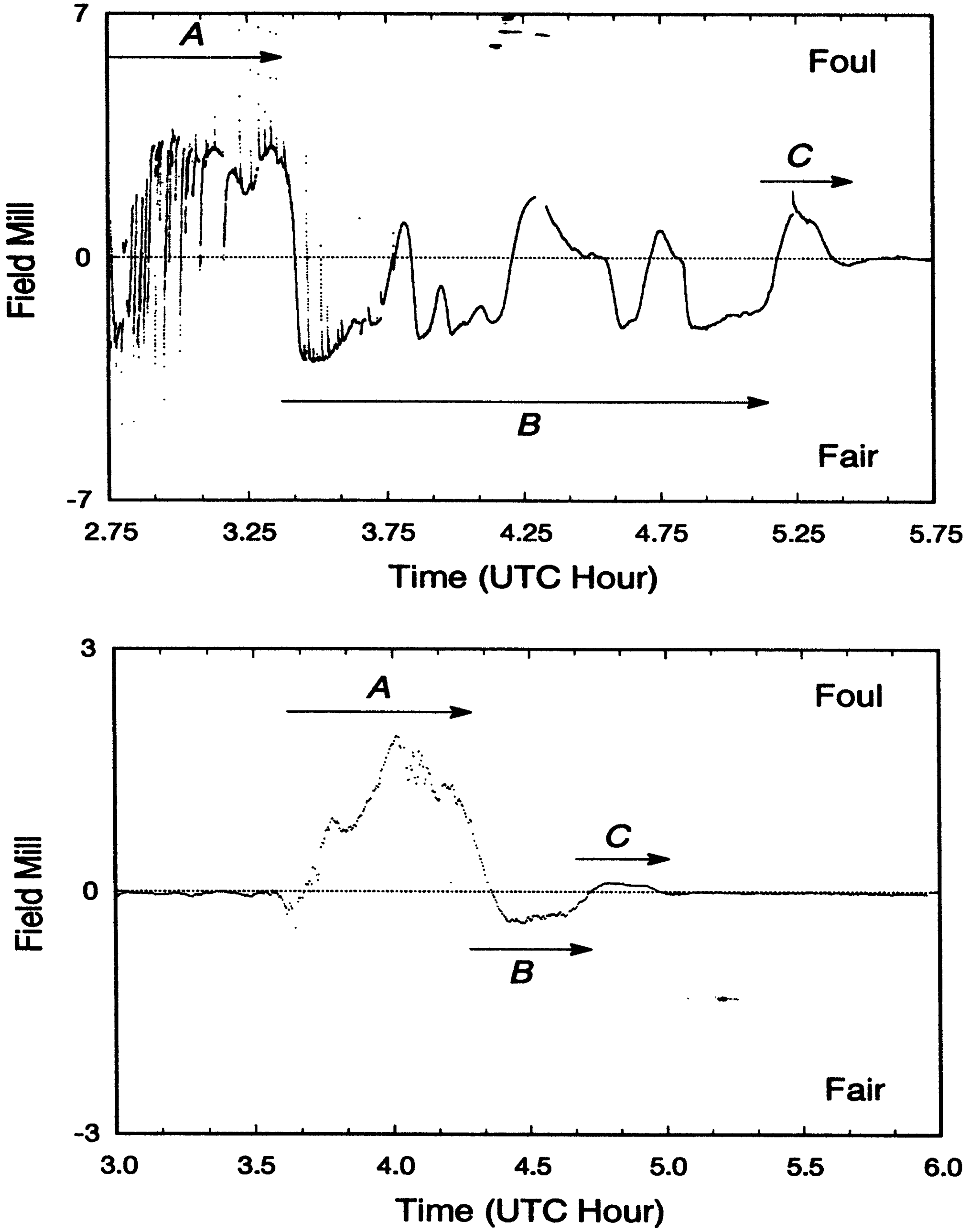

Figure 1.4: EOSO field traces from Albuquerque (top) and the Western Pacific (bottom).

Chapter 2

Single Doppler retrieval: the VVP technique

In order to predict the charging polarity of late-stage stratiform anvil systems, we seek to retrieve the saturation condition (and hence microphysical growth regime) characteristic of these clouds. Vertical velocities within these anvils are a crucial component of this retrieval, as they will determine the amount and rate of adiabatic water content supply to the microphysical system. As such, the accurate diagnosis of vertical velocity is essential to the study, and forms the starting point in the current investigation.

Time-evolving vertical velocities in this study are retrieved from single Doppler radar data. As a single radar only instantaneously detects one component of the three-dimensional flow field, an assumption of horizontal uniformity is required, as well as a linear or quadratic model of the ambient flow. The diagnosed horizontal winds and divergence (and hence vertical velocity) are fitted by multivariate regression, and are thus the kinematic fields most consistent with the simplified model.

Several approaches have historically been taken in the single-Doppler retrieval problem. A brief review of these approaches is given in section 2.1. The technique chosen here is a modified form of the "Volume Velocity Processing" (VVP) algorithm. The technique is described in section 2.2, as are a number of computational improvements implemented herein. Limitations in the technique (crucial to understanding the use and implications of these velocities later in the study) are presented in section 2.3. Finally, an extension of the technique to diagnose turbulence characteristics of the flow (previously suggested but never fully implemented in the literature) is given in section 2.4; results from these turbulence retrievals have some relevance to parameterizations in the microphysical retrievals discussed in Chapters 3 and 4.

2.1 Background

As discussed above, retrieval of the three-dimensional wind field from single Doppler radar observations is usually achieved by fitting the observed radial velocities to a simplified (linear or quadratic) model of the actual flow. This approach relies upon the geometry of the radar sampling: at different "look angles", the radial velocities represent different projections of the Cartesian coordinate flow onto the actual pointing vector of the antenna. If the simplified model adequately describes the actual flow, and observations are collected at enough different look angles, a heavily overdetermined system arises for the modeled wind field that can be solved easily via multivariate least squares regression. The usefulness of such a regression is fundamentally limited by two factors: the large-scale appropriateness of the chosen model and the adequacy of the sampling.

Two families of the regression-based retrievals have evolved during the last 30 years. The Velocity-Azimuth Display (VAD) technique is by far the most common, and was originally posited and tested by *Lhermitte and Atlas (1961), Caton (1963), Browning and Wexler (1968).* It employs a simple Fourier decomposition of the observed flow field, and retrieves both direct and combined measures of various wind components. Subsequent improvements *(Srivastava et al., 1986, Matejka and Srivastava, 1991)* allowed the separation of horizontal divergence and fall speed (the "Extended VAD", or EVAD technique) and incorporated the subsequent integration of divergence to yield robust vertical velocities (the "Concurrent EVAD", or CEVAD technique) *(Matejka, 1993).* Alternatively, the Volume Velocity Processing (VVP) approach *(Waldteufel and Corbin, 1979, Koscielny et al., 1982)* begins by assuming a linearized wind model, but ultimately retrieves wind field components and fall speeds similar to the VAD/EVAD-type retrievals. Recent work has incorporated automated velocity unfolding into the method *(Siggia and Holmes, 1991).* A complete diagnostic analysis of the technique was presented in *Boccippio (1995)*, and a comparison of EVAD, CEVAD, VVP and profiler retrievals of divergence and vertical velocity in stratiform anvils was recently given by *Cifelli et al. (1996).*

Although the retrieval families differ in the details of their regression formulations, they employ the same fundamental projection geometry. As such the intrinsic merits of either approach are mathematically somewhat comparable, despite a sporadic history of debate between proponents of each technique *(Boccippio, 1995).* The most significant gains in single Doppler retrieval appear to come not from the selection of a given wind model, but from the careful handling of bad or anomalous data in the regression sample and the rejection of individual retrievals that are statistically nonrobust. The mathematical elegance of the VVP technique lends it to direct and simple computation of certain crucial diagnostic parameters which play an important part in yielding stable vertical velocity profiles (i.e., profiles which are relatively consistent from one volume scan and retrieval to the next). As such, this technique is chosen for the present study.

2.2 VVP Methodology

2.2.1 Model formulation

Both the VVP and VAD families of retrievals can be formulated as a linear, multivariate least squares regression[1]:

$$\mathbf{V}_{\mathbf{r}n} = \mathbf{X}_{np}\boldsymbol{\beta}_p + \boldsymbol{\epsilon}_n \tag{2.1}$$

We attempt to model a radial velocity observation V_{r_i} as a combination of p fitted parameters β_j and independent variables X_{ij} $(i = 1, \cdots, n; j = 1, \cdots, p)$, as well as some model error ϵ_i. The independent variables ("basis functions") X_{ij} are functions of sampling location alone. In the matrix formulation of (2.1), the n observations V_{r_i} are collected in a vector, and the independent variables at each sampling location are assembled into an $n \times p$ matrix $\mathbf{X}$. A least-squares fit can then be sought for the

---

[1] When first cited, matrices and vectors will be subscripted with n or p to denote size.

model; that is, the parameters β_j can be chosen such that

$$\chi = \|\mathbf{X}\boldsymbol{\beta} - \mathbf{V}_\mathrm{r}\|_2 \tag{2.2}$$

is minimized (the bars and subscript denote the Euclidean norm). For the regression to be well behaved and robust, the basis functions $\mathbf{X}$ must exhibit sufficient dispersion in the p space of the multivariate regression; when such sampling dispersion is lacking, we do not have enough information to fit reliably p parameters, and one or more basis functions are collinear, i.e., nearly linear combinations of each other. This may result either from the definition of the function or its realization in a given sampling configuration.

The VVP approach begins by choosing which wind field components shall be sought as model parameters $\boldsymbol{\beta}$, and then determining the basis functions $\mathbf{X}$ that will appropriately yield these parameters in a regression model.[2] This is achieved by specifying the simple flow model as a linearly varying horizontal wind field (u, v) and fall speed w_p, Taylor series expanded about some reference point (x_0, y_0, z_0):

$$u = u_0 + u_x(x - x_0) + u_y(y - y_0) + u_z(z - z_0) \tag{2.3}$$

$$v = v_0 + v_x(x - x_0) + v_y(y - y_0) + v_z(z - z_0) \tag{2.4}$$

$$w_p = w_{p0} + w_{p_x}(x - x_0) + w_{p_y}(y - y_0) + w_{p_z}(z - z_0) \tag{2.5}$$

By converting the sampling locations $(x, y, z)_i$ to functions of azimuth, elevation and range, these position values become the desired independent variables X_{ij}. It is

---

[2] Alternatively, the VAD approach first selects a set of basis functions $\mathbf{X}$ (the Fourier decomposition) and then determines the flow parameters $\boldsymbol{\beta}$ to which these basis functions correspond.

conventional to set $(x_0, y_0, z_0) = (0, 0, z_0)$, thus yielding an analysis of a specific vertical layer of the atmosphere centered above the radar. Under these conditions, the basis functions reduce to those listed in Table 2.1. An important characteristic of these basis functions is that they are not inherently orthogonal. For example, the basis functions corresponding to the vertical shear parameters u_z, v_z and w_{p_z} are defined to be identical to the basic-state wind (i.e., u_0, v_0, w_{p0}) basis functions, scaled by the distance from the reference level $(z - z_0)$. When sampled, these basis functions may effectively be near linear combinations of each other. Other, less obvious collinearities exist among the 11 VVP basis functions. In practice, subsets of these parameters are used for specific applications. In the current study, the first six parameters are retained. The effects of discarding the remaining parameters, and of neglecting higher order wind components, are discussed below in Section 2.3 and are treated more extensively in *Boccippio (1995)*.

2.2.2 Minimization techniques

Two techniques for computing the fitted parameters, the regression variances, covariances and the "hat" matrix (useful in residuals analysis) are summarized below. The textbook approach (solution of the normal equations) is notoriously susceptible to roundoff error and ill conditioning; an alternative method of solution involving singular value decomposition (SVD) is often recommended operationally *(Golub and Loan, 1989, Press et al., 1992)*.

j	Basis function X_j	Reduced form	Parameter β_j
1	$\cos\phi\sin\theta$	$\hat{\imath}$	u_0
2	$\cos\phi\cos\theta$	$\hat{\jmath}$	v_0
3	$\cos\phi\sin\theta(r\cos\phi\sin\theta)$	$\hat{\imath}\delta x$	u_x
4	$\cos\phi\cos\theta(r\cos\phi\cos\theta)$	$\hat{\jmath}\delta y$	v_y
5	$\cos\phi(r\cos\phi\cos\theta\sin\theta)$	$\hat{\imath}\delta y + \hat{\jmath}\delta x$	$u_y + v_x$
6	$\sin\phi$	$\hat{k}$	w_p
7	$\cos\phi\sin\theta(r\sin\theta - \frac{r^2\cos^2\phi}{2R_e} - z_0)$	$\hat{\imath}\delta z$	u_z
8	$\cos\phi\cos\theta(r\sin\theta - \frac{r^2\cos^2\phi}{2R_e} - z_0)$	$\hat{\jmath}\delta z$	v_z
9	$\sin\phi(r\sin\theta - \frac{r^2\cos^2\phi}{2R_e} - z_0)$	$\hat{k}\delta z$	w_{p_z}
10	$\sin\phi(r\cos\phi\sin\theta)$	$\hat{k}\delta x$	w_{p_x}
11	$\sin\phi(r\cos\phi\cos\theta)$	$\hat{k}\delta y$	w_{p_y}
12	$\cos\phi\sin\theta\frac{(r\cos\phi\sin\theta)^2}{2}$	$\frac{\hat{\imath}\delta^2 x}{2}$	u_{xx}
13	$\cos\phi\sin\theta(r\cos\phi\sin\theta)(r\sin\theta - \frac{r^2\cos^2\phi}{2R_e} - z_0)$	$\hat{\imath}\delta x\delta z$	u_{xz}
14	$\cos\phi\sin\theta\frac{(r\sin\theta - \frac{r^2\cos^2\phi}{2R_e} - z_0)^2}{2}$	$\frac{\hat{\imath}\delta^2 z}{2}$	u_{zz}

Table 2.1: Basis-function/parameter decomposition for VVP under $(x_0, y_0, z_0) = (0, 0, z_0)$. θ is azimuth angle measured clockwise from north, r is slant range and ϕ is an elevation angle corrected for spherical geometry; $\phi = \phi_0 + \tan^{-1}(\frac{r\cos\phi_0}{R_e + r\sin\phi_0})$. Simplified forms of the basis functions are included in terms of the Cartesian projection functions $(\hat{\imath}, \hat{\jmath}, \hat{k})$ and datum offsets $(\delta x, \delta y, \delta z)$. Functions 12-14 are sample terms from an expanded quadratic wind field model; they will be used to demonstrate the bias effects of neglected wind field terms upon the regression.

Normal equations solution

Linear multivariate regressions are conventionally solved via the so-called normal equations *(Draper and Smith, 1981, Koscielny et al., 1982, Doviak and Zrnic, 1984)*. Premultiplication of (2.1) by $\mathbf{X}^T$ and rearrangement of terms yields the *best linear unbiased estimate* for the fitted parameters β_j:

$$\boldsymbol{\beta} = (\mathbf{X}^T\mathbf{X})^{-1}\mathbf{X}^T\mathbf{V}_r \tag{2.6}$$

If the observations V_{r_i} and model errors ϵ_i are normally distributed (as is frequently assumed), the β_j are also the *maximum-likelihood estimators (Rawlings, 1988).* Their variance can be found from the diagonal elements of the covariance matrix $\mathbf{C}$:

$$\mathbf{C}_{pp} = (\mathbf{X}^T\mathbf{X})^{-1}\frac{\mathbf{e}^T\mathbf{e}}{n-p} \tag{2.7}$$

$$\mathbf{e}_n = (\mathbf{V_r} - \mathbf{X}\boldsymbol{\beta}) \tag{2.8}$$

As will be discussed in Section 2.2.3, analysis of the regression residuals $\mathbf{e}$ frequently requires formulation of the hat (least-squares projection) matrix $\mathbf{H}$, or at least its diagonal elements,

$$\mathbf{H}_{nn} = \mathbf{X}(\mathbf{X}^T\mathbf{X})^{-1}\mathbf{X}^T \tag{2.9}$$

The hat matrix is useful as it is related to both the influence of an individual observation on the overall fit and also the distance (in the regression space) of a particular "sampling location" X_{ij} to the mean $\bar{X}_j$ *(Belsley et al., 1980).*

As noted above, computation of the cross-product matrix $\mathbf{X}^T\mathbf{X}$ is highly susceptible to roundoff error (in a typical VVP analysis, $n \sim 10^3 - 10^4$ points), as is its inversion, particularly when the matrix is very poorly conditioned. Alternative approaches to the regression include *QR decomposition* and *singular value decomposition.* The QR decomposition invokes an orthogonal transformation of the 2-norm (2.2) to generate a stabler and more numerically tractable problem. SVD is likewise more numerically stable, and as most efficient SVD algorithms include preliminary QR steps, a separate treatment of QR will not be given here.

Singular value decomposition solution

As discussed above, an alternative solution to the minimization of (2.2) is available from the products of a singular value decomposition. For diagnostic purposes, the SVD is best performed on the basis function matrix $\mathbf{X}$, scaled to have equal column lengths (this scaled matrix will be referred to as $\mathbf{Z}$), and results in an orthogonal decomposition of the form

$$\mathbf{Z}_{np} = \mathbf{U}_{np}\mathbf{D}_{np}\mathbf{V}^T_{pp} \tag{2.10}$$

that is, $\mathbf{U}^T\mathbf{U} = \mathbf{V}^T\mathbf{V} = \mathbf{I}_{pp}$, and the diagonal elements of $\mathbf{D}$ are the singular values $\boldsymbol{\lambda}_p$ of $\mathbf{Z}$ (i.e., $\lambda_j = D_{jj}$). It can easily be shown that the squares of these singular values are also the eigenvalues of the cross-product matrix $\mathbf{Z}^T\mathbf{Z}$ and the columns of the matrix $\mathbf{V}$ the corresponding eigenvectors. The scaling of $\mathbf{X}$ is particularly important due to the orders of magnitude numerical difference between fitted parameters in the single-Doppler retrieval wind models (e.g., between wind speed and divergence). In the framework of this decomposition, the fitted parameters β_j and covariance matrix $\mathbf{C}$ can be expressed as

$$\boldsymbol{\beta} = \sum_{j=1}^{p}\Big(\frac{\mathbf{U}_{(j)} \cdot \mathbf{V}_{\mathbf{r}}}{\lambda_j}\Big)\mathbf{V}_{(j)} \tag{2.11}$$

$$C_{kl} = \Big[\sum_{j=1}^{p}\Big(\frac{V_{kj}V_{lj}}{\lambda_j^2}\Big)\Big]\frac{\mathbf{e}^T\mathbf{e}}{n-p} \tag{2.12}$$

where $\mathbf{U}_{(j)}$ denotes the jth column of $\mathbf{U}$. Straightforward application of SVD can be about two to four times more costly (for large n) than LU-Cholesky solution of the normal equations, but efficient algorithms that perform a preliminary QR decomposition are available *(Golub and Loan, 1989)*. The hat matrix $\mathbf{H}$ can then be computed readily from the results of this preparatory step, or crudely as $\mathbf{ZCZ}^T$.

In addition to incorporating the numerical stability of QR decomposition, the SVD offers the added benefit of an eigenvalue analysis of the system. This analysis is extremely useful in determining whether there is sufficient dispersion in the basis functions, as sampled, to reliably fit the p desired parameters. Insufficient dispersion in one component (or a collinearity among the basis functions) will be manifest if one (or more) of the singular values λ_j is "small" *relative to the others.* Techniques to diagnose the potential damage of this condition are discussed in section 2.2.4. The primary effects of such collinearity are numerical instability in the solution, severe inflation of the variance of fitted parameters, and degradation of the robustness of the fits.

2.2.3 Operational algorithm

This section documents the VVP regression used in the current work. Its implementation differs somewhat from previously reported single-Doppler retrieval algorithms *(Koscielny et al., 1982, Matejka and Srivastava, 1991)* both in the solution technique and in the treatment of questionable data. It is believed to be stable, statistically robust, and particularly amenable to diagnostic evaluation.

Data preprocessing

Preliminary rejection of individual range bin data is often warranted based on large spectral widths (e.g., *(Koscielny et al., 1982)* in clear-air retrievals) or anomalous reflectivities (to guard against contamination from unretrievable horizontal gradients in fall speed). At low levels, it is also a good idea to more stringently screen near-zero velocity returns in order to reduce the effects of clutter breakthrough *(Matejka and Srivastava, 1991)*, which will contaminate the retrieval as bias from a basis function of unity not included in the model. It is thus helpful, in the field collection phase, to apply the same quality thresholding criteria to all data moments (e.g., reflectivity, velocity, spectral width). In this study, only near-zero velocity prefiltering is performed.

Although velocities may be manually unfolded prior to analysis, the current VVP uses the computationally efficient automatic unfolding algorithm of *Siggia and Holmes (1991)*, which is evaluated *during* the regression at relatively little extra cost (in both normal equation and SVD solution techniques). This algorithm is found to perform quite well in a variety of situations, and the conditions under which it is likely to fail (spatially unbalanced distributions of folded velocities) are probably, by definition, not amenable to single-Doppler analysis.

The VVP is typically applied to thin layers of data (two or more range bins thick) at successive heights to yield a vertical profile of retrieved parameters. A circular zone close to the radar (4 km ground range) is blanked from the regression; experience has shown that at low altitudes the high concentration of tilt intersections at close range tends to unbalance the regressions (i.e., velocity data at close range has greater weight than at far range. Since we will eventually combine divergences retrieved from all altitudes to yield a vertical velocity, it is important that these divergences accurately reflect the same spatial scales at each altitude).

Iterative regression

The regression proceeds by *once* calculating the independent variable (sampling) matrix $\mathbf{X}$. This is frequently the most time-consuming element in the retrieval process. A number of regression "passes" are then performed, each pass masking out data points that unduly influence the regression (due to their position in its $\mathbf{X}$ space) or appear to be outliers. Each pass is composed of the following:

1. Calculation of $\mathbf{X}^T\mathbf{X}$: In the normal equations solution, this matrix needs to be inverted for parameter estimation, covariance matrix and bias matrix (see below) calculation. In the solution by SVD, it is used to generate the scaled independent variables

$$\mathbf{Z} = \mathbf{X}\mathbf{S}^{-1} \tag{2.13}$$

   where $\mathbf{S}_{pp}$ is a diagonal matrix containing the roots of the diagonal elements of $\mathbf{X}^T\mathbf{X}$.

2. Parameter estimation: After inversion of $\mathbf{X}^T\mathbf{X}$ or calculation of the SVD of $\mathbf{Z}$, the fitted parameters β_j may be estimated directly from (2.6) or (2.11); this will be an $O(np^2 \text{ or } 2np^2)$ process for large n and LU or SVD solution, respectively. The unfolding algorithm of *(Siggia and Holmes, 1991)* further requires the computation of 22 "trial wind" unfoldings; the unfolding that minimizes the solution variance is assumed to be the correct unfolding. This process involves only trial wind calculations and 22 back substitutaion and is thus significantly less costly than 22 actual regressions.

3. Residuals, covariance and projection matrix calculation: This is the calculation of $\mathbf{e}, \mathbf{C}$ and the diagonals of $\mathbf{H}$ for rejection (below) and later diagnostics. These are $O(np)$, $O(p^3/3)$ and $O(2np^2)$, respectively.

4. Outlier rejection: *Matejka and Srivastava (1991)* recommend rejection of data points whose observed residuals e_i are greather than cs, where s^2 is the regression variance and $c \sim 2$. While this is in principle an effective technique to improve model performance, it relies partly on a faulty assumption. While it is generally assumed that the *model* errors ϵ_i are normally distributed with zero mean and common variance, the *observed* residuals e_i are in general not independent and do not have common variance *(Rawlings, 1988)*.[3] Thus, prior to using observed residuals to identify and reject outliers, they must be standardized to have unit variance; the standardized residuals $\mathbf{r}_n$ are thus defined by:

$$r_i = \frac{e_i}{s(1 - H_{ii})^{1/2}} \tag{2.14}$$

   The same outlier rejection criterion may then be applied based on the computed r_i.

5. Influence point rejection: Potentially influential samples are those that lie unusually far from the center of the $\mathbf{X}$ space. In multivariate regressions, this distance can be measured by H_{ii}, and points for which $(H_{ii} > 2p/n)$ are taken to have the potential for high leverage in the regression *(Belsley et al., 1980)*. However, not all the "remote" points are *necessarily* influential; the usual ap-

---

[3] Results from this study suggest that the residuals tend to be somewhat negatively skewed and leptokurtic.

proach to determine a sample's actual influence is to examine the behavior of the regression when it has been omitted from the dataset (fortunately, this can be calculated without reevaluating the regression). The current VVP implementation uses two such statistics: *Cook's D* and $DFFITS$. These analyze a data point's influence on the estimated $\boldsymbol{\beta}$ and $\mathbf{V_r}$, respectively. Other influence statistics, which analyze the effects on individual β_j and $\mathbf{C}$, can also be found in the literature. **Cook's $\mathbf{D}_n$** and **$\mathbf{DFFITS}_n$** are defined as

$$D_i = \frac{r_i^2}{p}\Big(\frac{H_{ii}}{1-H_{ii}}\Big) \tag{2.15}$$

$$DFFITS_i = \Big(\frac{H_{ii}}{1-H_{ii}}\Big)^{1/2}\frac{e_i}{s_{(i)}(1-H_{ii})^{1/2}} \tag{2.16}$$

Here, $s_{(i)}$ is the variance estimate omitting the ith observation and is obtained from

$$s_{(i)}^2(n-p-1) = s^2(n-p) - \frac{e_i^2}{1-H_{ii}} \tag{2.17}$$

Suitable threshold criteria for these statistics (i.e., properly scaled to account for regression sample size) are often taken as $(4/n)$ and $2(p/n)^{1/2}$, respectively. In the iterative regression described here, such points are flagged out of the dataset after each pass and account for about 10% of the total sample.

The current regression uses a fixed number of passes rather than an error convergence criterion. This procedure seems reasonable as successive rejection of data points will both homogenize the cluster of points in the $\mathbf{X}$ space *and* degrade the model's conditioning; it is unclear when the benefits of trade-off between these two effects is maximized. Furthermore, when looking at time- or height-evolving signatures, it will be useful to have a retrieved wind field that has been estimated using identical criteria. As such, a conservative fixed number of passes (two or three) is recommended; experience has shown that this can reduce model error by 10% to 80% with relatively little damage to the conditioning.

When directly implemented, the operational algorithm described above yields quite reasonable and consistent results. Fig. 2.1a-d shows retrieved wind parameter profiles in which the velocity unfolding algorithm has correctly handled lowlevel winds greater than the Nyquist velocity. These plots also demonstrate the flexibility of the VVP approach when used with radial velocity data collected in different ways: the profiles have been retrieved from a PPI volume scan (series of constant elevation tilts) and an RHI volume scan (series of constant azimuth tilts). The results are comparable despite the dramatically different sampling matrix $\mathbf{X}$. This generality suggests that innovative scan strategies may further improve VVP results. For example, platforms with simultaneous azimuth and elevation axis control could conceivably scan a larger storm volume more quickly than conventional single axis volume scans. Further, if phased-array meteorological radars become available, an iterative scan strategy in which the diagnostics to be described in section 2.2.4 are used to suggest radar echo "sampling holes" for the radar to automatically revisit and "oversample".

Fig. 2.2 presents time-evolutions of retrieved parameter vertical profiles for 2 August 1992. The strong consistency from level to level and from one volume scan to the next suggests robust results. However, noisy retrievals appear to dominate at the uppermost and lowermost levels. Further, multivariate regression using nonorthogonal basis functions is notoriously susceptible to producing qualitatively appealing

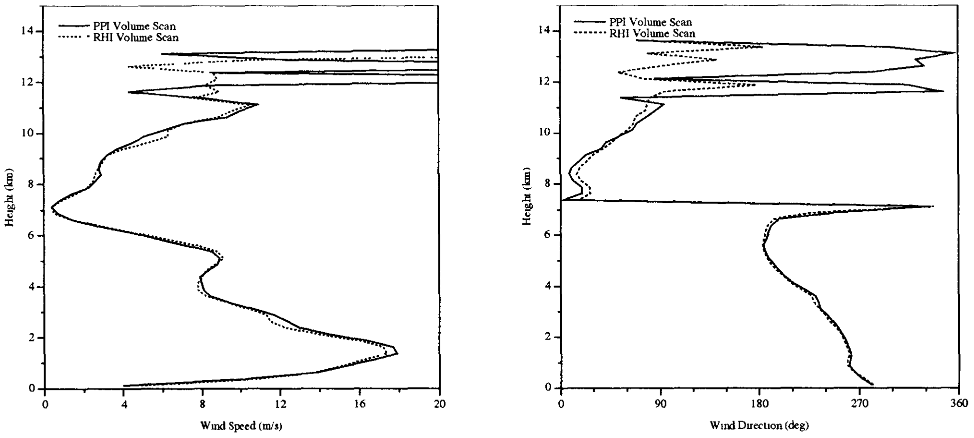

(a) Wind speed

(b) Wind direction

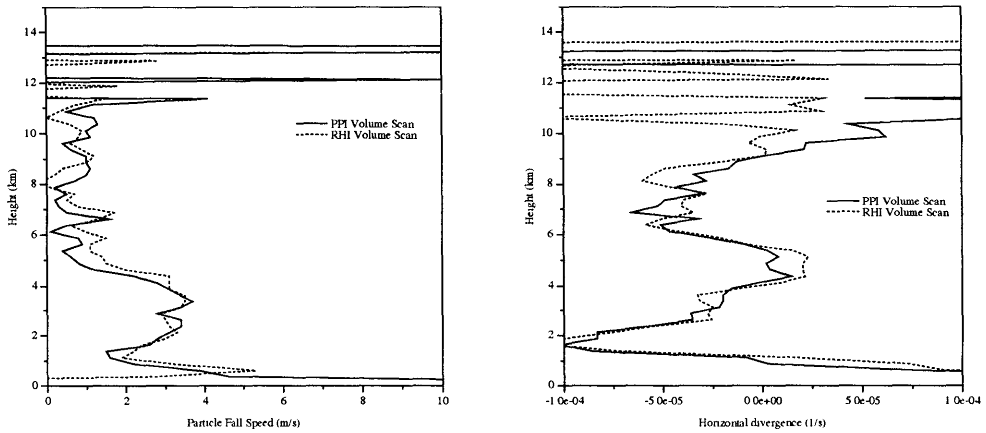

(c) Particle fall speed

(d) Horizontal divergence

Figure 2.1: Retrieved VVP parameter profiles for shallow tropical oceanic storm, 10 February 1993. Retrievals from a 12-tilt PPI scan (12 conical slices) and consecutive 24-tilt RHI scan (12 vertical slices). The Nyquist velocity for these scans is 12.5 m/s; correct VVP unfolding of wind speed is evident in (a) below 3 km AGL.

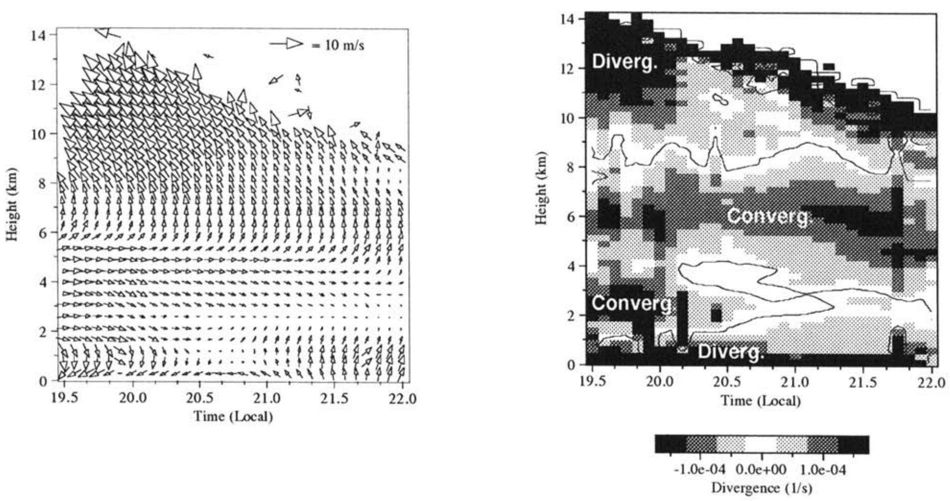

(a) Horizontal wind

(b) Horizontal divergence

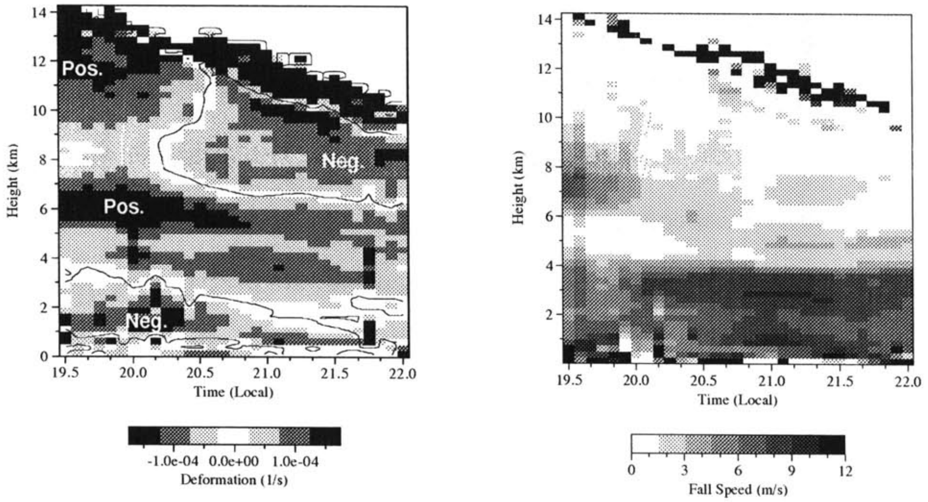

(c) Horizontal deformation

(d) Particle fall speed

Figure 2.2: Time-evolving retrieved VVP parameters for Florida storm, 2 August 1992. (a) Basic state winds u_0, v_0, (b) horizontal divergence $u_x + v_y$, (c) horizontal deformation $u_y + v_x$ and (d) particle fall speed w_p.

but spurious results. As such, diagnostic tools are needed to rigorously assess which individual retrievals in Fig. 2.2 should be trusted or rejected.

2.2.4 Diagnostics

Errors in the retrieved model parameters $\boldsymbol{\beta}$ fall into three general categories: (a) those attributable to non-systematic variation of the observed winds; (b) those due to systematic variation of the observed winds, which is not accounted for by the model; and (c) those arising from the degrading effects of intrinsic or realized collinearity in the model.

Nonsystematic variations (variance)

Nonsystematic variations in the observed wind field include the "random errors", as well as organization of the flow on scales smaller than the analysis domain. These may occur from individual convective cells etc., or from breakthrough of ground clutter or returns with broad Doppler spectra. In general, such errors simply contribute to the overall variance of the fit. Proper identification and rejection of outliers and influential points (as discussed in Section 2.2.3) can reduce the variance, but the best way to avoid undue contamination is to exercise restraint in the application of regression-type retrievals to flow fields where the simplified wind models are likely to hold.

In most reasonably homogeneous observed radial wind fields, the heavily overdetermined nature of the single-Doppler regression typically leads to quite good fits: wind variances of $O(1-2 \quad ms^{-1})^2$ and divergence variances of $O(10^{-6}-10^{-5} \quad s^{-1})^2$. However, such diagnostics are statistically meaningful only if the assumed model is indeed correct. Systematic wind field variations that are not resolved by the model must also be addressed in any reasonable treatment of regression error analysis; indeed, it will be shown that potential bias from such unresolved components often is comparable to or exceeds the actual model variance.

Unresolved systematic variations (bias)

Unresolved systematic variations include flow characteristics at or larger than the scale of the analysis domain that are not explicitly included in the simplified wind model. In VAD and EVAD retrievals or in VVP with a subset of retained parameters, these may include vertical shear (u_z, v_z, w_{p_z}) terms; even in full 11-parameter VVP, unresolved curvature components, such as u_{xx} and u_{zz}, may contribute to errors. Fortunately, the potential errors attributable to unresolved flow components are easily quantifiable. The effect of neglecting a set $(\boldsymbol{\beta}_{II}, \mathbf{X}_{II})$ of independent variables from a multivariate regression in which the the parameters $(\boldsymbol{\beta}_I, \mathbf{X}_I)$ are retained is a general model *bias (Draper and Smith, 1981)*:

$$bias(\boldsymbol{\beta}_I) = [(\mathbf{X}_I^T \mathbf{X}_I)^{-1} (\mathbf{X}_I^T \mathbf{X}_{II})] \boldsymbol{\beta}_{II}^T \tag{2.18}$$

The model bias is a distinct combination of a sampling configuration factor (***bias sensitivity***, bracketed term) and a "magnitude of neglected parameter" factor ($\boldsymbol{\beta}_{II}$ term). Note that the sensitivity term within the brackets contains a covariance matrix factor $(\mathbf{X}_I^T \mathbf{X}_I)^{-1}$. The magnitude of the $\boldsymbol{\beta}_{II}$ can either be taken as a worst-case scenario, or, in the case of neglected vertical shears, can be discretely "boot-strapped" from a profile of successive basic-state wind retrievals.[4] Further, since the model sensitivity can be expressed as a function of sampling locations alone, the behavior of potential scan strategies and flow models can be examined *before* field data collection.

For large to extreme values of the neglected parameters $\boldsymbol{\beta}_{II}$, certain sampling configurations can lead to biases on the order of the regressed parameter standard deviations. This shall be demonstrated quantitatively in section 2.3. One direct and important implication of this is that conventional confidence interval analyses, which rely fundamentally on the assumption of model accuracy, may be unrepresentative indicators of actual regression performance.

Collinearity in the regression (robustness)

The phenomenon of collinearity has been alluded to frequently in the preceding sections. Formally, it arises when either the scaled independent variable matrix $\mathbf{X}$ or the cross-product matrix $\mathbf{X}^T\mathbf{X}$ is poorly conditioned; i.e., they are nearly rank-deficient and contain rows that are near linear combinations of each other. Diagnostically, it is found when one or more singular values λ_j of the scaled independent variables $\mathbf{Z}$ are small *relative to the others.* A possible (but not recommended) way to detect collinearity is inspection of the covariance matrix $\mathbf{C}$; it is often incorrectly assumed that collinearity will be necessarily manifest in large off-diagonal terms.[5] A more appropriate (and quantitative) way to measure collinearity is of course the *condition*

---

[4] The retrieved parameters (u_0, v_0) tend to be relatively insensitive to the difficulties that beset the retrieval of horizontal shears and can thus be used in a finite-difference estimate of (u_z, v_z).

[5] In practice, collinearity involving several basis functions can easily be masked in $\mathbf{C}$ *(Belsley et al., 1980).*

number of **Z**:

$$CN = \frac{\lambda_{j_{max}}}{\lambda_{j_{min}}} \tag{2.19}$$

When large condition numbers are diagnosed, it is an indication that one of the variates is contributing little information to the regression, not necessarily because its associated parameter is insignificant but because it does not adequately explore the dimension of the p space of the regression which it purports to explain. Indeed, this lack of dispersion can actually damage the robustness and accuracy of the other fitted parameters. Determination of what constitutes a 'large' CN is somewhat empirical; *Belsley et al. (1980)* claim that values higher than about 30 are grounds for concern, although section 2.3 will show that in Doppler retrievals, values of around 9-12 are more appropriate.

As mentioned above, severe collinearity *may* have several damaging effects on the regression. The first effect is a purely numerical accumulation of errors; the earliest manifestation of this is in the LU-Cholesky solution of the normal equations *(Golub and Loan, 1989)*. The second effect is a degradation of the regression's robustness; in severely collinear cases, the values of the fitted parameters can fluctuate wildly in response to relatively small changes in the observations.[6] Again, analysis by *Golub and Loan (1989)* suggests that the *sensitivity* of the solution scales roughly as the square of CN. A third (related) effect is inflation of the variance of the fitted parameters β_j. The latter two conditions suggest that adding basis functions with poor sampling dispersion can have deleterious effects on otherwise "healthy" parameters;

---

[6] An excellent geometric visualization of this effect is given in *Rawlings (1988)*, pg. 63.

i.e., including more parameters is not necessarily better.[7] Finally, because the bias sensitivity matrix described above contains a covariance matrix factor, collinearities that do manifest themselves in large off-diagnoal terms may tend to increase this bias sensitivity. Indeed, the regression is often *most* sensitive to bias from neglected parameters that, on collinearity grounds, cannot be explicitly retrieved.

Collinearity may thus impact both adequate and inadequate regression models. However, it has been noted that not all collinearity is necessarily damaging. For example, the regression algorithm employed may be relatively insensitive to numerical effects (e.g., QR or SVD). More importantly, independent variables with nearly orthogonal basis functions may be partially *buffered* against collinearity elsewhere in the regression.[8] As such, a method is needed to assess the damage that collinearity does to the estimate of each parameter. Note from (2.12) that the fitted parameter variances C_{jj} can be decomposed into a sum of "components", each associated with an individual singular value λ_j. A near-dependency revealed by a large diagnosed CN may be causing problems if an "unusually high *proportion* of the variance of two or more parameters [is] concentrated in components associated with the same small singular value" *(Belsley et al., 1980)*. This concentration can be revealed in a matrix

---

[7] Although the addition of mutually orthogonal variates which contain no new information does not affect the error of the original parameter fits, the inclusion of even mildly collinear ones does.

[8] The effects of collinearity are not distributed equally among the regression variates. Although this may seem a benefit, it is also a hazard: if the basic state wind parameters are well buffered, a seemingly "reasonable" wind retrieval with largely spurious divergence and deformation estimates may result.

$\mathbf{\Pi}_{pp}$ of *variance-decomposition proportions*:

$$\phi_{kj} = \frac{V_{kj}^2}{\lambda_j^2} \quad \text{and} \quad \mathbf{\Phi}_k = \sum_{j=1}^{p} \phi_{kj} \tag{2.20}$$

$$\mathbf{\Pi}_{kj} = \frac{\phi_{kj}}{\mathbf{\Phi}_k} \tag{2.21}$$

Inspection of this matrix should reveal the parameters that are being damaged by the collinearity. Note, of course, that large variance decomposition proportions must be diagnosed for *two or more* parameter variances, as at least two variates are needed for a near dependency.[9]

The condition number and variance-decomposition proportions provide excellent diagnostics for the presence and impact of collinearity in the VVP model and can be formed almost trivially from the results of the SVD-based regression. Along with the fitted variances and alias matrices, they provide a rigorous *quantitative* means of determining when certain components are retrievable, or when certain sampling conditions (e.g., near echo top, or quadrant-biased echo configurations) are untenable.

2.3 VVP limitations

As discussed in sections 2.1, the performance of the VVP retrieval relies fundamentally upon both the large-scale appropriateness of the chosen (linear) wind model and the adequacy of the radar sampling. The variance, bias and robustness diagnostics developed in section 2.2.4 are excellent tools to assess this performance.

---

[9] Once can see that a single large VDP is not problematic, as in the limiting case of complete orthogonality, $\mathbf{\Pi}$ simply reduces to the identity matrix $\mathbf{I}_{pp}$ (i.e., a VDP of 1 for each singular value).

When applied to appropriate meteorological conditions (i.e., areally extensive stratiform anvil regions, clear-air boundary layers, etc.) the VVP linearity assumption is often valid to first order over typical weather radar volume scan domains (30-60 km range). When measurable radar echoes (either precipitation, insects or refractive index gradients) fill the analysis domain, contamination from higher order organized wind field components unresolved by the model is minimal. However, when sampling is limited and the analysis domain is not filled with radar echoes, significant problems can arise in VVP retrieval.

Such sampling constraints may arise for a number of reasons. They may be purely intentional: *Koscielny et al. (1982)* claimed that VVP could be applied to small (30 degree) sectors of radar data, and hence used to spatially map divergence in the clear-air boundary layer. A thorough examination of this technique's VDP matrices (2.21) and actual performance on a synthetic wind field by *Boccippio (1995)* revealed severe multicollinearity in the sector-based approach, leading to nonrobust results with spurious spatial signals in boundary layer divergence.

More commonly, sampling limitations arise from the actual distribution of radar echo within the domain. This may occur as a precipitating system advects over and past a fixed ground-based radar platform. It may also occur near the echo top of a stratiform anvil; if this top slopes rearward, individual thin analysis layers near the cloud top will contain large gaps in coverage. Because seemingly reasonable basic state winds may sometimes be retrieved with grossly inaccurate horizontal divergence estimates (see section 2.2.4), such sampling-limited retrievals must be screened very carefully.

A convenient approach to quantifying sampling effects upon VVP performance is the "sector gap", an artificial construct in which a fixed azimuthal sector contains no useful radial velocity information. For moderate to large (>60 deg) gap sizes, this geometry fairly represents actual imperfect echo distributions. Figure 2.3 depicts a 6-parameter VVP model's response to increasing sector gap size. The model's condition number CN and an arbitrary *variance inflation factor* are shown for 3 retrieval altitudes.[10] The results clearly relate the decrease in model robustness with worsen-

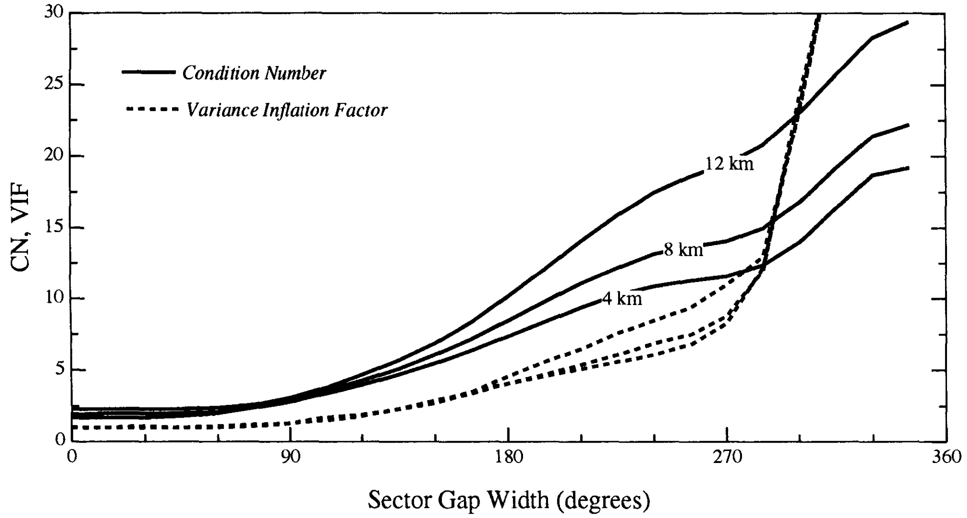

Figure 2.3: Condition numbers CN and variance inflation factors VIF for various altitudes and sector data gap widths, in a typical PPI volume scan and 6-parameter VVP retrieval.

---

[10] The VIF is defined as parameter variance in the degraded retrieval divided by parameter vari-

ing model condition, ultimately caused by the inadequate sampling's construction of model basis functions which poorly explore the regression's p-space.

The robustness limitations raised by Figure 2.3 certainly raise concern, but appear to leave room for fairly wide sector gaps before model degradation can be considered fatal. However, a related effect of worsening condition is an increasing sensitivity to unresolved model parameters (recall, the model bias from unresolved parameters (2.18) contains a covariance matrix factor $(\mathbf{X}_I^T\mathbf{X}_I)^{-1}$ which may have large off-diagonal terms in poorly-conditioned models). Figures 2.4 demonstrates this increasing sensitivity to parameters $(u_z, w_{p_x}, u_{xx}, u_{zz})$ which are not typically included in VVP models (or which are patently unretrievable due to their weak basis function definitions). The largest sensitivities appear to be to horizontal fall speed gradients w_{p_x} and horizontal curvature u_{xx}, and for large values of these neglected wind field components, such sensitivity appears to constrain acceptable gap sizes to 90-120 degrees. These results are of course only *potential* sources of bias, manifest only if such wind field components are indeed present and large in the sampled domain.

The effects of actual model and sampling limitations on VVP performance are shown in Figure 2.5(a-d). Fig. 2.5a shows the overall root mean square error ($RMSE$) of VVP fits for the 2 August retrievals presented in Fig. 2.2. The dominant contribution to retrieval $RMSE$ is actual heterogeneity (variance) in the sample radial velocity field; high $RMSE$ values during the late-stage convective period (first half-hour of the analyses) reflect this. The thin (and descending) band of moderately high $RMSE$ values at midlevels is likely due to particle fall speed effects, either from ac-

---

ance in the perfectly sampled retrieval, scaled for the decreased number of sampled points. It should not be confused with the more conventional variance inflation factor usually given as $((\mathbf{X}^T\mathbf{X})^{-1})_{ii}$.

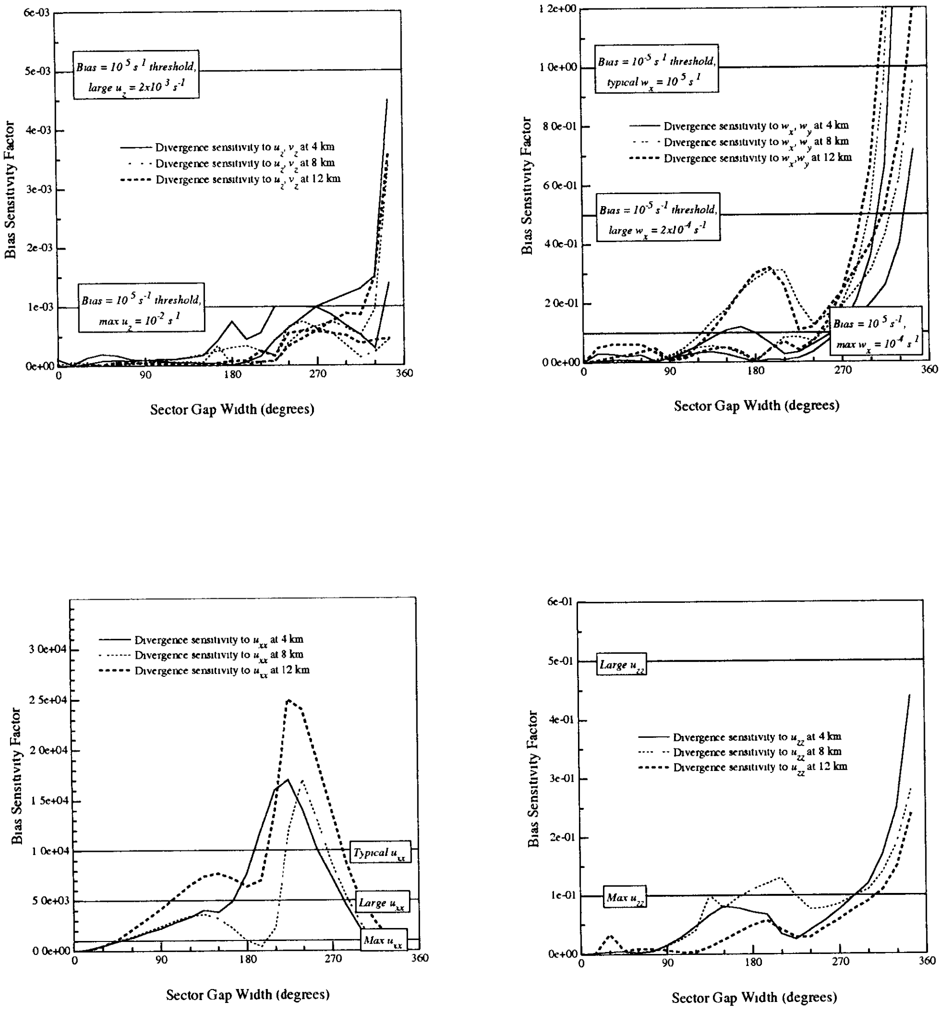

Figure 2.4: VVP retrieval sensitivity $[(\mathbf{X}_I^T\mathbf{X}_I)^{-1}(\mathbf{X}_I^T\mathbf{X}_{II})]$ to bias from unresolved components flow components, as per (2.18).

tual variability within the domain or from unresolved, systematic fall speed gradients w_{p_x} biasing the retrieval. VVP conditioning (Fig. 2.5b) is seen to be generally quite good throughout most of the analysis domain, although patchy returns at upper levels lead to a 1-2 km deep region of high CN. The lowest analysis layer also exhibits

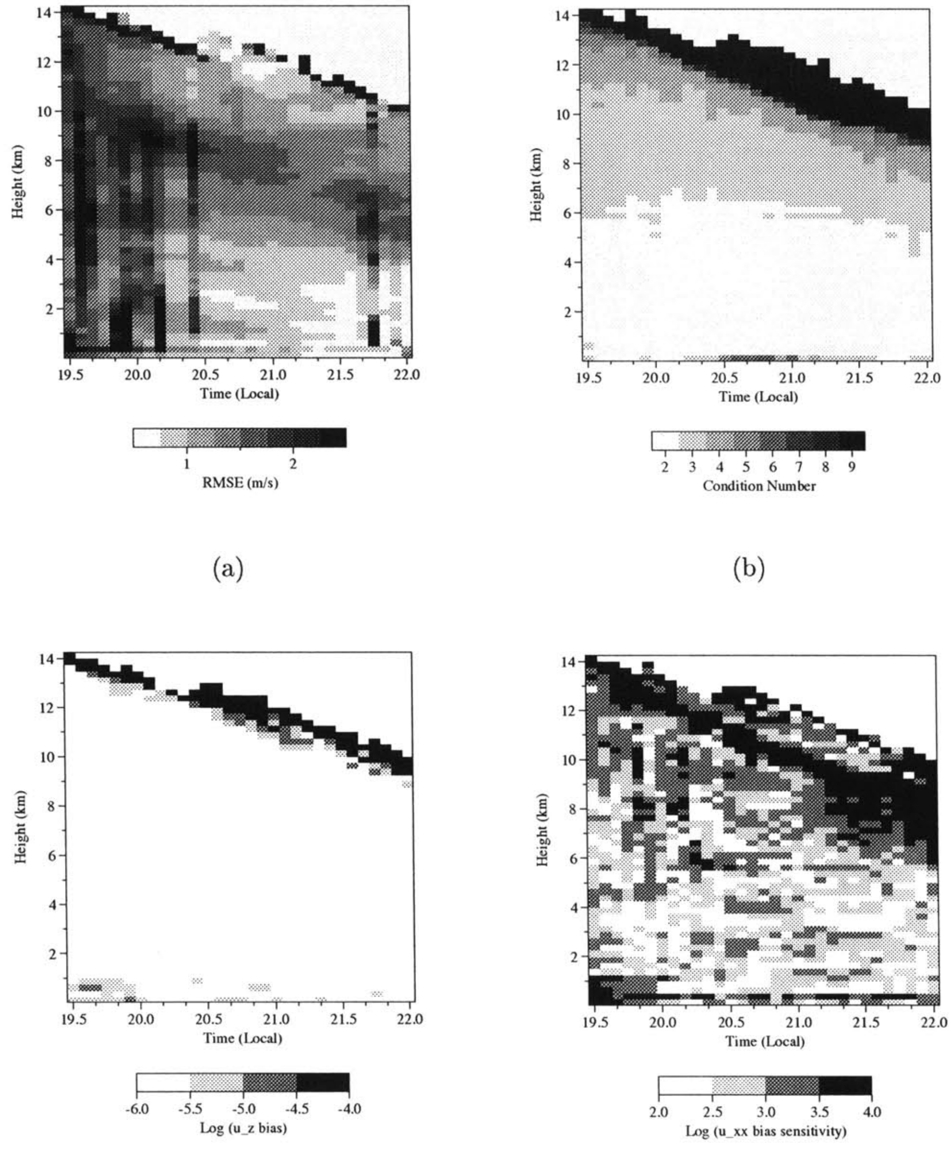

(a) (b)

(c) (d)

Figure 2.5: VVP diagnostics for retrievals on 2 August 1992, using components 1-6 of Table 2.1. (a) Root mean square error $RMSE$, (b) condition number CN, (c) estimated bias due to neglected vertical shear u_z, (d) log bias sensitivity to neglected horizontal curvature u_{xx}.

poor conditioning; this appears to be due to extensive rejection of near-surface range bins in which ground clutter has broken through. These regions of weak model basis function definition are very important, as poor retrieved divergences near the domain top and bottom can significantly contaminate subsequent integrations to yield vertical velocity profiles.

The effects of model bias are shown in Fig. 2.5c,d. Bias from neglected vertical shear is computed from (2.18), with the magnitude of $\boldsymbol{\beta}_{II} = u_z$ estimated by finite differencing the retrieved basic state wind (u_0) vertical profile. Again, shear contamination appears worst at the domain upper boundary. For $\boldsymbol{\beta}_{II} = u_{xx}$, no direct estimate of the neglected curvature magnitude is available and the model's bias sensitivity $(\mathbf{X}_I^T\mathbf{X}_I)^{-1}(\mathbf{X}_I^T\mathbf{X}_{II})$ is instead displayed. This sensitivity is generally highest at upper level regions of poor conditioning, although sporadic contamination is also possible at midlevels.

To generate consistent and error-free (t, z) fields of retrieved parameters (with the ultimate goal of estimating time-evolving vertical velocity profiles), we must thus be highly critical of poor individual layer retrievals. Fortunately, it should be noted from Fig. 2.2 that a high level of spatial and temporal continuity is generally found in the raw retrieved fields. This is certainly to be expected for domain-average quantities which are retrieved at 5-minute intervals. This continuity may thus be exploited to generate noise-free "best guesses" to the actual time-evolving fields. To this end, various filter "masks" are applied to the raw retrieved fields, based upon such diagnostics as those shown in Fig. 2.5. Suspect retrievals are thus removed from the (t, z)-gridded fields, and the missing data then interpolated from adjacent estimates using a kriging technique. The assumption here is that significant spatial or temporal evolution of the fields does not occur over the range in (t, z)-gridspace across which

Table 2.2: Diagnostic masks applied to the retrieved divergence field prior to kriging and subsequent integration.

Diagnostic	Mask A	Mask B	Mask C
$\lvert u_x + v_y \rvert$	$>6 \times 10^{-4}$	$>6 \times 10^{-4}$	$>6 \times 10^{-4}$
RMSE	-	>2.5	>2.5
CN	-	>12	>12
$\lvert u_z$ bias$\rvert$	-	$>10^{-5}$	$>10^{-5}$
$\lvert u_{xx}$ bias sensitivity$\rvert$	-	-	$>10^{3.5}$

interpolation occurs. While this likely will mean that some upper level divergence information will be lost, the presumption is that the merits of having a noise-free, smoothly evolving vertical velocity field outweigh the loss in absolute accuracy.

Table 2.2 presents three possible sets of diagnostic masking criteria. The results of such masking (as seen in eventual integration to yield vertical velocity) are presented in Fig. 2.6(a-c). It is clear from these integrations (which follow the variational integration scheme of *O'Brien (1970)* as implemented by *Matejka and Srivastava (1991)*) that spurious retrieved divergences near the domain boundaries lead to unacceptable (and, in a domain-average sense, unphysical) contamination (Fig. 2.6a). Slightly more stringent masking improves the time evolution significantly, while the strictest masking (i.e., that which assumes that unresolved horizontal curvature both exists and is biasing the model) likely rejects too much upper level divergence data (resulting in weaker upper level updrafts). As a point of interest, it should be noted that the actual altitude of the *crossover* between updrafts and downdrafts does not change under the various masking schemes; there is presumably a strong enough divergence signal at midlevels in the system to preserve the global shape of the vertical velocity profile, despite uncertainty in its absolute magnitude. This "robustness of

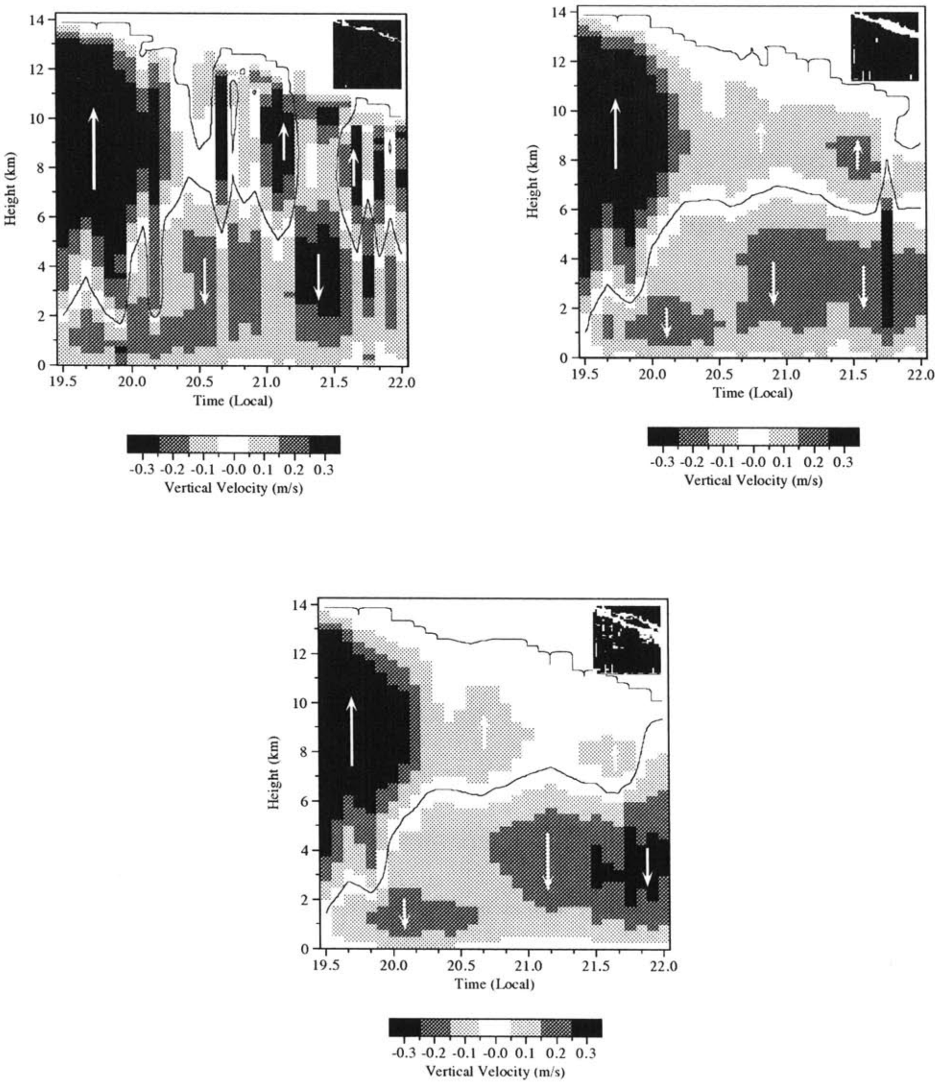

Figure 2.6: Time-evolving vertical velocity profiles integrated from retrieved horizontal divergence for 2 August 1992. Suspect divergence retrievals have been removed using various data quality masks as listed in Table 2.2; these masks are inset in the upper right corner of each plot.

shape" will be significant when such velocities are used to force the microphysical retrievals presented in Chapters 4 and 5.

2.4 Turbulence retrievals

Single Doppler radar data can not only provide estimates of domain-average horizontal wind, divergence and fall speeds, but also of various turbulence quantities (Reynolds stresses). The basic principle was detailed by *Lhermitte (1968)*, who noted that various Doppler estimates of radial velocity variance could be related to such quantities as turbulent kinetic energy (TKE) and momentum fluxes using the same approach as in VAD analysis. The methodology relies upon the decomposition of point velocity variances σ_p^2 *(Doviak and Zrnic, 1984)*:

$$\sigma_p^2 = \sigma_{\bar{v}}^2 + \langle \sigma_v^2 \rangle \tag{2.22}$$

where $\langle\rangle$ denotes an ensemble average and the overbar denotes a spatial average. The terms on the RHS correspond, respectively, to turbulent components on scales larger than the pulse resolution volume (PRV) but smaller than the domain, and on scales smaller than the PRV. Preliminary results by *Lhermitte (1968)* suggested that this scale separation was experimentaly valid. These turbulence components may be extracted by multivariate regression as in (2.1), with the independent variables given by the regression residuals e_i and the Doppler spectrum width $\sigma_{v_i}^2$, respectively. A discussion of the two approaches is given below.

2.4.1 Large scale turbulence

On scales larger than an individual PRV but smaller than the radar volume scan domain, variations of observed radial velocities from the domain average may be used to estimate turbulence. An assumption of horizontally homogeneous (though not necessarily isotropic) turbulence is required. If we also assume an unbiased (correct) wind model for the domain flow, then these variations are simply the residuals from a prior (VAD, EVAD, VVP, etc.) single Doppler retrieval. The turbulence retrieval can then be formulated in like fashion, assuming a model

$$\boldsymbol{\sigma}_{\mathbf{vr}n} = \mathbf{X}_{np}\boldsymbol{\beta}_p + \boldsymbol{\epsilon}_n \tag{2.23}$$

$$\sigma^2_{\bar{v}_{r_i}} = e_i^2 \tag{2.24}$$

The basis function/parameter decomposition for this model is shown in columns two and three of Table 2.3.

Table 2.3: Turbulence retrieval basis function and parameter decomposition. The first column of β_j are appropriate when using the VVP model residuals $\sigma^2_{\bar{v}_{r_i}} = e_i^2$ as independent variables (turbulence larger than the PRV scale). The second column of β_j are appropriate when using the observed spectrum widths $\sigma^2_{v_i}$ as independent variables (turbulence smaller than the PRV scale).

j	Basis function X_j	β_j for $\sigma^2_{\bar{v}_{r_i}}$	β_j for $\sigma^2_{v_i}$
1	$\cos^2\phi\sin^2\theta$	$\sigma^2_{\bar{u}}$	$\sigma^2_{u'}$
2	$\cos^2\phi\cos^2\theta$	$\sigma^2_{\bar{v}}$	$\sigma^2_{v'}$
3	$\sin^2\phi$	$\sigma^2_{\bar{w}_p}$	$\sigma^2_{w'_p}$
4	$\cos^2\phi\sin 2\theta$	$\mathrm{cov}(\bar{u}\bar{v})$	$\mathrm{cov}(u'v')$
5	$\sin 2\phi$	$\mathrm{cov}(\bar{v}\bar{w}_p)$	$\mathrm{cov}(v'w'_p)$
6	$\sin 2\phi$	$\mathrm{cov}(\bar{u}\bar{w}_p)$	$\mathrm{cov}(u'w'_p)$

Turbulence retrievals such as this were first suggested by *Lhermitte (1968, 1969), Wilson (1970)* using a VAD-type implementation. *Harris (1975)* attempted to implement it using S-band radar observations of an evaporating cloud base but met with little success (correlation coefficients less than 0.2 were found). Considerably greater success was obtained with X- and K-band radars *(Kropfli, 1986, Gal-Chen, 1989)* and a Doppler lidar *(Eberhard et al., 1989)* observing dry convective boundary layers. The technique was extended to a VVP-type framework and used with C-band radar data to study 20 hours of winter storm development *(Campistron et al., 1991b,a)*. In these latter studies, the results were found to be relatively robust from retrieval to retrieval, and to satisfy both physical constraints and internal consistency checks.

In the current study, attempts to apply this technique to full-volume, stratiform anvil conditions using C-band data have largely failed. Extremely low (<0.3) correlation coefficients have been found, recalling the early results of *Harris (1975)*. There are a number of reasons why this may be so. The turbulence field itself may be nonhomogeneous. Biases in the VVP model may also contaminate the residuals, which will thus contain information content beyond pure turbulence. (Any regression using residuals as an independent variable should of course be treated cautiously, at best). It is also quite possible to retrieve an apparent time- and height-evolution in the turbulence components and yet still explain very little of the observed variance. Not all of the apparently successful studies above calculated the nominal regression performance, and their results (however visually appealing) should thus be guardedly interpreted.

2.4.2 Small scale turbulence

On scales smaller than individual PRVs, velocity variances may be directly inferred from the observed Doppler spectrum width. If these variances are used as the independent variable in a turbulence regression (Table 2.3 columns two and four), estimates of small scale TKE and momentum fluxes may be obtained. This approach was first suggested in the original work by *Lhermitte (1968)* and attempted by *Harris (1975)*, who found much greater success (correlation coefficients of 0.4-0.8) than with residuals-based turbulence analysis. However, this technique has not been pursued, presumably because of the general lack of interest in Doppler spectrum width moments among radar meteorologists.

In the current study, spectrum widths were routinely recorded by the MIT radar. An excellent opportunity is thus afforded to merge, for the first time, the spectrum width-based approach with the VVP methodology, much as was recently done for the residuals-based approach *(Campistron et al., 1991b)*. Further, the robustness of this still-experimental technique can be directly tested by applying the diagnostic formalism developed in *Boccippio (1995)* and outlined in Section 2.2.4 above.

We first note that the observed spectrum width in fact contains contributions from sources other than turbulence:

$$\sigma_v^2 = \sigma_s^2 + \sigma_\alpha^2 + \sigma_d^2 + \sigma_t^2 \tag{2.25}$$

The RHS terms arise, respectively, from radial velocity shear, antenna motion, spread of the drop size distribution and actual wind turbulence. In the current study, the shear component is neglected with little justification beyond the computational difficulties in assessing it. The antenna motion component can be directly computed from *Doviak and Zrnic (1984)*:

$$\sigma_\alpha^2 = \left(\frac{\alpha\lambda\cos\phi}{2\pi\theta_1}\right)^2 \ln 2 \tag{2.26}$$

in which α is the angular velocity, θ_1 is the one-way half-power beamwidth and λ is wavelength. The drop-size spread component exhibits a geometric dependency which is already folded into the turbulence retrieval (basis function 3 in Table 2.3):

$$\sigma_d^2 = \sigma_{d_0}^2 \sin^2 \phi \tag{2.27}$$

and thus need not be removed from the observations. We thus assume the spectrum width due to turbulence to be given by the observed spectrum width less the antenna motion component, $\sigma_t^2 = \sigma_v^2 - \sigma_\alpha^2$, and use this as the independent variable in a turbulence regression:

$$\boldsymbol{\sigma}_{\mathbf{t}_n} = \mathbf{X}_{np}\boldsymbol{\beta}_p + \boldsymbol{\epsilon}_n \tag{2.28}$$

$$\sigma_{t_i}^2 = \sigma_{v_i}^2 - \sigma_\alpha^2 \tag{2.29}$$

This regression is evaluated using the same operational algorithm described in 2.2.3 for VVP retrieval of the model wind field. Note, however, that it regresses against an "independent" data moment, the Doppler velocity spectrum width.

Regressions on the datasets used in this study yield correlation coefficients of about 0.6 to 0.9, comparable with the results of *Harris (1975)*, with root mean square errors generally less than $1\text{m}^2/\text{s}^2$. An example is given in Fig. 2.7a-d. The retrievals show good vertical and temporal coherence, suggesting robust results. They also show time-varying features well coordinated with changes in the storm morphology (as revealed from reflectivity and VVP-retrieved data). These results may be used to assess the validity of various turbulence parameterization assumptions employed in the microphysical retrievals we ultimately seek (Chapters 3,4).

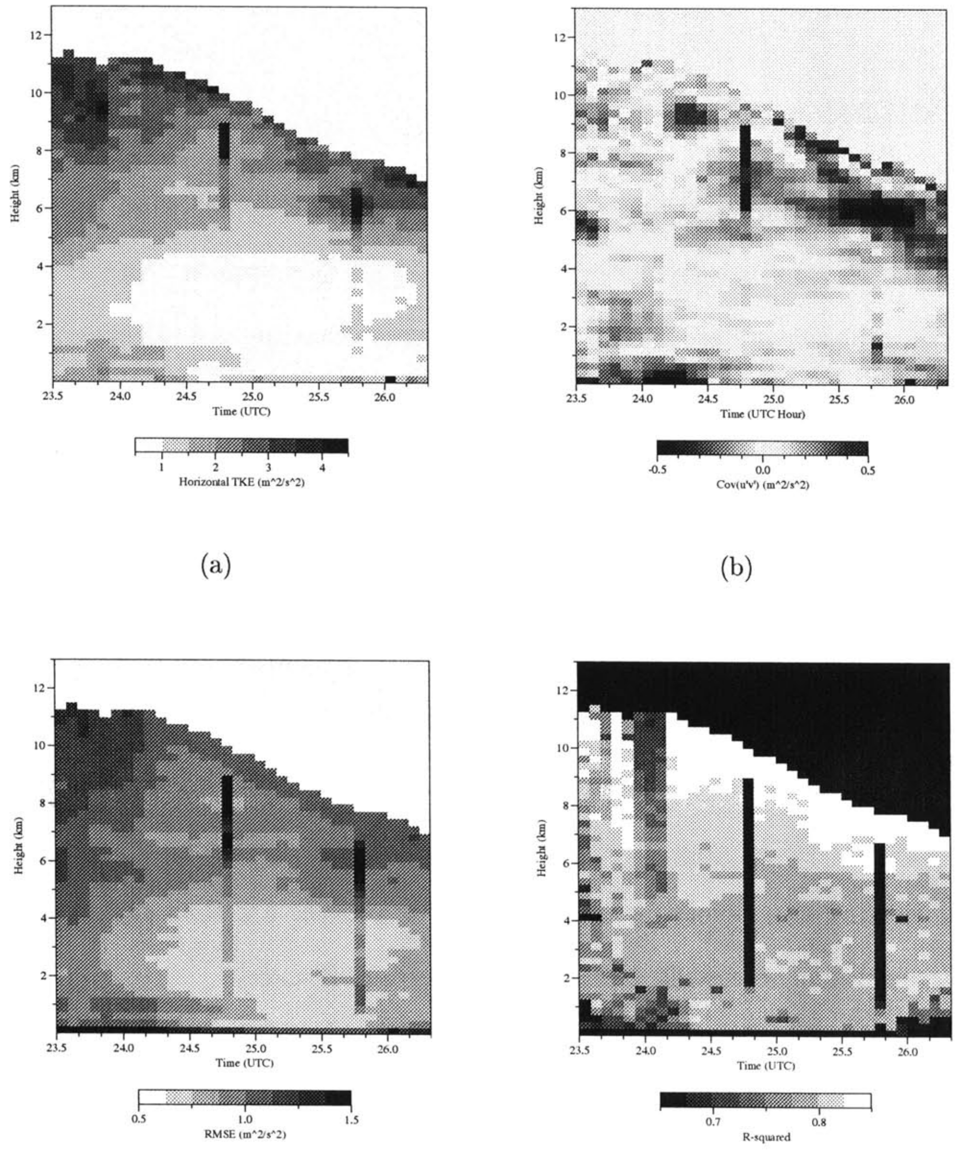

(a) (b)

(c) (d)

Figure 2.7: Sample small-scale turbulence retrievals and diagnostics from 2 August 1992. (a) Horizontal turbulent kinetic energy, (b) momentum flux cov$(u'v')$, (c) regression root mean square error, (d) regression R^2 coefficient, percent of variance explained by the model.

2.5 Summary

In this chapter, conventional approaches to VVP single-Doppler wind retrieval have been modified to a robust, numerically stable (SVD) formulation. An iterative solution algorithm has been described including data prefiltering and rejection of outliers and highly influential data in the multivariate regression. These modifications provide significant improvements in the variance of retrieved wind parameters. The mathematical elegance of the formulation also facilitates simple and direct computation of diagnostic parameters essential to identifying and rejecting nonrobust retrievals near the surface and at cloud top. Such questionable retrievals can severely damage vertical velocity estimates when horizontal divergence is integrated. The strong spatial and temporal coherence of retrieved parameters from "good" VVP regressions is thus used to estimate, via kriging, divergence values at the rejected times and altitudes. Smoothly varying time-evolving vertical velocity profiles are thus generated for use in the microphysical retrievals described in Chapters 3 and 4.

This VVP methodology is further applied to the retrieval of small-scale (radar PRV and smaller) turbulence parameters from direct measurements of the Doppler spectrum width. Coherent time-evolving fields of turbulence parameters are resolved, with acceptable root mean square errors and significant percentages of variance explained. While these retrievals are yet to be validated, they may still be of some use in estimating the variability in the vertical structure of turbulence, as well as assessing the validity of assumptions regarding horizontal eddy fluxes of hydrometeors. Both results have direct application to retrievals of bulk microphysical quantities.

Chapter 3

Microphysical retrieval: methodology

In chapter 2 a robust, noise-free time evolution of vertical velocity profiles was diagnosed for the stratiform anvil systems under study. These vertical velocities may now be used as the primary input (forcing) to a one-dimensional retrieval of bulk microphysical properties of these systems. The ultimate goal is to assess the characteristic saturation conditions and microphysical growth regimes, as we hypothesize that these determine the electrical charging behavior of these systems.

3.1 Historical review

The approaches to modeling and retrieval of the bulk microphysical properties of cloud systems can generally be broken into two distinct families. In one approach, the detailed size spectra of each hydrometeor species or ice crystal habit is explicitly tracked in either a dynamic time evolution or a progression to steady-state conditions.

This approach may generally favor a fairly physically rigorous description of cloud processes. However, it is both computationally expensive and, for retrieval purposes, underconstrained. Detailed initial or boundary conditions for complete hydrometeor spectra are rarely available from observational studies.

An alternate approach (and the one to be employed here) is to parameterize the size spectra of various hydrometeor classes and evaluate the conservation equations for various parameters associated with these spectra (e.g., mean mixing ratio, spectrum slope and intercept, etc.). This latter approach typically distinguishes between precipitating and nonprecipitating hydrometeors of each phase. Once appropriate hydrometeor spectrum and particle interaction parameterizations have been formulated, they are then interfaced with 1-, 2- or 3-dimensional kinematic/dynamic and thermodynamic models with varying degrees of complexity. Again, the calculation may proceed in either a time-evolving (prognostic) or steady-state (diagnostic) fashion. This "bulk microphysical" approach is more suitable for retrieval purposes, as initial and/or boundary conditions will usually be inferred from radar reflectivity data, which are in themselves "bulk" measurements of the cloud microphysics. For the same reasons, double-moment bulk schemes which track two spectrum parameters (e.g., an exponential size distribution slope and intercept) are disfavored for retrieval purposes. Again, in a retrieval context with minimal observational constraints, it seems advisable to avoid overparameterized models.

The single-moment bulk approach has been implemented for nearly thirty years, with subsequent researchers generally offering refinements and improvements to the needed parameterizations. The retrieval used in this study originated in early work by *Wisner et al. (1972)*, who developed a time dependent model including water vapor, cloud water, rainwater and hail, with the latter two species being exponentially distributed with constant intercept. A cloud ice category was subsequently added by *(Orville and Kopp, 1977)*, as well as an approximation to the Bergeron-Findeisen process. This important approximation was subsequently refined by *Hsie et al. (1980)*, in the context of a very similar model including vapor, cloud water, rainwater and a generic "precipitating ice" category. These authors also included several cloud ice interaction mechanisms neglected in previous models. This family of microphysical models reached its "modern" form in the work of *Lin et al. (1983)* (hereafter, LFO83), who again refined many of the interaction parameterizations (including the Bergeron process) and reintroduced a category for the hail (graupel) hydrometeor.

The model of LFO83 was subsequently used (and, again, slightly modified) by *Rutledge and Hobbs (1983)* (hereafter, RH83) in a modeling study of warm frontal rainbands. The elusive graupel/hail hydrometeor category was neglected in this model, while alternative approaches to cloud ice initiation and frozen precipitation melting were implemented. A shift in emphasis from modeling to retrieval was undertaken by *Hauser et al. (1988)*, who used an actual (retrieved) wind field to drive a microphysical retrieval based largely upon RH83 microphysics (although replacing snow with hail). This retrieval approach was extended by *Braun and Houze (1994)* in a 2-D analysis of a midlatitude MCS system. *Braun and Houze (1995)* subsequently relaxed the 2-D assumption and demonstrated that under certain conditions, horizontal eddy fluxes were negligible and a steady-state, 1-D microphysical retrieval was tractable. A summary of parameterized bulk microphysical processes in these models is given in Table 3.1. It is again noted that double-moment (e.g., hydrometeor slope and intercept tracking schemes) are not treated here; examples of such schemes may be found in *Ziegler (1985), Ferrier (1995)*.

3.2 Basic model

As noted above, the retrieval model to be used here is based primarily upon that used in *Braun and Houze (1995)*, with several modifications to be described below. It is essentially comprised of a 1-dimensional, strongly coupled system of PDEs for the continuity equations of various hydrometeor species. While horizontal and vertical transport terms are included in these equations, the primary balance is generally between *in situ* microphysical generation/depletion and fallout due to fall speed flux divergence. Vertical velocities essentially drive the model through vertical transport of water vapor.

3.2.1 Conservation equations

The conservation equation for a generic water substance with mixing ratio q_χ is given by:

$$\frac{Dq_\chi}{Dt} = \frac{\partial q_\chi}{\partial t} + \nabla_h \cdot (\mathbf{V} q_\chi) + \frac{1}{\rho_a} \frac{\partial(\rho_a w q_\chi)}{\partial z} \tag{3.1}$$

Closely following the treatment of *Braun and Houze (1995)*, this may be expressed in an areally-averaged form. Here we denote the average and deviations over an area A by $(\overline{q_\chi}, q'_\chi)$, and the average and deviations around the perimeter L of A by $(\overline{\overline{q_\chi}}, q''_\chi)$.

Table 3.1: Summary of microphysical source-sink terms included in various single-moment bulk parameterization schemes. Models are as employed by Wisner 1972 (W72), Orville and Kopp 1977 (OK77), Hsie et al. 1980 (HFO80), Lin et al 1983 (LFO83), Rutledge and Hobbs 1983 (RH83), Hauser 1988 (H88), Braun and Houze 1995 (BH95) and this thesis (B96).

	W72	OK77	HFO80	LFO83	RH83	H88	BH95	B96
Collision/coalescence	√	√	√	√	√	√	√	√
Rain accr. cld water	√	√	√	√	√	√	√	√
Rain evaporation	√	√	√	√	√	√	√	√
Rain (Biggs) freezing	√	√	√	√			√	√
Rain accr. cld ice			√	√		√	√	√
Rain accr. snow				√			√	√
Cloud ice accr. rain			√	√			√	√
Bergeron/deposition		√	√	√	√		√	√
Bergeron/riming		√	√	√			√	√
Cld ice initiation			√	√	√		√	√
Cld ice melting			√	√	√		√	√
Secondary ice prod'n								√
Snow accr. cld ice				√	√		√	√
Snow accr. cld water				√	√		√	√
Snow accr. rain				√			√	√
Snow aggreg.				√	√		√	√
Snow deposition				√	√		√	√
Snow melting				√	√		√	√
Evap. of melting snow					√		√	
Graupel accr. snow				√				
Graupel aggreg.			√	√		√		
Graupel accr. cld water	√	√	√	√		√		
Graupel accr. cld ice		√	√	√		√		
Graupel accr. rain	√	√	√	√				
Graupel wet growth		√	√	√				
Graupel sublimation		√	√	√				
Graupel melting	√	√	√	√				

Thus:

$$\begin{aligned}
\overline{\frac{Dq_\chi}{Dt}} &= \frac{\partial \overline{q_\chi}}{\partial t} + \frac{L}{A}\overline{\overline{V_n q_\chi}} + \frac{1}{\rho_a}\frac{\partial(\rho_a \overline{w q_\chi})}{\partial z} \\
&= \frac{\partial \overline{q_\chi}}{\partial t} + \frac{L}{A}\overline{\overline{V_n}}\,\overline{\overline{q_\chi}} + \frac{L}{A}\overline{\overline{V_n'' q_\chi''}} + \frac{1}{\rho_a}\frac{\partial(\rho_a \overline{w}\,\overline{q_\chi})}{\partial z} + \frac{1}{\rho_a}\frac{\partial(\rho_a \overline{w' q_\chi{}'})}{\partial z} \\
&\approx \frac{\partial \overline{q_\chi}}{\partial t} + \frac{L}{A}\overline{\overline{V_n}}\,\overline{\overline{q_\chi}} + \frac{1}{\rho_a}\frac{\partial(\rho_a \overline{w}\,\overline{q_\chi})}{\partial z} - \frac{\partial}{\partial z}\Big(K\frac{\partial \overline{q_\chi}}{\partial z}\Big)
\end{aligned} \tag{3.2}$$

In the last step of (3.2), the horizontal eddy flux component $\frac{L}{A}\overline{\overline{V_n'' q_\chi''}}$ has been neglected. *Braun and Houze (1995)* suggested that if the analysis domain boundary exists in clear air or within a horizontally uniform stratiform region, this assumption would hold. By comparing against 2-D retrievals of a midlatitude MCS system *(Braun and Houze, 1994)*, they demonstrated that neglect of these terms leads to no more than about 10-20% discrepancies in the retrieved fields. Also above, the vertical eddy flux component $\frac{1}{\rho_a}\frac{\partial(\rho_a \overline{w' q_\chi{}'})}{\partial z}$ has been replaced with the conventional $K-$parameterization for turbulent mixing. A more detailed discussion of the appropriate choice of K values (and their vertical structure) will be given in section ().

Equation (3.2) can be further simplified by recognizing that the areally averaged continuity equation is given by:

$$\frac{L}{A}\overline{\overline{V_n}} = -\frac{1}{\rho_a}\frac{\partial(\rho_a \overline{w})}{\partial z} \tag{3.3}$$

The areal average $\overline{\overline{V_n}}$ terms of (3.2) can thus be replaced, and upon regrouping,

$$\begin{aligned}
\overline{\frac{Dq_\chi}{Dt}} &= \frac{\partial \overline{q_\chi}}{\partial t} - \frac{\overline{\overline{q_\chi}}}{\rho_a}\frac{\partial(\rho_a \overline{w})}{\partial z} + \overline{q_\chi}\frac{\partial(\rho_a \overline{w})}{\partial z} + \overline{w}\frac{\partial \overline{q_\chi}}{\partial z} - \frac{\partial}{\partial z}\Big(K\frac{\partial \overline{q_\chi}}{\partial z}\Big) \\
&= \frac{\partial \overline{q_\chi}}{\partial t} + (\overline{q_\chi} - \overline{\overline{q_\chi}})\frac{\partial(\rho_a \overline{w})}{\partial z} + \overline{w}\frac{\partial \overline{q_\chi}}{\partial z} - \frac{\partial}{\partial z}\Big(K\frac{\partial \overline{q_\chi}}{\partial z}\Big)
\end{aligned} \tag{3.4}$$

The final step is to parameterize the perimeter average $\overline{\overline{q_\chi}}$; *Braun and Houze (1995)* assume it proportional to the areal mean; i.e., $\overline{\overline{q_\chi}} = \alpha\overline{q_\chi}$. Steady state conditions are further assumed, thus leaving the local generation terms to be parameterized. These will be a combination of microphysical sources and sinks $\overline{S_\chi}$ and, for precipitating hydrometeors, a fall speed flux divergence term:

$$\overline{S_\chi} + \frac{1}{\rho_a}\frac{\partial}{\partial z}(\rho_a \overline{V_{t_\chi}}\overline{q_\chi}) = (1-\alpha)\overline{q_\chi}\frac{\partial(\rho_a \overline{w})}{\partial z} + \overline{w}\frac{\partial \overline{q_\chi}}{\partial z} - \frac{\partial}{\partial z}\left(K\frac{\partial \overline{q_\chi}}{\partial z}\right) \tag{3.5}$$

In stratiform regions, $\alpha = 1$ and the first RHS term will drop out.

3.2.2 Solution methodology

The second-order conservation equations (3.5) for precipitation ice, rain, cloud ice and total water are reduced to a set of 8 linear first order differential equations in (q_s, q_r, q_{ci}, q_T) and $(q_{s_z}, q_{r_z}, q_{ci_z}, q_{T_z})$ and solved via a relaxation technique using 2-point coupling *(Press et al., 1992)*. Retrieved profiles from the initial volume scan are used as first guesses in subsequent retrievals; this reduces computation time and improves convergence significantly. Boundary conditions on the eight variables and values for the parameters K and α are discussed in greater depth in Chapter 5. Parameterization of the hydrometeor distributions, fall speeds and source/sink terms $\overline{S_\chi}$ are described in sections 3.2.3 and 3.3 below.

3.2.3 Basic parameterizations

Hydrometeor distributions

In bulk parameterization schemes, it is conventional to assume precipitation-sized hydrometeors to be inverse exponentially distributed, e.g. as based on the observations of *Leary and Houze (1979), Lo and Passarelli (1982), Stewart et al. (1984)*:

$$N_\chi(D_\chi) = N_{0_\chi} \exp(-\lambda_\chi D_\chi) \tag{3.6}$$

with χ denoting rain or precipitation ice (snow), and D_χ denoting particle melted diameter *(Potter, 1991)*. The models surveyed in Table 3.1 all assume a constant-intercept (N_{0_χ}) distribution, hence for a given mixing ratio q_χ the distribution slope can be calculated as

$$\lambda_\chi = \left(\frac{\pi \rho_w N_{0_\chi}}{\rho_a q_\chi}\right)^{\frac{1}{4}} \tag{3.7}$$

In the case of precipitation ice, this constant-intercept assumption has persisted despite compelling evidence that an equilibrium relationship, balancing aggregation and deposition, may exist between N_{0_χ} and λ_χ *(Passarelli, 1978)*, and that if anything, λ_χ tends to vary less than N_{0_χ} *(Lo and Passarelli, 1982)*.

Cloud ice is assumed monodisperse in this model, with a characteristic diameter of 12.9 μm. Cloud water, though not treated explicitly, is also assumed monodisperse where appropriate.

Fall speed

Precipitation fall speed is a crucial parameter in the microphysical retrieval, entering directly into the conservation equations for water substance. Precipitation terminal velocity is typically represented by a power-law relation to a representative particle diameter $\mathbf{D}_\chi$, scaled by an ambient density factor:

$$V_{t_\chi} = a_\chi \mathbf{D}_\chi^{b_\chi} \left(\frac{\rho_0}{\rho_a}\right)^\gamma \tag{3.8}$$

It is conventional to set γ to 0.5, although *Heymsfield and Kajikawa (1987)* provide a detailed treatment which suggests values of 0.31-0.33 are more appropriate. Integrating (3.8) over all diameters, and assuming $\mathbf{D}_\chi$ to be the particle melted diameter D_χ, the mass-weighted mean terminal velocity of a constant-intercept inverse exponential precipitation distribution is thus

$$\overline{V}_{t_\chi} = \frac{a_\chi \Gamma(4 + b_\chi)}{6\lambda_\chi^{b_\chi}} \left(\frac{\rho_0}{\rho_a}\right)^\gamma \tag{3.9}$$

Similarly, the reflectivity-weighted mean terminal velocity (useful for comparisons with VVP-retrieved w_p) is given by

$$\widetilde{V}_{t_\chi} = \frac{6}{720} \frac{\Gamma(7 + b_\chi)}{\Gamma(4 + b_\chi)} \overline{V}_{t_\chi} \tag{3.10}$$

$\widetilde{V}_{t_\chi}$ is greater than $\overline{V}_{t_\chi}$ by a factor of 1.24-1.61 for graupel species, and 1.14-1.31 for rimed and unrimed aggregates, dendrites and columnar species.

For rain, values for (a_χ, b_χ) are well established. However, for precipitation ice, the appropriate treatment of (a_χ, b_χ) in (3.8),(3.9) is often a confusing issue. *Potter*

(1991) has noted that a discrepancy exists between the use of particle melted diameter D_χ in the spectrum formulation (3.6) *(Gunn and Marshall, 1958)* and the use of particle maximum diameter $\mathbf{D}_\chi$ in empirical formulations of fall speed relationships (3.8) *(Locatelli and Hobbs, 1974)*. D_χ and $\mathbf{D}_\chi$ are of course not interchangeable, and significantly different mass-weighted fall speeds result when the two are confused. The situation is complicated further by modeling studies which cite numerical values for (a_χ, b_χ) without noting the unit system (CGS,MKS) employed. For these reasons, and because of the critical connection between fall speed values and retrieved bulk mixing ratio, a thorough retreatment is warranted here.

We first note that *Locatelli and Hobbs (1974)* present three independent sets of empirical regressions for various frozen hydrometeor species:

$$V_{t_\chi} \approx A'_\chi \mathbf{D}_\chi^{B'_\chi} \tag{3.11}$$

$$V_{t_\chi} \approx a'_\chi M_\chi^{b'_\chi} \tag{3.12}$$

$$M_\chi \approx c'_\chi \mathbf{D}_\chi^{d'_\chi} \tag{3.13}$$

These relations are of course empirical fits to noisy data, and thus are not strictly interchangeable. Typographical errors in *Locatelli and Hobbs (1974)* further complicate matters. This is demonstrated quantitatively in Table 3.2; substituting (3.13) into (3.12) we may test:

$$A'_\chi \mathbf{D}_\chi^{B'_\chi} \approx a'_\chi {c'_\chi}^{b'_\chi} \mathbf{D}_\chi^{b'_\chi d'_\chi} \tag{3.14}$$

It is apparent that significant differences exist for species such as Lump Graupel 1, Densely Rimed Columns, and Miscellaneous Unrimed Aggregates. Nonetheless, most

Table 3.2: Comparison of terminal velocity relationship coeffecients using maximum diameter $\mathbf{D}_\chi$ and mass M as independent variables; see 3.14. The coeffecients are specified assuming units as in Locatelli and Hobbs (1974); i.e., $\mathbf{D}_\chi$ in mm, M in mg, yielding $\overline{V}_{t_\chi}$ in m/s.

Ice habit χ	A'_χ	$a'_\chi {c'_\chi}^{b'_\chi}$	B'_χ	$b'_\chi d'_\chi$
Lump graupel 1	1.2	.81	.46	.45
Lump graupel 2	1.3	1.3	.66	.67
Lump graupel 3	1.5	1.4	.37	.32
Conical graupel	1.2	1.2	.65	.73
Hexagonal graupel	1.1	1.1	.57	.52
Graupel-like snow, lump	1.1	1.1	.28	.17
Graupel-like snow, hexag	.86	.82	.25	.34
Densely rimed columns	1.1	1.2	.56	.25
Densely rimed dendrite	.62	.61	.33	.37
Densely rimed dendrite 2	1.1	1.0	.12	.17
Aggreg unrimed dendrite	.81	.89	.16	.11
Aggreg rimed dendrite	.79	.79	.27	.29
Misc unrimed aggreg	.69	.95	.41	.13
Aggreg unrimed plane	.82	.76	.12	.20

of the coefficients agree well. Furthermore, correlations for Locatelli and Hobbs' fall speed relations with $\mathbf{D}_\chi$ were not particularly better than with M_χ, and it appears that the use of either independent variable is acceptable.

Following *Potter (1991)*, we next express mass M_χ in terms of melted diameter D_χ, and rederive the fall speed relation (3.8):

$$\begin{aligned} V_{t_\chi} = a_\chi D_\chi^{b_\chi} &= \left(100 a'_\chi \left(\frac{10^3\pi}{6}\right)^{b'_\chi}\right) D_\chi^{3b'_\chi} \quad \text{(CGS)} \\ &= \left(a'_\chi \left(\frac{10^9\pi}{6}\right)^{b'_\chi}\right) D_\chi^{3b'_\chi} \quad \text{(MKS)} \end{aligned} \tag{3.15}$$

The results are presented in Table 3.3; these are values of (a_χ, b_χ) now appropriate for use in (3.9). Note that the melted diameter formulation requires the use of water

Table 3.3: Terminal velocity fall speed coefficients from Locatelli and Hobbs (1974). "Incorrect values" would be those used by employing coefficients from (3.11) in (3.9). "Corrected values" are adjusted for use with melted diameter D_χ as per (3.15) and Potter (1991). Internally consistent unit systems (CGS,MKS) are used here, and the coeffecients calculated to yield terminal velocities in cm/s (CGS) or m/s (MKS). Note that the incorrect and correct coefficients are not strictly comparable, as calculation of mean fall speed $\overline{V}_{t_\chi}$ (3.9) requires the use of either ρ_χ or ρ_w in the "incorrect" and "correct" calculation of λ_χ, respectively.

	Incorrect	(CGS)	Correct	(CGS)	Correct	(MKS)
Ice habit χ	A'_χ	B'_χ	a_χ	b_χ	a_χ	b_χ
Lump graupel 1	334	.46	333	.45	26.4	.45
Lump graupel 2	594	.66	1080	.72	297	.72
Lump graupel 3	352	.37	382	.36	20.0	.36
Conical graupel	536	.70	1440	.84	691	.84
Hexagonal graupel	409	.57	617	.54	74.2	.54
Graupellike snow, lump	210	.28	231	.24	6.98	.24
Graupellike snow, hexag	153	.25	336	.42	23.3	.42
Densely rimed columns	399	.56	358	.33	16.4	.33
Densely rimed dendrite	133	.33	327	.48	29.8	.48
Densely rimed dendrite 2	145	.12	215	.24	6.48	.24
Aggreg unrimed dendrite	116	.16	182	.24	5.48	.24
Aggreg rimed dendrite	147	.27	333	.45	26.4	.45
Misc unrimed aggreg	177	.41	186	.21	4.89	.21
Aggreg unrimed plane	108	.12	288	.42	19.9	.42

density ρ_w in (3.7),(3.9), thus obviating the need for an assumption of precipitation ice density in calculating mass-weighted mean fall speeds $\overline{V}_{t_\chi}$.

3.3 Source/sink parameterizations

This section documents the specific parameterizations for source/sink terms S_χ in equations (3.5). Readers interested in only the significant changes from earlier versions of these parameterizations should skip to section 3.4 on page 116. Note that all source/sink terms documented below are calculated as mixing ratio source/sinks, and thus have units of $\frac{g_\chi}{g_a\, s}$, where g_χ is the mass of hydrometeor species χ.

3.3.1 Precipitating ice

Precipitation ice q_s (loosely, "snow") is taken here to include all frozen condensate with appreciable terminal velocities (i.e., greater than the updraft magnitude by a factor of two or so). In the context of Bergeron processes parameterized elsewhere in this model, this effectively means all frozen condensate with melted diameter greater than about 100 μm. At midlevels in the cloud, this size cutoff corresponds to terminal velocities of about 20 cm/s for Heymsfield and Kajikawa-type lump graupel, or 50 cm/s for Locatelli and Hobbs-type graupel-like snow. These terminal velocities are comparable to retrieved anvil updraft magnitudes, suggesting the 100 μm should be appropriate.

Precipitation ice is formed from the aggregation of small ice crystals, accretion of precipitation and cloud sized particles (both liquid and solid) and depositional (Bergeron) growth. As noted above, it is assumed to have an exponential distribution with *constant intercept.*

Accretion

Accretional terms dominate the precipitation ice (snow) source terms. These include snow accretion of cloud ice, snow accretion of cloud water, snow accretion of rain, rain accretion of snow, rain accretion of cloud ice (collisional freezing) and cloud ice accretion of rain. Accretion terms in which the 'accreting' species has lower *mean* terminal velocity than the 'accreted' species (e.g., 'snow accretes rain') are included because the contributions from smaller sized hydrometeors in the overall spectra may still contribute.

1. *Snow accretion of cloud ice (SACI)* is parameterized as in LFO83; integrating geometric sweepout over the q_s distribution yields:

$$SACI = \frac{\pi E_{s,ci}(T) N_{0_s} a_s \Gamma(3+b_s) q_i}{4\lambda_s^{3+b_s}} \left(\frac{\rho_0}{\rho_a}\right)^{\gamma} \tag{3.16}$$

$$E_{s,ci}(T) = \exp(.025(T - T_0)) \tag{3.17}$$

   The temperature-dependent collection efficiency is intended to crudely parameterize crystal habit effects. For typical snow and graupel-like snow at midlevels, this relation is roughly linear in both cloud ice and snow ($SACI \propto q_{ci} q_s^{0.9}$), and the exact form of the fall speed relation chosen has little impact on this scaling. Magnitudes may range from 10^{-8} to 10^{-6} g/gs.

2. *Snow accretion of cloud water (SACW)* has a form similar to $SACI$:

$$SACW = \frac{\pi E_{s,cw} N_{0_s} a_s \Gamma(3+b_s) q_{cw}}{4\lambda_s^{3+b_s}} \left(\frac{\rho_0}{\rho_a}\right)^{\gamma} \tag{3.18}$$

Hobbs (1974) notes that riming appears not to occur for crystals smaller than about 200 μm. This is roughly consistent with the chosen size cutoff between cloud ice and snow of 100 μm. *Hobbs (1974)* also presents results for a range of snow and droplet diameter suggesting that the collection efficiency is typically much lower than unity. However, since the efficiency appears to be a strong function of these diameters, a compromise value of $E_{s,cw} = 0.5$ is used here. As with $SACI$, this source term is roughly linear in cloud water and snow ($SACW \propto q_{cw}q_s^{0.9}$), and magnitudes are about 10^{-7} g/gs.

3. *Snow accretes rain (SACR).* The treatment of snow-rain and rain-snow accretion terms is somewhat problematic, as the double integral over both distributions is extremely difficult to evaluate. The traditional approach to this problem *(Wisner et al., 1972, Lin et al., 1983)* is to assume that all particles are falling at their mass-weighted terminal velocities $\overline{V}_{t_x}$ *(Wisner et al., 1972)*, hence:

$$SACR = \int_0^\infty \int_0^\infty E_{s,r} \frac{\pi(D_r + D_s)^2}{4} |V_{t_s} - V_{t_r}| \frac{\pi D_r^3}{6} \rho_w N_{0_r} e^{-\lambda_r D_r} N_{0_s} e^{-\lambda_s D_s} dD_r dD_s \tag{3.19}$$

$$\approx \pi^2 E_{s,r} N_{0_r} N_{0_s} |\overline{V}_{t_s} - \overline{V}_{t_r}| \frac{\rho_w}{\rho} \left(\frac{5}{\lambda_r^6 \lambda_s} + \frac{2}{\lambda_r^5 \lambda_s^2} + \frac{\frac{1}{2}}{\lambda_r^4 \lambda_s^3} \right) \tag{3.20}$$

The mean fall-speed assumption is necessary for analytic evaluation of the double integral. LFO83 expressed concern over this assumption, but did not attempt to assess its validity. As such, (3.19) and (3.20) have been evaluated over the full range of (q_s, q_r) parameter space. Hexagonal graupel-like snow has been assumed, with $\rho_a = 5 \times 10^{-4}$ g/cm^3. (3.19) was Simpson-integrated from 100 μm to 1 cm melted snow diameter, and 100 μm to 5 mm raindrop diameter, to 0.1% accuracy. The full integration of (3.19) is shown in Fig. 3.1a, while the

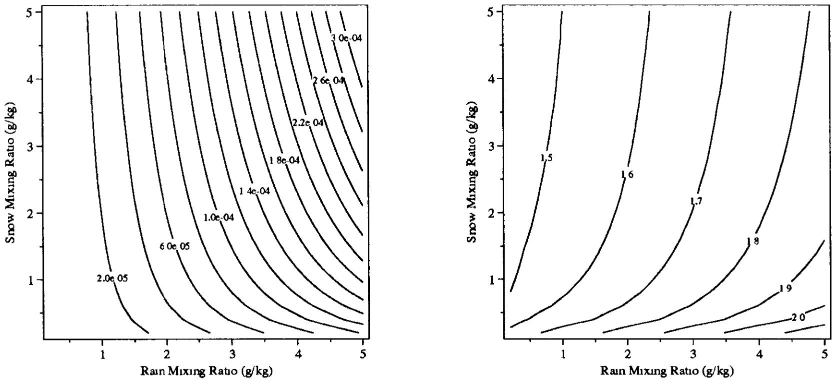

(a) Full SACR

(b) Approximate/Full ratio

Figure 3.1: (a) Full numerical integration of snow/rain accretion term SACR, in g/gs, over the range of (q_s, q_r) parameter space. (b) Ratio of SACR computed by (3.20) to SACR computed by approximation (3.19).

ratio of (3.20) to (3.19) is given in Fig. 3.1b. It is clear that the mean fall speed assumption significantly overestimates the actual accretion rates, often by as much as 50-80%. A simple scaling of (3.20) by (1/1.6), however, yields better than 10% accuracy over most mixing ratio values likely to obtain in stratiform regions ($< 3\,\mathrm{g/kg}\, q_s, < 2 - 4\,\mathrm{g/kg}\, q_r$). This scaling is used in the current study, as explicit numerical integration is too time-consuming for full-scale retrieval purposes.

LFO83 also parameterized a *rain accretes snow (RACS)* term, similar in form to (3.20). However, in their model this term acted as a snow sink (graupel source) term. Here we assume that all rain/snow interaction ends with frozen rain, acting as a snow source. Since the collection equation is integrated with respect to snow melted diameter D_s, and the fall speed differences are positive definite,

$RACS$ will simply also be given by (3.19). Hence, the final parameterization for rain/snow accretion, acting as a snow source term, is simply (2.0/1.6) times equation (3.20), or:

$$SACR + RACS = 1.25\pi^2 E_{s,r} N_{0_r} N_{0_s} |\overline{V}_{t_s} - \overline{V}_{t_r}| \frac{\rho_w}{\rho} \Big(\frac{5}{\lambda_r^6 \lambda_s} + \frac{2}{\lambda_r^5 \lambda_s^2} + \frac{\frac{1}{2}}{\lambda_r^4 \lambda_s^3} \Big) \tag{3.21}$$

4. *Rain accretion of cloud ice (RACI)*, unsurprisingly, is quite similar in form to (3.16) and (3.18):

$$RACI = \frac{\pi E_{r,ci} N_{0_r} a_r \Gamma(3 + b_r)}{4\lambda_r^{3+b_r}} q_{ci} \Big(\frac{\rho_0}{\rho_a} \Big)^{\gamma} \tag{3.22}$$

and, as $SACI$ and $SACW$, is nearly linear in both rain and cloud ice. LFO83 note that this type of collisional freezing of raindrops usually dominates over probabilistic (Biggs) type freezing (see page 115).

5. *Cloud ice accretion of rain (IACR)* is also implemented following LFO83; cloud ice is assumed monodisperse with individual crystal mass M_i. Unlike LFO83, this mass is computed explicitly as we allow for temperature-dependent crystal habits. Otherwise, integration of geometric sweepout again yields:

$$IACR = \frac{\pi^2 E_{ci,r} N_{0_r} a_r \rho_w \Gamma(6 + b_r)}{24 M_i \lambda_r^{6+b_r}} q_{ci} \Big(\frac{\rho_0}{\rho_a} \Big)^{\gamma} \tag{3.23}$$

$IACR$ is linear and cloud ice and nearly quadratic in rain ($\propto q_{ci} q_r^{1.7}$), and a *very* strong sink term for both cloud ice and rainwater, typically keeping profiles of the two species generally nonoverlapping in actual retrievals.

Aggregation

Self-aggregation of cloud ice to form precipitation ice (similar to "autoconversion" processes of rain formation from cloud droplets) is crudely parameterized here, taken as linear in cloud ice mixing ratio above a threshold q_{ci_0} of 1 g/kg:

$$SAUT = E_{ci,ci}(q_{ci} - q_{ci_0}) \tag{3.24}$$

$$E_{ci,ci} = .001\exp(.025(T - T_0)) \tag{3.25}$$

The temperature-dependent parameterization of collection efficiency is intended to mirror crystal habit effects, and thus may be at odds with explicit crystal habits used here. However, the only temperature regime where the model typically retrieves cloud ice mixing ratios greater than the aggregation threshold is from -30 to -50 C, where naturally-grown crystal habits are relatively uniform. As an additional note, the concept of self-aggregation conflicts with the assumption of a monodisperse cloud ice population: with no differential fall speeds, such aggregation will not occur. However, since the parameterization is purely empirical (i.e. doesn't explicitly depend on differential collection kernels), this inconsistency is of limited importance.

Riming and deposition

Direct riming of precipitation ice was considered above with the $SACW$ term. Riming of cloud ice (a precipitation ice source term) is discussed in the cloud ice section (3.3.2) below. Deposition follows the standard formulation *(Pruppacher and Klett, 1978)*, integrated over the snow distribution:

$$SDEP = \frac{2\pi(\frac{q_v}{q_i^*} - 1)}{\rho(A''_T + A''_v)} N_{0_s} C_{vent} \tag{3.26}$$

$$C_{vent} = \frac{0.78}{\lambda_s^2} + 0.31 Sc^{\frac{1}{3}} \Gamma(\frac{b_s + 5}{2}) a_s^{0.5} \left(\frac{\rho_0}{\rho_a}\right)^{\frac{\gamma}{2}} \nu^{-0.5} \lambda_s^{\frac{-(b_s+5)}{2}} \tag{3.27}$$

The thermal and vapor diffusive terms A''_T and A''_v are given by:

$$A''_T = \frac{L_s}{K_a T}\left(\frac{L_s}{R_w T} - 1\right) \tag{3.28}$$

$$A''_v = \frac{1}{\rho q_i^* \Psi} \tag{3.29}$$

The dynamic viscosity $\mu = \rho\nu$, air thermal conductivity K_a, air vapor diffusivity Ψ and latent heat of sublimation L_s are all weakly temperature dependent. The Schmidt number is defined as $Sc = \frac{\mu}{\rho_a \Psi}$. Empirical fits for the above have been constructed from tabulated data:

$$\mu = 5.00595 \times 10^{-7} T + 3.47479 \times 10^{-5} \qquad (\text{to } 0.1\%) \tag{3.30}$$

$$K_a = 10^7 (7.94048 \times 10^{-7} T + 2.26932 \times 10^{-5}) \qquad (\text{to } 0.2\%) \tag{3.31}$$

$$\Psi = 1.52262 \times 10^{-3} T - 0.194181 \qquad (\text{to } 0.4\%) \tag{3.32}$$

$$L_s = 10^{10} (2.637 + 0.0017 T - 3.5629 \times 10^{-6} T^2) \qquad (\text{to } \%) \tag{3.33}$$

For subsaturated conditions, the depositional growth term $SDEP$ will of course yield sublimation as well. The term C_{vent} can be loosely construed as a ventilation factor, is roughly linear in snow mixing ratio, and has a weak (±5%) temperature dependence. As a whole, (3.26) exhibits the characteristic peak at -15 C, and at water saturation is nearly linear in snow mixing ratio. It is also typically one to two orders of magnitude less than deposition onto ice crystals (see *IDEP* in section 3.3.2 below).

Melting

Melting is calculated as from LFO83, who cite *Mason (1971), Wisner et al. (1972).* It is formulated from basic heat balance considerations; the melting cooling is balanced by conduction and convection of heat to the particle surface, the latent heats involved in vapor transfer and the sensible heat of the accreted water:

$$\begin{split} SMLT = \Big(\frac{-2\pi N_{0_s}}{\rho_a L_f}\Big(K_a(T-T_0) - \\ L_v \Psi \rho_a (q_v - q_v^*)\Big)\Big) C_{vent} - \frac{C_w(T-T_0)}{L_f}(SACW + SACR) \end{split} \tag{3.34}$$

K_a, Ψ and C_{vent} are given by (3.31), (3.32) and (3.27) above. Additional empirical fits are given by:

$$\begin{split} C_w = 10^4(1.117934 \times 10^{-4}T^4 - 0.130419T^3 + \\ 54.0939T^2 - 9977.18T + 694912) \qquad (\text{to } 0.5\%) \end{split} \tag{3.35}$$

$$L_f = 10^{10}(-1.161 + 0.009T - 1.2929 \times 10^{-5}T^2) \qquad (\text{to } \%) \tag{3.36}$$

The separate "evaporation of melting snow" term *SMLTEV* used by *Rutledge and Hobbs (1983)* is redundant and not included here: (3.34) already accounts for vapor transfer from the melting particle.

3.3.2 Cloud ice

Cloud ice includes all ice crystals without appreciable terminal velocity. It is assumed monodisperse, with a crystal diameter of 12.9 μm *(Rutledge and Hobbs, 1983)*. Crystal habit is allowed to vary with temperature following *Koenig (1971), Cotton and Anthes (1989)*. Cloud ice is formed primarily by activation of ice nuclei and depositional growth, and removed via a variety of mechanisms to form precipitation ice. Despite the apparent detail in the current parameterizations, the treatment of cloud ice remains the most uncertain link in the retrieval. This is primarily because of the limited observational data available on actual in-cloud distributions of subprecipitation size ice crystals and ice nuclei. Strong assumptions must be made to facilitate the parameterizations used here. Since depositional transfer of available cloud water and water vapor to numerous, small cloud ice particles may dominate the retrieved saturation conditions, further observational constraints on cloud ice populations are essential to improving these estimates.

Aggregation and accretion

Aggregation and accretional sinks of cloud ice have already been treated in the terms $SAUT, RACI, IACR$ and $SACI$ (pages 98-102).

Bergeron process

1. *Deposition* The Bergeron process of ice crystal growth includes both depositional growth and riming of cloud ice-sized particles. The original parameterizations by *Orville and Kopp (1977), Hsie et al. (1980), Lin et al. (1983)* are somewhat empirical: they essentially promote a fraction of cloud ice to pre-

cipitation size based upon the growth time of a hypothetical 40 μm ice crystal to 50 μm. Depositional growth was approximated by a power-law fit from calculations by *Koenig (1971)*; however this formulation was only approximate, positive definite, and failed to account for sublimation in subsaturated conditions. A model timestep-dependence was also included, which is inappropriate for use in the steady state retrieval considered here.

Most of these approximations are no longer necessary. The ice crystal growth rates can now be efficiently numerically integrated using 10-point Gaussian quadrature, to better than 1% accuracy over exact (and more costly) Simpson integration (despite the non-polynomial form of the growth curve).

The timestep dependence is more difficult to resolve. The parameterization employed here follows the same principle as LFO83 (computing the promotion from crystal to precipitation size based upon crystal growth rates), but is more tuned to the assumed steady-state conditions. A "Bergeron fraction" B_F is defined, and applied to computed ice deposition rates $IDEP$, with $B_F \times IDEP$ of the term used as a precipitation ice source, and $(1 - B_F) \times IDEP$ used as a cloud ice source. B_F is the ratio of the time taken to grow from ice nucleus (.05 μm) activation to the mean (monodisperse) crystal diameter (12.9 μm), to the time it takes to grow from that mean size to a precipitation size (100 μm).[1] This assumes a continuum of growth from activation (assumed immediate) to

---

[1] The assumed nucleus diameter is likely somewhat small; *Hobbs (1974)* cites studies which find typical activation nucleus diameters of 0.5-3.0 μm. As it turns out, the actual assumed nucleus diameter has very little bearing on the growth time from nucleus to mean diameter, as the initial growth is very rapid.

precipitation. Note that this relaxation of the assumed monodisperse cloud ice distribution is taken *only* to estimate the fraction of cloud ice undergoing depositional growth which is promoted to precipitation size.

The first step here is to calculate the bulk deposition rate onto cloud ice. The formulation is very similar to (3.26), except that the cloud ice population is monodisperse, and that the diameter-dependent crystal "capacitance" $C_{ci}(D_{ci})$ which scales the vapor transfer to the crystal surface, is included:

$$\frac{1}{2}\frac{4\pi C_{ci}(\frac{q_v}{q_i^*}-1)}{(A_T''+A_v'')}\frac{q_{ci}}{\overline{M}_{ci}} \tag{3.37}$$

The $1/2$ prefactor is an empirical fix by *Koenig (1971)* to reflect observed growth rate reductions due to restrictions on water vapor "fitting in to the ice lattice". The empirical, temperature-dependent shape factors α^* and bulk densities ρ^* given in Table 1 of *Koenig (1971)* are also employed to calculate crystal ellipticity (used in calculation of the habit-dependent C_{ci} and mass M_{ci}).

For computation of B_F, we begin by defining the growth rate τ for a single ice crystal of mass M_{ci}:

$$\tau(M_{ci}) = \Big(\frac{1}{2}\frac{4\pi C_{ci}(\frac{q_v}{q_i^*}-1)}{(A_T''+A_v'')}\Big)^{-1} \tag{3.38}$$

Since we will be integrating the growth time in mass (from ice nucleus mass to precipitation ice mass), the capacitance C_{ci} is actually a strongly implicit function of crystal mass M_{ci}; i.e., $C_{ci} = C_{ci}(D_{ci}(M_{ci}))$. $D_{ci}(M_{ci})$ is a major axis function defined by specific temperature-dependent crystal habit and Koenig shape and density factors, and is easily calculated numerically by simple root-finding algorithms.

The Bergeron fraction B_F is then simply given by:

$$B_F = \frac{t_{nuc,mean}}{t_{mean,precip}} = \frac{\int_{M_{ci}(.05\mu\text{m})}^{M_{ci}(12.9\mu\text{m})} \tau(M_{ci})dM_{ci}}{\int_{M_{ci}(12.9\mu\text{m})}^{M_{ci}(100\mu\text{m})} \tau(M_{ci})dM_{ci}} \tag{3.39}$$

For typical anvil conditions, B_F is typically about 0.05, comparable with equivalent scaling numbers from the LFO83 parameterization.

2. *Riming of ice crystals* is enabled under water saturation. This implementation may be redundant with snow/cloud water accretion $SACW$, as *Hobbs (1974)* notes that riming appears ineffective for ice less than 200 μm in diameter. Nevertheless, this is close to the assumed precipitation ice size (which we are assuming that a small fraction of the cloud ice growing by deposition is attaining), so consistency might dictate that this portion of the cloud ice population be allowed to rime. LFO83 used a hypothetical 40-50 μm crystal growth rate and a timestep and temperature dependent factor to estimate the number of ice crystals N_{ci} involved in the riming process. As the current retrieval assumes steady-state (and timestep-dependent factors should be, in general, avoided), the Bergeron fraction B_F is instead used here:

$$N_{ci} = B_F \frac{q_{ci}}{\overline{M}_{ci}} \tag{3.40}$$

$$IRIM = N_{ci} E_{ci,cw} \rho_a q_{cw} \pi \frac{D^2_{100\mu\text{m}}}{4} a_s D^{b_s}_{100\mu\text{m}} \left(\frac{\rho_0}{\rho_a}\right)^\gamma \tag{3.41}$$

$E_{ci,cw}$ is assumed to have a value of 1.0, although again the results of *Hobbs (1974)* strongly challenge this assumption. Under typical midlevel anvil conditions (0.1 g/kg q_{ci} and q_{cw}, -15 C), the modelled crystal riming is comparable in magnitude with depositional growth.

Initiation

Cloud ice initiation (activation of natural atmospheric ice nuclei) is also a challenging problem, particularly in the context of a steady-state, cloudy environment assumed here. Most previous modelling studies (specifically, time-dependent ones) have relied upon expansion-chamber measurements of natural ice nuclei, as reviewed by *Fletcher (1962)*, who proposed a parameterization of the active nucleus concentration n_{nuc} of the form:

$$n_{nuc} = n_{nuc_0} \exp(\beta_{nuc}(T_0 - T)) \tag{3.42}$$

However, the Fletcher parameterization should be viewed with extreme caution. First, the measurements were of active ice nuclei in clear, not cloudy air. Second, the measurements only spanned a temperature range from -5 C to -30 C; use of (3.42) at colder temperatures is clearly an extrapolation, and given the exponential form, a severe one. Finally, *Fletcher (1962)* notes that n_{nuc} is highly variable in space and time, and that variations of n_{nuc_0} of several orders of magnitude are possible. Overall, while the use of (3.42) in the early, warm temperature, cloud development stages of a time-dependent numerical model may be a reasonable starting point, it is by no means clear that its continued application throughout the entire depth of an already cloudy region is at all appropriate.

A further difficulty arises from the fact that cloud ice concentrations observed in cumuliform clouds often cannot be explained by natural ice nucleus concentrations alone (e.g., *Hallett et al. (1978)*). While a secondary production process incorporating ice splintering during riming is included below, it appears to be fairly ineffective at the low LWC values expected in stratiform anvils. Alternative ice multiplication mechanisms which may be active in such anvils may play a crucial role in setting LWC and supersaturation values. However, given the limitations in our current understanding of such mechanisms, we are forced to rely primarily upon traditional nucleus activation schemes. This remains a fundamental limitation in the retrieval process.

Cloud ice nucleation was parameterized in such a fashion by *Hsie et al. (1980), Lin et al. (1983)* and *Rutledge and Hobbs (1983)*:

$$IINT_{LFO83} = \frac{n_{nuc}}{\rho_a}\frac{dM_{nuc}}{dt} \tag{3.43}$$

$$IINT_{RH83} = \min\left(\frac{M_{nuc}n_{nuc}}{\rho_a \delta t}, \frac{q_v - q_i^*}{\delta t}\right) \tag{3.44}$$

In addition to the dangers of using Fletcher's n_{nuc} discussed above, these parameterizations have additional problems. The initial ice crystal growth rate $\frac{dM_{nuc}}{dt}$ in (3.43) is very large; at modest ice supersaturations, growth from the nucleus to mean ice crystal diameter is very rapid (about 15 sec). Combined with large (and extrapolated) values of n_{nuc} at low temperatures, (3.43) may easily demand more water vapor than is available for ice initiation. *(Rutledge and Hobbs, 1983)* partially addressed this by assuming $IINT$ to denote both nucleus activation and growth to the mean crystal size (supported by the rapid growth rates), and by constraining initiation by the available vapor supply. However, this approach leaves no vapor available for other microphysical processes (e.g., deposition onto precipitation ice $SDEP$) and introduces the arbitrary model timestep factor δt, both questionable and inappropriate for a steady-state implementation.

A further redundancy appears to exist between the parameterization of the Bergeron process (vapor growth of ice crystals) in this thesis and the initiation of of ice nuclei and growth to the mean crystal size. Under the assumed steady-state conditions, the parameterized Bergeron process describes the entire continuum of growth from nucleation to promotion to precipitation size. As such, it already encompasses nucleus activation and growth to the mean crystal size. This is tantamount to claiming that active ice nuclei are made available at whatever rate is necessary to support steady-state depositional growth of the retrieved ice spectrum.

Suprisingly, this assertion appears to hold. For temperatures warmer than -20 C to -30 C, $IINT$ as parameterized by (3.43) or (3.44) is a tiny source term compared to comparable cloud ice sinks (precipitation accretion of cloud ice $SACI, RACI,$etc.) at these levels. For lower temperatures, the exponential increase of the Fletcher spectrum (3.42) almost invariably guarantees that initiation is limited by the available vapor supply. Hence, Fletcher-based ice nucleus initiation (the only even marginally physically-based approach we have) is largely irrelevant at warm temperatures in previously-formed, glaciated clouds, and vapor-limited at cold temperatures anyway. As such, for the current retrieval assumptions (steady-state conditions and an extant cloud), ice initiation and growth to the mean ice crystal size is already fully accounted for by the parameterization of ice deposition $IDEP$, and a separate initiation term

$IINT$ is not explicitly included in the model.

Secondary production

Under water-saturated conditions and low supercooling (-3 C to -8 C), secondary production of ice splinters is a possible mechanism for further cloud ice production. Such splintering appears to occur occasionally when cloud droplets greater than about 24 μm diameter impact precipitation ice; an assumption of 1 splinter per 200 impacts is conventional *(Hallett et al., 1978, Willis and Hallett, 1991, Rangno and Hobbs, 1994)*. This ice splinter production can thus be expressed as:

$$ISPL = \frac{1}{200} \int E_{s,cw} N_d M_{ci} \frac{\pi D_s^2}{4} V_{t_s} N_{0_s} e^{-\lambda_s D_s} dD_s \tag{3.45}$$

with N_d the number concentration of droplets greater than 24 μm diameter per gram of air and M_{ci} the mass of the splintered fragment (assumed to be the mean, i.e., monodisperse cloud ice crystal size). Assuming all cloud water to be monodisperse at 24 μm (thus $N_d = q_{cw}/M_d$), an upper limit on $ISPL$ as a mass (mixing ratio) production term is then simply:

$$ISPL \leq \frac{M_{ci}}{M_d} \frac{SACW}{200} \tag{3.46}$$

with $SACW$ as defined by (3.18).[2] For typical snow and cloud water concentrations in the -3 C to -8 C range, this term is of O(10^{-10} to 10^{-9} g/gs), about two orders

---

[2] Note that *Willis and Hallett (1991), Rangno and Hobbs (1994)* cite a form of the collection equation which is *per unit snow diameter* (but not clearly described as such), and thus appears dimensionally inconsistent with the results of *Hallett et al. (1978)*. Equations (3.45) and (3.46) are of course the actual physical representations of snow/cloud water collection and dimensionally consistent.

of magnitude less than comparable cloud ice sink terms. Although included in the current retrieval for completeness, secondary production in this temperature range is a relatively inefficient *mass* conversion term (from precipitation to cloud ice).

3.3.3 Rain

"Rain" is the conventional precipitation-sized liquid condensate, with a Marshall/Palmer type distribution. Although a collision/coalescence source term is included, it is rarely active in the 1D steady state calculations and rain is primarily formed by melting of ice.

Collision/coalescence

Collision/coalescence (cloud droplet "autoconversion" in modelling terminology) follows the conventional Kessler-type parameterization:

$$RAUT = \max(0, .001(q_{cw} - q_{cw_0})) \tag{3.47}$$

with the threshold for activation q_{cw_0} set to 0.5 g/kg. The relation is obviously linear in q_{cw}. The Kessler formulation was preferred by *Braun and Houze (1994)* over an alternate parameterization by *Berry (1968)* used by LFO83, which had a much higher threshold q_{cw_0} of 2 g/kg.

Accretion

Rain accretion of cloud water of course follows the same form as precipitation ice accretion ($SACW$ and $SACI$), as the precipitation distribution is again exponential and the cloud particle population assumed monodisperse:

$$RACW = \frac{\pi E_{r,cw} N_{0_r} a_r \Gamma(3+b_r)}{4\lambda_r^{3+b_r}} q_{cw} \left(\frac{\rho_0}{\rho_a}\right)^{\gamma} \tag{3.48}$$

As with the other precipitation/cloud particle accretion terms, it is roughly linear in both cloud water and rain mixing ratio ($RACW \propto q_r^{0.95} q_{cw}$).
Accretional terms which are sinks for rain water ($SACR/RACS, RACI, IACR$) have already been defined by equations (3.21),(3.22) and (3.23).

Evaporation

Rain evaporation follows the same form as for snow and ice deposition/sublimation. The ventilation term, again, is based on results by *Beard and Pruppacher (1971)*.

$$REVP = \frac{2\pi(\frac{q_v}{q^*} - 1)}{\rho(A_T' + A_v')} N_{0_r} C_{vent_r} \tag{3.49}$$

$$C_{vent_r} = \frac{0.78}{\lambda_r^2} + 0.31 Sc^{\frac{1}{3}} \Gamma(\frac{b_r+5}{2}) a_r^{0.5} \left(\frac{\rho_0}{\rho_a}\right)^{\frac{\gamma}{2}} \nu^{-0.5} \lambda_r^{\frac{-(b_r+5)}{2}} \tag{3.50}$$

$$A_T' = \frac{L_v}{K_a T}\left(\frac{L_v}{R_w T} - 1\right) \tag{3.51}$$

$$A_v' = \frac{1}{\rho q^* \Psi} \tag{3.52}$$

$$L_v = 10^{10}(2.5008 - .00236(T - T_0)) \tag{3.53}$$

The evaporation rate is linear in q_v, and roughly linear in rain for typical q_r values.

Freezing

In addition to collisional freezing as per rain/cloud ice accretion ($IACR$ and $RACI$), probabilistic (immersion) raindrop freezing is included *(Bigg, 1953)*. The parameterization follows LFO83:

$$RFRZ = \frac{20\pi^2 B_{Bigg} N_{0_r} \frac{rho_w}{rho_a} \exp(A_{Bigg}(T_0 - T) - 1)}{\lambda_r^7} \tag{3.54}$$

Although this process is weak in the lower mixed phase region, the exponential term makes it a very efficient rain removal mechanism far aloft. There is considerable uncertainty in the coefficients (A_{Bigg}, B_{Bigg}), but the main purpose of the mechanism is simply to prevent rain from being lofted too high. Under the weak updraft forcing ranges used in this study, it should rarely be of much importance.

3.3.4 Total water, cloud water and water vapor

As noted above, cloud water mixing ratio q_{cw} and water vapor mixing ratio q_v do not have explicit conservation equations in this retrieval. Instead, following *Braun and Houze (1995)*, we conserve total water mixing ratio q_T, and diagnose cloud water and vapor content by:

$$q' = q_T - q_r - q_s - q_{ci} - q^* \tag{3.55}$$

$$q_{cw} = \begin{cases} q' & \text{if } q' > 0, \\ 0 & \text{if } q' < 0. \end{cases} \tag{3.56}$$

$$q_v = \begin{cases} q^* & \text{if } q' > 0, \\ q' - q_r - q_s - q_{ci} & \text{if } q' < 0. \end{cases} \tag{3.57}$$

3.4 Summary of microphysical improvements

This section summarizes significant changes and improvements to the steady-state retrieval of *Braun and Houze (1994)*, itself based primarily upon parameterizations given in *Lin et al. (1983), Rutledge and Hobbs (1983)*.

1. Dimensionally consistent corrections to terminal velocity relations V_{t_x} have been calculated and analyzed, following *Potter (1991)* (pages 93-96, Table 3.3). Correction factors for comparison of reflectivity-weighted terminal velocity $\widetilde{V}_{t_x}$ with mass-weighted terminal velocity $\overline{V}_{t_x}$ have also been calculated (equation (3.10), pg. 93).

2. The assumption of mean terminal velocities in rain/snow and snow/rain accretion terms has been relaxed; a correction factor good to within 10% has been estimated from full numerical integration of the accretion kernels (pages 99-101, equation (3.21)).

3. Temperature-dependent relations for μ, K_a, Ψ, C_w, L_v, $L_s$andL_f have been developed from tabulated data (equations (3.31),(3.32),(3.35), (3.53),(3.33),(3.36)).

4. The redundant "evaporation of melting snow" $SMLTEV$ term from *Rutledge and Hobbs (1983)* has been removed (page 104).

5. Temperature-dependent cloud ice shape and bulk density parameters α^* and ρ^* as determined by *Koenig (1971)* have been implemented (page 107).

6. Koenig's power-law approximation to cloud ice depositional growth has been replaced with an explicit deposition calculation, improving accuracy and correctly allowing for crystal sublimation in subsaturated conditions. Timestep-dependencies involved in parameterization of the Bergeron process (depositional and riming growth of cloud ice) have been removed to improve consistency with steady-state assumptions. A continuum of growth from ice nucleus to precipitation ice has been assumed, and the fraction B_F of cloud ice promoted to precipitation ice estimated from direct integration of the depositional growth equation (pages 105-109).

7. The redundant cloud ice nucleus initation term is now implicit in the Bergeron parameterization, relaxing the reliance upon clear-air natural ice nuclei spectra parameterized by *Fletcher (1962)*. Ice initiation is thus implicitly limited by the available vapor supply. Again, model timestep dependencies from earlier parameterizations have been removed (pages 109-112).

8. Secondary production of cloud ice splinters under water saturation has been included in the temperature range -3 C to -8 C (pages 112-113).

Finally, it is again noted that the separate "high density precipitation ice" category (graupel or hail) used by LFO83 has been neglected in this study. The motivation for this is twofold: first, the retrieval is only being applied to systems with very weak retrieved vertical velocities. Second, inadequate observational constraints (i.e., boundary conditions) are available to support retrieval of two independent precipitation ice species whose mixing ratios are largely confined to midlevels in the analyzed vertical profile. It is again emphasized that this approach is a steady-state retrieval of cloud properties consistent with the observed forcing and boundary conditions, not a time-dependent cloud model.

3.5 Charging rates

The final step in the retrieval process is to use the inferred stratiform anvil cloud conditions to estimate actual values for the generator current. A local charge separation rate may be calculated via a lookup table of Takahashi's (1978) laboratory charging results, given the local temperature and saturation conditions. Equal and opposite amounts of charge are assumed separated onto precipitation- and crystal-sized ice. The full generator current in principle could be estimated as the net charge flux divergence by using this local separation rate as a source term in a 1-D retrieval, based upon the charge conservation equations. However, these equations would be underconstrained: appropriate boundary conditions at the surface and cloud-top for precipitation and space (cloud) charge are not known *a priori*. Local charge sink terms due to lightning discharges abd surface corona production are also unknown.

As a proxy, the local flux divergence of the charge separation rate itself may be calculated. This calculation is of course incomplete, but not necessarily unjustified. Divergence of the actual charge distribution will indeed contribute to the generator current, however such "larger-scale" charge separation will likely be depleted by lightning discharges at rates comparable to the separation itself. The divergence of the local separation *rate*, however, may be more indicative of the actual processes driving the electrical system.

The local charge separation rate $\delta\dot{Q}$ is computed over the full spectrum of target precipitation ice diameters D_s. This is necessary, as *Keith and Saunders (1990)* have found a strong dependence (4 decades) of charge separation magnitude on impacting crystal size (Fig. 3.3). This size dependence is coupled with the laboratory results of *Takahashi (1978)* (Fig. 3.2) to yield a per-collision charge separation $\delta Q(D_1, D_2, T, q_{cw})$:

$$\delta Q(D_1, D_2, T, q_{cw}) = \delta Q_{Tak}(T, q_{cw}) C_{KS90}(D_1, D_2) \tag{3.58}$$

The Keith-Saunders correction is computed using an effective diameter computed from the relative kinetic energies of the two ice specimens, as this the impact energy is believed to be the cause of the observed charging size dependence.

Total charge transfer is computed by integrating the snow/ice and snow/snow accretion/aggregation kernels over the entire range of ice diameter. Here, separate integrations are performed (using Simpson quadrature) over five diameter ranges to improve computational speed and overall accuracy (Table 3.4). The actual collection

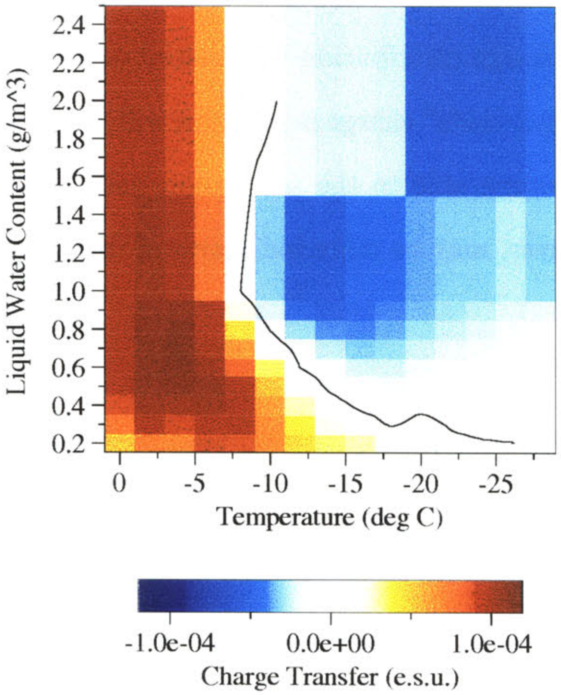

Figure 3.2: Discretization of precipitation ice charge transfer per collision, as per ***Takahashi (1978)***. These results are assumed valid for a nominal 100 μm target; charge separation for other diameters is scaled as in ***Keith and Saunders (1990)***. For water subsaturation and ice supersaturation, charging is assumed positive at the lowest magnitude observed by Takahashi.

Table 3.4: Ice diameter ranges used in collection kernel integration.

i	D_{l_i}	D_{h_i}
1	15 μm	100 μm
2	100 μm	500 μm
3	500 μm	1 mm
4	1 mm	5 mm
5	5 mm	1 cm

kernel integrations have the form:

$$\Delta\dot{Q}(T, q_{cw}) = \sum_{i=1}^{5}\left[\rho_a \int_{D_{1_{l_i}}}^{D_{1_{h_i}}} \left(\Delta\dot{Q}_{SACI}(D_1, T, q_{cw}) + \Delta\dot{Q}_{SACS}(D_1, T, q_{cw})\right) dD_1\right] \tag{3.59}$$

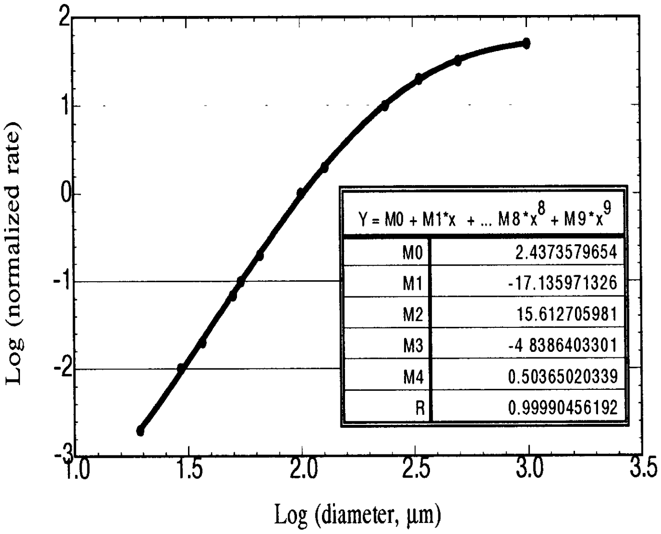

Figure 3.3: Relative charge transfer as a function of target crystal diameter, as determined by *Keith and Saunders (1990)*.

Where $\Delta\dot{Q}_{SACI}$ and $\Delta\dot{Q}_{SACS}$ denote the charge transfers from snow/ice and snow/snow collisions, respectively:

$$\Delta\dot{Q}_{SACI}(D_1,T,q_{cw}) = E_{s,i}\frac{q_{ci}}{M_{ci}}\pi\frac{D_1^2}{4}V_t(D_1)N_{0_s}e^{-\lambda_s D_1}\delta Q(T,q_{cw},D_1,12.9\mu\text{m}) \tag{3.60}$$

$$\Delta\dot{Q}_{SACS}(D_1,T,q_{cw}) = \int_{15\mu\text{m}}^{1\text{cm}} E_{s,s}\pi\frac{(D_1+D_2)^2}{4}|V_t(D_1)-V_t(D_2)|N_{0_s}^2 e^{-\lambda_s(D_1+D_2)}\delta Q(T,q_{cw},D_1,D_2)dD_2 \tag{3.61}$$

This charge transfer rate $\Delta\dot{Q}$ has units of $\frac{\text{C}}{\text{cm}^3\text{s}}$.

The charge flux is of course given by the above terms integrated with appropriate

$V_t(D)$ terms, and the "generator current term" is the vertical divergence of this charge flux, as equal and opposite charge separation is assumed here:[3]

$$\dot{J}_{net} = \sum_{i=1}^{5}\left[\frac{\partial}{\partial z}\int_{D_{1_{l_i}}}^{D_{1_{h_i}}} \rho_a\left(\Delta\dot{Q}_{SACI}V_t + \Delta\dot{Q}_{SACS}V_t\right)dD_1\right] \tag{3.62}$$

This flux divergence has units of $\frac{\mathrm{C}}{\mathrm{cm}^3\mathrm{s}^2}$ and is somewhat awkward to interpret. However, the relative magnitude and sign of this parameter will still be useful in diagnosing the generator current driving the system: by assuming $\Delta\dot{Q}$ active over a time interval comparable to a late-stage interflash interval, it may be considered as having units of current density $\frac{\mathrm{A}}{\mathrm{cm}^3}$.

3.6 Conclusion

The microphysical and generator current retrieval has now been fully documented. Clearly the individual terms are heavily overparameterized and the retrieval as a whole subject to severe limitations. The absolute magnitudes of retrieved parameters should certainly be suspect. However, the retrieval should nonetheless prove insightful in documenting the general evolution of late-stage stratiform systems. Fortunately, the critical parameter desired from the retrieval is the local relative humidity with respect to ice, as this will directly dictate the laboratory-measured charging regime at each altitude. Since depositional growth is one of the most physically-based pa-

---

[3] The volumetric units cm^3 may be neglected throughout the above derivation. The actual "generator" is conventionally expressed in units of power, and must be calculated from $\frac{\partial}{\partial z}(V_t\Phi\int_t \Delta\dot{Q})$, where Φ is the local potential. (Simple use of the local field $E_z = \frac{\partial\Phi}{\partial z}$ in the power calculation is inappropriate, as the vertical derivative must encompass all three terms). Since the actual charge distribution $Q(z)$ and hence potential Φ is unrecoverable from these retrievals, the proper generator term cannot be calculated. The "generator current" described above is still useful, as it reflects the local net charge separation at each altitude of the retrieval.

rameterizations included in the retrieval, this saturation condition may be reasonably well-determined. As will be shown in the next chapter, the retrieval indeed does yield sensible profiles of the cloud microphysics at each stage of the EOSO evolution. Further, the inferred generator currents will next be shown to match well the observed surface field evolution and lightning discharge polarity.

Chapter 4

Case studies of stratiform anvils

4.1 Introduction

Having documented the retrieval techniques for vertical velocity, hydrometeor and water vapor mixing ratio and charge separation (Chapters 2 and 3), we may now apply these retrievals to actual end-of-storm case studies observed jointly with single-Doppler radars and surface electrical sensors. The goals here are to determine whether significant charging can be maintained once downdrafts have penetrated above the melting level (thus severely depleting or removing the ambient LWC), and whether a hypothesized inverted dipole structure can be maintained under the observed time-evolving kinematic forcing. As noted in Chapter 1, these conditions will be largely determined by the ability of the system to maintain water (or, less optimally ice) saturation at low-mid levels (4-7 km AGL) in the stratiform cloud. In the crudest sense, the retrievals can be considered a simple mapping of vertical velocity to microphysical state to charging regime. The flux divergence of this microphysical charging (a function of both precipitation ice fall speed and charging rate) then determines the actual local current *from the diagnosed local charge separation.*

End of storm cases from Orlando, 1992 are used in this thesis. Electrical EOSO signals were observed frequently in August of this year (Fig. 4.1), as loosely organized convection was triggered[1], evolved, and detrained extensive upper level anvils above the observation network (see Fig. 5.2 on page 196 for the layout of this network). EOSOs were observed on 2,3,4,6,8,12,13,14 and 20 August. Of these, the events on 2 and 20 August are examined here: the former illustrates a case in which active convection had ceased during the electrical reversal, while the latter presents a case in which the active convection had persisted but propagated far northeast of the observation network. The remaining EOSO cases were less optimally positioned above the MIT radar for single-Doppler VVP retrieval throughout the entire duration of the electrical event, although lightning data from 6 August is still highly instructive and will be presented in Chapter 5 to support inferences made below.

Case studies from a squall line system in Albuquerque, NM (31 Jul 1994) and loosely organized convection in the Western Pacific warm pool (10 Feb 1993) are also presented below. The Albuquerque study is included to show that the hypothesized inverted dipole structure may also be present in more highly shear-organized systems occurring in drier environments. The Pacific (TOGA/COARE) case maps the results into more tropical regimes, and is important as surface corona over the ocean may be largely ruled out as a complicating factor in interpretation of the surface fields.

Suitable concurrent radar and surface electric data are not yet available for a midwestern Mesoscale Convective System. However, the results in more highly shear-

---

[1] Triggering usually was by either the eastern or western Florida sea breezes, and sometimes, by both in conjunction.

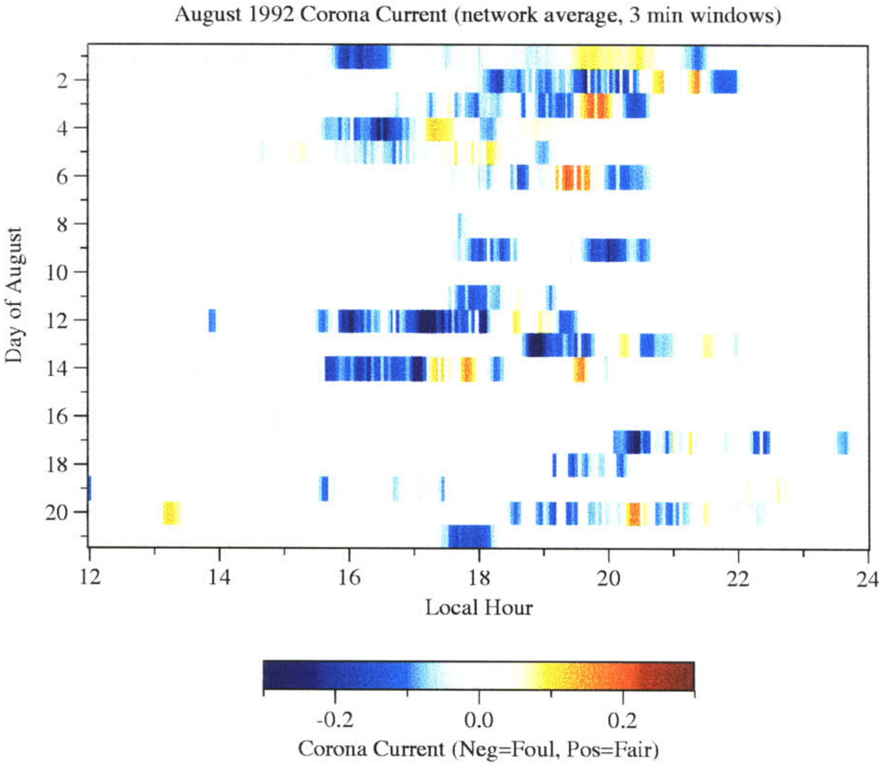

Figure 4.1: 3-minute smoothed, network-average corona currents for the Orlando, FL region in August, 1992. Currents corresponding to foul (positive) fields are shown in blue, those corresponding to fair (negative) fields in red. This color convention shall be used in all future current and field plots. EOSO events show up as late-stage excursions to fair field, e.g. on 2, 3 and 12 August.

organized systems presented here may be tentatively extrapolated to these systems provided the inferred electrical structure is not inconsistent with in-situ measurements of charge in these systems *(Stolzenburg et al., 1994, Shepherd et al., 1996, Marshall et al., 1996)*. Further, it shall be shown in Chapter 5 that the Orlando late-stage positive CGs and spider flashes exhibit structural and energetic characteristics comparable to the anomalous lightning actually observed in MCS stratiform regions. Since the hypothesized causal factor for late-stage electrical inversion is the microphysical state (saturation regime) of stratiform clouds, the results should be conceptually transferrable as well.

4.2 Orlando, 2 Aug 1992

The first case to be examined here involves the evolution of a cluster of weakly organized convection south of Orlando on 2 August 1992. The convective cores of this system evolved more or less in place, detrained an extensive upper level anvil, then dissipated after very little horizontal translation. The anvil cloud remained overhead for another two hours after convective cells had dissipated, slowly drifting northwest. A relatively simple EOSO electrical event was recorded by the corona point network (Fig. 4.2,4.3d, Tab. 4.1), and positive CG and spider IC lightning was recorded during the surface field inversion. This event offers the most straightforward test of the active inverted dipole hypothesis for loosely organized convection and its accompanying stratiform anvil.

4.2.1 Kinematics

Retrieved kinematic parameters for this storm are shown in Fig.4.3a-d, with a representative surface corona current trace added for reference. The two levels of this corona plot include the raw (1 Hz sampling) data (upper) and data filtered by a 5-minute moving average (lower). The VVP retrievals for this storm were presented in greater detail in Chapter 2 (Fig. 2.2,2.5), and horizontal divergence has been integrated using the masking scheme shown in Fig. 2.6. The retrieved wind field shows "strong" upper level velocities (up to 10 m/s, strong for summertime Florida) associated with the detrained anvil. A shear interface is evident near the updraft base, just above the melting level (Fig. 4.3a). Peak retrieved terminal velocities (retrieved fall speed less the calculated vertical velocity) well match the areal average reflectivity field, with the stratiform rain maximum showing good agreement between the two observations (Fig. 4.3c,d). The rise of the updraft base to subfreezing temperatures (above 4.5 km AGL) is exactly coincident with the onset of radar bright band, a feature which will be seen in all the cases presented here (Fig. 4.3c). Lightning discharges removing positive charge from overhead begin near time 24:10 (00:10 UTC 3 August) (Fig. 4.2), also coincident with the bright band onset. DC surface fields begin their reversal at 24:25 UTC, coincident with the enhancement of lowlevel stratiform rain. Discharges cease by 25:00 (01:00 UTC), and the surface field reverses to positive (foul) values by 25:30 (01:30 UTC), concurrent with the decline in stratiform rain.

Retrieved vertical velocities are relatively weak and uniform (5-15 cm/s) throughout the anvil duration. A slight deepening of low-mid level downdrafts appears to be associated with the peak in bright band intensity. The updraft/downdraft crossover occurs well above the melting level throughout this event. As noted in Chapter 2, this result is robust under different levels of divergence quality scrutiny. Overall, this case offers a high-quality VVP retrieval and simple electrical evolution for study.

4.2.2 Microphysics

Retrieved microphysical fields for this case are presented in Figure 4.4a-d. An 80% surface relative humidity was used as a lower boundary condition on total water q_T, with the turbulence parameter K set to 800 $\mathrm{m^s/s}$.[2] The observed surface reflectivity sets the lower boundary condition on rain mixing ratio q_r, while the domain top is set to the altitude of 0 dBZ areally averaged reflectivity. At domain top, precipitation mixing ratio q_s is set by this reflectivity to be 0.02 g/kg, and cloud ice mixing ratio q_{ci} is set to zero. In the domain interior, imposed constraints during the retrieval solution zero cloud water q_{cw} and rain q_r at temperatures lower than -40 C, and precipitation ice q_s at temperatures higher than +5 C. The entrainment parameter α is set to zero throughout the analysis, despite non domain-filling radar echoes during the first half-hour of the analysis period. These parameter values and boundary conditions shall be termed the "control run", and unless otherwise noted are used for all cases presented herein. The general sensitivity to the parameters is dicussed in *Braun and Houze (1995)*, and treated with a focus on the inferred electrification in section 4.2.4 below.

The retrieved precipitation bulk mixing ratios are not particularly surprising: precipitation ice peaks just above the melting level during the late active stages of

---

[2] The K value was chosen as the lowest value for which *Braun and Houze (1995)* achieved model convergence in a stratiform region retrieval.

the storm, as does surface rain. The secondary stratiform rain maximum is not resolved by the model, unsurprising as the retrieval has no "memory" from timestep to timestep and it is well accepted that this secondary peak arises from previously detrained and settling ice. Failure to retrieve this important component is worrisome, but may be of secondary importance in light of the objective here: to quantify the relative microphysical source/sink terms and their subsequent mapping into charging regimes. It will be shown that the domain boundaries and updraft structure are far more important to these terms than the retrieved amounts of lowlevel precipitation.

Cloud particle mixing ratios (ice and water) show interesting patterns. The strong updrafts from times 23:30-24:00 appear to depress mid level cloud ice concentrations, favoring a partitioning of total water into precipitation ice and cloud water. As the updrafts weaken and the domain top drops, cloud ice concentrations at mid levels increase. Cloud water mixing ratios drop to near 0.1 g/kg during the stratiform period. Some ice supersaturation is maintained below the updraft base here, as deposition and other vapor sink terms are not strong enough to subsaturate the cloud in these regions.[3] The recovery of midlevel cloud water from 25:30-26:00 appears to be a result of the extremely low domain tops: insufficient ice nuclei are activated near these warmer tops to act as a cloud water sink / precipitation ice source. It is unknown whether this effect is real or an artefact of the retrieval; in-situ microphysical measurements of actual evolving stratiform clouds are necessary to determine this.

---

[3] This saturation is a strong function of the assumed turbulence parameter K, as model turbulence effectively acts as an upward transport of total water mixing ratio q_T (which decreases with height). It will be shown that lower values of K cause the cloud water profile to more closely "hug" the updraft base. However, sensitivity runs suggest that the model equations are stiffer under these lower values and robust results are difficult to achieve (*Braun and Houze (1995)* also cite a difficulty in model convergence using smaller K values).

4.2.3 Electrification

Inferred charging characteristics of the 2 August cloud are shown in Fig. 4.5a-d. The first panel shows the source term *SACI* (snow accretion of cloud ice), which comprises the bulk of the total ice-ice collisions.[4] The collision rate peaks from times 24:00-24:30, only after deep updrafts have weakened and concurrent with the onset of anomalous polarity discharges and later surface field reversal (24:05 and 24:20). The next panel maps the collision rate through the inferred charge transfers, given retrieved cloud water mixing ratios and local temperatures. This mapping yields more total charge transfer during the late-active period (23:30-24:00), despite fewer collisions. Nonetheless, it is evident that charging persists through the duration of the stratiform anvil, down by only a factor of two from the late-active stage charge transfer. This charging further extends slightly below the updraft base, despite extremely low retrieved cloud water. The higher concentrations of cloud ice and number of snow-ice collisions appear to compensate for the reduced charging efficiency under depleted cloud water conditions (the portion of Fig. 3.2 below 0.5 g/m^3 LWC). This yields an important first result: local in-situ charge transfer and separation is indeed possible, and relatively effective, under the liquid water-depleted environment of the detrained stratiform cloud.[5]

As previously noted, this charge transfer will not directly lead to charge centers within the cloud, as charge is simply transferred from large to small cloud particles.

---

[4] Snow-snow collisions, also included in equation (3.59), are about 10-100 times fewer than snow-ice collisions. Specifically, snow-ice collisions involving precipitation ice in the 1-5 mm diameter size range dominates, followed by ice in the 500 μm- 1 mm range.

[5] This result is also not inconsistent with the observed transient activity although lightning flash rates drop by an order of magnitude during the late stage, the total charge transfer of late-stage +CG flashes appears to be at least an order of magnitude greater than that of active-stage -CG flashes (see Chapter 5).

A net flux divergence of this charge (a result of differential fall speeds and structure in the vertical profile of fall speed) is required to yield local net charge regions. This vertical derivative is here called the "generator term", and is shown in Figure 4.5c. While displayed with a hot/cool color scale, it should be remembered that this variable is not the distribution of actual charge, but rather of the local generator current directly due to collisional charge separation.

The generator term plot reveals a basic 'inverted dipole' net charging structure. This charging must of course be superposed on any local net charge deposited *prior* to the analysis window. Clearly an inverted dipole charging cannot explain the foul fields and normal polarity discharges (-CGs) from times 23:30-24:00. It is further likely that the model under-retrieves representative cloud water mixing ratios during this period, as the VVP clearly underestimates vertical velocities characteristic of convective cell cores (although these values may still be representative of domain-average updrafts). Cloud water underestimation will be discussed below. Again, it is important to remember that an inverted dipole generator may still not be inconsistent with the observed electrical activity, as this must be superposed on previously separated charge regions (the -CG flash rate *is* declining from 23:30-24:00, Fig. 4.2).

It is also interesting to note that a quadrupolar generator structure is found from 23:30-24:00 UTC, despite a unipolar precipitation charging regime. This is a result of the fine structure in retrieved cloud water, cloud ice and precipitation ice fields (and hence charge transfer rate), and the associated flux divergence. It is important to recognize that this flux divergence is the ultimate determinant of *any* overall net charge structure. Thus, multilayer charge centers as observed with balloon-borne field mills *(Stolzenburg et al., 1994, Shepherd et al., 1996, Marshall et al., 1996)* are *not* inconsistent with a simple mixed-phase microphysics, noninductive charging theory. Many factors in microphysical growth (temperature-dependent ice crystal habits, collection efficiencies, nucleus activation rates, and depositional growth rates) may all contribute to a rich fine-scale vertical structure leading to charge distributions more complex than simple dipoles. Consistency with the surface field and cloud-base lightning measurements simply dictates that the lowermost component of the vertical structure robustly exhibit a dominantly inverted dipole element; more complicated structure aloft does not necessarily invalidate the reversed ice-ice collisional charge separation mechanism in these clouds.

As noted above, it is likely that the microphysical retrieval (and VVP) are inappropriately employed from 23:30-24:00, and vertical velocities and cloud water contents underestimated. This possibility is explored in Figure 4.5d, which shows the generator term calculated from charging rates assuming three times the retrieved cloud water content.[6] This forces a pocket of negative per-collision charge transfer from -10 to -30 C, as might be characteristic under "normal" storm conditions. The resulting generator term closely resembles a "normal" storm tripole: lower net positive charging confined to just above the melt level, net negative charging from -5 to -18 C, and net positive charging aloft to -35 C. The negative net charging region ascends as cloud water diminishes and the per-collision charge transfer returns to the positive regime.[7] It is interesting to note that during this period of ascent (23:50-24:20), the

---

[6] A more physical approach might be to increase the vertical velocity profile uniformly in pressure (mass) coordinates. However, for this type of areal average technique to retrieve LWC high enough to enter the negative precipitation charging regime, extremely strong updrafts are required. Under such conditions, the model becomes unstable and a high-density ice species (such as hail or graupel) should really be included.

[7] This ascent emulates the hypothetical dipole "inversion", here from -5 to -25 C.

total vertical separation of the lower positive and negative charging centers is quite large, and that this is precisely the period when +CG flashes begin to dominate the electrical transient activity. It is also interesting to note that transient activity ceases at 25:00 (01:00 UTC), when the midlevel generator terms are starting to decline.

The actual generator behavior likely lies somewhere between panels *(c)* and *(d)*; without better estimates of late-active stage cloud water contents and hydrometeor distributions, more detailed analysis of the initial EOSO stage is hardly wise. Fortunately, the storm on 20 August (section 4.3) provides a case study in which the EOSO onset is delayed until a time in which radar echo distributions justify use of the 1-D assumption in both VVP and microphysical retrieval.

4.2.4 Sensitivity

A brief treatment of the sensitivity of inferred electrical activity to microphysical retrieval parameters and boundary conditions is warranted here. For the most part, the *structure* of the inferred electrical behavior is relatively robust, although actual magnitudes vary somewhat with chosen parameters.

Fig. 4.6 presents the charge transfer rate and generator terms for the control run (panels *(a,b)*) and a retrieval using a lower (500 m^2/s vs. 800 m^2/s) value for the turbulence parameter K (panels *(c,d)*).[8] Several differences are relevant here. First, the transfer rate now hugs the updraft base, a result of cloud water also following this level closely under this microphysical retrieval. Nonetheless, lower positive generator

---

[8] The retrieval failed to converge for K values lower than 500 m^2/s.

terms persist from times 24:00-25:00 (interestingly, the latter is again the time of the last observed lightning transient). The overall charging and generator structure are roughly comparable to the control run, although the magnitudes are down by a factor of 5 (again, an indirect result of overall LWC depletion and thus reduced charging efficiency). In the reduced turbulence run, a feature less discernible but still present in the control run is also evident: from 24:00-24:45, the peak lower positive generator "lags" the upper negative generator. This may have some relevance to the observed surface fields (which are inverting during this period, possibly because of the delayed dominance of lower positive charging), but again, model limitations at the early stage preclude firm conclusions.

Figure 4.7 shows results from a reduced (70%) surface relative humidity run (panels *(a,b)*) and a run in which the Fletcher natural ice nucleus concentrations have been arbitrarily increased by a factor of 10 (panels *(c,d)*).[9] The sensitivity to surface relative humidity is almost minimal when mapped through to charging behavior. With the artificially increased ice nucleus concentrations, the "depressing" effects of stronger updrafts upon retrieved cloud ice mixing ratio appears to have been partially offset, and strong charging is now found earlier in the analysis window. The overall structure of the generator terms is similar to the control run, however.

In summary, the following conclusions can be drawn from the 2 August 1992 case. First, continued charging and charge separation is indeed possible (and effective) through the stratiform period, despite depressed cloud water contents (0.1-0.2 g/kg) and midlevel (subfreezing) downdrafts. Second, during the stratiform period the

---

[9] Since cloud ice is assumed monodisperse at 13 μm diameter, the mixing ratio values plotted can be approximately converted to number concentrations in units of $\frac{1}{\text{kg}}$ by multiplying by 10^8.

generator current has a simple, inverted dipolar structure. Finally, a diversity of charge layers appears to be possible even in unipolar per-collision charge-transfer regimes, given sufficient fine-scale structure in cloud hydrometeor distributions and vertical velocity.

Table 4.1: Key times (UTC hour+24) in the electrical EOSO event on 2-3 August 1992.

Event	Time
First positive flash	24:10
DC field turns fair	24:25 - 24:35
Last positive flash	25:00
DC field turns foul	25:25-25:30

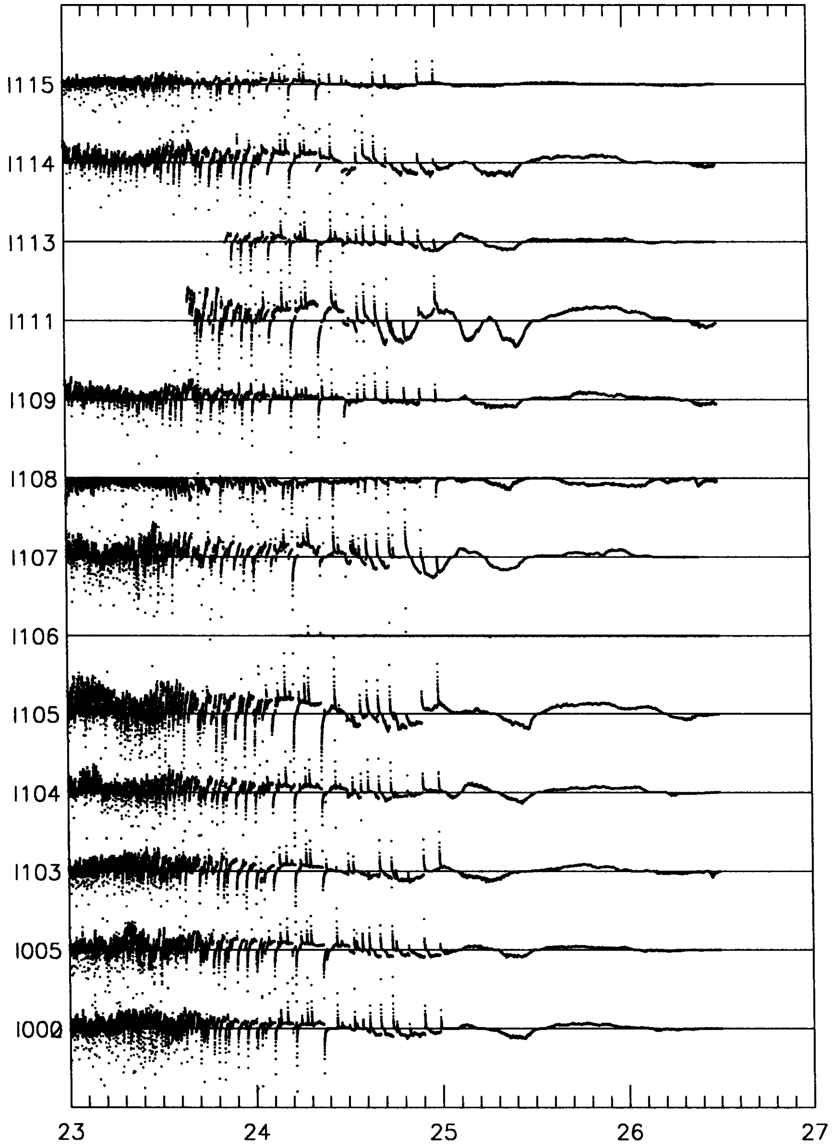

Figure 4.2: Corona point network currents for 2 August 1992 Orlando EOSO event. Positive values denote foul (positive) fields, negative values denote fair (negative) fields.

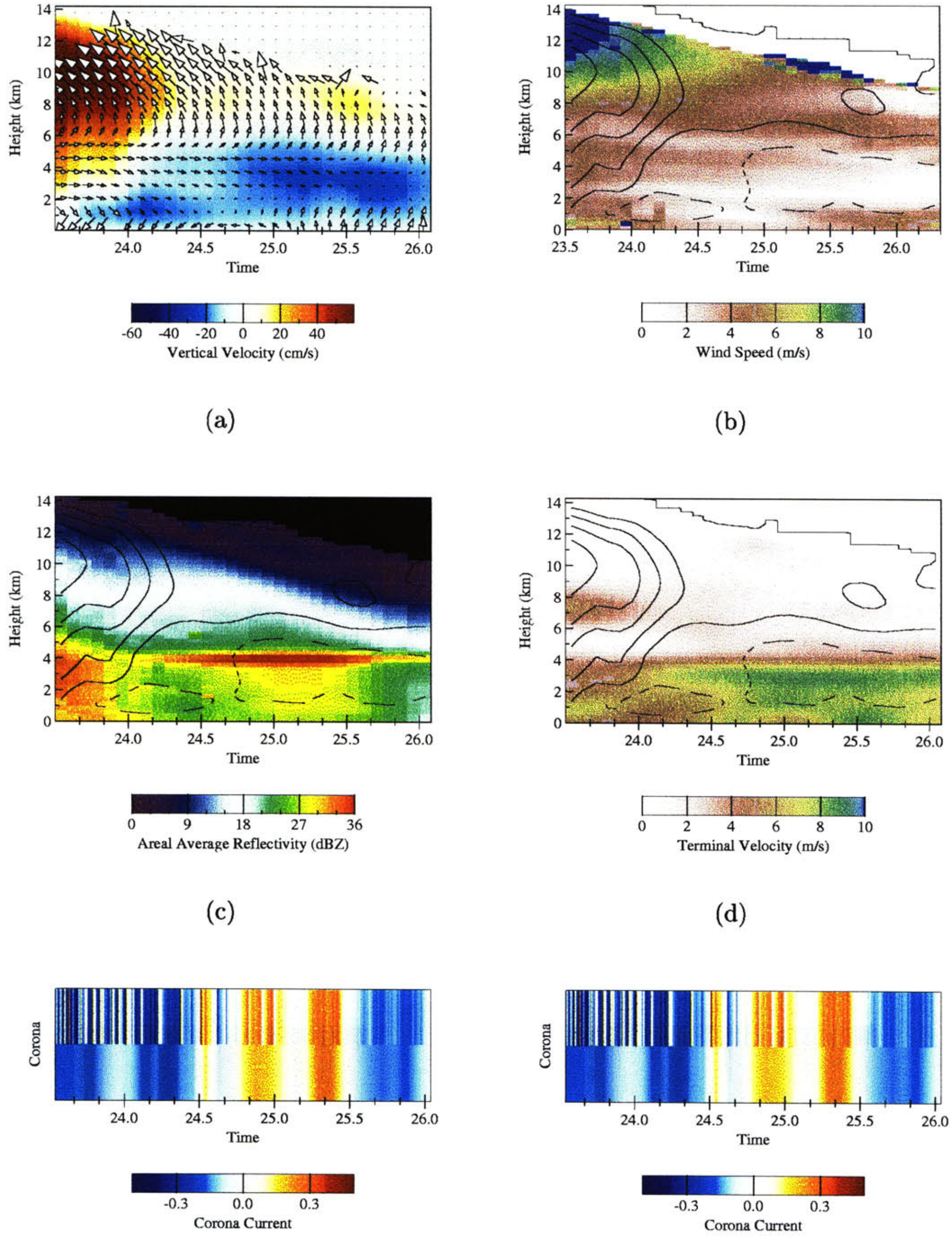

Figure 4.3: Retrieved kinematic parameters for 2 Aug 1992 Orlando storm, control run. Horizontal vector winds are overlaid in (a), vertical velocity is overlaid in (b)-(d). Representative surface corona current is shown in (e) with fair fields in "warm" and foul fields "cool" colors. Time is shown in units of hours, (UTC hour + 24).

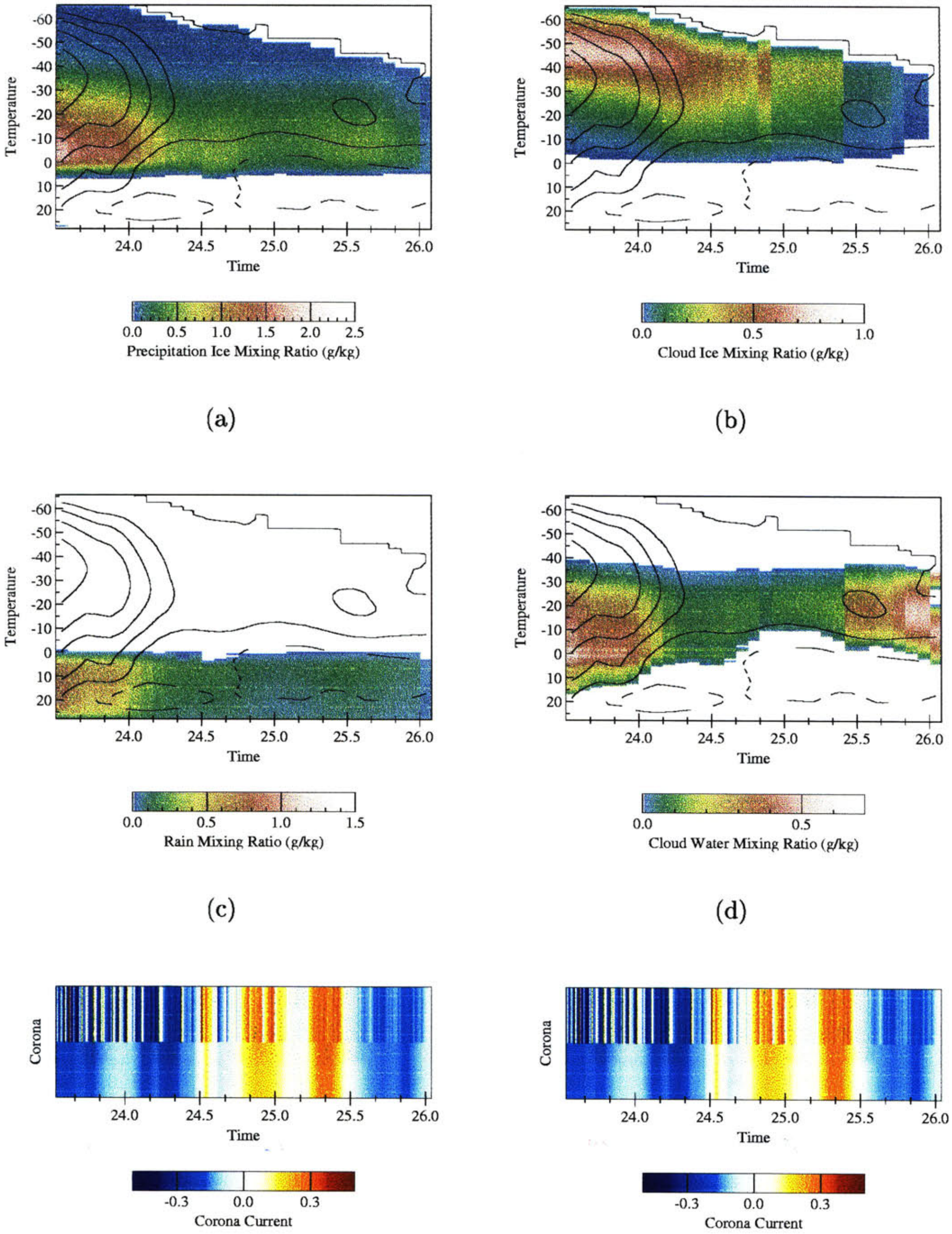

(a) (b)

(c) (d)

Figure 4.4: Retrieved microphysical parameters for 2 Aug 1992 Orlando storm, control run. Vertical velocity is overlaid.

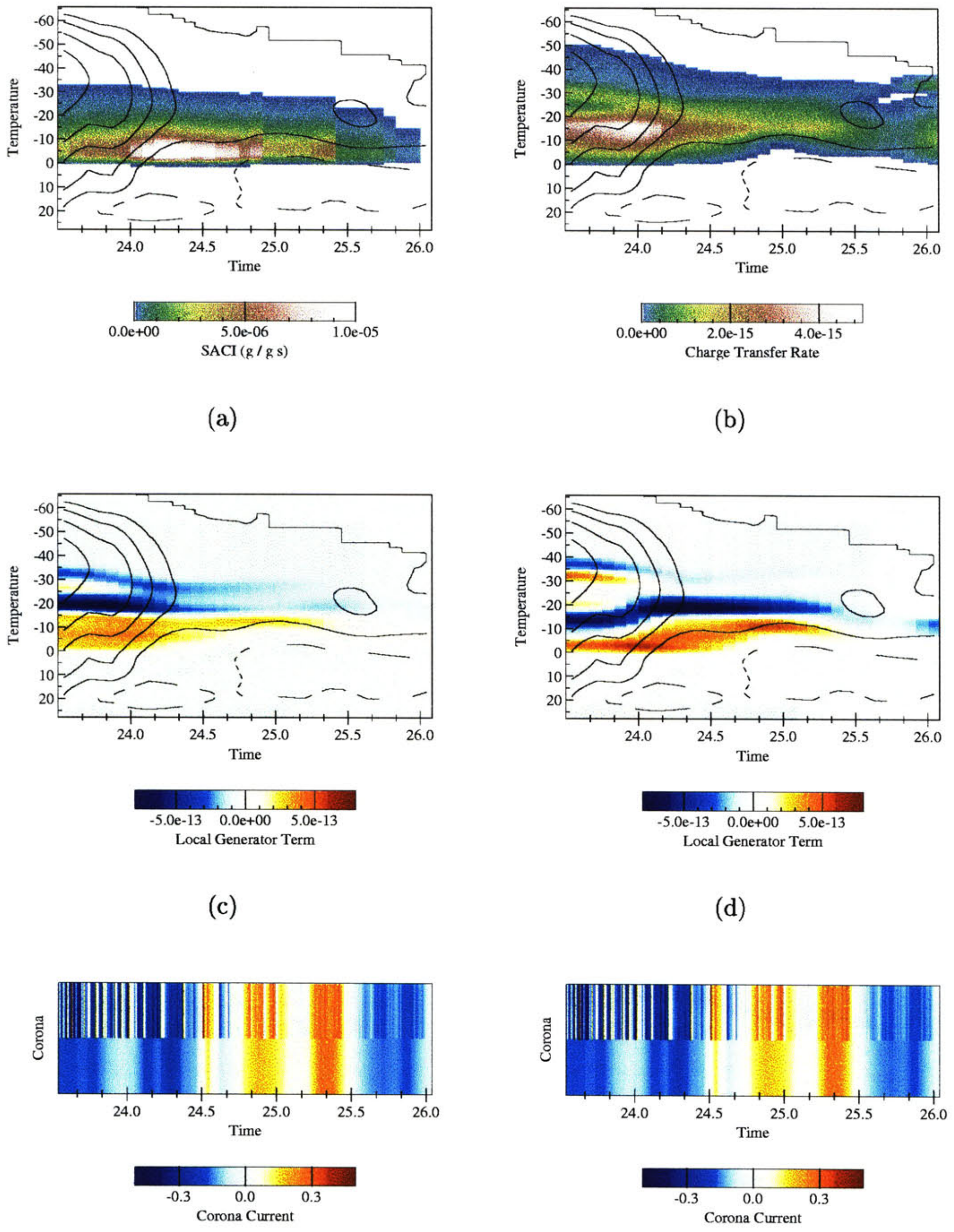

Figure 4.5: Electrical parameters for 2 Aug 1992 Orlando storm. (a) Snow/ice accretion term SACI, a proxy for total collision rate. (b) Unsigned total charge transfer rate, in $\frac{C}{cm^3 s}$. (c) Charging flux divergence, or "generator current" term, in $\frac{C}{cm^3 s^2}$. (d) Generator current under 3x retrieved liquid water content.

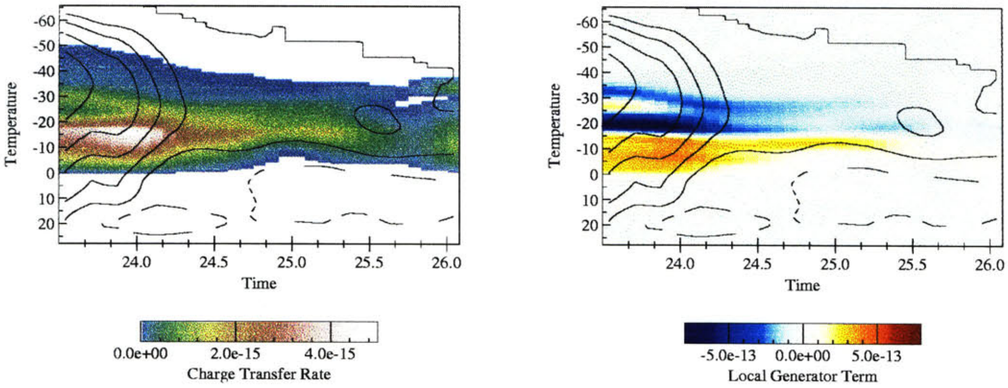

(a) Control run (b) Control run

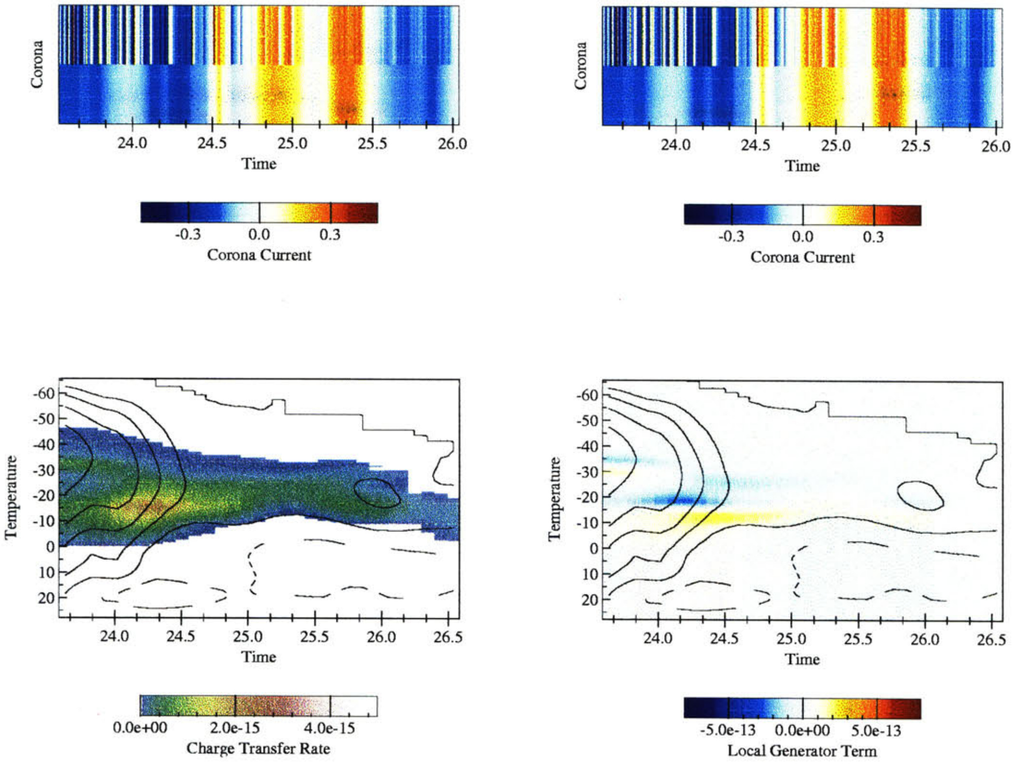

(e) Reduced turbulence (f) Reduced turbulence

Figure 4.6: Sensitivity tests on 2 Aug 1992 electrical retrievals. Upper panels (a),(b) show the control run; lower panels (c),(d) are with turbulence parameter K reduced by 40%.

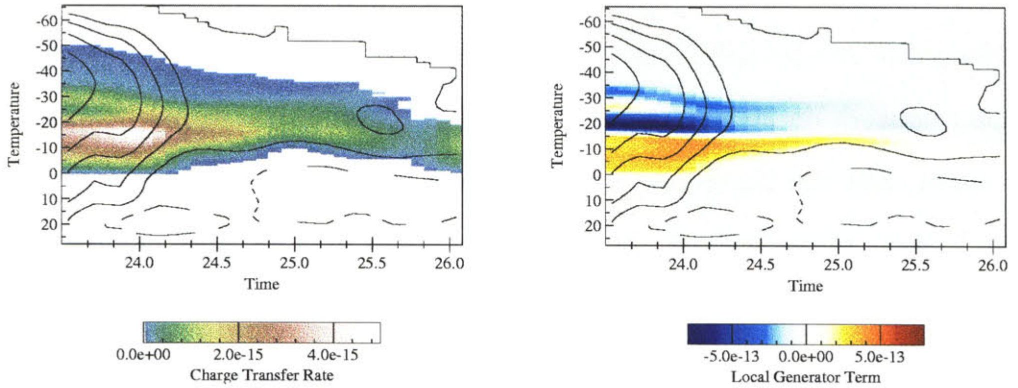

(a) Lower surface RH

(b) Lower surface RH

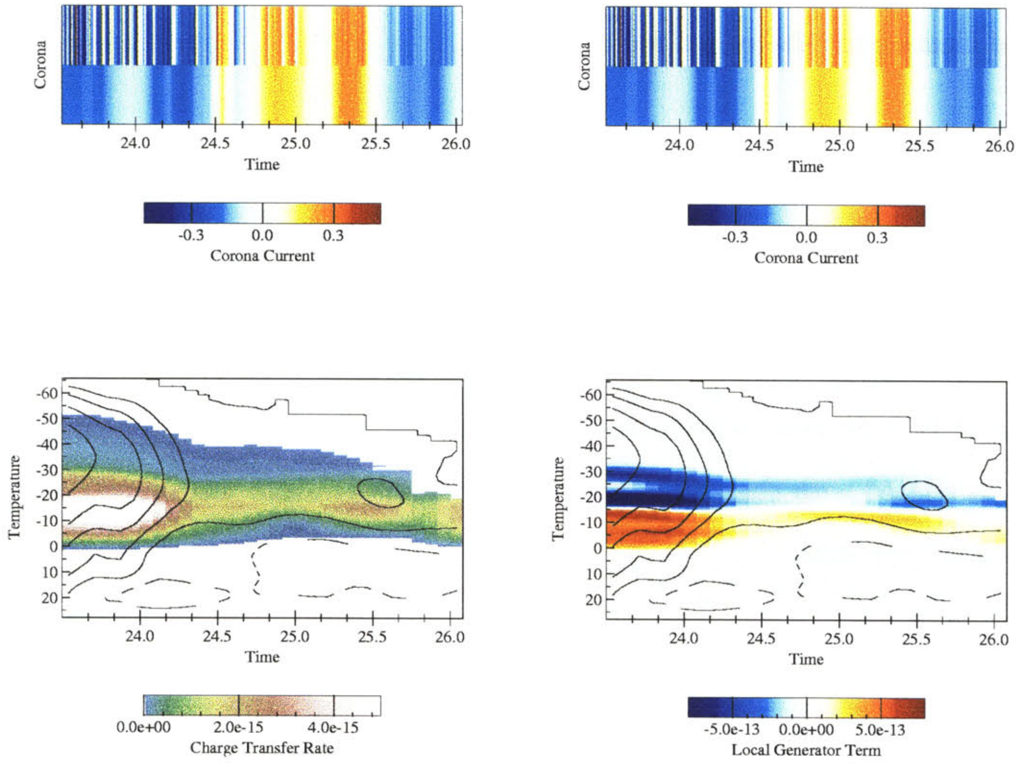

(e) 10x Fletcher ice

(f) 10x Fletcher ice

Figure 4.7: Sensitivity tests on 2 Aug 1992 electrical retrievals. Upper panels (a),(b) employ surface relative humidity reduced by 10% over the control run; lower panels (c),(d) use 10 times greater natural ice nucleus concentrations.

4.3 Orlando, 20 Aug 1992

A widespread, moderately organized cluster of storms formed over the Orlando triple Doppler network on 20 August 1992. Surface rainfall in the region persisted for over four hours, and the convective cells remained active but propagated northeastward to the Florida Atlantic coast. As such, this system may be more analogous to squall line systems than the isolated convection study of 2 August 1992, although it will be shown that the storm's velocity structure was not fully organized into regimes typical of higher latitude or midwestern squall lines. The case can thus be thought of as representative of the "transitional" part of the convective activity spectrum from cloud clusters to fully organized squall lines.

Figure 4.8 shows corona current traces within the Orlando network for this storm. A single, clear EOSO signal is not evident; rather, the surface fields appear to switch between positive and negative several times, and dominantly positive CGs do not appear until the second such reversal. However, it will be shown below that this surface complexity is actually a boon to analysis, as the complicated electrical evolution is well correlated with changes in the retrieved kinematic and microphysical characteristics of this system.

4.3.1 Kinematics

Figure 4.9 shows the basic retrieved kinematic and areal average reflectivity structure of the late stages of this system. The active phase was particularly vigorous, with reflectivities of 25 dBZ penetrating nearly to the tropopause. These values drop precipitously when the deep convection ceases (00:00-00:30 UTC 21 August, or times

24:00 to 24:30 on the plots). A strong bright band is present, and its onset slightly precedes the first surface field reversal. A second period of weak convection (times 25:00-25:50, or 01:00-01:50 UTC) appears to have renewed the midlevel ice contents.

The retrieved vertical velocity field well matches the observed reflectivity evolution. The peak retrieved updrafts of 1.2 m/s in the convective phase are likely unrepresentative of the fine scale updrafts in individual convective cells, although the general updraft profile and evolution is likely robust.[10] Once again, the formation of mid-low level downdrafts is well correlated with the onset of radar bright band. Most importantly, the period of renewed midlevel reflectivities is matched by a concomitant increase in average updraft magnitude.

Other retrieved kinematic parameters are also consistent with the apparent storm evolution. A sharp shear interface is evident through the melting level. The wind speed full-period time evolution is reminiscent of the ascending "rear inflow jet" seen in instantaneous cross-sections of true squall lines (e.g., Fig. 1.2). Particle terminal velocities are in good agreement with the low level reflectivity structure, with the stratiform rain peak from times 24:30-25:30 (00:30-01:30 UTC) clearly retrieved. A modest terminal velocity enhancement associated with the secondary updraft peak may also have been detected aloft. Overall, the single Doppler analysis on this day seems to be robust and in excellent agreement with the observed reflectivity evolution.

---

[10] The vertical velocities are comparable to convective region updrafts in Doppler radar and profiler *composites* (1-2 m/s), as summarized by *Cifelli and Rutledge (1994)*. However, they are a factor of 2-3 less than 2-D Dual-Doppler composites as reported by *Braun and Houze (1994)* in a midlatitude squall line active region. They are almost certainly unrepresentative of values in individual updraft cores, the likely regions of primary charge separation.

4.3.2 Microphysics

As on 2 August, the retrieved bulk microphysical fields (Fig. 4.10) can be interpreted as a partitioning of total water content controlled primarily by the updraft magnitude and peak altitude, and the domain top location. Peak precipitation ice, rain and cloud water mixing ratios are in phase with the updraft maxima, and when these peaks occur, they come at the expense of midlevel cloud ice. Cloud ice peaks in periods of updraft decline (after both the initial and secondary updraft pulses). As on 2 August, it will be shown that this differential partitioning is important to total charging, as precipitation and cloud ice collisions are the crucial element of this charging.

The primary stratiform rainfall maximum from times 24:30 to 25:30 is, as on 2 August, not well resolved by the retrievals; here, the secondary updraft maximum appears to have led to greater surface rainfall than the observations support. Again, this is a result of the steady-state assumption employed in the retrieval itself, as the secondary rainfall maxima in such small-scale systems appear to derive from previously detrained and settling precipitation ice.

4.3.3 Electrification

Electrification parameters for 20 August are shown in Fig. 4.11. In this event, the total collision rate appears to be out of phase with the updraft maxima (panel *a*), with peak collisions occurring near time 25:10 (01:10 UTC). As noted above, this is effectively a result of depressed cloud ice concentrations prior to this time, as stronger updrafts and enhanced cloud water favor growth of precipitation ice.[11] When the two ice hydrometeor distributions are integrated in the *SACI* and *SACS* collection kernels (and charge transfer scaled by mapping through the cloud water field), the peak charging rates are found to occur during this transition period. This is consistent with the observed reflectivity increases at 5-10 km AGL (Fig. 4.9c), which precede the actual updraft extremum.

The local flux divergence of this charging again reveals a dominant "inverted dipole" structure. Upon comparison with the surface field measurements, several other features are evident. First, the two surface field transitions from positive to negative (times 24:12-24:24 and 25:21-25:27, 00:12-00:24 and 01:21-01:27 UTC) occur just *after* the peaks in flux divergence (local charge separation). The first of these also just precedes the onset of midlevel downdrafts and bright band formation; comparison with the overlaid vertical velocity field and observed reflectivity field (Fig. 4.9c) clearly indicates that this preferentially positively charged precipitation ice is precisely the same as that which form the initial bright band and stratiform rain peaks (assuming no charge reversal upon melting).

Also notable in these results is the timing of the initial onset of +CG lightning: positive strokes are first observed near time 25:12 (01:12 UTC), and the lightning is exclusively positive after 25:20 (01:20 UTC). This period is concurrent with a descent of the lower (positive) local generator extremum to temperatures of 0 to -10 C. Not only does the local generator peak at lower altitudes in this period, but the total dipole separation is significantly greater than at earlier times. It is tempting

---

[11] It is interesting to note that this charging maximum occurs despite relatively low retrieved cloud water contents between the two updraft maxima.

to speculate that the wider dipole and lower positive charging favor +CG over intracloud flashes at this time, but little evidence is available to support this hypothesis.

As on 2 August, weak retrieved area-average updrafts likely lead to an underestimation of cloud LWC in the microphysical retrievals, particularly during the late-active stages of the storm. To emulate a hypothetical dipole inversion, the generator current terms are again recomputed under 3x retrieved LWC mixing ratios (Fig. 4.11d). The pattern is similar to that on 2 August: during the storm's late-active stages (23:30-24:00), 'normal' negative per-collision charge transfer to precipitation ice leads to a 'normal' tripolar (here, slightly quadrupolar) net charging structure, which at midlevels (-5 to -25 C) inverts at times 24:10-24:20. A similar pattern is found after the second updraft peak. It is interesting to note that the large vertical charging dipole separation from 25:10 (01:10 UTC) onward is retained in this scenario; it is again speculated that this separation may favor +CG discharges. As on 2 August, the actual instantaneous, local net charg*ing* structure likely lies between panels *(c)* and *(d)*.

In summary, the secondary updraft maximum on 20 August is a fortunate coincidence. In effect, the more uniform reflectivity distribution at this time suggests that this period resembled a "mesoscale convective cell", at least as seen by the areal-average wind and microphysical retrievals. A true 'large-scale' EOSO was thus present at scales appropriate for use with these retrievals, and the transition from normal to inverted electrical conditions may be more confidently explained by the present results than the reversal near the initial convective-to-stratiform transition, when model assumptions are challenged.

Table 4.2: Key times (UTC hour+24) in the electrical EOSO event on 20-21 August 1992.

Event (1st EOSO)	Time	Event (2nd EOSO)	Time
First positive flash	24:12	First positive flash	25:12-25:18
DC field turns fair	24:12-24:24	DC field turns fair	25:21-25:27
Last positive flash	24:33	Last positive flash	after 26:30
DC field turns foul	24:39-24:48	DC field turns foul	25:42-25:51

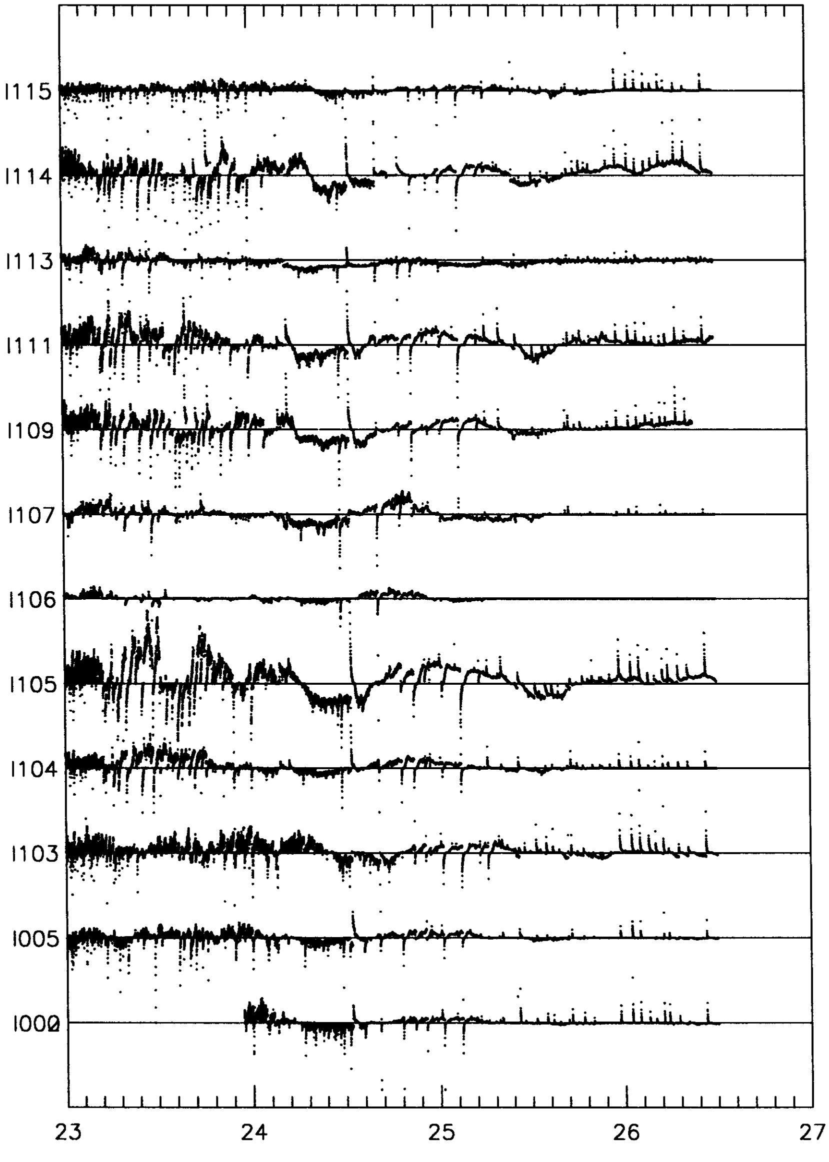

Figure 4.8: Corona point network currents for 20 August 1992 Orlando EOSO event. Positive values denote foul (positive) fields, negative values denote fair (negative) fields.

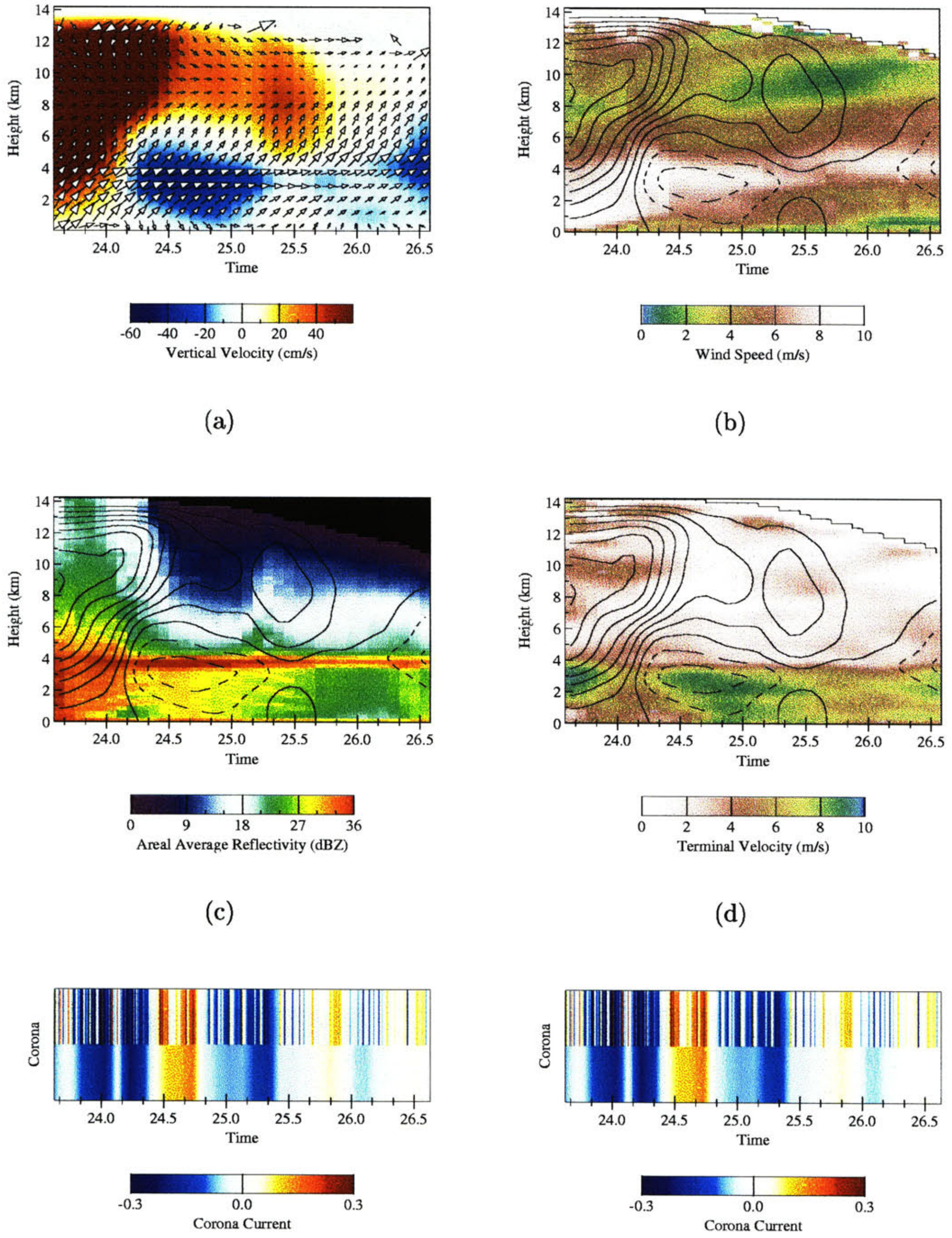

(a) (b)

(c) (d)

Figure 4.9: Retrieved kinematic parameters for 20 Aug 1992 Orlando storm, control run. Horizontal vector winds are overlaid in (a), vertical velocity is overlaid in (b)-(d). Representative surface corona current is shown in (e) with fair fields in "warm" and foul fields "cool" colors.

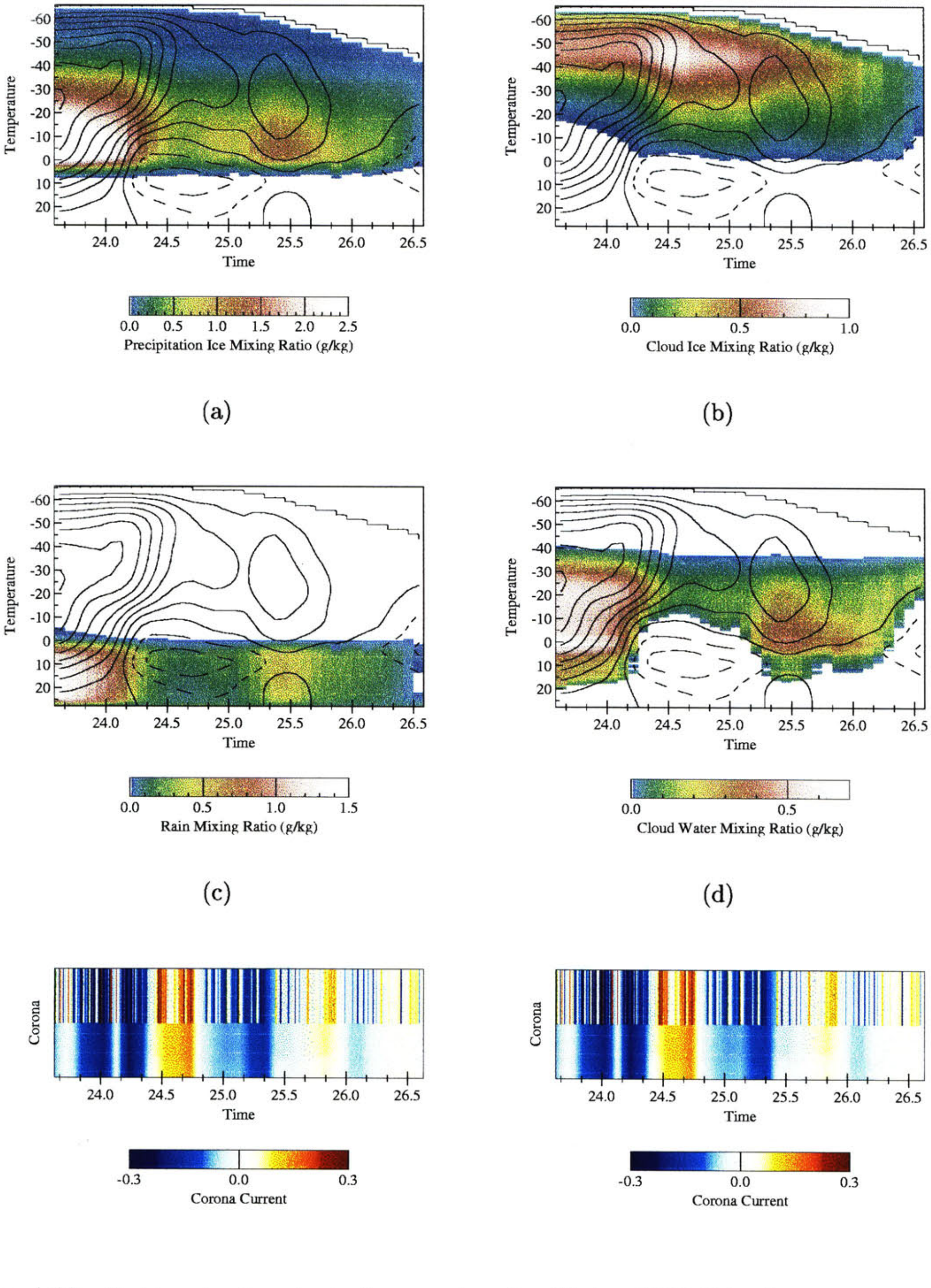

(a) (b)

(c) (d)

Figure 4.10: Retrieved microphysical parameters for 20 Aug 1992 Orlando storm, control run. Vertical velocity is overlaid.

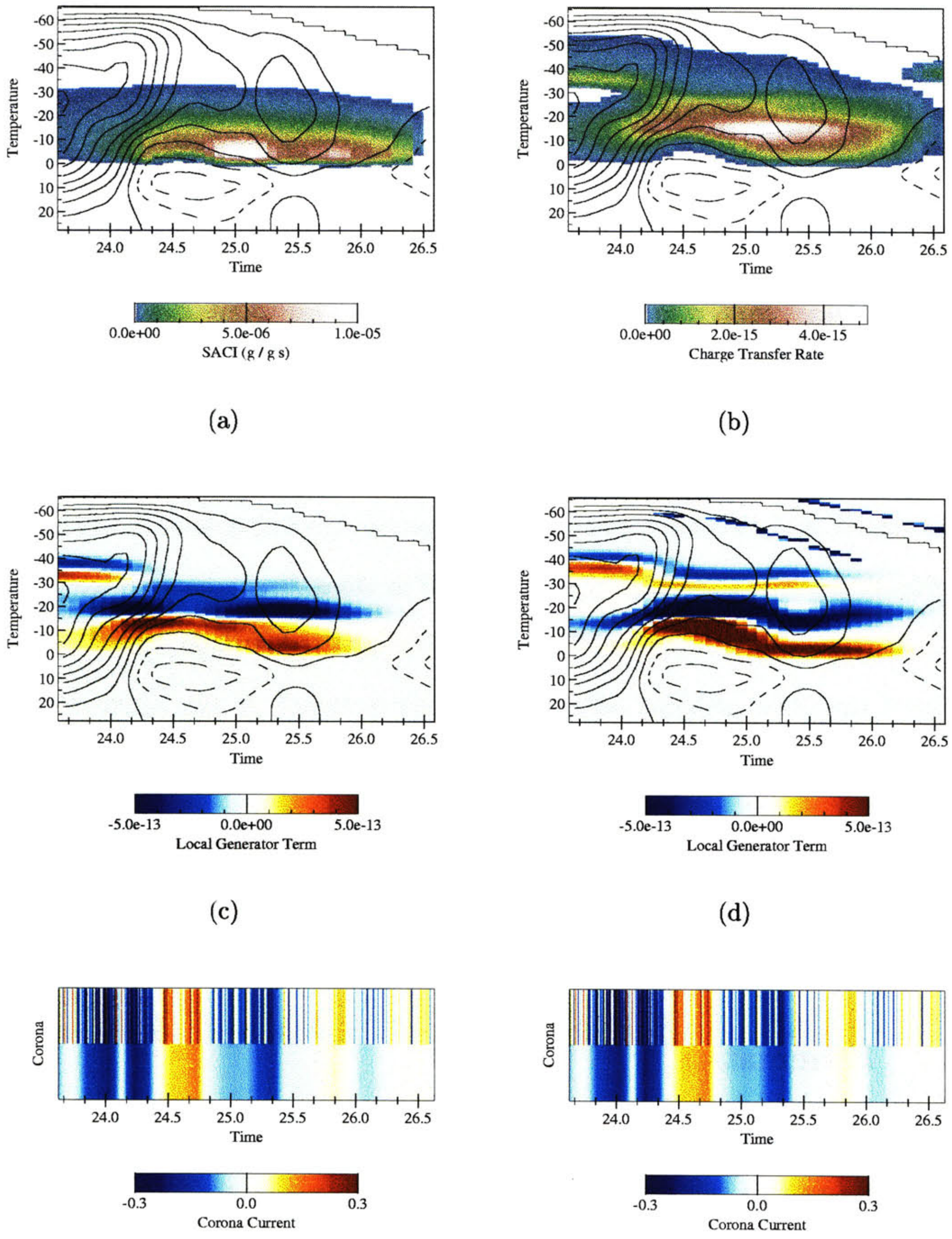

(a) (b)

(c) (d)

Figure 4.11: Electrical parameters for 20 Aug 1992 Orlando storm. (a) Snow/ice accretion term SACI, a proxy for total collision rate. (b) Unsigned total charge transfer rate. (c) Charging flux divergence, or "generator term". (d) Generator term under 3x retrieved liquid water content.

4.4 Albuquerque, 31 July 1994

A small squall line with trailing stratiform region was observed on 31 July 1994 (local time; 1 Aug 1994 UTC) just south of Albuquerque, NM. Enhancements to the MIT radar and experience with scanning strategies had by this time facilitated volume scans with 3 minute updates; this storm was thus observed at higher time resolution than the Orlando systems (5 minute update). The system exhibit dominantly -CGs during its passage over the radar, followed by an extended (2 hour) period of overhead anvil with negative (fair) surface fields. Positive CG strokes (and indeed, any late-stage lightning activity at all) were only observed during the first half hour of this reversed field. In this more organized system, several questions arise which may be addressed with the available retrievals. Why does discharge activity cease during the later stages of this event, despite persistent inverted surface fields? What are the effects of the drier ambient Albuquerque environment? Is the inferred charging at all consistent with electric field soundings through other shear-organized stratiform regions, such as those of the midwestern MCS *(Schuur et al., 1991, Hunter et al., 1992, Stolzenburg et al., 1994, Shepherd et al., 1996, Marshall et al., 1996)*?

4.4.1 Kinematics

Observed reflectivities and VVP-retrieved kinematic parameters for this system are presented in Fig. 4.12. The reflectivity structure differs from the Orlando storms in several ways. First, the bright band is nearly 5 dB weaker than in the Florida storms. At a comparable stage of late-active electrical development, penetration of deep reflectivity cores aloft is significantly shallower. Reflectivities at midlevels is comparable (15-20 dBZ) through the stratiform period, but reflectivities far aloft are much weaker (by 5-10 dB).

The retrieved wind fields again suggest a three-layer flow regime (e.g., time 02:30), although separation into clear FTR/RTF regimes is poor. Through the stratiform period, some flow separation near the updraft/downdraft interface is evident, although not as strong as in the 20 August 1992 Orlando event. Most notably, the mid-low level downdrafts are significantly stronger in this case, and the updraft base is consistently 1-2 km above the melting level. This is of course consistent with the drier ambient Albuquerque environment, as cooling by melting and evaporating precipitation is enhanced and thus drives stronger and deeper downdrafts. Generally stronger mesoscale updrafts are also found through the stratiform period, also a natural result of stronger midlevel negative buoyancy forcing, which has been found in sheared environments to enhance midlevel convergence above the melting level and result in weak upper level updrafts *(Lin and Stewart, 1986, Szeto et al., 1988a,b)*.

4.4.2 Microphysics

Retrieved microphysical parameters for 31 July (Fig. 4.13a-d) also differ considerably from the shear-organized 20 August 1992 Orlando event. Total precipitation ice mixing ratios are nearly 1 g/kg lower, despite the stronger mesoscale updrafts. Cloud ice is dominant far aloft throughout the observation period, as the observed domain top remained high and continued nucleus activation was maintained in the retrievals. As on 20 August, stronger mesoscale updrafts tend to depress retrieved cloud ice mixing ratios, as relatively more total water is partitioned into precipitation ice during these periods. Cloud water is confined to a shallower midlevel region, and peaks are more narrowly focused near -5 to -20 C. Cloud water profiles also show more fine scale structure, apparently a result of a higher sensitivity to preferred depositional growth regions under these updraft forcing and ambient environment conditions. Under the drier ambient environment and stronger low level downdrafts, cloud water is not retrieved below the updraft base.

4.4.3 Electrification

The inferred charging and generator currents for the 31 July storm are shown in Figure 4.14, and are not inconsistent with the observed surface field evolution. In this event, peak charge transfer rates are found during the late-active phase (02:30-03:30 UTC), with a secondary peak from 03:50-04:40 UTC. As before, the local flux divergence of charging (i.e., local generator current) is a more instructive variable to examine. The surface field reversal (03:25 UTC) again follows the initial extremum in lower positive charging from 02:50-03:20 UTC. However, positive discharges are first evident near 03:00 UTC, during strengthening of this lower positive maximum. Positive discharges cease near 03:40 UTC, as deepening updrafts and lower retrieved cloud water diminish the total charge transfer rate. The inverted dipole structure returns afte 03:50, but discharges are not observed. A perhaps critical difference is found in the dipole structure: a smaller total dipole separation. The positive and negative generator regions are tightly coupled in this second charging period, and the charging dipole separation is much smaller than from 02:30-03:20 UTC. This is of course a direct result of the higher updraft base more closely "hugging" the preferred charging temperature of -15 C, as well as of the retrieved hydrometeor profiles. The effects of inferred dipole separation are again speculative, but when paired with the observations on 20 August 1992 (in which positive discharges did not appear until a significant dipole separation evolved), the case is strengthened. This suggests a further effect of the location of the mesoscale updraft base: in addition to determining the hydrometeor profiles, collision rates and charging regime, it may also set the relative total dipole separation distance. If this separation distance is too small (or separation rates too small), discharges may not be supported by the system, or these discharges may be primarily intracloud.[12] If the separation is large enough, and the lower positive center electrically close enough to ground, positive CG flashes may be supported. On 31 July 1994, the latter condition appears not to have obtained.

As in the Orlando cases, the effects of underestimating cloud LWC are shown in Fig 4.14d, where generator terms under 3x retrieved LWC conditions are shown. The already multipolar charging structure of Fig. 4.14c is further complicated under the higher LWC conditions, as the charging regime intermittently switches to negative precipitation charging in fairly narrow vertical bands. The relationship to surface field evolution is less apparent under these (artificially imposed) conditions. However, it is again emphasized that the multipolar generator structure does not correspond to a comparable number of charging regime reversals. *Relative* increases or decreases in unipolar charging rates can lead to oppositely signed flux divergences - hence the complicated net generator structure. Again, this is a direct result of fine scale structure in the retrieved hydrometeor vertical distributions.

---

[12] This may help explain a storm observed in Orlando with areally extensive anvil but relatively high cloud base (as determined by RHI scans). VVP retrieval was not possible for this storm, but negative surface fields were observed and discharges not apparent. An inverted dipole may have been formed in this anvil, but the total separation distance limited by the higher cloud base.

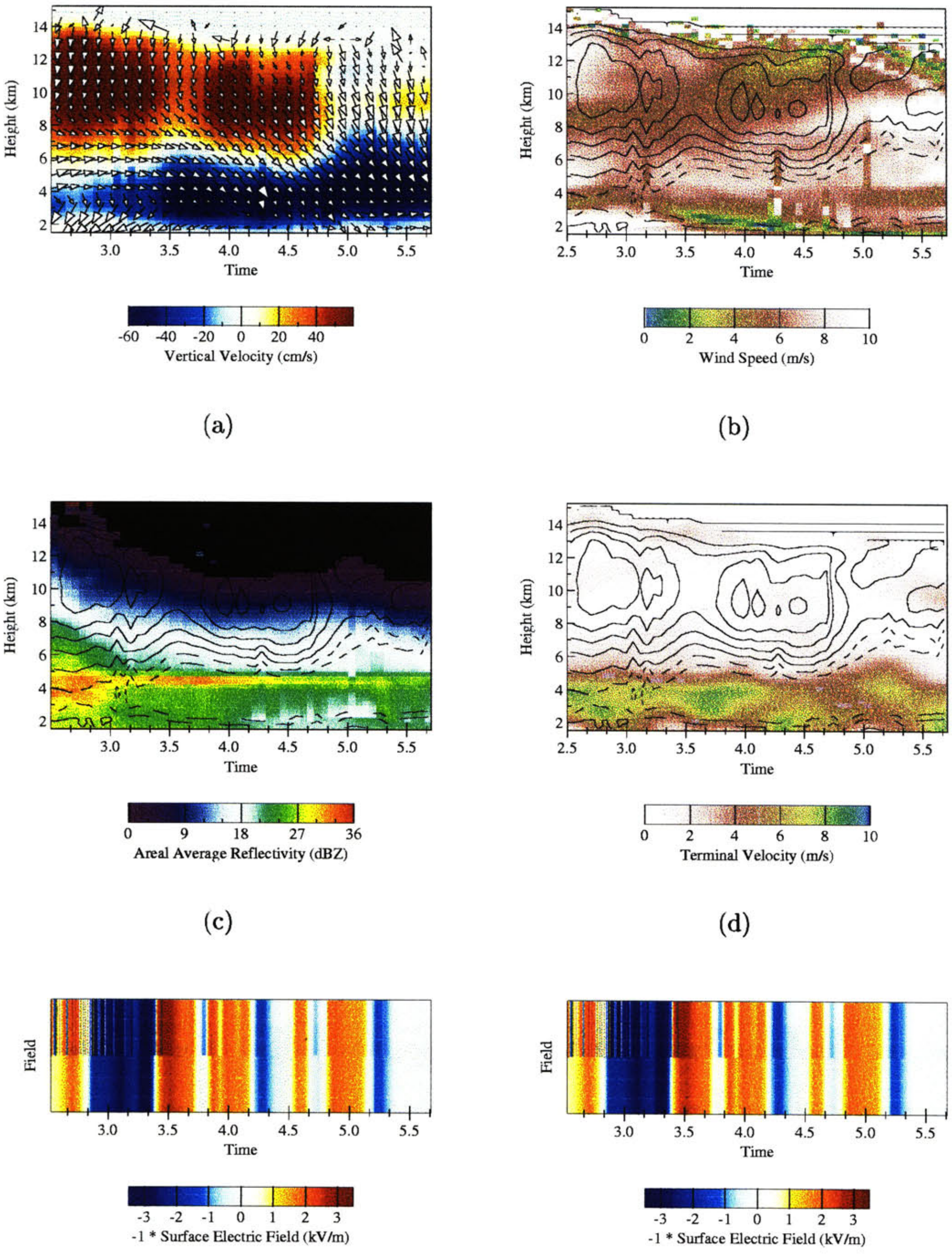

(a) (b)

(c) (d)

Figure 4.12: Retrieved kinematic parameters for 31 Jul 1994 Albuquerque storm, control run. Horizontal vector winds are overlaid in (a), vertical velocity is overlaid in (b)-(d). Representative surface corona current is shown in (e) with fair fields in "warm" and foul fields "cool" colors.

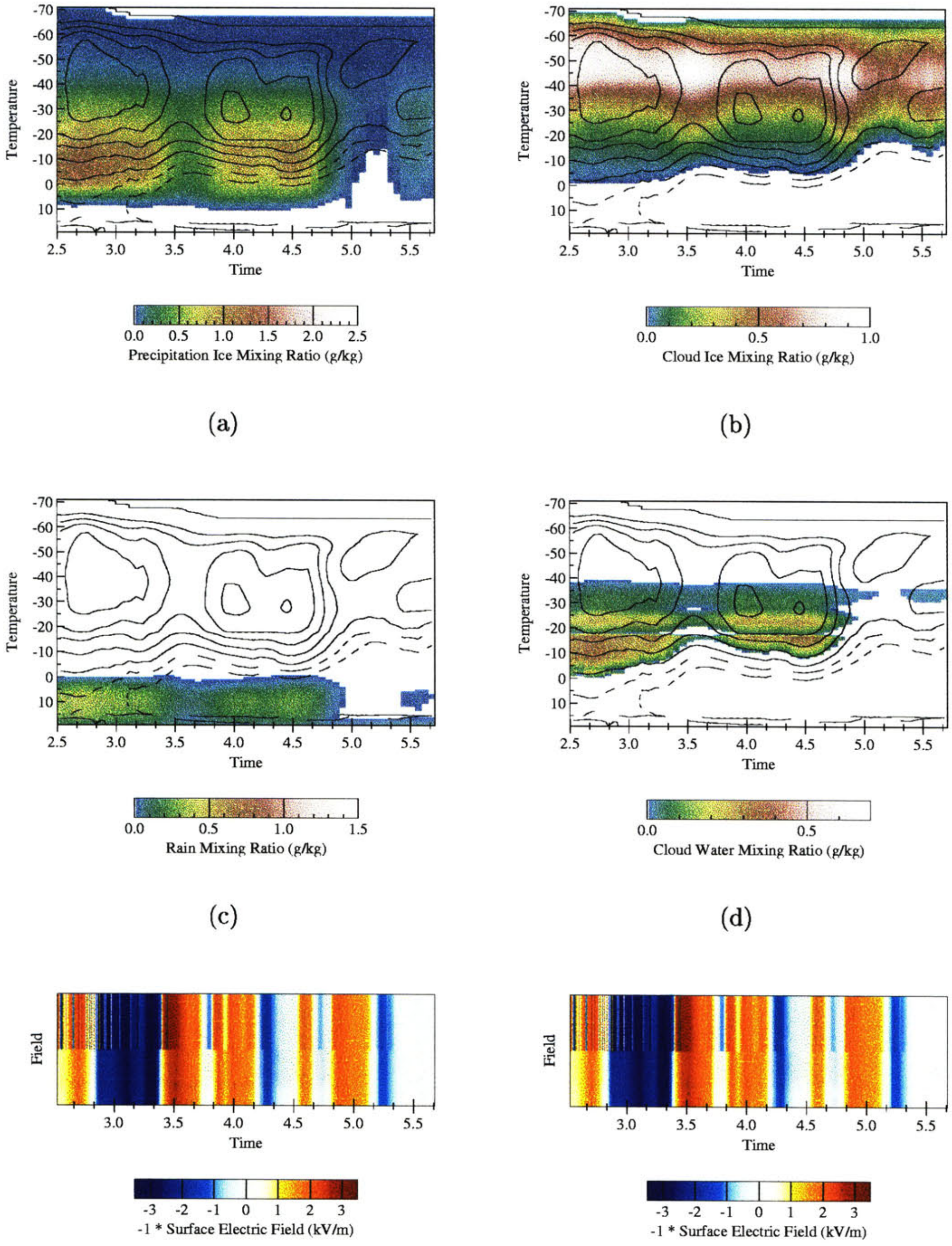

(a) (b)

(c) (d)

Figure 4.13: Retrieved microphysical parameters for 31 Jul 1994 Albuquerque storm, control run. Vertical velocity is overlaid.

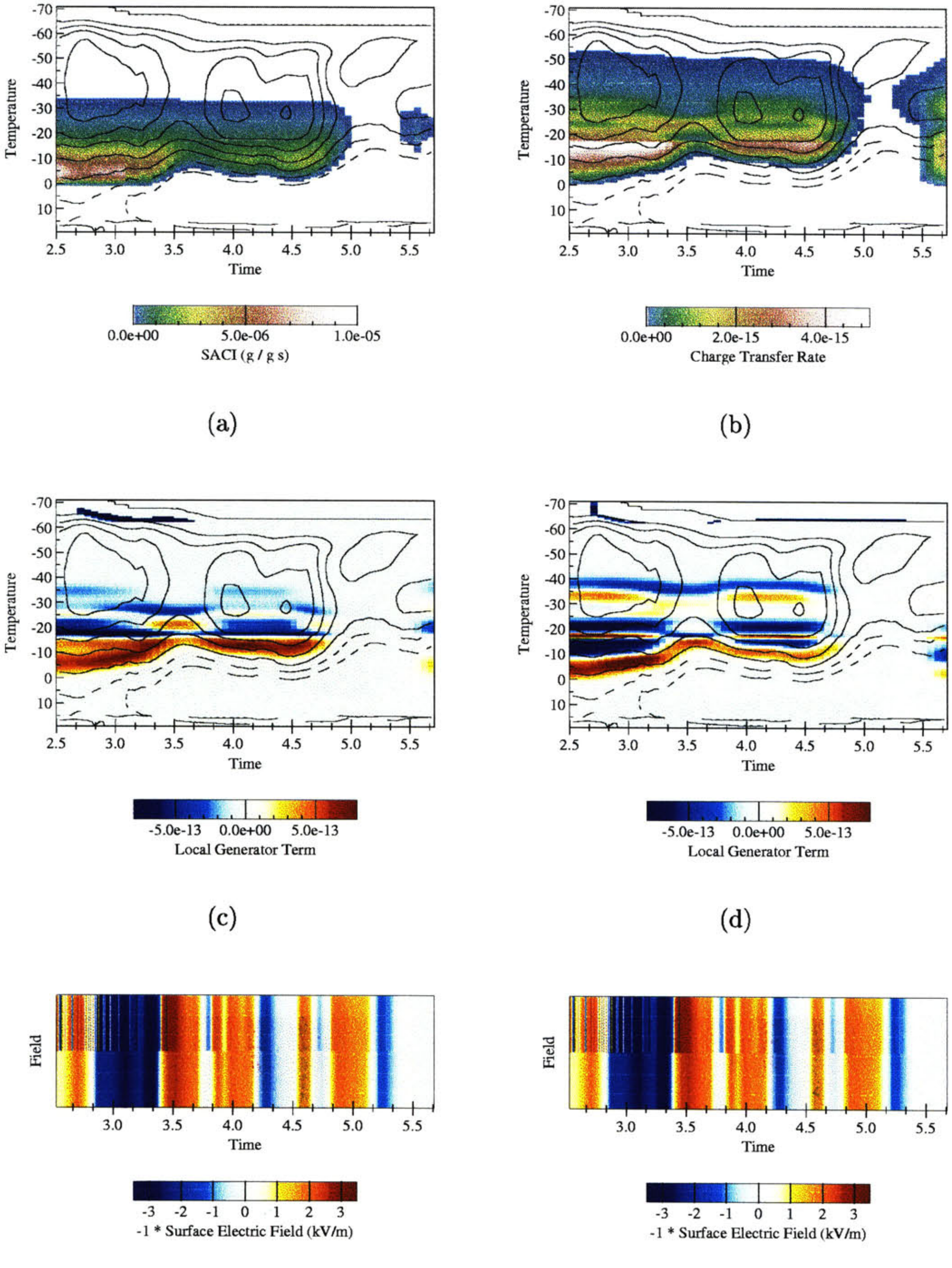

(a)

(b)

(c)

(d)

Figure 4.14: Electrical parameters for 31 Jul 1994 Albuquerque storm. (a) Snow/ice accretion term SACI, a proxy for total collision rate. (b) Unsigned total charge transfer rate. (c) Charging flux divergence, or "generator term". (d) Generator term under 3x retrieved liquid water content.

4.5 Western Pacific, 10 Febuary 1993

A widespread convective event with electrical EOSO was observed by the MIT C-band radar on 10 February 1993, during the third IOP of the TOGA/COARE experiment. The radar on this date was mounted aboard the *R/V John V. Vickers*, located at (2 S, 155 E), on the edge of the Western Pacific warm pool. The radar was stabilized with feedback from a shipboard Inertial Navigation Unit (INU), providing both reflectivity and accurate radial velocity data. Scanning strategies during this period provided full-depth volume scans (PPI tilt sets) at 10-minute intervals.

The storm in question was characteristic of other moderately organized precipitation in the warm pool during this period. While initially convective in character, the storm cells gradually evolved into a broad precipitation region that could best be characterized as "stratiform with embedded convection". Nevertheless, the large-scale (domain average) behavior followed an evolution similar to convective clusters observed in the summertime Orlando environment. Electrical measurements were taken with an inverted field mill located aboard the *Vickers* flying bridge. The mill was likely sensitive to electrified clouds to about 10-20 km range. Surface corona was not observed from any elements of the ship infrastructure, and corona above open ocean is generally fairly low. As such, the electrical measurements taken during this

Table 4.3: Key times (UTC hour) in the electrical EOSO event on 31 July - 1 August 1994.

Event	Time
First positive flash	03:00
DC field turns fair	03:26
Last positive flash	03:38
DC field turns foul	05:15

EOSO likely screen out the complicating effects of surface corona, as are found in land-based surface field measurements. The large observed surface fields (10 kV/m positive (foul) fields; 2 kV/m negative (fair) fields) support this inference. Transient activity (lightning discharges) was not observed in the field mill data.

4.5.1 Kinematics

VVP-retrieved kinematic variables from 10 Febuary 1993 are presented in Fig. 4.15a-d. Throughout the period of observation, convection was relatively shallow-topped (about 12 km ASL) with updraft peaks located at compartively low altitudes (5-7 km ASL). The typical warm pool 'first baroclinic mode' wind structure of lowlevel westerlies topped by upper level easterlies is clearly evident in the retrieved wind fields, with the sharpest directional shear occurring near 6 km ASL. The lowlevel westerly jet (also a common feature of warm pool winds during COARE) is clearly apparent, and appears to ascend with time during the study period. This jet frequently appeared to be a critical factor in organizing warm pool convection.

Areal average reflectivities tended to be comparatively weak, especially above the melting level. Midlevel reflectivities are at least 5 dB down from the weak values found in the Albuquerque storm, as are peak bright band reflectivities. Retrieved rain terminal velocities are also found to be lower by 1-2 m/s. As in the previous cases, the surface electric field reversal is closely coincident with the onset of radar bright band, appearance of midlevel mesoscale downdrafts, and rise of the mesoscale updraft peak altitude (04:15-04:30 UTC).

4.5.2 Microphysics

Microphysical retrievals for the 10 Febuary 1993 storm are shown in Fig. 4.16a-d. As in previous retrievals with low domain-top altitudes, the model tended to jump discretely between different hydrometeor partitioning regimes. For example, from 03:30-03:50, hardly any cloud ice is predicted (due to the low concentrations of natural ice nuclei at the warm temperatures comprising the vertical domain) and large amounts of cloud water and midlevel rain are retrieved. While this is perhaps not unrepresentative of shallow-topped convection, the retrieved rain and snow fields during this period perhaps suggest that a distinct graupel hydrometeor subcategory would be needed at this stage, as the retrieved lowlevel rainfall does not match the observed reflectivity values in Fig. 4.15c. Fortunately, this window is prior to the period of electrical interest (03:40-04:50 UTC).[13]

The low domain tops led to very low upper level cloud ice concentrations through the analysis period, although concentrations at warmer temperatures are comparable to the cases previously studied. When midlevel updrafts are present, retrieved cloud water is relatively high, and generally peaks near the melting level. This occurs despite comparatively weak mesoscale updrafts, as the ice-deficient environment is connected to smaller sink terms for cloud water in the retrieval. The retrieved cloud microphysical variables are thus fairly different from the storms observed in Orlando and Albuquerque.

---

[13] It should be noted that the *Vickers* was spatially removed from clouds aloft until 03:30 UTC. The squall passed overhead after this time. At 05:00 UTC, the ship was repositioned outside of the squall, and as such echo distributions after this time are suboptimal for VVP retrieval, and electrical observations unrepresentative of below-storm conditions. The electric field trace thus presents only a brief window of the overall electrical evolution of the system.

4.5.3 Electrification

The unique hydrometeor distributions retrieved for this event have some fairly interesting implications for the inferred electrification. From Fig. 4.17a, it is apparent that snow/ice accretion is not profoundly smaller than in the Orlando or Albuquerque storms, and indeed is greater than in the New Mexico squall line stratiform region. Further, accretion persists fairly consistently throughout the late stage evolution of the cloud at temperatures of 0 to -10 C. However, the total charge transferred to precipitation particles (Fig. 4.17b) never reaches the peak rates of any of the other systems. Intriguingly, it never rises above about 3×10^{-15} (whitish on the raster plot). In the other systems, actual lightning activity ceased when total charge transfer rates fell below about this value. While apparent actual numerical "cutoff" magnitude (if such an effect is truly in play) is clearly suspect, this result does suggest that the overall analysis technique (wind, microphysical and electrical retrieval) does have some skill at describing the bulk electrical behavior of systems in a *relative* sense.

Despite the high retrieved LWC, the charge transfer per collision is again unipolar (positive charge transferred to larger ice). This leads to the generator structure shown in Fig. 4.17c. Charge transfer and hydrometeor distributions are compartively uniform in the vertical from -5 to -15 C, leading to a small net flux divergence and little net charging. Net charging is thus confined to narrow bands from -15 to -25 C and 0 to -5 C. As in previous cases, the lower net positive generator center rises during the period of bright band formation / downdraft appearance / surface field reversal, coincident with a weakening of the upper negative generator. Alternatively, under the artificial 3x LWC scaling used in the previous cases, the "normal" charging regime (negative charge transferred to larger ice) is again emulated during the active stage, leading to a lower negative/positive net generator dipole which ascends during the transition period from 04:15-04:40 UTC. Again, the deepening of the lower net positive generator may be important in explaining the observed surface fields, as the positive generator "erases" the effects of previous net negative charging from -5 to -15 C.

As noted before, this event is important in that very little surface corona is to be expected over the open ocean (and none observed from ship infrastructure). Thus this storm is strong evidence that the electrical EOSO phenomenon is not just a surface corona response to in-cloud electrical activity; rather, the reversal must indeed be indicating rearrangements of actual in-cloud charge distributions.[14] The implicit assumption in previous analysis of the surface field records from Orlando and Albuquerque was that near-surface corona effects were negligible. While the COARE measurements do not confirm that assumption, they do demonstrate that the EOSO can be manifest in corona-free environments.

Table 4.4: Key times (UTC hour) in the electrical EOSO event on 10 February 1993.

Event	Time
First positive flash	n.a.
DC field turns fair	04:19
Last positive flash	n.a.
DC field turns foul	04:41

---

[14] Actually, corona effects alone cannot yield a field *reversal*, as the phenomenon is inherently dissipative, responding to near-surface fields determined by the charge structure aloft. At worst, corona delays surface field response to internal charge reconfiguration.

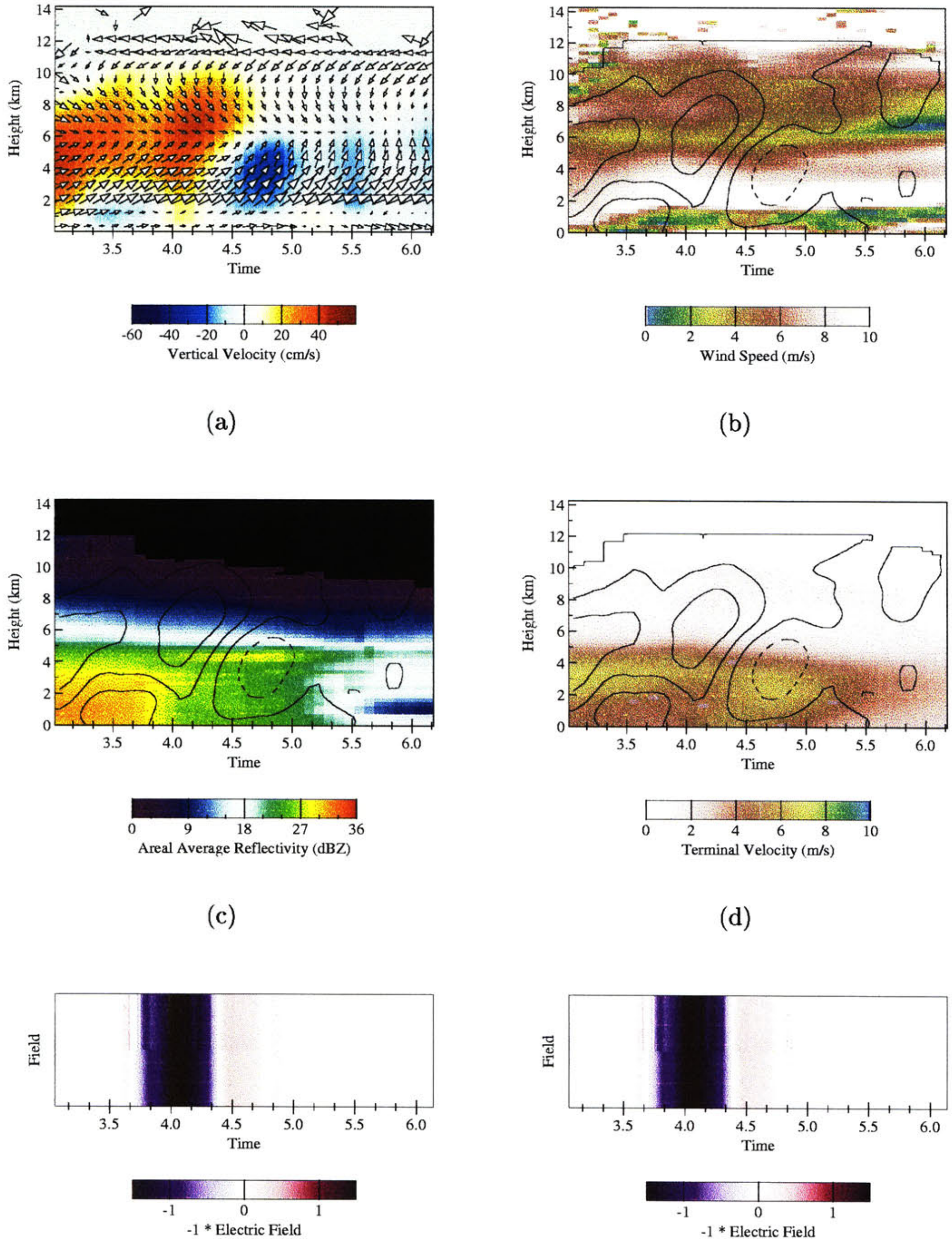

(a) (b)

(c) (d)

Figure 4.15: Retrieved kinematic parameters for 10 Feb 1993 western Pacific storm, control run. Horizontal vector winds are overlaid in (a), vertical velocity is overlaid in (b)-(d). Representative surface corona current is shown in (e) with fair fields in "warm" and foul fields "cool" colors.

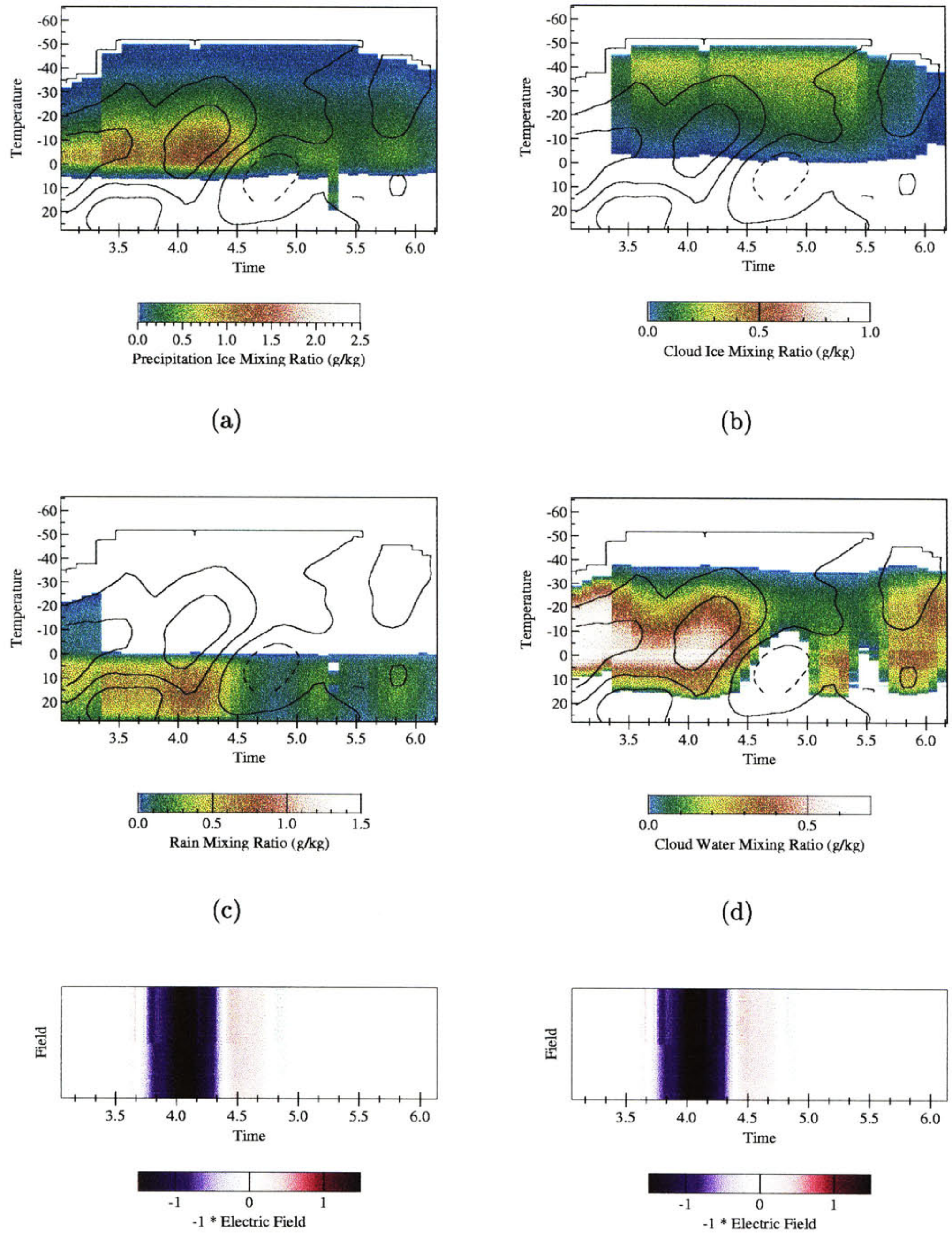

(a) (b)

(c) (d)

Figure 4.16: Retrieved microphysical parameters for 10 Feb 1993 western Pacific storm, control run. Vertical velocity is overlaid.

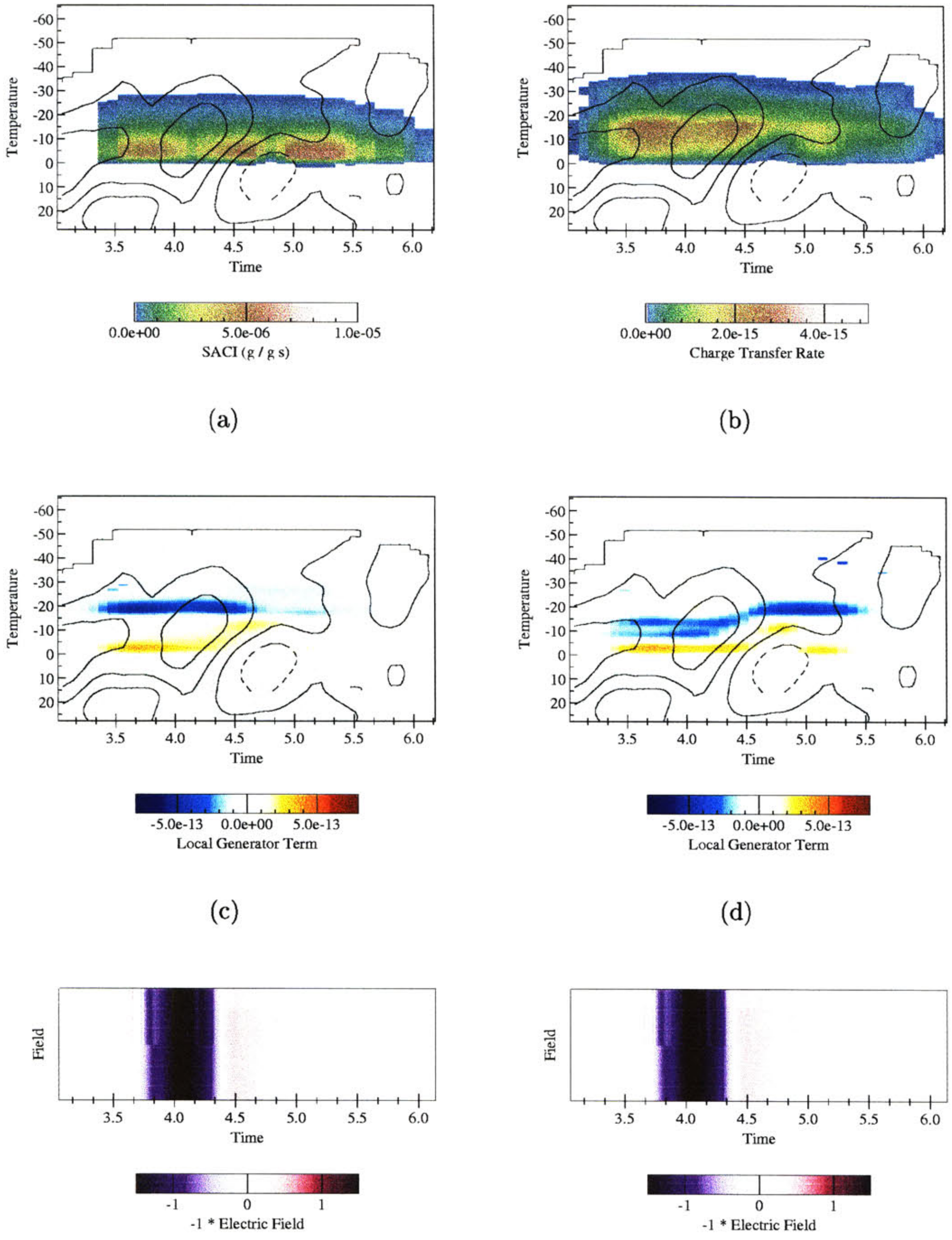

(a) (b)

(c) (d)

Figure 4.17: Electrical parameters for 10 Feb 1993 western Pacific storm. (a) Snow/ice accretion term SACI, a proxy for total collision rate. (b) Unsigned total charge transfer rate. (c) Charging flux divergence, or "generator term". (d) Generator term under 3x retrieved liquid water content.

4.6 Summary

The kinematic, microphysical and electrical retrievals employed here are clearly suboptimal ways to describe the actual electrical evolution of late-stage stratiform anvils. However, they do appear to yield conceptually consistent results which are sometimes reasonably correlated with the observed electrical evolution of the systems. The inferences and conclusions from these studies will be summarized in greater detail in Chapter 6. Here, it may be useful to pause briefly and suggest ways that the analysis technique may be improved.

Clearly, a fundamental limitation in the overall mapping of updraft forcing to charging behavior is the areal-average approach, a constraint provided by the use of single-Doppler radar data. Multiple Doppler analysis of comparable systems would be an obvious way to (a) validate the areal-average results of single Doppler analysis, and (b) assess the smale scale variability in updraft structure within late-stage systems. Dedicated multiple Doppler field campaigns are rare and expensive to mount; a more feasible approach would be implementation of a multistatic Doppler system *(Wurman et al., 1993)* with high transmit power or enhanced quasidirectional receiver sensitivity (to offset the lower reflectivities in anvil systems). Aircraft-based multiple Doppler analysis is another possibility, but again the cost of such campaigns are often prohibitive, and long missions would have to be scheduled to fully document the time-evolution of stratiform systems in the same way a fixed surface platform could offer. Surface wind profilers *(Cifelli et al., 1996)* could provide direct vertical velocity measurements, but would be limited to point sampling (and thus perhaps not indicative of "characteristic" domain-average behavior). Either way, improvement of the magnitudes of late-active stage vertical velocity profiles would most likely improve the technique's ability to predict an electrical dipole inversion at these times.

Most of the microphysical source/sink terms included in the bulk retrievals are reasonably physically based and well-constrained by observations. An exception lies in the cloud ice crystal category, which as noted in Chapter 3, evolves from the poorly-quantified and perhaps inappropriate Fletcher clear-air natural ice nucleus spectra. The retrieval sensitivity to domain top (and hence ambient Fletcher nucleus concentration) suggests that this is an important parameter to constrain. In-situ observations of cloud ice concentrations in stratiform anvils are *extremely* rare, and operationally difficult (many aircraft-borne probes only detect particles greater than 100 μm diameter). Observational constraints on cloud ice distributions are critical not only to the overall hydrometeor partitioning (by setting the ultimate sinks for cloud water under Bergeron growth), but to the actual snow/ice collision rate, critical to the inferred charging. While observations of stratiform cloud LWC would more directly aid our electrical inferences, better observations of cloud ice are ultimately necessary to improve our modelling capabilities for these clouds.

Finally, the microphysical retrievals are clearly overparameterized. Either of the two abovementioned observation sets would assist in constraining some of the free parameters (entrainment α, turbulence K, etc.). Given unlimited computational resources, some existing data (reflectivity vertical structure, etc.) could be used in a nonlinear optimization of the model for these parameter values; however, given the more fundamental unresolved physical components, such optimization would amount to fine-tuning with little justification. Ultimately, appropriate observations will likely contribute far more to improvements in technique performance than numerical massaging.

Chapter 5

New observations of stratiform region lightning

Several recent field programs and sensor deployments have provided useful new observations of the structural and energetic characteristics of stratiform region lightning (positive CGs and "spider" intracloud discharges). These observations support earlier, isolated reports of anomalous peak current, charge transfer, luminosity and areal extent in these flashes *(Teer and Few, 1974, Fuquay, 1982, Brook et al., 1983, Rust, 1986, Orville et al., 1987, Mach and Rust, 1993)*. They also provide new insights into the charge regions being tapped by these discharges.

Observations from the National Lightning Detection Network (NLDN), the Optical Transient Detector (OTD), the ONERA 3-D lightning mapping interferometer, the NSSL high-speed all-sky video system and the MIT Schumann resonance (SR) station are presented here. The OTD, NLDN and SR observations are particularly valuable in that they provide a statistically large sample of +CG characteristics, something lacking in many previous case studies because of the relatively low +CG flash rate in most storms. The relevant data have been communicated by Ken Cummins (NLDN), Steve Goodman (OTD), Pierre LaRoche (ONERA), Vlad Mazur (NSSL) and Earle Williams (SR), and appreciation is extended to each of these investigators for early release of their field data.

5.1 Structural characteristics

Previous chapters have referred indirectly to the anomalous spatial character of stratiform region lightning flashes - their extensive horizontal dendritic channel networks, preferential location near the melting level, large areal extent, etc. Most of these characteristics are well-known to field investigators, but few are well documented in the literature. This section strives to remedy some of these citation gaps, and to place flashes occurring in the isolated Orlando stratiform regions within the larger context of +CG and spider IC flash observations.

5.1.1 Areal extent

It has been conventional wisdom that late-stage (or trailing stratiform) "spider" (+CG and intracloud) flashes have extensive horizontal components and large areal extent *(Ligda, 1956, Teer and Few, 1974)*. This concept is important in explaining their apparent role as a trigger for mesospheric red sprites *(Wilson, 1956, Boccippio et al., 1995)*. Recent global measurements of lightning with the spaceborne Optical Transient Detector (OTD) have now made this feature strongly quantifiable in a statistical sense. The OTD measures individual optical pulses of lightning with a narrow-band interference filter from a near-polar orbit of 70 degree inclination, at 750 km altitude and with 2 ms / 10 km resolution. As part of the calibration/validation procedures for the instrument, we have isolated 3449 OTD flashes coincident with CG flashes detected by the National Lightning Detection Network (NLDN) from May-July 1995.[1] The OTD performs, in software, a grouping of individual lightning pulses into clusters roughly analogous to lightning strokes (return strokes or K-changes) and flashes. Thus, for this set of coincident flashes, the joint observables include flash location, polarity, number of return strokes and peak current (NLDN) and areal extent, duration and total radiance / optical energy (OTD). If we assume 100% confidence in NLDN data for nominal +CGs, the new OTD observables may be related to CG flash polarity.[2]

Figure 5.1 shows the distribution function of the "positive fraction" of the total OTD/NLDN CG sample, as well as the individual PDFs of areal extent for both positive and negative flashes. Several features are noteworthy: first, the PDF of areal extent for positive CGs always "leads" that for negative CGs; i.e., positive CGs are statistically "larger" than negatives. Also, the "positive fraction" rises sharply as a function of areal extent, suggesting that at least 50 % of cloud-to-ground discharges

---

[1] Coincidence was determined when NLDN and OTD locations agreed to within 100 milliseconds and 200 km. The loose tolerance was necessary because of periods of poor performance of navigation instruments and clocks aboard the OTD platform, Microlab-1.

[2] 100% confidence in NLDN isolation of anomalous positive discharges is not necessarily warranted. Recent analysis by K. Cummins (pers. comm. to E. Williams) has suggested that the very largest +CGs may "swamp" the NLDN systems and go unreported. Also, in the 1995 NLDN dataset, changes in the NLDN detection algorithms appears to have led to a number of intracloud flashes being misreported as low peak current +CGs. Finally, it will be shown (pg. 186) that intracloud components of large spider lightning may also be misreported as CG events of either positive or negative polarity.

observed from space with areal extent greater than 1000 km^2 are positive. [3] It should be noted, however, that this result is for the population of *all* +CG flashes, not just those occurring in stratiform regions.[4] It is also evident from Figure 5.1 that the largest flashes are also a relatively small fraction of the total +CG population, as well as of the overall population.

Some quantification of the areal extent of lightning discharges in storms similar to those treated in Chapter 4 of this thesis is available from the ONERA 3-D lightning mapping interferometer, deployed in Orlando, 1992 and operated concurrently with other radar and electrical observations. The ONERA system included two ground stations south and southeast of the MIT radar, and the detection field loosely resembles the equivalent dual-Doppler lobes that would be formed from this configuration, with optimal coverage over the Orlando triple-Doppler network (see Figure 5.2). Even so, the available data is range-limited to approximately the region represented in Fig. 5.2 and thus provides at best a lower bound on actual flash areal extent. This lower bound can be extended somewhat in instances where the NLDN detected a nearby +CG clearly associated (in time) with the interferometer flash but outside its range. A single straight channel is assumed in these cases connecting the outermost ONERA source with the NLDN CG location. 10 km x 10 km grid units are used to maintain consistency with the OTD results.

Table 5.1 shows the minimum areal extents of a series of late-stage flashes recorded by the ONERA system on 6 August 1992. The maximum extent mea-

---

[3] This feature was used by *Boccippio et al. (1996)* to isolate global flashes likely to cause Schumann resonance transients or Q-bursts.

[4] If the study population were limited to only stratiform-region flashes, we would expect an even greater positive/negative asymmetry in areal extent.

surable for this storm location and data clipping is 900 km^2.

Table 5.1: Areal extents of late-stage flashes, 6 August 1992. ">" areas are extrapolated based upon coincident NLDN +CG locations beyond the ONERA data range. Flashes marked with "*" are indeterminate as they occur partially within the ONERA system null regions.

Date/time	Type	Area (km^2)
08/06/92 22:43	IC?	400
08/06/92 22:58	?	600
08/06/92 23:02	?	500
08/06/92 23:06	+CG	>700
08/06/92 23:15	+CG	>600
08/06/92 23:17	IC	200
08/06/92 23:30	+CG	*200
08/06/92 23:37	IC	500
08/06/92 23:46	IC	600

As a final note, the observed Orlando flashes were found to be not only areally extensive but also reasonably *domain-filling.* Overlays of the ONERA sources upon CAPPI radar sections (not shown) reveal that the flashes effectively explore almost all of the precipitating portion of the midlevel detrained anvil. On 6 August, the maximum correlation between VHF burst extent and radar echoes appears to occur for the 4-5 km AGL radar echo boundary, consistent with the hypothesized importance of lower mixed-phase region / melting level charging to late-stage lightning development. This is also consistent with the results of *Williams et al. (1985)*, who found that laboratory-simulated discharges tend to effectively pervade regions of accumulated space charge.

5.1.2 Flash duration and precursor activity

Visual observations of late-stage spider IC and CG flashes also leave the impression that these are unusually long-duration flashes, and that the CG component is usually preceded by extensive in-cloud development. This is also quantifiable from the U.S. OTD/NLDN dataset, as well as from joint global OTD/Schumann resonance measurements and direct local video observations of the Florida flashes.

Figure 5.3 presents the "positive fraction" and +CG and -CG distribution functions for various flash duration thresholds. The methodology used is the same as for Fig. 5.1. As above, the results are constrained by limitations in the OTD software clustering and grouping of optical pulses into lightning flashes (this is documented in the *LIS Algorithm Theoretical Basis Document (ATBD).*) Nonetheless, clear trends are evident, with nominal NLDN +CG flashes exhibiting consistently longer duration as observed by the OTD. Flashes lasting longer than a full second are sometimes observed.

Rust (1986) has noted that positive CG strokes may be preceded by several hundred milliseconds of in-cloud channel development. This is also quantifiable by OTD observations. Here we present a set of 20 positive CG flashes observed by both the OTD and the MIT Schumann resonance (SR) station located in West Greenwich, Rhode Island (Table 5.2). Flash polarity is confirmed by the initial rise of the vertical electric (E_z) component of the observed SR transient. Flash start is determined by the first OTD-observed optical pulse; the actual CG stroke is identifiable both by large-radiance OTD pulses and the initial spike of the SR waveform, delayed by appropriate source/receiver travel times at ELF. A sample of the data used in this compilation is shown in Fig. 5.4.

Table 5.2: Flash durations and activity prior to the ground stroke for 20 positive CG flashes observed jointly by the OTD and the MIT SR station. Flashes are scattered globally. Precursor times are estimated to 25 ms resolution. The flashes come from a subset of "large bright flashes" observed by OTD with criteria of area greater than 1000 km^2 and optical energy greater than 5 MJ.

Date/time	Duration (ms)	Precursor (ms)	Area (km^2)
95/225 03:42:31.540	214	50	1400
95/225 03:43:22.454	331	50	2200
95/225 04:59:03.344	224	0	1300
95/225 05:47:52.166	211	50	1600
95/225 06:36:06.876	945	125	3200
95/227 04:16:57.398	203	50	1100
95/227 04:17:23.442	134	0	1000
95/228 06:03:22.064	857	0	1700
95/229 16:47:31.688	247	225	1800
95/230 17:25:20.128	428	150	1300
95/232 17:27:35.608	244	100	2200
95/232 19:21:29.592	2	0	1300
95/233 04:09:04.558	21	0	1400
95/233 05:09:36.938	910	300	2600
95/233 05:45:21.678	407	275	4800
95/235 14:05:43.848	1299	425	2800
95/236 05:06:46.590	275	100	2400
95/238 22:38:36.128	216	200	2600
95/239 04:34:13.172	984	450	2000

Such extensive precursor development, in conjunction with the aforementioned large areal extent, may help explain the anomalously large peak currents and total charge transfers associated with +CG flashes, as noted in the literature and discussed in further detail in section 5.2 below.

As in section 5.1.1, the Orlando-region flashes may be placed in context by examination of their respective durations, as observed by a high-speed (1 ms resolution), all-sky video system deployed by V. Mazur of the NSSL. Table 5.3 presents flash durations for several of the 6 August 1992 flashes discussed above.

Table 5.3: Durations and intracloud precursor activity for flashes observed on 6 August 1992 with NSSL high-speed all-sky video system. Times estimated to 25 ms resolution.

Date/time	Type	Duration (ms)	Precursor (ms)
08/06/92 23:02	?	1075	-
08/06/92 23:06	CG	1300	?
08/06/92 23:10	CG	825	200
08/06/92 23:15	CG	850	125
08/06/92 23:30	CG	1050	?
08/06/92 23:46	IC	1475	-

The two precursor durations cited are consistent with OTD-observed results in Table 5.2. The total flash durations are somewhat longer; the very last optical emissions from the Florida flashes tend to be very dim, impulsive bursts buried within the cloud, which may be too weak to be routinely seen by the OTD.

5.1.3 Flash channel structure

The ONERA lightning mapping interferometer was used in section 5.1.1 to estimate lower bounds on late-stage flash areal extent in the Florida storms. The interferometer is also capable of isolating source bursts in altitude, thus providing a crude 3-D map of channel structure. The quality of such mapping may be poor in late-stage spider flashes, when simultaneous activity at various ends of the dendrite structure "confuses" the interferometer. Nevertheless, a rough picture of many flashes is still retrievable from the ONERA data.

These data can be used to address several questions about spider flash structure. Are the visible dendrites at cloud base actually propagating at or near the melting level? Do flashes in the isolated Florida storms propagate rearward from the most recently convective regions, as is often cited in MCS stratiform flashes? At what altitudes do the upper branches of the lightning tree (visible as dim, buried channels in the NSSL high-speed video imagery) occur? Do these preferred altitudes support or reject the inferred charge structure?

The Orlando sample is far too small (and inconclusive) to firmly resolve these questions, but it does aid in understanding them. Further, it shall be shown that the flashes are not inconsistent with an inferred inverted dipole, if we consider the system to be evolving from a normal to inverted condition.

To illustrate, 9 flashes during the Orlando EOSO of 6 August 1992 are examined in detail. This EOSO event consisted of a relatively small detrained anvil, poorly configured for the areally-averaged and quasi-steady state analysis performed in Chapter 4. Nevertheless, examination of the flash structure may still be useful. For comparison, an interferometer signature from "normal" -CG flashes on 13 August 1992 will first be presented.

Typical -CGs: 08/13/92, 23:31:56 and 23:33:57

Though sampled in a different storm than the EOSO flashes to be treated below, these two flashes are representative of typical negative CG flashes as seen by the ONERA interferometer. The flashes are shown in plan view and N/S projection in Figure 5.5. The color scheme used depicts relative burst time in grayscale, with darkest symbols occurring earliest and lightest symbols latest. The extent of incloud activity is relatively small, perhaps 15-20 km horizontal extent, and firmly located near the 6-8 km altitude level. The general structure is not inconsistent with -CGs analyzed with the New Mexico Tech 2-D interferometer (a more sensitive system) by *(Shao, 1993)*. The conventional interpretation is that these flashes remove charge from the 7-8 km AGL negative charge center of a "normal" dipole or tripole.

Early EOSO IC: 08/06/92, 22:34

An unusual intracloud flash was recorded at 22:34 UTC on 6 August, the onset of that day's EOSO. A representative set of corona current traces for this day is given in Fig. 5.6. The mesoscale updraft base had just risen to the melting level, and anomalous field changes were starting to be recorded at the ground stations. An extensive anvil had formed over the triple-Doppler network, with active convection detached and moving northwest of the MIT radar (NW corner of the Doppler network), over 40 km distant. The anvil above the network was thus "newest" to the northwest and "oldest" to the southeast. Corona stations along the southeastern regions of the anvil (stations 106,107,113,002,005) generally switched to fair surface fields (and subsequently recovered to foul fields) earlier than the northwestern stations (104,105,111,109). The flash at 22:34 UTC is presented in plan and profile projection view in Fig. 5.7. Color coding is again grayscale in time. This flash produced a bipolar field change at various corona point stations, although the dominant signal is of negative charge being removed (NCR) from overhead. The N/S projection clearly presents a conventional "I-beam" structure to the flash, similar to IC flashes documented by *Shao (1996)*. However, the altitudes spanned are somewhat surprising. The initial breakdown appears to have been from 4-7 km AGL along the northwestern edge of the anvil, and joined regions between 4 km AGL and 11 km AGL on this edge. In a "normal tripole" configuration, these would both have been positive charge centers; however, the NCR transient record suggests that the lower branch is tapping negative charge. This negative charge may be charged precipitation from the original negative charge center now settling to lower levels upon cessation of convective updrafts. Subsequent propagation was rearward (southward) at these two altitudes. The lower branch proceeded through the entire extent of anvil above the Doppler network, closely confined to the melt-level altitudes of 4-5 km AGL. Note from the plan view that a significant portion of this propagation was RF-"quiet" at ONERA frequencies; the few bursts at grid location (+8,+2) km are the only clues to the existence of an extensive low-altitude channel. The upper branch also appears to have propagated rearward, descending from 11 km AGL to 8 km AGL, perhaps indicating a concomitant descent of the parent storms' upper positive charge center.

IC: 08/06/92, 22:43

At 22:43 UTC, the DC surface field was still positive (foul) but building negative (fair). An areally extensive IC flash occurred, exhibiting a clear but sloping two-level structure (Fig. 5.8). The flash appears to have initiated just west of the MIT radar at

8 km AGL. This region is important, as it appears to be a focal point for subsequent activity in this storm. Upper level channels then extended northward and upward from 9-10 km AGL, and rearward and downward to 7-8 km AGL. Subsequent channels proceeded northward at both upper and lower levels, rising from 8-11 km AGL and descending to 4-5 km AGL. A final channel extended at lower levels into the Doppler network at 3-4 km AGL. Again extending the "normal tripole" hypothesis, the rear, "middle" 7-8 km channels may have been the negative branches of a structure with joint positive branches at both upper (9-11 km) and lower (3-5 km) levels.

IC: 08/06/92, 23:02

By 23:02 UTC, the DC field had switched to negative (fair) and was continuing to build negative. Mesoscale updrafts had decreased to below 20 cm/s, and flashes were consistently of anomalous polarity. Another areally extensive (apparently IC) flash occurred, again beginning just west of the MIT radar at 8 km AGL (Fig. 5.9). This flash appears to have initially connected regions at 8 km AGL and 3 km AGL - well *below* cloud base. Subsequent propagation was again northward and upward (to 10-11 km AGL) and rearward at 4-6 km AGL. This rearward propagation passed over the corona point network, which recorded positive field changes (i.e., positive charge removed from overhead) at stations 106, 107, 113 and 002, 005. Negative field changes were observed at stations closer to the initial 3 km / 8 km channel (105, 109 and 111). A tentative inference is thus that positive charge was located in the 4-6 km altitude range at this time over the Doppler network.

+CG: 08/06/92, 23:06

Conditions at 23:06 UTC were similar to at 23:02. Active convection had moved to beyond 40 km NW of the MIT radar, and a thin (10 km wide) reflectivity "bridge" less than 20 dBZ connected the local anvil and the active cells, from 4-10 km AGL. Surface reflectivity patches were still disjointed. A positive CG was recorded in the active cells northwest[5], apparently a consequence of earlier extensive "spider" development in the anvil (Fig. 5.10). This flash again initiated at 8 km AGL west of MIT and developed both upper (10 km AGL) and lower (3-5 km AGL) branches in the trailing stratiform region. As before, upper level branches also propagated northward and upward (9-12 km AGL). The actual channel leading NW to the +CG location (outside of ONERA range) is visible at grid location (-12,+27 km), and appears to have become active midway through the flash lifetime. As at 23:02, field changes suggest that positive charge was removed from above the corona network, again substantiating an inference of positive charge at lower (5 km AGL) levels in this region.

+CGs: 08/06/92, 23:15

A spider flash apparently supporting two positive CGs was recorded at 23:15 UTC. The reflectivity structure was fairly similar to that at 23:02 and 23:06, although active cells had moved further northwest and diminished significantly. The flash itself (Fig. 5.11) was again areally extensive and produced a complicated dendrite network at many levels. Common features with earlier flashes included early initiation at about 8 km AGL just northwest of the MIT radar, lower and upper level dendrites at 4-6 km AGL and 8-11 km AGL in the anvil covering the triple Doppler network, and

---

[5] No visible CG was observed in the NSSL video records, consistent with a remote flash.

upper level (8-11 km AGL) channels propagating north. A 56 kA peak current flash was located beneath the anvil, within 5 km of a location independently determined by the two all-sky video cameras deployed by NSSL. This CG followed in-cloud precursor development of two clear channels (as determined from the video). Its peak illumination (and stroke propagation through these already-extant channels) lasted nearly 4 ms, and the CG channel itself remained illuminated for nearly 30 ms. A second positive CG of 33 kA peak current was recorded in the nearly-detached cells 30 km NW of the MIT radar, and was not visible to the video. Also, portions of the intracloud components of this flash apparently triggered the false location of a 15 kA negative CG beneath the anvil itself; the nominal location was quite close to the video systems and would have been visible had it been real. The flash removed positive charge from above the network, although the in-cloud channel structure (as seen by the interferometer) is too noisy and complicated to speculate on source charge locations.

IC: 08/06/92, 23:37

By 23:37 UTC, the bright band intensity above the triple-Doppler network was near its maximum. The DC fields had neared saturation negative, and were about to begin building positive again. A large IC flash with two clear channels extending rearward into the anvil region was recorded by the interferometer and video systems (Fig. 5.12). Assuming accurate altitude locations, these channels were located at 3-6 km AGL (west of the corona network) and 7-8 km AGL (above the network). A noisy cluster of bursts were located well north at 6-8 km AGL. Field changes at the ground stations revealed positive charge removed, which leads to a dilemma. The profile view of the flash suggests a simple I-beam IC flash structure, perhaps consisting of lower positive and upper negative branches. However, the upper branch (which passed over the network) appears to have depleted *positive* charge. An alternative interpretation is to assume both anvil channels are propagating through positive charge regions, with the negative "end of the tree" located in the noisy region to the north. This picture would be consistent with the tri-level IC structure which seemed to dominate at 22:43 and ?, with an inferred positive-negative-positive layering of channels. It is interesting to note that the altitude of the upper (positive?) branch in the above-network anvil is now 2-3 km lower than at 23:15 UTC. Such a descent is too rapid to be accounted for by settling precipitation; it is more likely that the previous flashes have now depleted the uppermost positive charge.

IC: 08/06/92, 23:46

The "granddaddy spider" for this storm was captured at 23:46 UTC by both interferometer and video. This flash has been extensively documented by *(Mazur et al., 1994)*. It was again a rearward-propagating flash (Fig. 5.13). It lasted at least 1475 ms, with over a second of precursor in-cloud activity before the formation of bright dendrites below cloud base. The persistent 'focal region' west of the MIT radar was again in play, although at this point the relevant bursts were located at 3-4 km AGL, clearly *below* the melting level. These bursts (as well as a later cluster 15 km to the south) were coincident with "bifurcation points" in the below-cloud dendrite network, as located by the dual all-sky video systems. The location of these sources below the melting level (and yet coincident with earlier focii of activty at 8 km AGL) is intriguing. Was there a concentration of previously charged precipitation in this region, which had now settled below the melt level? The flash again removed positive charge from above the network, suggesting that this low-level propagation was tapping positive charge at temperatures warmer than 0 deg C (although a "conventional" channel was also located at 5-6 km AGL to the west). A few isolated bursts also suggest the formation of an upper level (8-10 km AGL) channel above the network as well. This flash raises more questions than it answers, and introduces the possibility that strongly charged rain may also be present and affecting channel development.

IC: 08/07/92, 00:05

The final IC recorded by the interferometer for this storm occurred at 00:05 UTC. The DC field had swung back to positive (foul) values, and the reflectivity centroid below about 5 km AGL had drifted west of the corona network (although anvil above that was still centered over the network). This flash perhaps most closely resembles a traditional "I-beam" IC structure, with distinct upper and lower branches (Fig. 5.14). With a significant leap of faith, one might connect the 4 km AGL sources far north and south in the profile view to form a single lower-level channel (this leap is not unjustified: recall the extensive length of "RF-quiet" channel seen in the flash at 22:34 UTC). The upper level appears well-confined to the 6-8 km AGL altitudes. The flash weakly removed positive charge from above the corona network. There is little direct evidence in the 00:05 surface and interferometer data to suggest a "negative-over-positive" charge configuration here, but such a dipole would not be inconsistent with the apparent channel structure and the history of flashes up to this point.

As noted before, the 6 August EOSO event was significantly less organized than the case studies treated in Chapter 4, and included detached but active cells for a significant period of its lifetime. The anvil itself was also smaller in extent. Nonetheless, the flashes observed may still provide some insights into electrical activity in the more widespread and isolated cases. The "focal region" located just west of the MIT radar suggests either local regions of in-situ charging (not necessarily supported by the reflectivity CAPPIs, which were uniform to the 2-5 dBZ level), or a relative importance and persistence of previously charged regions of precipitation. The consistent layering of flash channels is also intriguing; a tri-level structure was frequently observed, with lower and upper channels consistently exploring the older anvil regions, and middle channels confined to the newer regions, until the very last flashes. The surface field changes also suggest that both lower and upper channels were depleting positive charge, although more detailed and highly time-resolved analysis is clearly necessary to confirm this (examination of the New Mexico Tech 2-D interferometer and RF amplitude data, as performed by *Shao (1993)*, would be ideal). Overall, the flash structures are certainly consistent with, but not necessarily proof of, an inverted dipole structure (or at least a normal tripole structure in which the lower positive and middle negative charge regions are dominant).

5.2 Energetic characteristics

Krehbiel (1981), *Brook et al. (1982, 1983)* and *Goto and Narita (1995)* have documented unusually large charge transfers in positive flashes in summertime Florida and wintertime Japan storms. Median +CG peak currents documented by the NLDN are slightly higher than -CG peak currents, although extremely high peak current flashes are more common for positive than negative CGs. Field investigators have noted that

+CGs may be much brighter than -CGs. Finally, +CGs tend to have *long continuing currents* and relatively few (one or two) return strokes, and these strokes may remain bright for several milliseconds and luminous for tens (and even hundreds) of milliseconds (see IC flash at 23:15 UTC 6 August 1992, above).

Recent observations by both the OTD and the MIT Schumann resonance station have also provided new insights into the energetic characteristics of +CG flashes. The OTD measurements confirm that positive flashes are statistically brighter than negative flashes (at least as seen from cloud top). The Schumann resonance measurements confirm that these flashes dominate the amplitude distribution of SR/ELF transients; from this we may directly infer statistically larger total dipole moment changes in +CGs and hence total charge transfer.

5.2.1 Radiance and optical energy

The OTD/NLDN coincidence dataset employed in sections 5.1.1 and 5.1.2 may also be used to examine the relative brightness of positive and negative CG flashes. The OTD measures a pixel intensity for each optical burst ("event"). These intensities may be coupled with pre-flight laboratory calibrations to calculate a burst radiance. These radiances may then be summed under a plane-parallel assumption to yield total cloud-top optical energy.[6]

Figure 5.15 presents the distribution functions of positive and negative flashes

---

[6] Here we further assume that the OTD narrow-band interference filter passes approximately 10% of the optical band (*W. Koshak, R. Blakeslee, pers. comm. (1995)*). This is a crude assumption, but adequate for relative comparisons between flashes.

against increasing total optical energy thresholds, as well as the "positive fraction" of flashes exceeding these energy thresholds. The differences between positive and negative CGs are even greater for optical energy than for areal extent (Fig. 5.1) or flash duration (Fig. 5.3). Again, positive CGs always "lead" negative CGs in the distribution. These results must be interpreted cautiously, in light of the relative storm stage in which +CGs tend to occur. The OTD observations are a cloud-top measurement. Although the interferometer measurements clearly indicate upper level channels in spider IC and CG flashes (section 5.1.3), the extremely bright components of +CG flashes appear confined to near cloud base and within the CG channel. The total LWC (and hence optical depth) of the stratiform anvils in which these flashes form is much less than that of active convective cells; thus, more optical energy will reach the OTD sensor for equally bright "active-stage" -CGs and "late-stage" +CGs. Numerous below-cloud optical measurements or detailed calculations of stratiform anvil optical depth are required to fully confirm that the +CG strokes themselves are indeed brighter, on average, than -CG strokes.

5.2.2 Dipole moment change and charge transfer

The larger areal extents, durations, luminosities, and long continuing currents observed in +CG flashes certainly support the idea that these tend to produce, on average, larger charge transfers than -CG flashes, as observed in the case studies cited above. A large sample of these flashes is available from the single-station Schumann resonance (SR) measurements cited in section 5.1.2 above. These measurements are of course global, responding to the coupling of energy radiated by lightning into the Earth-ionosphere cavity. The SR responds directly to the total dipole moment change (charge transfer × twice the vertical channel length) of lightning flashes, with strokes lasting close to a quarter SR period (30 ms or greater) most efficiently coupling into the cavity (*D. Sentman, pers. comm. (1995)*). As noted above, +CG flashes may be identified in SR measurements by the polarity of the initial rise of SR transients (Q-bursts).

We first note that positive CG flashes, on average, produce larger SR transients than negative CG flashes. This result comes from a dataset of (count) flashes observed concurrently in the continental U.S. by the NLDN and the MIT SR station. The relative histograms of positive and negative flashes remaining in the sample under different transient "trigger" (initial ELF waveform rise amplitude) levels is given in Figure 5.16. At the lowest trigger levels in which transients are uniquely identifiable above the background SR noise (about 9 pT), the positive/negative distribution closely resembles previous CG climatological distributions (*K. Cummins, pers. comm. to E. Williams (1994)*), with positive flashes comprising about 15% of the total CG population. As the thresholds are raised, +CGs come to dominate the remaining population.[7]

This result also holds true for the subset of +CG flashes occurring within the trailing stratiform regions of Mesoscale Convective Systems, as might be expected. Figure 5.17 shows the distributions of initial SR transient amplitude as a function of flash polarity and peak current for a sprite-producing MCS on 7 September 1994, as studied by *Boccippio et al. (1995)*. Again, it is seen that both low and high

---

[7] These flashes also tend to produce waveforms which stand out more strongly against the SR background, and therefore are more amenable to analytical inversion of the SR signal and location of the parent flashes *(Boccippio et al., 1996)*.

peak-current +CGs preferentially excite the SR (all flashes here are roughly the same distance from the receiver, so range-effects may be neglected). Peak current is certainly not the optimal metric for such a comparison, but it is the only one available, and the results as stratified by polarity alone are still robust.

Total dipole moment changes may be estimated from the SR measurements as well. Moment changes of over 1000 C-km are not uncommon (*D. Sentman, E. Williams, M. Brook, pers. comm. (1994)*). Assuming channel lengths of about 5 km (consistent with the hypothesis of a dominant lower positive charge center), this implies total charge transfers in large flashes of 100 C or greater.

5.2.3 Flash multiplicity

It is already well-established that +CG flashes tend to have only one or two strokes, typically containing long continuing currents. However, examination of NLDN records during several of the Orlando EOSO events studied here indicates a general decline in *negative CG stroke multiplicity* as the storm enters its decaying phase. Fig. 5.18 shows time series of flash multiplicity for the 2 August, 6 August and 20 August 1992 storms. The general decline in each case is unmistakable. As the actual mechanisms leading to multiple return stroke formation (channel cutoff) are not yet firmly established *(Heckman, 1992)*, inferences from these observations are limited; they are presented here for completeness.

5.3 Summary

The global (OTD, SR) and large-scale (NLDN) nature of the measurements employed in this chapter have allowed the compilation of statistically large samples of positive lightning flashes, something lacking in many previous studies. From these datasets, we may strongly confirm that positive CG flashes have consistently larger areal extent, longer duration and higher optical energy than negative CG flashes. They also couple more effectively into the Earth-ionosphere cavity (Schumann resonance), and lead to larger amplitude transients, implying statistically larger total dipole moment changes and hence total charge transfer than negative CG flashes. As noted above, these concepts are not new; however, they have not previously been confirmed with large datasets spanning many individual storms and storm types.

The joint measurements (radar, video, corona current and interferometer) in Orlando also provide new insights into the character of +CG and IC "spider" flashes in late-stage storms. These flashes are indeed areally extensive (although the data limitations prevent direct comparison with the global OTD observations), and of long duration. They also may contain several hundred milliseconds of precursor IC activity and extensive channel network formation prior to the +CG flash. Upper level (8-11 km AGL) channels are present in most of the flashes studied on 6 August, although activity at the uppermost levels is absent in the very last flashes of the storm. Propagation of these channels at both upper and lower levels is consistently rearward from the newest to oldest regions of anvil cloud, and the dendrite networks appear reasonably space-filling of the lateral extent of reflectivity bounds. Connectivity to the detached active cells in this system is indeterminate, due to range limitations in the interferometer data provided. However, the last flashes in this storm showed no evidence of connectivity to the remote convective cells. After 22:34 UTC (the onset of this storm's EOSO), those channels extending rearward over the corona point network at 4-6 km AGL consistently removed positive charge from overhead, suggesting a strong (and replenishing) lower positive charge center. Inferences about charge layers above this are more speculative. While they do not necessarily support an "inverted dipole" model, they are also not inconsistent with one.

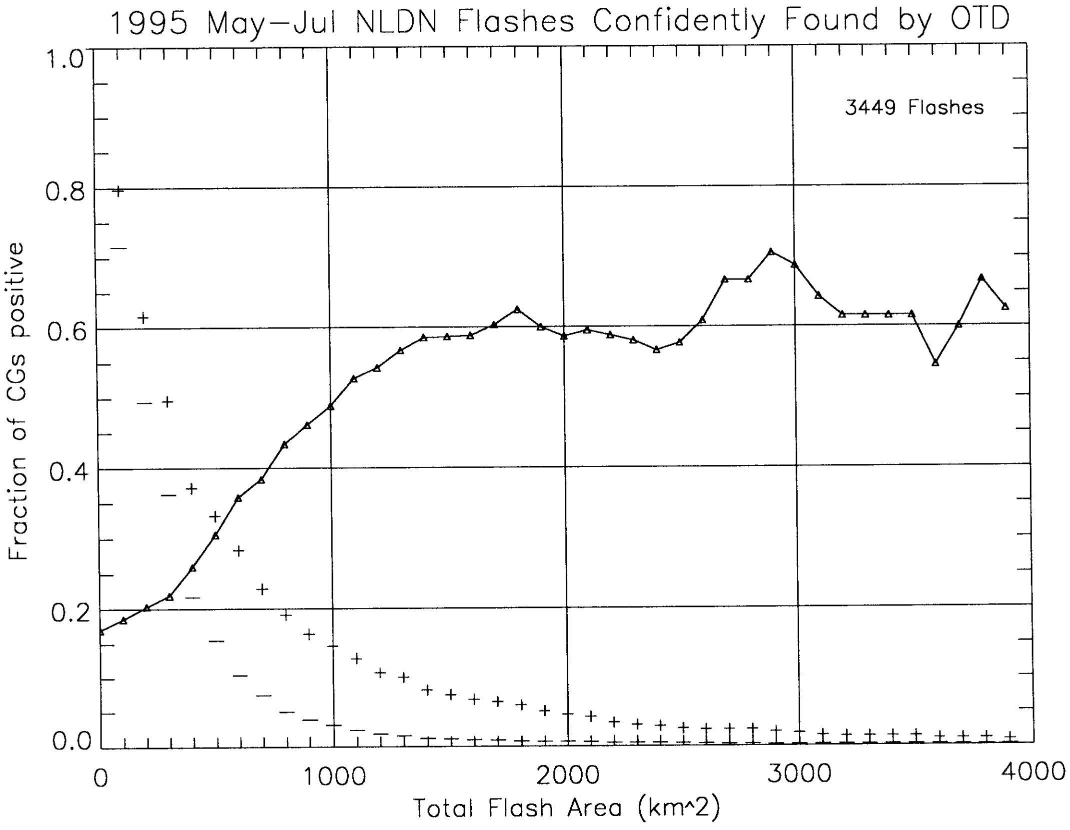

Figure 5.1: Probability distribution of positive and negative flashes in the OTD/NLDN coincidence dataset, as a function of flash area. Fraction of positive CGs in the sample as a function of area threshold is also shown above (solid curve).

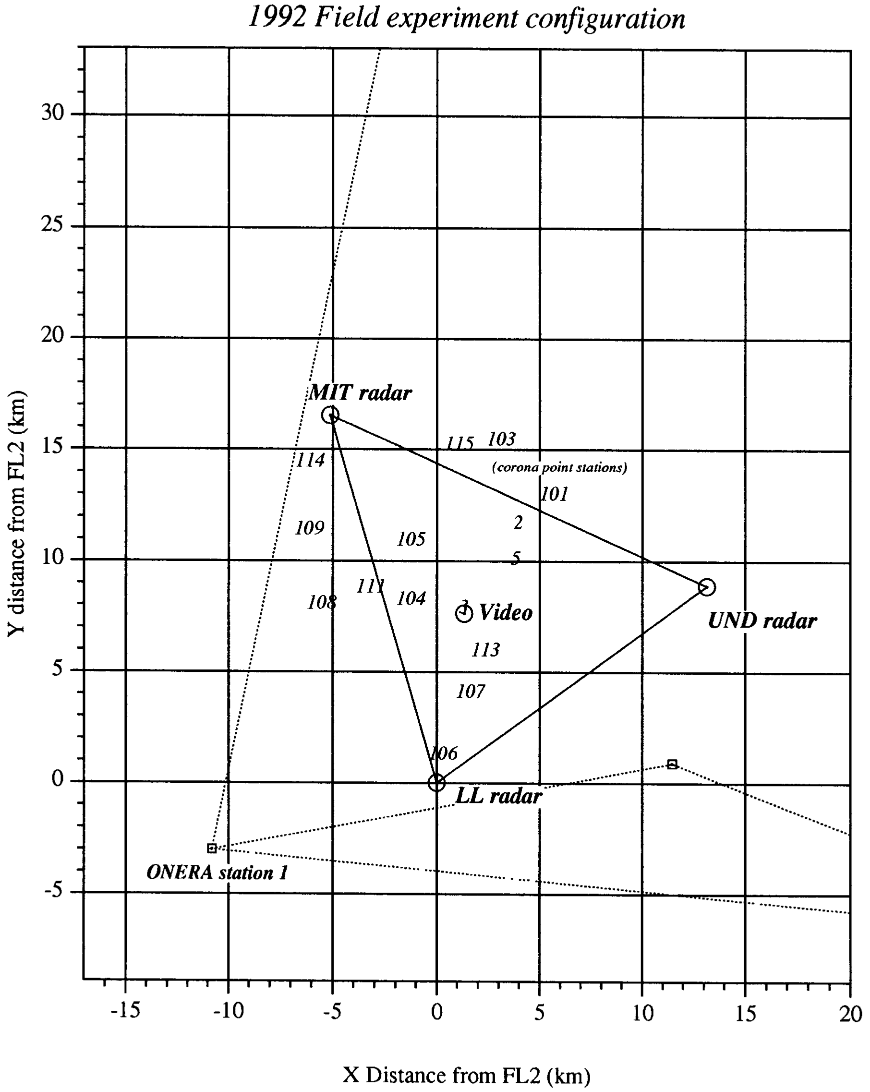

Figure 5.2: Configuration of field instruments in 1992 Orlando campaign. MIT radar formed the northwestern corner of a triple Doppler network (tridop data was not available for EOSO periods). High speed video was colocated with the FL-3 ASR-9 radar in the center of the network. Corona current stations were scattered in a mesonetwork throughout the domain. ONERA interferometer stations were located south and southeast (latter not shown). The vertices of the polygon connecting these indicate rough bounds of the equivalent "dual Doppler lobes" for effective interferometer view regions and nulls.

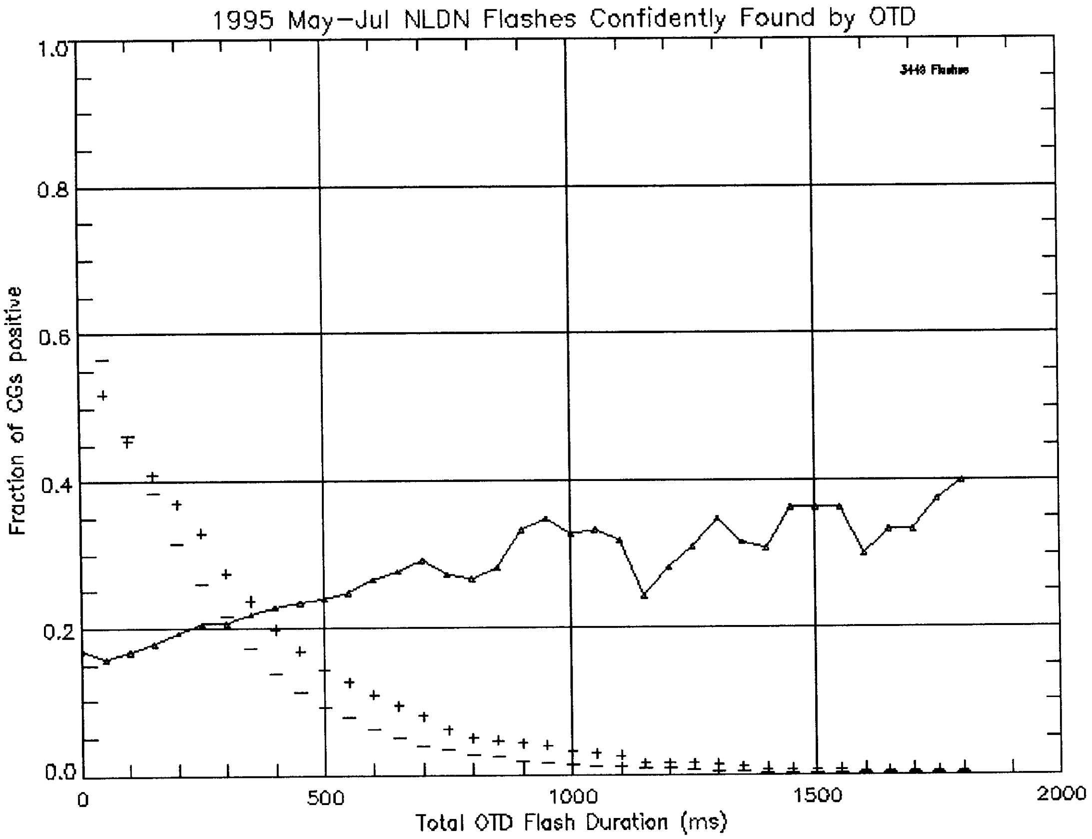

Figure 5.3: Distribution functions of flash duration for positive and negative CGs in the OTD/NLDN coincdence dataset.

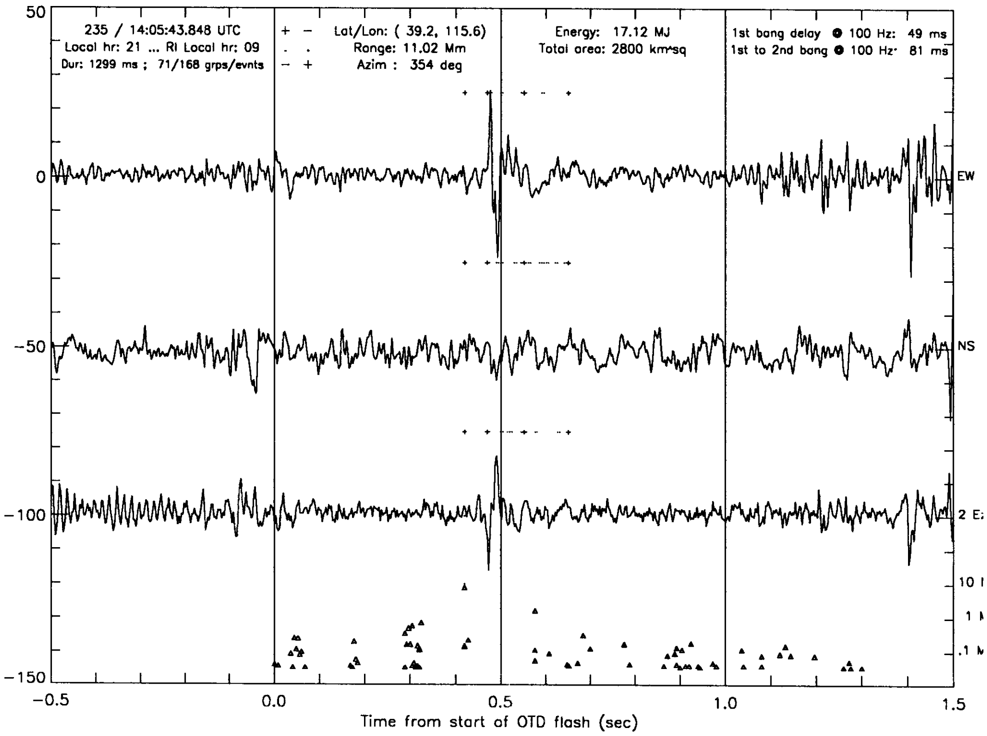

Figure 5.4: Sample OTD and Schumann resonance measurements of a large positive CG flash located in east Asia. SR fields (horizontal magnetic H_{ew}, H_{ns} and vertical electric E_z are shown in units of pT and mV/m. OTD "groups" (clusters of optical pulses coincident in time) are plotted along the bottom with a log scale for group radiance. The +CG stroke is clearly evident in the optical data, as well as several hundred milliseconds of intracloud precursor activity.

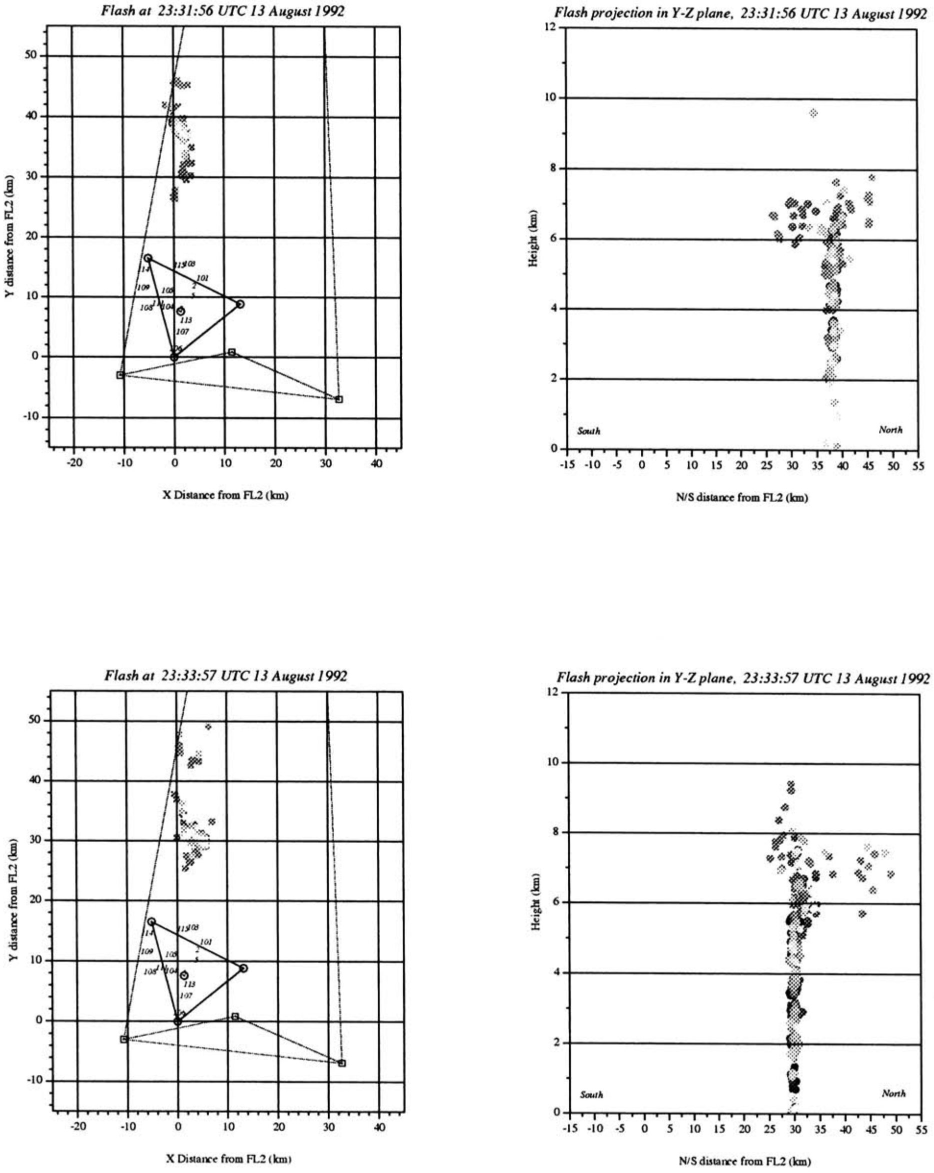

Figure 5.5: Typical negative CG flashes, active-late stage of storm on 13 August 1992 (23:31:56 and 23:33:57 UTC).

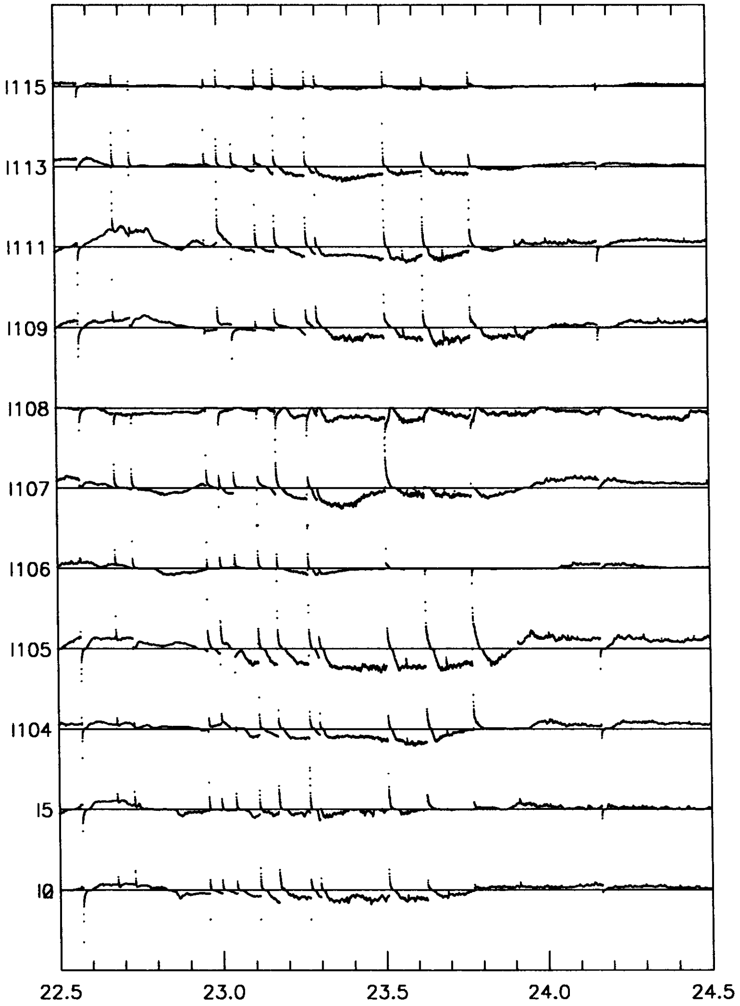

Figure 5.6: Corona current traces for Aug 06 1992. The station numbers correspond to those shown in Figure 5.2. Field convention is positive for foul field (negative charge overhead) and negative for fair field (positive charge overhead). Data for station 108 is suspect on this day.

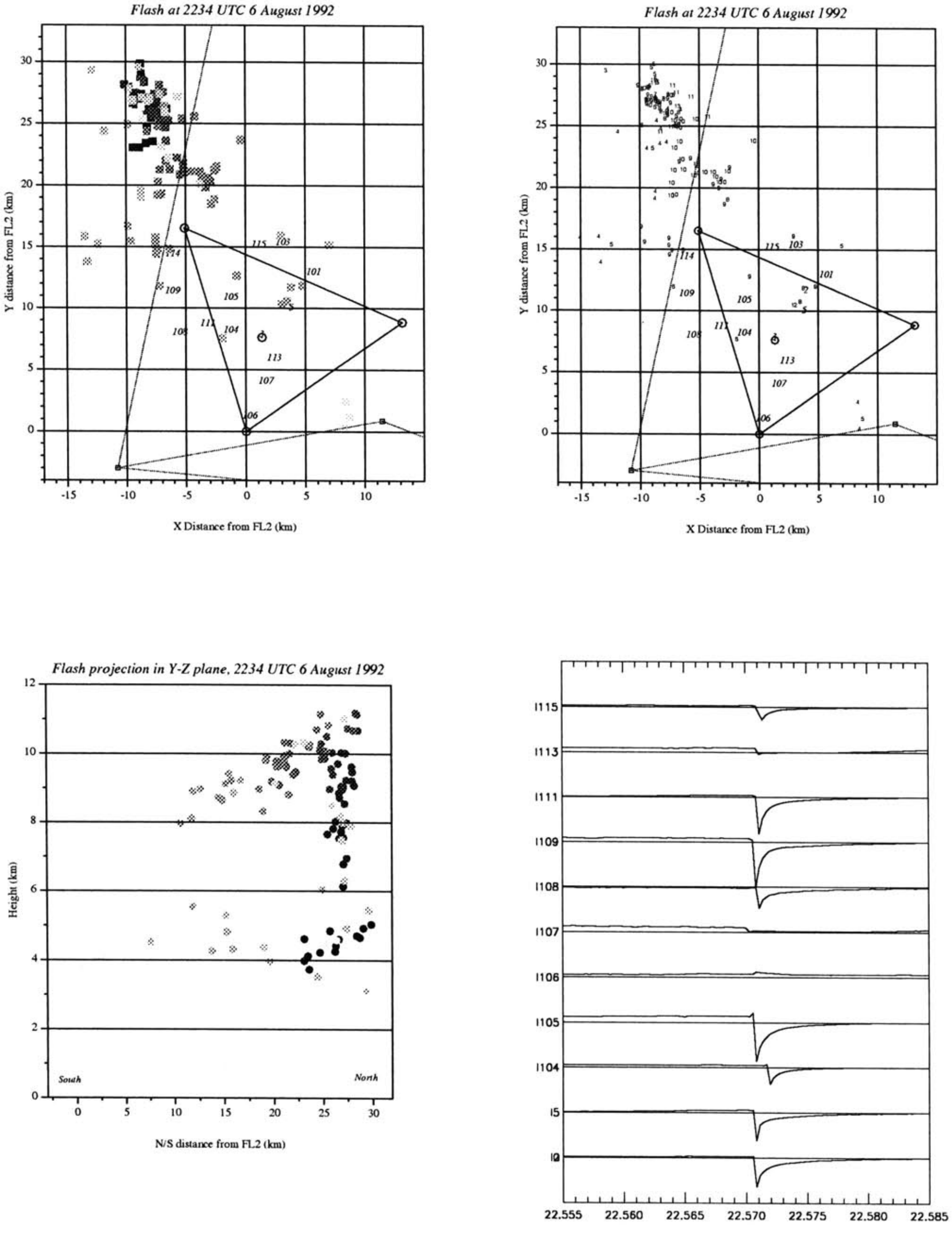

Figure 5.7: Intracloud flash at 22:34 UTC, 6 August 1992. Grayscale shading indicates relative VHF burst time, from earliest (dark) to latest (light). Numbers in the upper right plan view indicate burst altitude in kilometers.

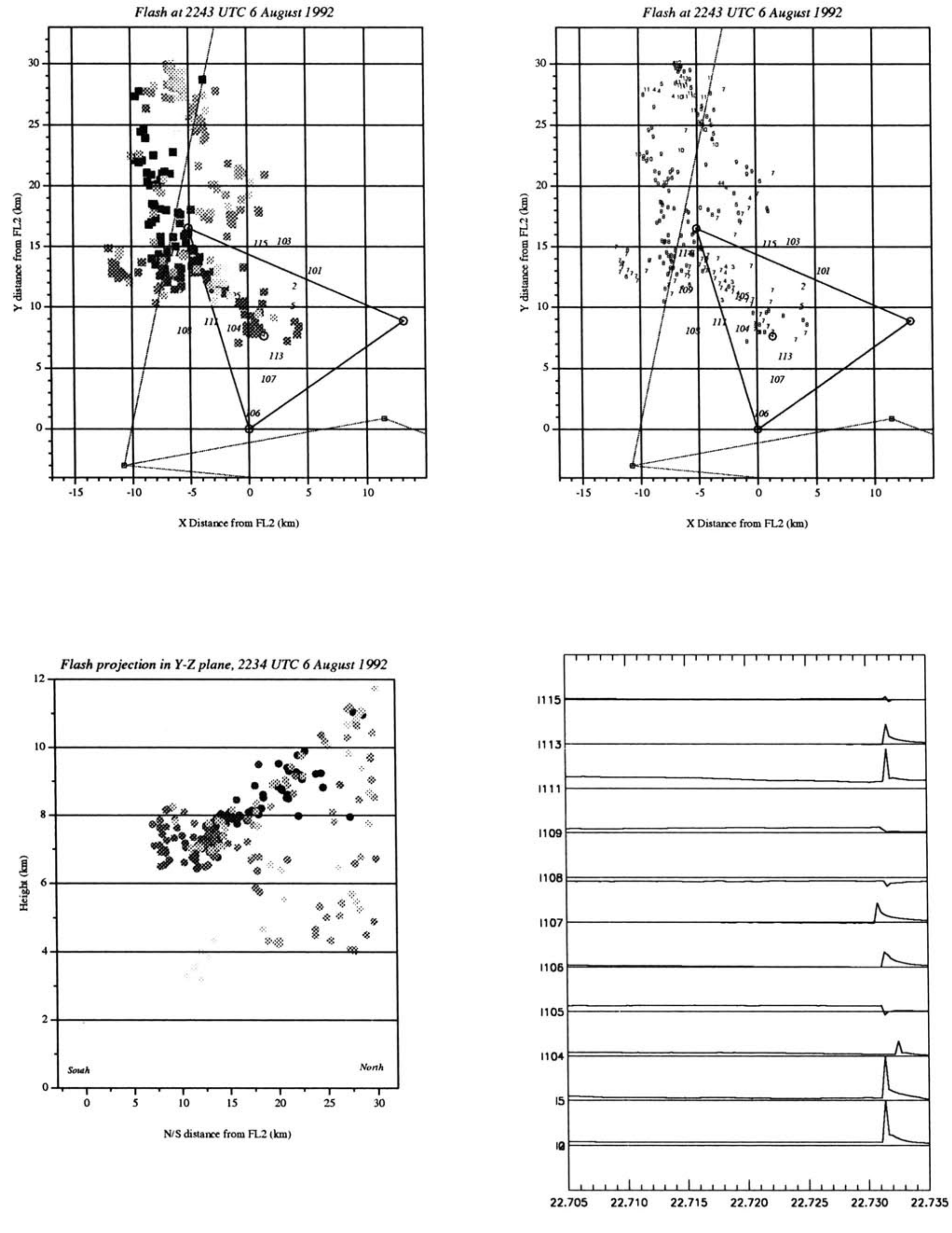

Figure 5.8: Intracloud flash at 22:43 UTC, 6 August 1992.

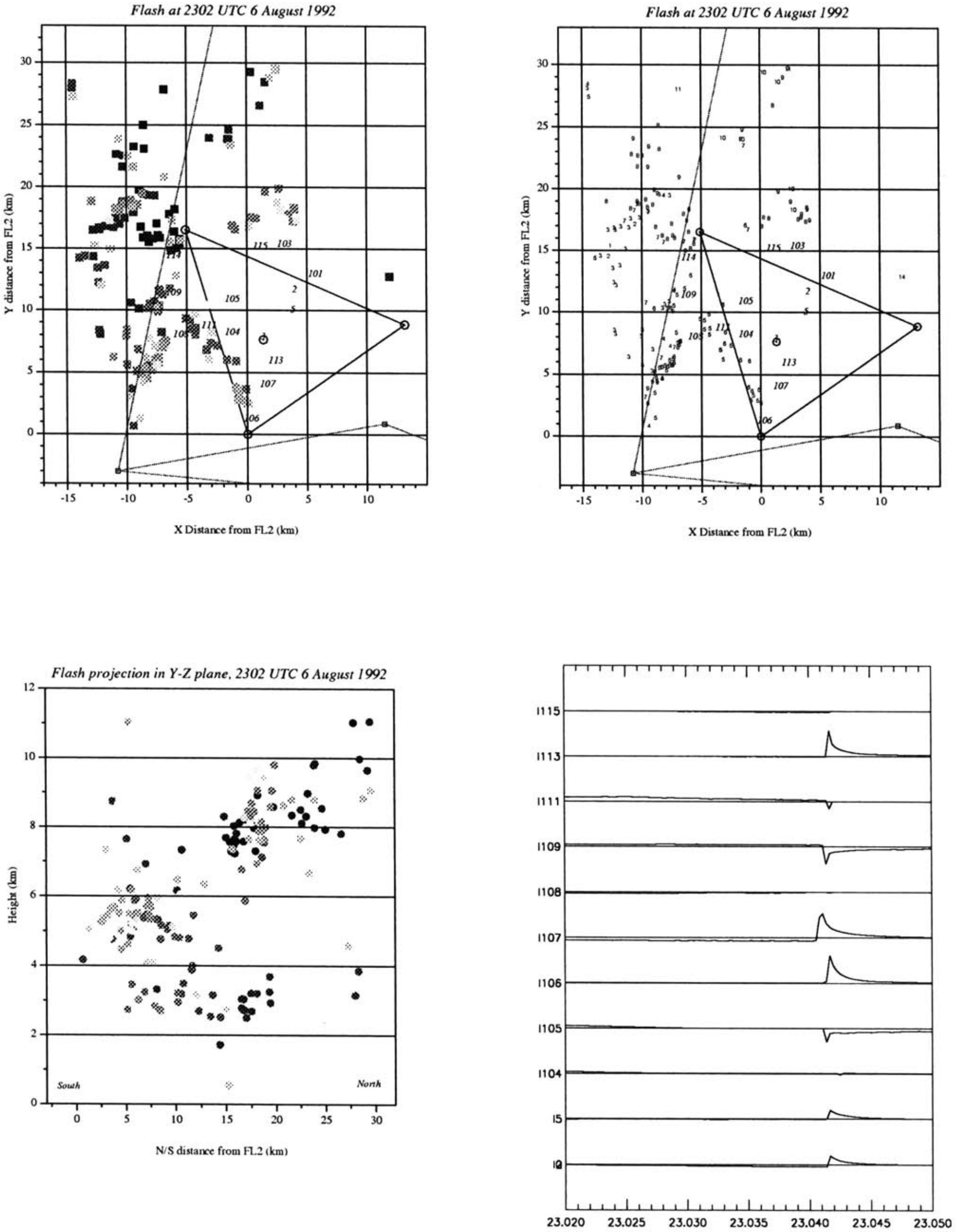

Figure 5.9: Intracloud flash at 23:02 UTC, 6 August 1992.

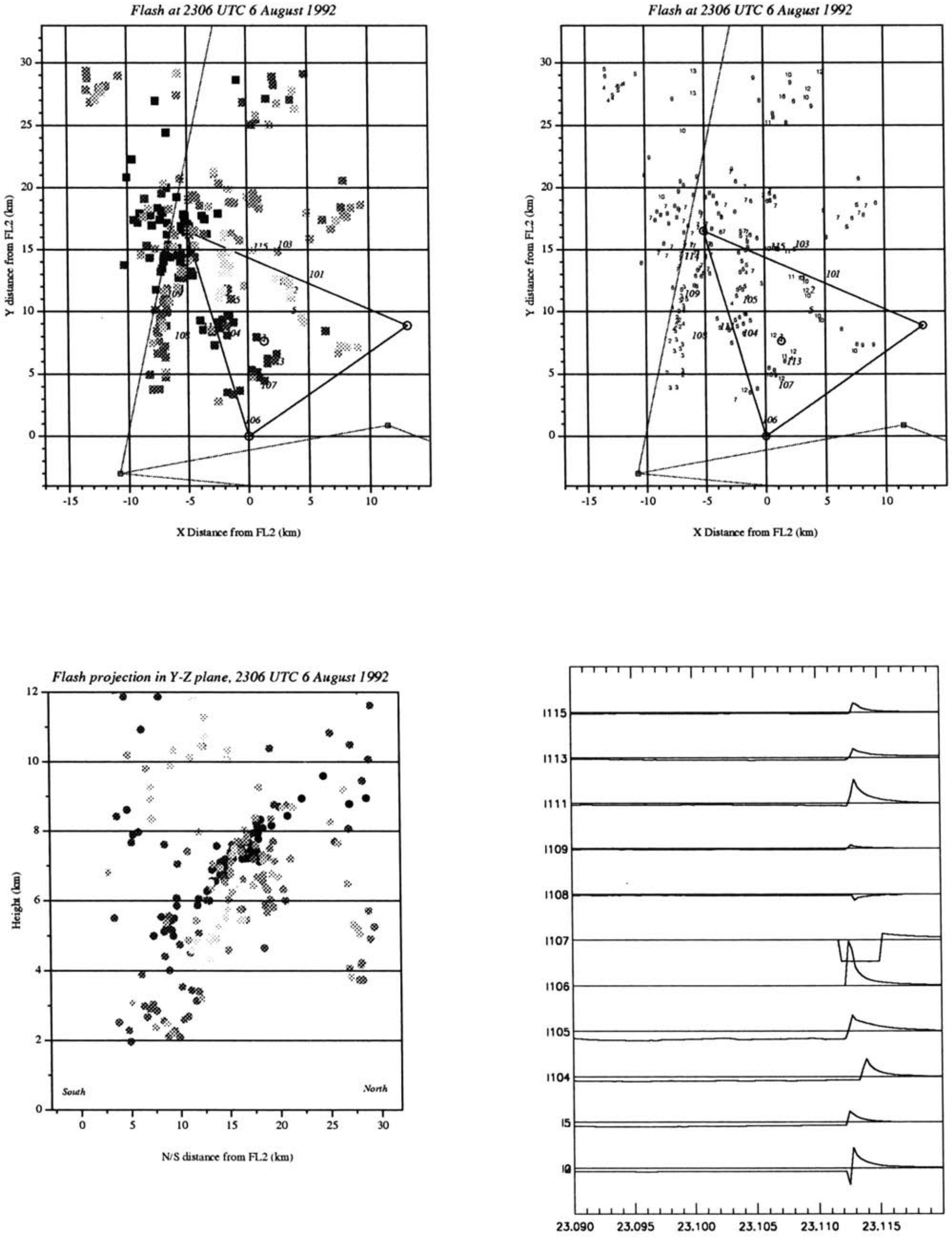

Figure 5.10: Positive cloud-to-ground flash at 23:06 UTC, 6 August 1992.

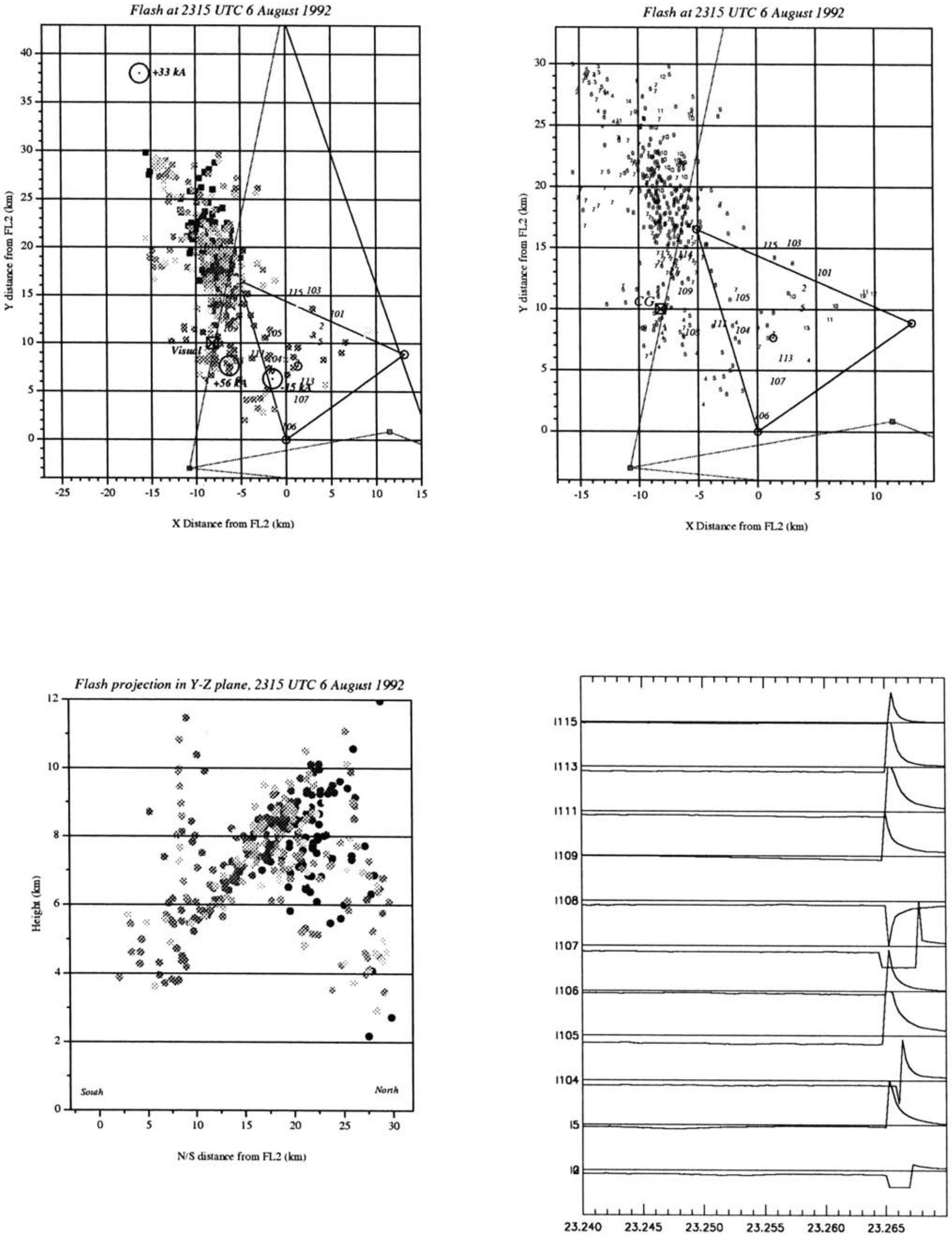

Figure 5.11: Positive cloud-to-ground flashes at 23:15 UTC, 6 August 1992.

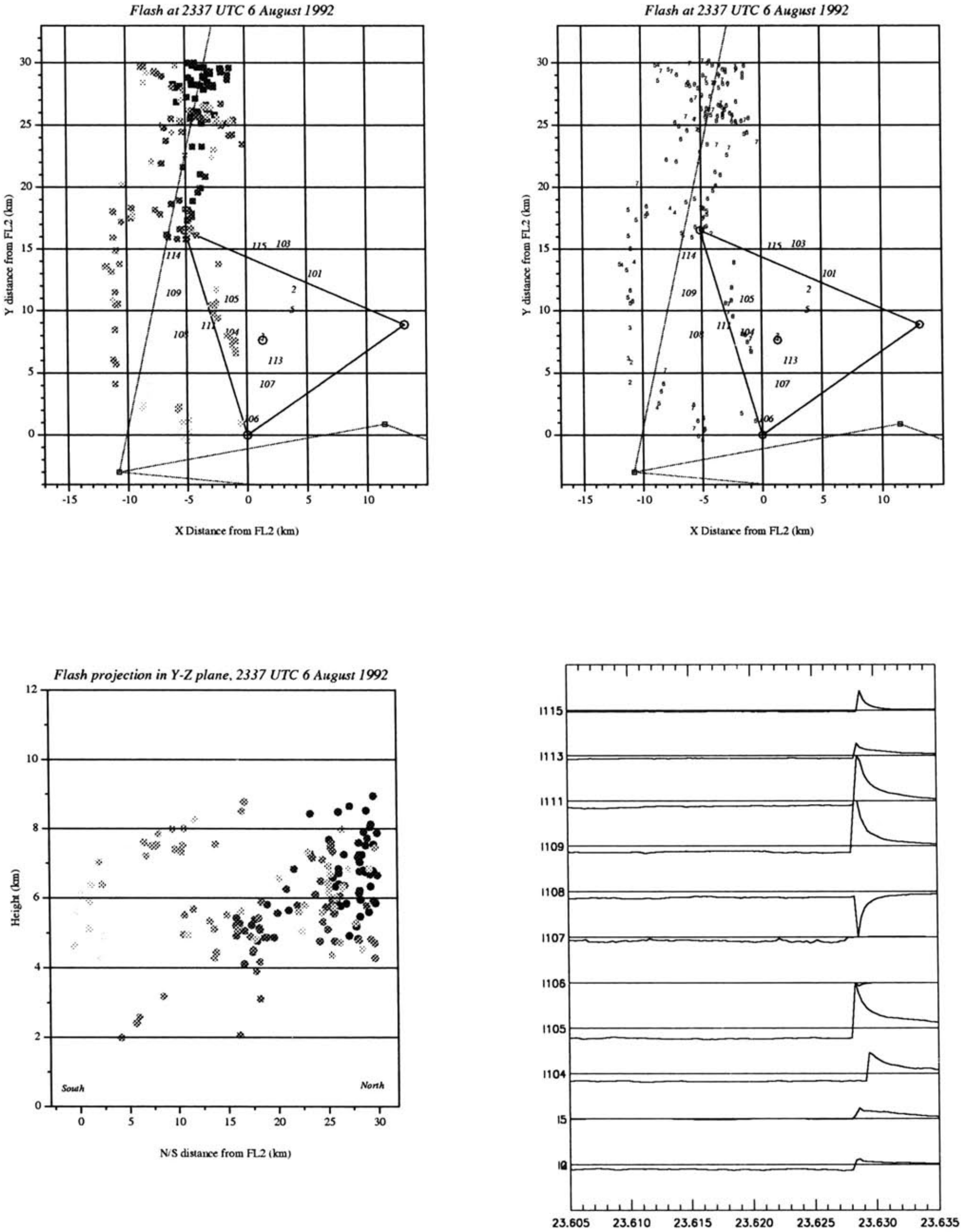

Figure 5.12: Intracloud flash at 23:37 UTC, 6 August 1992.

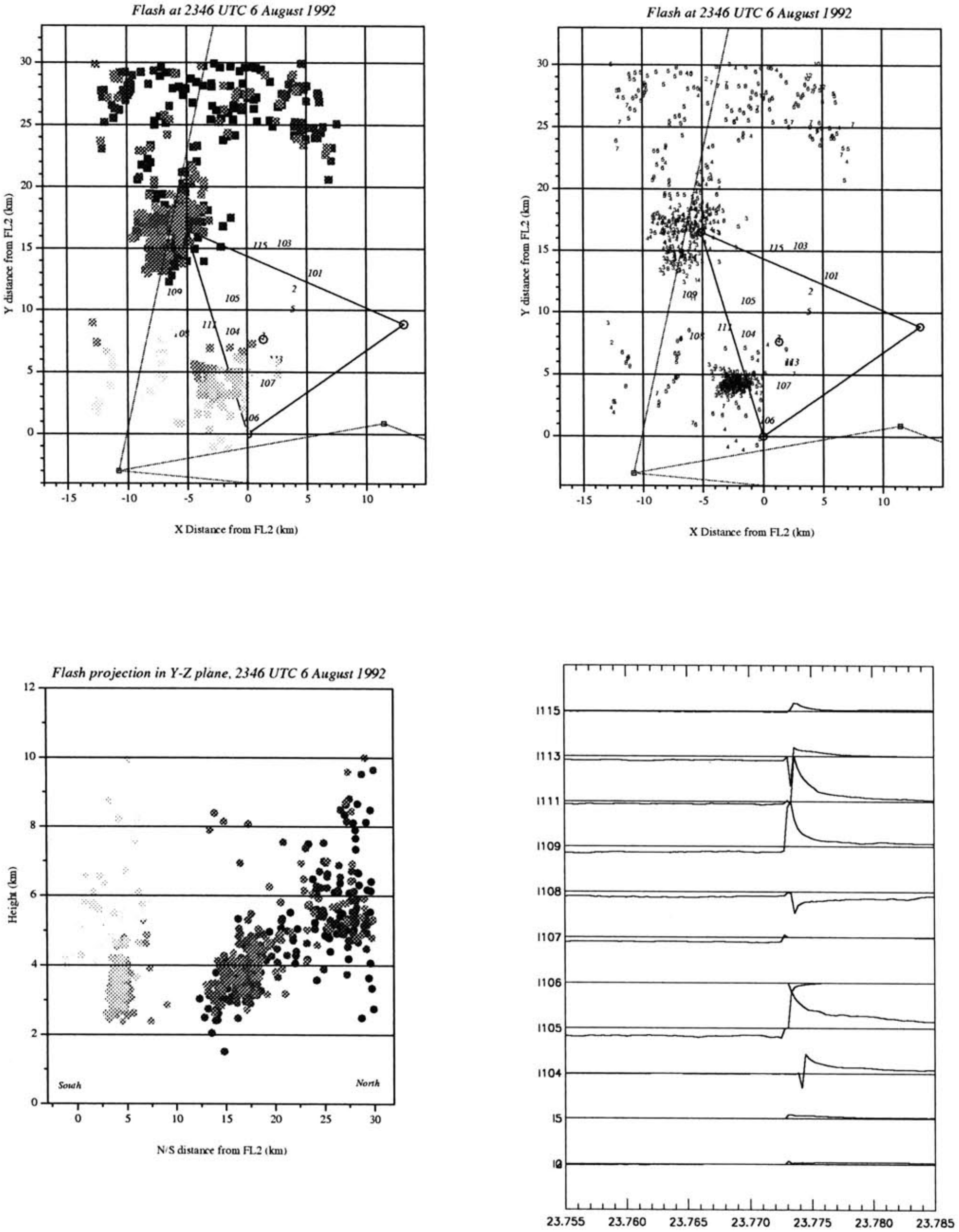

Flash at 2346 UTC 6 August 1992

Flash at 2346 UTC 6 August 1992

Flash projection in Y-Z plane, 2346 UTC 6 August 1992

Figure 5.13: Intracloud flash at 23:46 UTC, 6 August 1992.

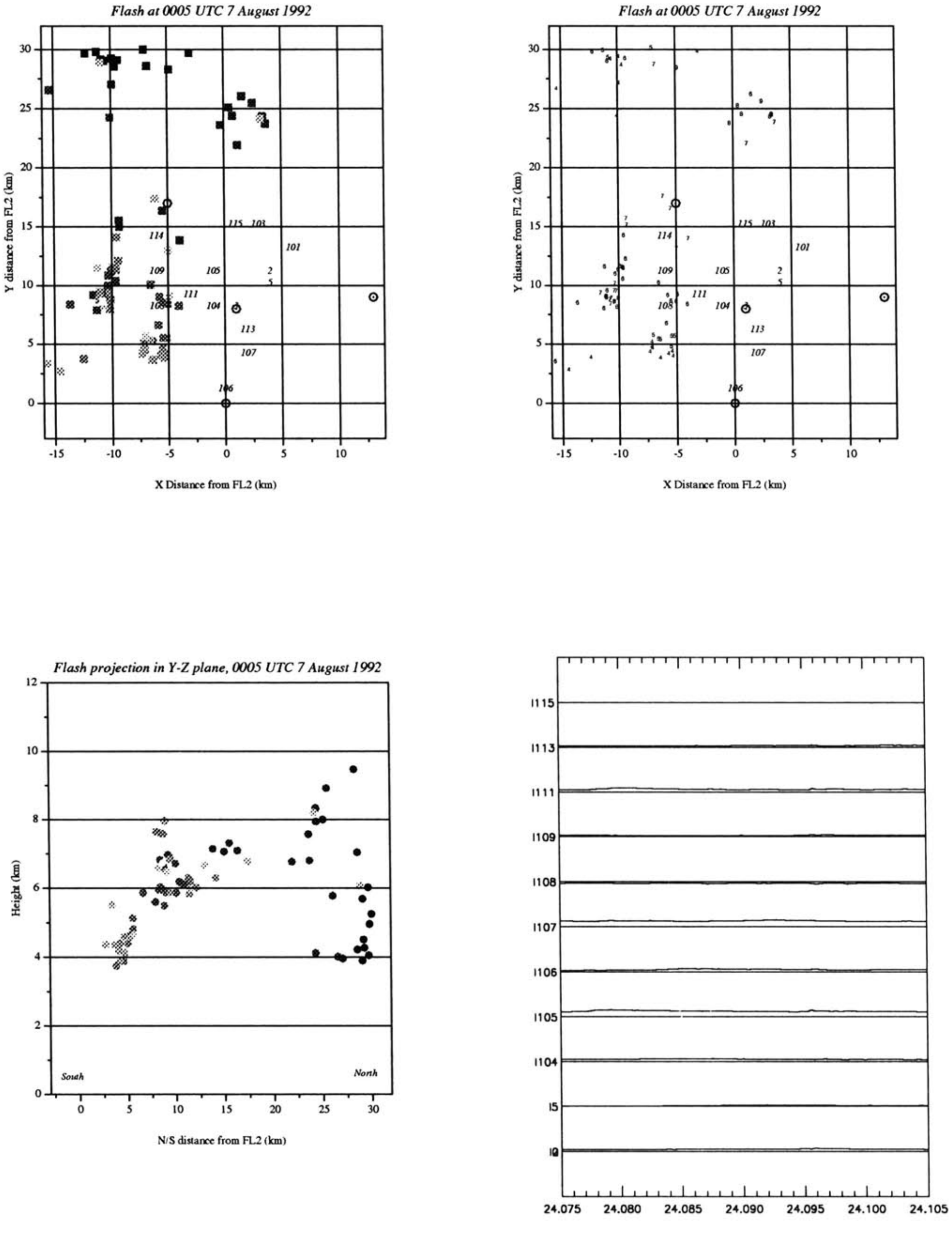

Figure 5.14: Intracloud flash at 00:05 UTC, 7 August 1992.

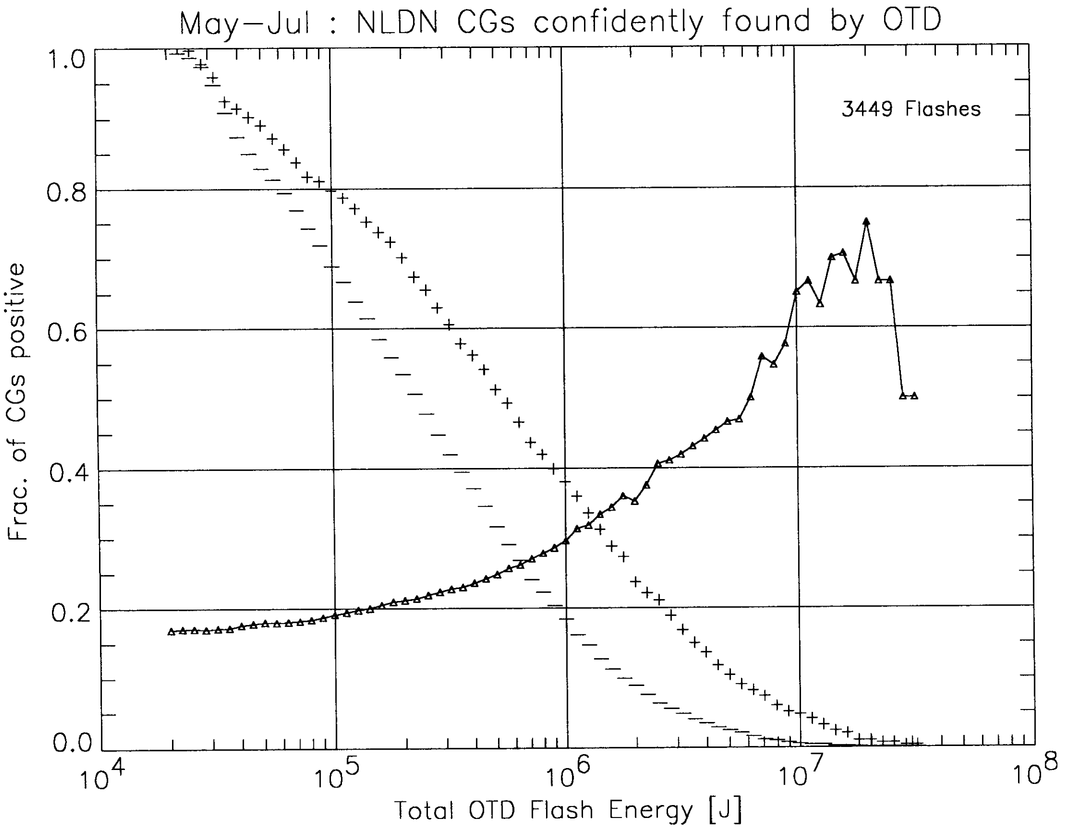

Figure 5.15: Distribution functions of flash total optical energy for positive and negative CGs in the OTD/NLDN coincdence dataset.

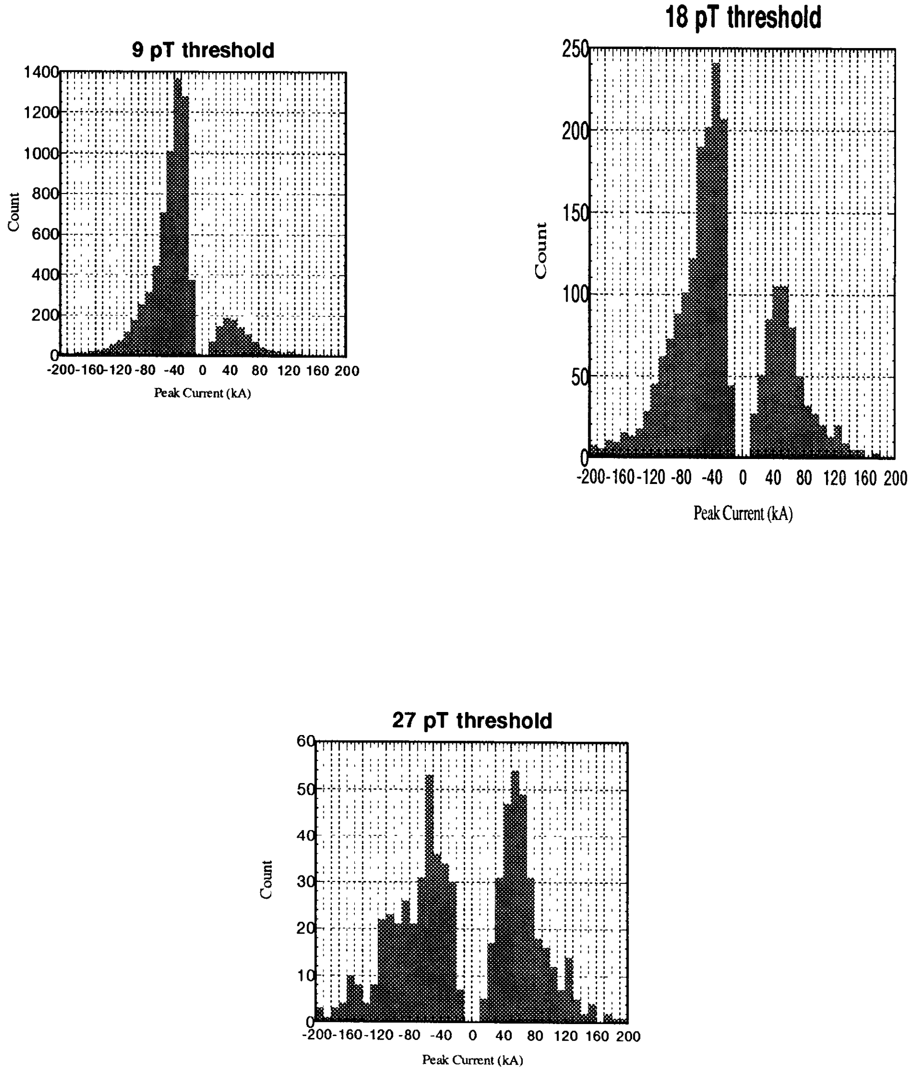

Figure 5.16: Peak current distributions of CG flashes observed jointly by the OTD and MIT Schumann resonance station, under various SR magnetic field trigger thresholds. The very largest amplitude SR transients are dominated by +CG flashes.

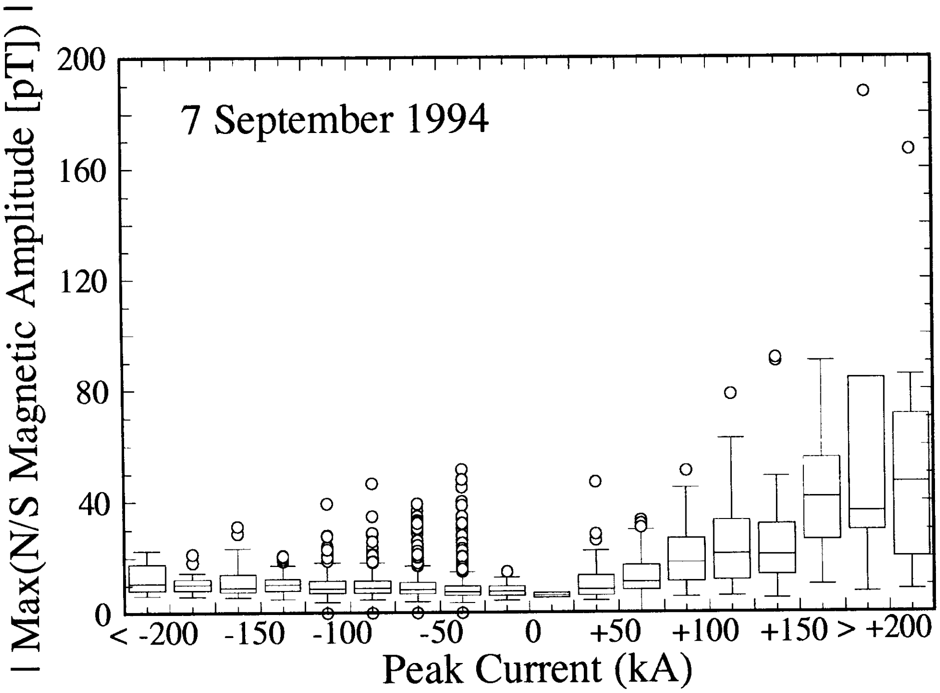

Figure 5.17: Distributions of SR transient initial rise amplitudes (in pT) for CG flashes during the 7 September 1994 midwestern MCS.

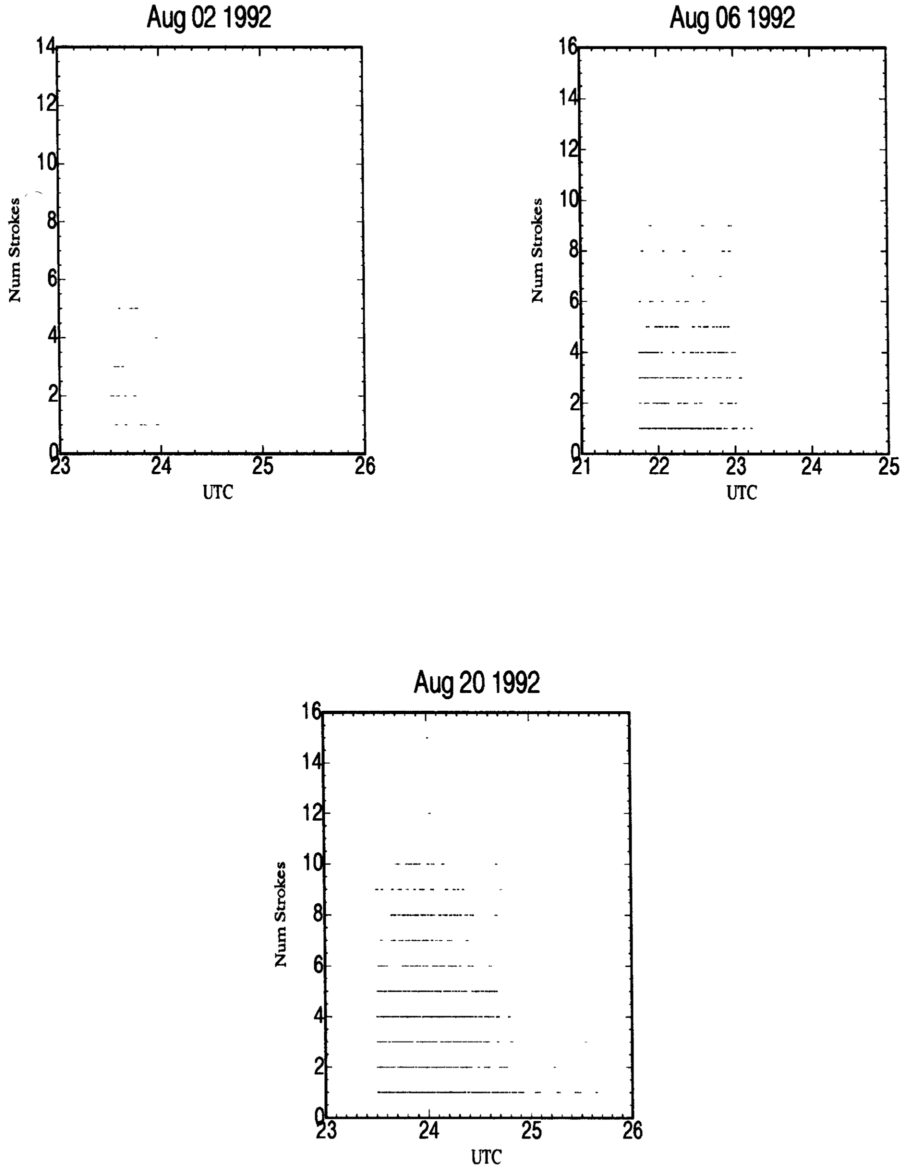

Figure 5.18: Negative CG return stroke multiplicity for three Orlando EOSO events; flashes within 50 km of the MIT radar. General decline in stroke multiplicity is evident in each case.

Chapter 6

Conclusions

To summarize the results of this investigation, it is important to recall the basic hypothesis and methodology employed herein. It was hypothesized that a continued, active generator is present in evolving stratiform anvil clouds, and that this generator is ultimately caused by the same ice-ice collisional charge transfer process believed present in "normal" convection. The anomalous electrification observed (negative surface fields and positive lightning discharges) is assumed to arise when the depleted liquid water environment of these clouds forces the collisional charge transfer into a reversed regime, as found in laboratory experiments. We speculate that this reversed charging leads to a large scale "inverted dipole" structure in the stratiform cloud.

As such, we have sought to map the observed kinematic (updraft) structure of the evolving cloud through to a characteristic microphysical state, and hence to a relevant charging regime and distribution. The hypothesized generator and charge structure requires that we demonstrate:

1. That ice saturation (at the very least) and water saturation (preferably) be

maintained at and below the altitude of about -20 C, the favored region for collisional charge separation. Such saturation is apparently needed for effective charge transfer, and is not inferrable *a priori* given the observed mesoscale updraft evolution.

2. That hydrometeor collisions are numerous enough to support effective, continued charge separation.

3. That the flux divergences of charged hydrometeors (the actual local net generator current) yield an essentially inverted dipole structure.

In addition, it would be fortunate if the results also demonstrate:

1. An evolution from normal to inverted dipole structure, as the storm enters the stratiform phase.

2. A correlation between the inferred evolution of charging behavior and the observed electrical evolution of the system.

Fundamental limitations in the available data and selected analysis techniques obviously preclude a "smoking gun" demonstration of the above characteristics. Nevertheless, taken as a whole (and with the limitations in mind), the results are consistent with, if not indicative of, the basic hypothesized electrical evolution. Below, the procedural constraints and basic results of each step in the process are summarized in context.

6.1 Retrieval performace

6.1.1 Kinematic retrieval

As discussed in Chapter 2, the VVP kinematic retrieval technique suffers several crucial limitations: it yields essentially linearized, areal-average quantities over a large analysis domain, and is fundamentally constrained by the volumetric radar echo distribution. Sufficiently nonlinear large scale wind fields, or radar echo distributions which are spatially biased, lead to detectable but essentially unquantifiable errors in retrieved parameters. These are manifest both as parameter biases which preclude conventional confidence interval analysis, and degradations of the retrieval's robustness caused by multicollinearity in the regression equations.

Nonetheless, VVP analysis appears to have been well-suited for the late-stage storm evolutions examined herein. Reasonably domain-filling echo distributions dominated the study periods, leading to acceptable VVP root mean square errors (about 1-2 m/s) and correlation coefficients. Retrieved kinematic fields are only moderately influenced by actual scan strategies, and improvements in inferred vertical velocity consistency stem more from careful rejection of statistically nonrobust individual layer retrievals, as identified by formal diagnostic techniques.

The kinematic retrievals may be less quantitatively "validated" by their external consistency with independent radar data moments (such as reflectivity) and the internal consistency between retrieved wind field parameters. On 2 and 20 August 1992, there was excellent correlation between the inferred vertical velocity and areal average reflectivity field evolution, with lower tropospheric downdrafts coincident with bright band onset. On 20 August, a secondary peak in mesoscale updraft strength was perfectly matched by observed increases in midlevel reflectivities. In all of the events, rain hydrometeor terminal velocity (the noisiest of all retrieved parameters) showed excellent correlation with modest enhancements in stratiform rainfall reflectivity. In the Orlando cases, the mesoscale updraft and downdraft regimes showed a clear vertical wind shear interface, suggesting that separate flow regimes were accurately diagnosed. Inferred mesoscale downdrafts were also well correlated with rain hydrometeor terminal velocity, an expected feature during periods of enhanced melting and evaporatively induced downdrafts.

6.1.2 Microphysical retrieval

The microphysical retrievals employed here likewise suffer severe limitations. They implicitly assume horizontal uniformity and negligible horizontal water fluxes, features likely to dominate only after the late-active convective stages of the analyzed storms. The steady-state assumptions are clearly suboptimal. However, it should be re-emphasized that most of the bulk microphysical source/sink terms presented in Chapter 3 were nearly linear in mixing ratio, and strongly temperature-dependent. Thus, the lack of a hydrometeor "memory" in the retrieval may be of secondary importance when the model partitions total water under time-evolving vertical forcing profiles. The vertical structure of the source/sink terms and updraft forcing, and the domain upper boundary, appear to be the primary determinants of the retrieved hydrometeor fields.

The most severe limitation in the retrievals arise from the cloud ice hydrometeor category, and its initiation terms based upon Fletcher clear-air natural ice nucleus profiles. The poorly-quantified clear-air distributions of these nuclei (especially at low temperatures), the lack of cloud ice "memory" in the model, and the ongoing uncertainty about actual ice-multiplication processes are the fundamental limits on the usefulness of this technique. These limitations are partially mitigated by the fact that cloud ice growth far aloft is ultimately constrained by the availability of water vapor for depositional growth, and not by the natural nucleus concentrations.

Ultimately, the retrievals should be viewed more as a set of quasi-independent "generic" stratiform cloud responses to variable updraft forcing, than as strongly-linked and time-evolving descriptions of the actual observed cloud. This of course means that correlations with the observed electrical evolution should be tentative, at best. Nonetheless, as described in Chapter 4 and summarized below, even with this crude approach, the technique appears to generate reasonable descriptions of charging processes which *may* explain the observed electrical behavior.

The general response of the retrieval technique has been discussed in detail in Chapter 4, and by *Braun and Houze (1995)*. In the crudest sense, it performs a simple partitioning of total water content between various hydrometeor categories under variable updraft conditions and domain boundaries. A common model response to increased updraft strength is to favor precipitation ice and cloud water over cloud ice in the partitioning, with cloud ice concentrations increasing as updrafts diminish. This leads to snow/ice collision rates which do not necessarily peak in phase with updraft maxima. Another model characteristic is a strong sensitivity of total precipitation hydrometeor content to the domain upper boundary; this is caused primarily by the strong temperature-sensitivity of upper level cloud ice nucleus concentrations, which strongly determine lower level precipitation ice content. The typical low level downdraft / upper level updraft structure typical of stratiform regions yields a stronger "top-down" than "bottom-up" sensitivity in the retrievals; mesoscale downdraft regions are generally deep enough (in summertime conditions) that surface boundary conditions in vapor content or rain mixing ratio barely affect retrieved mixing ratios within the actual cloud. The "top-down" sensitivity may not necessarily be a model flaw: it may indeed be capturing some of the basic structural characteristics of low-topped mesoscale convection, as in the western Pacific case study.

A critical and robust model result is the maintenance of ice saturation for up to a kilometer below the mesoscale updraft base, and, depending on the mesoscale downdraft strength, the occasional retrieval of cloud water below the updraft base. This saturation is necessary to support continued microphysical charging upon hydrometeor collisions in this region, a central feature of the hypothesized active inverted generator we have attempted to demonstrate.

6.2 Inferences of cloud electrification

In addition to the limitations inherent in the kinematic and microphysical retrievals, it is again emphasized that the inferred electrical behavior is subject to an inherent constraint: we can only derive the *local charging behavior* of the cloud at each timestep, and not the overall charge profile. This is a result of:

- the unknown charging history prior to the window amenable to 1-D analysis,

- the unknown strength and vertical distribution of charge sinks due to lightning discharges,
- the upper and lower boundary conditions on space charge, and
- the difficult-to-parameterize effects of cloud-edge screening layers, surface corona release and (possible) charging by melting.

Furthermore, it should be emphasized that ice-ice collisional charge separation in the 0 to -10 C temperature range is relatively poorly explored by the experimental studies, primarily because of the difficulty of maintaining steady-state microphysical conditions in the laboratory environment at these temperatures. Nonetheless, the studies do seem to agree that the "normal" negative precipitation charging regime is confined to lower temperatures. As such, a lower positive precipitation charging region is almost inevitable in actual clouds, even if its strength and net flux divergence (generator current) are open to question.

Even subject to these limitations, the overall technique appears to yield consistent results, from which we may infer:

1. The total *retrieved* collisional charge separation rate appears to fall by only a factor of two or so during the stratiform period, from (admittedly dubious) values found for the late-active stage. This is a direct result of persistent ice- and water-saturation within the critical charging region of -5 to -20 C, despite mesoscale downdrafts which penetrate substantially above the melting level. This is also a result of enhanced cloud ice crystal concentrations during periods of weak mesoscale updrafts, which maintain high collision rates between precipitation and cloud ice. A continued storm generator is thus not only plausible

within the stratiform cloud, but may be more effective than expected. The larger total charge transfers of late-stage spider and positive CG flashes (as previously reported in the literature and confirmed herein, Chapter 5) appears to offset the higher duty cycle (flash rate) of lightning in the active convective phase. It was previously thought that the large areal extent of stratiform regions was alone responsible for the extra charge for these large discharges. However, the results of Chapter 4 suggest that the actual generator current itself may be of comparable magnitude in the stratiform regions of these storms.[1]

2. There is some indication that the retrievals have found a "charging rate cutoff" below which lightning discharges are not supported. This may have been evident in the 31 July 1994 and 10 February 1993 case studies. While the model limitations clearly leave the numerical magnitude of such a cutoff suspect, the possibility is intriguing.

3. The flux divergence of this local charge separation does indeed yield a characteristic inverted dipole signature through the electrical EOSO period. However, the use of areally-averaged vertical velocities and a 1-D cloud model lead to underestimation of actual cloud liquid water content in the late-active stages of convection, and the technique fails to show an electrical "inversion". However, such an inversion may be simulated by a modest (3x) increase of the retrieved LWC field, and appears to agree well with the observed surface electrical evolution. Further, the fortunate occurrence of a secondary updraft peak in the 20 August case offers a case in which *relative* changes in the magnitudes of a *unipolar* charge-separation regime appear consistent with a second EOSO observed

---

[1] If so, then an resolved question is why the observed flash rate is so much lower than during the active storm phase.

at the surface.

4. A multipolar structure is possible in the generator term (flux divergence) profiles *despite* a retrieved unipolar collisional charge transfer regime. This structure is associated with fine-scale vertical structure in the cloud LWC, precipitation ice and collision rate profiles. Variations in these fields are a direct result of the strong temperature dependence of many characteristics of three-phase microphysical growth, such as ice nucleus concentration, crystal habit, collection efficiency and relative depositional growth rates. Thus, *sounding-observed multipolar charge structures are not inconsistent with a mixed-phase microphysics, ice-ice collisional charge transfer theory* of cloud electrification. New theories of internal charge transfer or large scale horizontal advection are thus *not necessarily required* to explain a rich vertical charge structure in stratiform anvils, as reported by *Schuur et al. (1991), Hunter et al. (1992), Stolzenburg et al. (1994), Shepherd et al. (1996).*

5. Charge transfer associated with melting is *not required* to yield a lower positive charging regime, and hence a lower positive charge center in these clouds. Attempts to invoke melting charging *(Shepherd et al., 1996)* have also been shown to be inconsistent with the actual laboratory work in which this phenomenon was observed (see pages 31-34). Further, a large net flux divergence will occur near the 0 deg isotherm simply due to (a) enhanced snow-snow aggregation below about -5 C, and (b) the particle fall speed increase associated with snowmelt. If the relevant snow has been positively charged in collisions with cloud ice in the lower mixed phase region (as shown in Chapter 4), such flux divergence will inevitably lead to a large positive charge layer at or above the melting level. Thus, while melting charging *may* be present in actual clouds,

there is little direct evidence for such a phenomenon, and no need to invoke it to explain the observations.

6. In the two Orlando cases, the end of the inverted surface field regime (and subsequent reversal to positive or foul fields) appears well correlated with a general decline in the strength of the lower positive generator current, slightly preceding the decline in upper negative generator current. Such a relationship is certainly competitive with a latest-stage "geometric" interpretation of this secondary field reversal.

7. There are possible indications that the total vertical separation of the generator dipole may be related to positive CG occurrence, or the preference of CG over IC late-stage lightning. This would be a secondary effect of higher mesoscale updraft bases; their position relative to the preferred charging region partially determines this net charg*ing* dipole separation. This effect is highly speculative, but intriguing as it may explain the relative presence or absence of late-stage lightning in various anvil clouds.[2]

The new observations of spider IC and positive CG lightning discharges may further refine our interpretation of late-stage stratiform anvil electrification. First, we have statistically confirmed the anomalous spatial, temporal and energetic characteristics of positive CG lightning previously reported in isolated case studies in the literature. We have also demonstrated that the late-stage lightning observed in relatively small-scale systems near Orlando is comparable to positive lightning observed in large MCS systems, and around the world (at least in terms of its temporal, and

---

[2] An alternative interpretation would be invoke the relative height of the lower positive charging region relative to ground level; at times where the charging region lies closer to the melting level, positive CGs might be favored.

to a lesser extent spatial, characteristics). This may support the idea that the mechanisms hypothesized (and partially shown) to operate in the storms studied may be present in other stratiform systems with comparable microphysical environments.

The structural characteristics of late-stage lightning observed by the ONERA interferometer on 6 August 1992 (an event with even less organization than our four case studies) are somewhat inconclusive, at least in terms of inferred overall charge structure. However, several features are relevant. First, the lowermost channels in the discharge dendrite network all propagated rearward through the stratiform anvil, and appeared to be fairly domain-filling. Through the EOSO, these channels, located anywhere from 3-6 km AGL, all appeared to remove positive charge from overhead, consistent with an inverted dipole model. Finally, the locus of activity from 6-8 km AGL just west of the MIT radar is precisely in the -5 to -20 C temperature range, found to be a preferred charge-transfer region in the (unrelated) retrieval studies, even through the late-stage period. The spatial and temporal characteristics of the 6 August flashes, as well as the repeated activity in the 6-8 km AGL locus, are all suggestive of (though not conclusive of) a continued active generator in this system.

Finally, it is again emphasized that several of the case studies presented here argue strongly against alternative theories of stratiform anvil electrification. Active convection had ceased during the 2 August 1992 Orlando event, thus disfavoring a tilted-dipole hypothesis. As noted above, melting charging, while possible, is neither necessary to explain the observations or even supported by the observations in any of the case studies. Finally, the oceanic event studied on 10 February 1993 suggests that the effects of surface corona release (at best a dissipative phenomenon, and not one which can lead to field reversal) are of secondary importance in interpretation of the surface fields. We are left with a set of weakly-organized anvil systems whose observed electrical behavior and evolution is *not inconsistent* with a continued, active generator in an "inverted" charging regime.

References

Armstrong, R., J. Shorter, W. Lyons, N. Carron, and W. Blumberg, Assessment of nitric oxide formation in discharge regions above thunderstorms *(in review)*, *Geophys. Res. Lett.*, *23*, –, 1996.

Baker, B., M. Baker, E. Jayaratne, J. Latham, and C. Saunders, The influence of diffusional growth rates on the charge transfer accompanying rebounding collisions between ice crystals and hailstones, *QJRMS*, *113*, 1193–1219, 1987.

Beard, K., and H. Pruppacher, A wind tunnel investigation of the rate of evaporation of small water drops falling at terminal velocity in air, *J. Atmos. Sci.*, *28*, 1455–1464, 1971.

Belsley, D., E. Kuh, and R. Welsh, *Regression diagnostics: Identifying influential data and sources of collinearity*, John Wiley and Sons, 1980.

Berry, E., Modification of the warm rain process, in *Prepr. 1st Nat. Conf. Weather Modification*, 1968.

Bigg, E., The supercooling of water, *Proc. Phys. Soc. London*, *B66*, 688–694, 1953.

Boccippio, D., A diagnostic analysis of the VVP single Doppler retrieval technique, *J. Atmos. Oceanic. Tech.*, *12*, 230–248, 1995.

Boccippio, D., E. Williams, S. Heckman, W. Lyons, I. Baker, and R. Boldi, Sprites, ELF transients and positive ground strokes, *Science*, *269*, 1088–1091, 1995.

Boccippio, D., C. Wong, E. Williams, R. Boldi, H. Christian, and S. Goodman, Global validation of single-station schumann resonance lightning location *(in review)*, *J. Atmos. Terr. Phys.*, 1996.

Braun, S., and R. J. Houze, The transition zone and secondary maximum of radar reflectivity behind a midlatitude squall line: Results retrieved from doppler radar data, *J. Atmos. Sci.*, *51*, 2733–2755, 1994.

Braun, S., and R. J. Houze, Diagnosis of hydrometeor profiles from mean vertical motion data, *Quart. J. Roy. Met. Soc.*, *121*, 23–53, 1995.

Brook, M., M. Nakano, P. Krehbiel, and T. Takeuti, The electrical strucutre of the Hokuiriku winter thunderstorms, *J. Geophys. Res.*, *87*, 1207–1215, 1982.

Brook, M., P. Krehbiel, and D. MacLaughlan, Positive ground stroke observations in Japanese and Florida storms, in *Proceedings in Atmospheric Electricity*, 1983.

Browning, K., and R. Wexler, The determination of kinematic properties of a wind field using Doppler radar, *J. Appl. Met.*, *7*, 105–113, 1968.

Burke, C., and D. Jones, On the polarity and continuing currents in unusually large lightning flashes deduced from ELF events, *J. Atmos. Terr. Phys.*, *58*, 531–540, 1996.

Byrne, G., A. Few, and M. Stewart, Electric field measurements within a severe thunderstorm anvil, *J. Geophys. Res.*, *94*, 6297–6307, 1989.

Campistron, B., A. Huggins, and A. Long, Investigations of a winter mountain storm in Utah. Part III: Single-Doppler radar measurements of turbulence, *J. Atmos. Sci.*, *48*, 1306–1318, 1991a.

Campistron, B., A. Long, and A. Huggins, A method of retrieving turbulence parameters from volume processing of single-Doppler radar measurements, *J. Atmos. Oceanic. Tech.*, *8*, 491–505, 1991b.

Caranti, G., E. Avila, and M. Re, Charge transfer during individual collisions in ice growing from vapor deposition, *J. Geophys. Res.*, *90*, 6091–6098, 1991.

Caton, P., The measurement of wind and convergence by Doppler radar, in *In: Proc. 10th Weather Radar Conference*, 1963.

Chauzy, S., M. Chong, A. Delannoy, and S. Despian, The June 22 tropical squall line observed during COPT 81 experiment: Electrical signature associated with dynamical structure and precipitation, *J. Geophys. Res.*, *90*, 6091–6098, 1985.

Cifelli, R., and S. Rutledge, Vertical motion structure in maritime continent mesoscale convective systems: Results from a 50 MHz profiler, *J. Atmos. Sci.*, *51*, 2631–2652, 1994.

Cifelli, R., S. Rutledge, D. Boccippio, and T. Matejka, Horizontal divergence and vertical velocity retrievals from Doppler radar and wind profiler observations, *J. Atmos. Oceanic. Tech.*, *13*, –, 1996.

Cotton, W., and R. Anthes, *Storm and cloud dynamics*, San Diego, Academic Press, 1989.

Dinger, J., and R. Gunn, Electrical effects associated with a change in state of water, *Terr. Mag. Atmos. Elec.*, *51*, 477, 1946.

Doviak, R., and D. Zrnic, *Doppler radar and weather observations*, Academic Press, 1984.

Drake, J., Electrification accompanying the melting of ice particles., *Quart. J. Roy. Met. Soc.*, *94*, 176–191, 1968.

Drake, J., and B. Mason, Melting of small ice spheres and cones, *Quart. J. Roy. Met. Soc.*, *92*, 500–509, 1966.

Draper, W., and H. Smith, *Applied regression analysis*, John Wiley and Sons, 1981.

Eberhard, W., R. Cupp, and K. Healy, Doppler lidar measurement of profiles of turbulence and momentum flux, *J. Atmos. Oceanic. Tech.*, *6*, 809–819, 1989.

Engholm, C., E. Williams, and R. Dole, Meteorological and electrical conditions associated with positive cloud-to-ground lightning., *Mon. Wea. Rev.*, *118*, 470–487, 1990.

Ferrier, B., A double-moment multiple-phase four-class bulk ice scheme. Part II: Simulations of convective storms in different large-scale environments and comparisons with other bulk parameterizations, *J. Atmos. Sci.*, *52*, 1001–1033, 1995.

Findeisen, F., Die entstehung der 0 deg-isothermie und die fraktocumulus-bildung unter numbostratus, *Meteorologische Zeitschrift*, *57*, 49–54, 1940.

Fletcher, N., *The physics of rain clouds*, Cambridge University Press, 1962.

Fuquay, D., Positive cloud-to-ground lightning in summer thunderstorms, *J. Geophys. Res.*, *87*, 7131–7140, 1982.

Gal-Chen, T., Single-Doppler radar measurements of the convective planetary boundary layer, in *In: Proc 24th Conference on Radar Meteorology*, 1989.

Golub, G., and C. V. Loan, *Matrix Computations*, Johns Hopkins University Press, 1989.

Goto, Y., and K. Narita, Electrical characteristics of winter lightning, *J. Atmos. Terr. Phys.*, *57*, 449–458, 1995.

Gunn, K., and J. Marshall, The distribution with size of aggregate snowflakes, *J. Meteor*, *15*, 452–461, 1958.

Hallett, J., R. Sax, D. Lamb, and A. Ramachandramurty, Aircraft measurements of ice in Florida cumuli, *Quart. J. Roy. Met. Soc.*, *104*, 631–651, 1978.

Harris, F., Motion field characteristics of the evaporative base region of a stratiform precipitation layer as determined by andasce, in *In: Proc. 16th Radar Meteorology Conference*, 1975.

Hauser, D., F. Roux, and P. Amayenc, Comparison of two methods for the retrieval of thermodynamic and microphysical variables from Doppler radar measurements: Application to the case of a tropical squall line, *J. Atmos. Sci.*, *45*, 1285–1303, 1988.

Heckman, S., Why does a lightning flash have multiple strokes?, Ph.D. thesis, Massachusetts Institute of Technology, 1992.

Heymsfield, A., and M. Kajikawa, An improved approach to calculating terminal velocities of plate-like crystals and graupel, *J. Atmos. Sci.*, *44*, 1088–1099, 1987.

Hill, R., Interpretation of bipole patterns in a mesoscale storm, *Geophys. Res. Lett.*, *23*, 643–645, 1988.

Hobbs, P., *Ice physics*, Clarendon Press, 1974.

Houze, R. J., Structure and dynamics of a tropical squall-line system, *Mon. Wea. Rev.*, *105*, 1540–1567, 1977.

Houze, R. J., Observed structure of mesoscale convective systems and implications for large-scale heating, *Quart. J. Roy. Met. Soc.*, *115*, 425–461, 1989.

Hsie, E.-Y., R. Farley, and H. Orville, Numerical simulation of ice-phase convective cloud seeding, *J. Appl. Met.*, *19*, 950–977, 1980.

Hunter, S., T. Schuur, T. Marshall, and W. Rust, Electric and kinematic structure of the Oklahoma mesoscale convective system of 7 June 1989, *Mon. Wea. Rev.*, *120*, 2226–2239, 1992.

Jayaratne, E., C. Saunders, and J. Hallett, Laboratory studies of the charging of soft-hail during ice crystal interactions, *Quart. J. Roy. Met. Soc.*, *109*, 609–630, 1983.

Keith, W., and C. Saunders, Further laboratory studies of the charging of graupel during ice crystal interactions, *Atmos. Res.*, *25*, 445–464, 1990.

Kikuchi, K., On the positive electrification of snow crystals in the process of their melting (III): the relationship between air bubble concentration and charge generated in ice specimen during their melting, *J. Met. Soc. Japan*, *43*, 343–350, 1965a.

Kikuchi, K., On the positive electrification of snow crystals in the process of their melting (IV): charge of droplets produced from bursting of air bubbles in ice specimen, *J. Met. Soc. Japan*, *43*, 351–357, 1965b.

Klimowski, B., Radar observations of the development of rear inflow within a high plains squall line, in *Proc. 26th AMS International Conf. on Radar Meteorology*, 1993.

Koenig, L., Numerical modeling of ice deposition, *J. Atmos. Sci.*, *28*, 226–237, 1971.

Koscielny, A., R. Doviak, and R. Rabin, Statistical considerations in the estimation of divergence from single-Doppler radar and application to prestorm boundary-layer observations, *J. Appl. Met.*, *21*, 197–210, 1982.

Krehbiel, P., An analysis of the electric field change produced by lightning, Ph.D. thesis, University of Manchester, 1981.

Krehbiel, P., The electrical structure of thunderstorms, in *The Earth's electrical environment*, National Academy Press, 1986.

Kropfli, R., Single Doppler radar measurements of turbulence profiles in the convective boundary layer, *J. Atmos. Oceanic. Tech.*, *3*, 305–314, 1986.

Leary, C., and R. J. Houze, Melting and evaporation of hydrometeors in precipitation from the anvil clouds of deep tropical convection, *J. Atmos. Sci.*, *36*, 669–679, 1979.

Lhermitte, R., Turbulent air motion as observed by Doppler radar, in *In: Proc. 13th Radar Meteorology Conference*, 1968.

Lhermitte, R., Note on the observation of small-scale atmospheric turbulence by Doppler radar techniques, *Rad. Sci.*, *4*, 1241–1246, 1969.

Lhermitte, R., and D. Atlas, Precipitation motion by pulse Doppler, in *In: Proc. 9th Weather Radar Conference*, 1961.

Ligda, M., The radar observation of lightning, *J. Atmos. Terr. Phys.*, *9*, 326–346, 1956.

Lin, C., and R. Stewart, Mesoscale circulation initiated by melting snow, *J. Geophys. Res.*, *91*, 13299–13302, 1986.

Lin, Y.-L., R. Farley, and H. Orville, Bulk parameterization of the snow field in a cloud model, *J. Clim. Appl. Met.*, *22*, 1065–1092, 1983.

Livingston, J., and E. Krider, Electric fields produced by Florida thunderstorms, *J. Geophys. Res.*, *83*, 385–401, 1978.

Lo, K., and R. Passarelli, The growth of snow in winter storms: An airborne observational study, *J. Atmos. Sci.*, *39*, 697–706, 1982.

Locatelli, J., and P. Hobbs, Fall speeds and masses of solid precipitation particles, *J. Geophys. Res.*, *79*, 2185–2197, 1974.

Lyons, W., Sprite observations above the U.S. High Plains in relation to their parent thunderstorm systems *(in review)*, *J. Geophys. Res.*, 1996.

Mach, D., and W. Rust, Two-dimensional velocity, optical risetime, and peak current estimates for natural positive lightning return strokes, *J. Geophys. Res.*, *98*, 2635–2638, 1993.

MacReady, P., and A. Proudfit, Self-charging of melting ice, *Quart. J. Roy. Met. Soc.*, *91*, 54–59, 1965a.

MacReady, P., and A. Proudfit, Thunderstorm hydrometeor charging, *Quart. J. Roy. Met. Soc.*, *91*, 44–53, 1965b.

Magono, C., and K. Kikuchi, On the positive electrification of snow crystals in the process of their melting, *J. Met. Soc. Japan*, *41*, 270–277, 1963.

Magono, C., and K. Kikuchi, On the positive electrification of snow crystals in the process of their melting (II), *J. Met. Soc. Japan*, *43*, 331–342, 1965.

Markson, R., and B. Anderson, Inverted cloud polarity, in *Proc. 8th International Conference on Atmospheric Electricity, Uppsala, Sweden*, 1988.

Marshall, T., W. Rust, W. Winn, and K. Gilbert, Electrical structure in two thunderstorm anvil clouds, *J. Geophys. Res.*, *94*, 2171–2181, 1989.

Marshall, T., M. Stolzenburg, and W. Rust, Electric field measurements above mesoscale convective systems *(in review)*, *Mon. Wea. Rev.*, *124*, –, 1996.

Mason, B., *The physics of clouds, 2nd ed.*, Oxford University Press, 1971.

Matejka, T., Concurrent extended velocity-azimuth display (CEVAD) analysis of single-Doppler radar data, in *Proc. 26th AMS International Conf. on Radar Meteorology*, 1993.

Matejka, T., and R. Srivastava, An improved version of the extended VAD analysis of single-Doppler radar data, *J. Atmos. Oceanic. Tech.*, *8*, 453–466, 1991.

Mazur, V., X. Shao, and P. Krehbiel, "spider" intracloud and positive cloud-to-ground lightning in the late stage of Florida storms, in *Proc. 1994 ICOLSE Conference*, 1994.

Moore, C., and B. Vonnegut, The thundercloud, in *Lightning, Vol. 1*, Academic Press, 1977.

Moore, C., B. Vonnegut, and A. Botka, An assessment of thunderstorm electrification and precipitation in thunderstorms, in *Recent Advances in Atmospheric Electricity*, Pergamon, New York, 1958.

O'Brien, J., Alternative solutions to the classical vertical velocity problem, *J. Appl. Met.*, *9*, 197–203, 1970.

Orville, H., and F. Kopp, Numerical simulation of the life history of a hailstorm, *J. Atmos. Sci.*, *34*, 1596–1618, 1977.

Orville, R., R. Weisman, R. Pyle, R. Henderson, and R. O. Jr., Cloud-to-ground flash characteristics from June 1984 through May 1985, *J. Geophys. Res.*, *92*, 5640–5644, 1987.

Orville, R., R. Henderson, and L. Bosart, Bipole patterns revelaed by lightning locations in mesoscale storm systems, *Geophys. Res. Lett.*, *15*, 129–132, 1988.

Passarelli, R., An approximate analytical model of the vapor deposition and aggregation growth of snowflakes, *J. Atmos. Sci.*, *35*, 118–124, 1978.

Potter, B., Improvements to a commonly used cloud microphysical bulk parameterization, *J. Appl. Met.*, *30*, 1040–1042, 1991.

Press, W., S. Teukolsky, W. Vetterling, and B. Flannery, *Numerical recipes in C: the art of scientific computing, 2nd ed.*, Cambridge University Press, 1992.

Pruppacher, H., and J. Klett, *Microphysics of clouds and precipitation*, D. Reidel, 1978.

Randell, S., S. Rutledge, R. Farley, and J. H. Jr., A modeling study on the early electrical developent of tropical convection: Continental and oceanic (monsoon) storms, *Mon. Wea. Rev.*, *122*, 1852–1877, 1994.

Rangno, A., and P. Hobbs, Ice particle concentrations and precipitation development in small continental cumuliform clouds, *Quart. J. Roy. Met. Soc.*, *120*, 573–601, 1994.

Rawlings, J., *Applied regression analysis: a research tool*, Wadsworth and Brooks/Cole, 1988.

Rust, W., Positive cloud-to-ground lightning, in *The earth's electrical environment*, National Academy Press, 1986.

Rutledge, S., and P. Hobbs, The mesoscale and microscale structure and organization of clouds and precipitation in midlatitude cyclones. viii: A model for the "seeder-feeder" process in warm-frontal rainbands, *J. Atmos. Sci.*, *40*, 1185–1206, 1983.

Rutledge, S., and D. MacGorman, Cloud-to-ground lightning activity in the 10-11 June 1985 MCS observed during PRE-STORM, *Mon. Wea. Rev.*, *116*, 1409–1430, 1988.

Rutledge, S., C. Lu, and D. MacGorman, Positive cloud-to-ground lightning in mesoscale convective systems, *J. Atmos. Sci.*, *47*, 2085–2100, 1990.

Rutledge, S., E. Williams, and W. Petersen, Lightning and electrical structure of mesoscale convective systems, in *Atmospheric Research*, Elsevier, 1995.

Saunders, C., Thunderstorm electrification laboratory experiments and charging mechanisms, *J. Geophys. Res.*, *99*, 10773–10779, 1994.

Saunders, C., W. Keith, and R. Mitzeva, The effect of liquid water content on thunderstorm charging, *J. Geophys. Res.*, *96*, 11007–11017, 1991.

Schuur, T., B. Smull, W. Rust, and T. Marshall, Electrical and kinematic structure of the stratiform precipitation region trailing an Oklahoma squall line, *J. Atmos. Sci.*, *48*, 825–842, 1991.

Sentman, D., *EOS Suppl.*, *67*, 1069, 1987.

Shao, X., The development and structure of lightning discharges observed by VHF radio interferometer., Ph.D. thesis, New Mexico Institute of Mining and Technology, 1993.

Shepherd, T., W. Rust, and T. Marshall, Electric fields and charges near 0 deg c in stratiform clouds *(in review)*, *Mon. Wea. Rev.*, *124*, –, 1996.

Siggia, A., and J. Holmes, One-pass velocity unfolding for VVP analysis, in *Proc. 25th AMS International Conf. on Radar Meteorology*, 1991.

Smull, B., and R. J. Houze, Rear inflow in squall lines with trailing stratiform precipitation, *Mon. Wea. Rev.*, *115*, 2869–2889, 1987.

Srivastava, R., T. Matejka, and T. Lorello, Doppler radar study of the trailing anvil region associated with a squall line, *J. Atmos. Sci.*, *43*, 356–377, 1986.

Stewart, R., J. Marwitz, and J. Pace, Characteristics through the melting layer of stratiform clouds, *J. Atmos. Sci.*, *41*, 3227–3237, 1984.

Stolzenburg, M., T. Marshall, W. Rust, and B. Smull, Horizontal distribution of electrical and meteorological conditions across the stratiform region of a mesoscale convective system, *Mon. Wea. Rev.*, *122*, 1777–1797, 1994.

Szeto, K., C. Lin, and R. Stewart, Mesoscale circulations forced by melting snow. Part I: Basic simulations and dynamics, *J. Atmos. Sci.*, *45*, 1629–1641, 1988a.

Szeto, K., R. Stewart, and C. Lin, Mesoscale circulations forced by melting snow. Part II: Application to meteorological features, *J. Atmos. Sci.*, *45*, 1642–1650, 1988b.

Takahashi, T., Riming electrification as a charge generation mechanism in thunderstorms, *J. Atmos. Sci.*, *35*, 1536–1548, 1978.

Teer, T., and A. Few, Horizontal lightning, *J. Geophys. Res.*, *79*, 3426–3441, 1974.

Waldteufel, P., and H. Corbin, On the analysis of single-Doppler radar data, *J. Appl. Met.*, *18*, 532–542, 1979.

Williams, E., The tripole structure of thunderstorms, *J. Geophys. Res.*, *94*, 13151–13167, 1989.

Williams, E., The Schumann resonance: a global tropical thermometer, *Science*, *256*, 1184–1187, 1992.

Williams, E., Comment on "Thunderstorm electrification laboratory experiments and charging mechanisms", *J. Geophys. Res.*, *100*, 1503–1505, 1995.

Williams, E., C. Cooke, and K. Wright, Electrical discharge propagation in and around space charge clouds, *J. Geophys. Res.*, *90*, 6059–6070, 1985.

Williams, E., R. Zhang, and J. Rydock, Mixed-phase microphysics and cloud electrification, *J. Atmos. Sci.*, *48*, 2195–2203, 1991.

Williams, E., R. Zhang, and D. Boccippio, Microphysical growth state of ice particles and large-scale electrical structure of clouds, *J. Geophys. Res.*, *99*, 10787–10792, 1994.

Willis, P., and J. Hallett, Microphysical measurements from an aircraft ascending with a growing isolated maritime cumulus tower, *J. Atmos. Sci.*, *48*, 283–300, 1991.

Willis, P., and A. Heymsfield, Structure of the melting layer in mesoscale convective system stratiform precipitation, *J. Atmos. Sci.*, *46*, 2008–2025, 1989.

Wilson, C., Investigations on lightning discharges and on the electric field of thunderstorms, *Phil. Trans. R. Soc. Ser. A*, *221*, 73–115, 1920.

Wilson, C., A theory of thundercloud electricity, *Proc. Roy. Soc. (A)*, *236*, 297–317, 1956.

Wilson, D., Doppler radar studies of boundary-layer wind profile and turbulence in snow conditions, in *In: Proc. 14th Radar Meteorology Conference*, 1970.

Wisner, C., H. Orville, and C. Myers, A numerical model of a hail-bearing cloud, *J. Atmos. Sci.*, *29*, 1160–1181, 1972.

Wong, C., A global lightning transients detector, Master's thesis, Massachusetts Institute of Technology, 1996.

Wurman, J., S. Heckman, and D. Boccippio, A bistatic multiple-Doppler radar network, *J. Appl. Met.*, *32*, 1802–1814, 1993.

Zhang, D., and K. Gao, Numerical simulation of an intense squall line during 10-11 June 1985 PRE-STORM. Part II: Rear inflow, surface pressure perturbations and stratiform precipitation, *Mon. Wea. Rev.*, *117*, 2067–2093, 1989.

Ziegler, C., Retrieval of thermal and microphysical variables in observed convective storms. Part I: Model development and preliminary testing, *J. Atmos. Sci.*, *42*, 1487–1509, 1985.

Zipser, E., Mesoscale and convective scale downdrafts as distinct components of squall-line structure, *Mon. Wea. Rev.*, *105*, 1568–1589, 1977.

Zrnic, D., N. Balakrishnan, C. Ziegler, V. Bringi, K. Aydin, and T. Matejka, Polarimetric signatures in the stratiform region of a mesoscale convective system, *J. Appl. Met.*, *32*, 678–693, 1993.

6530-72